Syracuse University

SURFACE

Dissertations - ALL

SURFACE

May 2019

# Geometric and Topological Aspects of Soft & Active Matter

Suraj Shankar
*Syracuse University*

Follow this and additional works at: https://surface.syr.edu/etd

Part of the Physical Sciences and Mathematics Commons

## Recommended Citation

Shankar, Suraj, "Geometric and Topological Aspects of Soft & Active Matter" (2019). *Dissertations - ALL*. 1048.
https://surface.syr.edu/etd/1048

This Dissertation is brought to you for free and open access by the SURFACE at SURFACE. It has been accepted for inclusion in Dissertations - ALL by an authorized administrator of SURFACE. For more information, please contact surface@syr.edu.

# ABSTRACT

Topological and geometric ideas are now a mainstay of condensed matter physics, underlying much of our understanding of conventional materials in terms of defects and geometric frustration in ordered media, and protected edge states in topological insulators. In this thesis, I will argue that such an approach successfully identifies the relevant physics in metamaterials and living matter as well, even when traditional techniques fail. I begin with the problem of kirigami mechanics, i.e., designing a pattern of holes in a thin elastic sheet to engineer a specific mechanical response. Using an electrostatic analogy, I show that holes act as sources of geometric incompatibility, a feature that can fruitfully guide design principles for kirigami metamaterials. Next I consider nonequilibrium active matter composed of self-driven interacting units that exhibit large scale collective and emergent behaviour, as commonly seen in living systems. By focusing on active liquid crystals in two dimensions, with both polar and nematic orientational order, I show how broken time-reversal symmetry due to the active drive allows polar flocks on a curved surface to support topologically protected sound modes. In an active nematic, activity instead causes topological disclinations to become spontaneously motile, driving defect unbinding to organize novel phases of defect order and chaos. In all three cases, geometric and topological ideas enable the relevant degrees of freedom to be identified, allowing complex phenomena to be treated in a tractable fashion, with novel and surprising consequences along the way.

# Geometric and Topological Aspects of Soft & Active Matter

By

**Suraj Shankar**

B. Tech (Honours) Chemical Engineering
Indian Institute of Technology Madras (IIT-M), 2014

Dissertation
Submitted in Partial Fulfillment of the Requirements
for the degree of
Doctor of Philosophy in Physics

Syracuse University
May 2019

Copyright © 2019 Suraj Shankar

All rights reserved.

*Dedicated to amma and appa...*

# ACKNOWLEDGEMENTS

It has been a remarkable five year journey that wouldn't have been possible without the help and support of numerous individuals. I shall do my best to acknowledge everyone here. First and foremost, I am eternally grateful and indebted to Cristina Marchetti and Mark Bowick for taking me under their wing, helping shape my scientific identity, while still allowing me to freely explore my interests. Their undiluted passion for physics is deeply inspiring and is a constant reminder of why science is exciting, even during the gloomiest of times. I have learnt a great deal of physics from them over the years, but more importantly, they have imparted upon me the importance of asking the right questions as part of being a good researcher. I cherish all the open ended, free flowing conversations and discussions we have had, and hope to have many more in the future.

I am incredibly fortunate to have collaborated with Sriram Ramaswamy, whom I greatly admire. His unbridled excitement combined with a deep insight into various matters of interest (scientific or otherwise) have left me awestruck numerous times. At KITP, I am grateful to Boris Shraiman for giving me perspective on the role of physics in biology, and for making me realize that biologically relevant questions can often pose genuinely hard and fundamental problems for physicists. I feel extraordinarily lucky to have had such a diverse set of strong mentors who have influenced me both scientifically and personally. I thank Sebastian Streichan for teaching me much of the biology I know now, all while entertaining my many questions that highlighted my ignorance as a theorist. I've thoroughly enjoyed all my conversations with Zvonimir Dogic, learning much about active nematics and soft matter in the process. Teng Zhang, Joey Paulson, Jennifer Schwarz and Simon Catterall served as the perfect thesis committee and ensured my remote defense went smoothly. I'd also like to specially mention Yuan Yuan, Peter Horn and Simon Catterall for their absolutely marvelous courses on Riemannian geometry, algebraic topology and quantum field theory respectively. Finally, I am thankful for the support and encouragement I received in IIT Madras from P. B. Sunil Kumar, L. Sriramkumar, Suresh Govindarajan, and the inspiration from V. Balakrishnan, that motivated me to pursue a career in physics.

In my first year at Syracuse, Nupur Gokhale, Aishik Barua, Lois Mrinalini, Pratyusha Dasari and Thomas J West were a delightfully queer group I didn't know I needed. I thank Swetha Bhagwat for being a close friend and a partner in crime through our many crazy adventures. I ardently treasure the various feasts (and raki), conversations and trips with Gizem Şengör, Cem Eröncel and Francesco Serafin, and the numerous game nights along with Raghav Govind Jha, Nouman Butt, Anam Mano, Sourav Bhabesh, Ogan Öszoy and Prashant Mishra. Thank you Flaviyan Jerome Irudayanathan, Kiran Bhimani and Nandhini Rajagopal for the many sumptuous dinners filled with all sorts of random and playful discussions and Preeti Sahu for being a wonderful officemate who partook in all of my silliness. Special thanks to both Nandhini and Preeti for the exciting music sessions and singing escapades. I enormously appreciate my discussions with Daniel Sussman, Matteo Paoluzzi, Matthias Merkel, David Yllanes, Michael Moshe from whom I have learnt many fascinating things in diverse topics. I also thank Oksana Manyuhina, Pragya Srivastava, Benjamin Loewe, Adam Patch, Michael Czajkowski, Gonca Erdemci-Tandogan and Kazage Utuje for useful and entertaining conversations at different times throughout the years.

My stay in Santa Barbara has been thoroughly enriched by my friends both in

UCSB and KITP. I have had great fun chatting science with Eyal Karzbrun, Noah Mitchell, Alex Tayar, Jie Zhang, Shahriar Shadkhoo, Le Yan, Itamar Kolvin, Rémi Boros, Dillon Cislo, Chaitanya Murthy, Linnea Lemma and Bez Lemma. In addition, my visits to KITP have exposed me to a number of diverse topics in physics, allowing me to develop an appreciation for fields vastly different from my own. I strongly believe that this is KITP's greatest strength and I am incredibly grateful for having received the opportunity to come here. I heartily enjoyed the varied excursions I embarked on with Soorya Gopal and Rachel Redberg and the classical music expositions with Puneet Chakravarthula. I would also like to sincerely thank the administrative staff, particularly Patty Whitmore and Yudaisy Salomón Sargentón at Syracuse, and Bibi Rojas, Lori Staggs and Lisa Stewart at KITP for being ever welcoming, helpful and always cheering up everyone around them.

Finally, but most importantly, I would like to thank my parents and family for unconditionally believing in me and letting me freely follow my passion. Thank you for bearing with my impatience, the missed and bad quality Skype calls, the time difference and the geographical separation. Without your constant support and encouragement, this would not have been possible.

# Contents

**1 Introduction 1**

1.1 Topology, order and phase transitions in condensed matter . . . . . . 1

1.1.1 Topological defects in ordered media . . . . . . . . . . . . . . 2

1.1.2 Topological insulators and beyond . . . . . . . . . . . . . . . . 5

1.2 Geometry, mechanics and frustration in two-dimensional matter . . . 7

1.2.1 From membranes to metamaterials . . . . . . . . . . . . . . . 8

1.3 Active matter . . . . . . . . . . . . . . . . . . . . . . . . . . . . . 11

1.4 Outline . . . . . . . . . . . . . . . . . . . . . . . . . . . . . . . . . 14

**2 Mechanics of kirigami metamaterials: stress relief by elastic charges 17**

2.1 Geometry in elasticity . . . . . . . . . . . . . . . . . . . . . . . . 18

2.1.1 Geometric mechanics of kirigami . . . . . . . . . . . . . . . . 20

2.2 Table-top observations: Multistability and curvature localization . . . 21

2.3 Image charges in thin plate elasticity . . . . . . . . . . . . . . . . 24

2.3.1 Planar frames: Sheared annulus . . . . . . . . . . . . . . . . . 25

2.3.2 Arbitrary planar frames: General strategy . . . . . . . . . . . 29

2.3.3 Buckled frames: Screening of charges . . . . . . . . . . . . . . 33

2.4 Nonlinear mechanics of a square frame . . . . . . . . . . . . . . . . 36

2.4.1 Pre-buckling planar mechanics . . . . . . . . . . . . . . . . . . 38

2.4.2 Post-buckling mechanics: Multiscaling . . . . . . . . . . . . . . 39
2.4.3 Buckling transition . . . . . . . . . . . . . . . . . . . . . . . . 43
2.4.4 Local deformation field . . . . . . . . . . . . . . . . . . . . . . 44
2.5 Kirigami as interacting charges: Relaxing pre-stress . . . . . . . . . . 45

**3 Melting the active nematic: defect unbinding and the motile BKT class 49**

3.1 Active nematics . . . . . . . . . . . . . . . . . . . . . . . . . . . . 49
3.2 The paradox: do ordered active nematics exist? . . . . . . . . . . . . 52
3.3 Defects as quasiparticles . . . . . . . . . . . . . . . . . . . . . . . . 54
3.3.1 Hydrodynamic model . . . . . . . . . . . . . . . . . . . . . . . 54
3.3.2 Defect positional dynamics . . . . . . . . . . . . . . . . . . . . 56
3.3.3 Defect orientational dynamics . . . . . . . . . . . . . . . . . . . 58
3.3.4 Including noise . . . . . . . . . . . . . . . . . . . . . . . . . . . 61
3.4 Defect unbinding and re-entrant melting . . . . . . . . . . . . . . . . 64
Appendix 3.A Derivation of equations of motion for ±1/2 disclinations . . 70
Appendix 3.B Derivation of polarization dynamics of the +1/2 disclination 78
Appendix 3.C Non-quasistatic solution for +1/2 disclination: Rotational diffusion . . . . . . . . . . . . . . . . . . . . . . . . . . . . . . . . . 82

**4 Topological sound modes and collective motion on curved geometries 86**

4.1 Flocks, curvature & quantum Hall fluids . . . . . . . . . . . . . . . . 86
4.1.1 Toner-Tu equations on a curved surface . . . . . . . . . . . . . 90
4.2 Polar flock on a sphere . . . . . . . . . . . . . . . . . . . . . . . . . . 92
4.2.1 The steady state of a polar flock on the sphere . . . . . . . . . 92
4.2.2 Linearizing about the steady state . . . . . . . . . . . . . . . . . 96

4.3 Symmetry protected topological sound . . . . . . . . . . . . . . . . . . 101

4.4 Polar flock on a negatively curved surface . . . . . . . . . . . . . . . . 108

Appendix 4.A Spherical flock: steady state and linearization for $\lambda_2, \lambda_3 \neq 0$ 112

Appendix 4.B Polar flock on the catenoid . . . . . . . . . . . . . . . . . . 115

4.B.1 Linearizing about the steady state . . . . . . . . . . . . . . . . . 116

**5 Discussion and conclusion** **119**

**Bibliography** **184**

# List of Tables

1 A summary of the effective spring constants $k_{\text{eff}}$ for different frame aspect ratios $w/L$, for planar and buckled configurations. . . . . . . . 41

2 A summary of the parameters redefinitions in the model. . . . . . . . 99

# List of Figures

1 Lowest strength topological defects in two-dimensional orientationally ordered media. The red dots indicate the defect cores. In the case of polar order in the plane, the order parameter manifold is the circle $S^1$ and defects are classified by the fundamental group $\pi_1(S^1) = \mathbb{Z}$ (the integers). For planar nematic order, the order parameter manifold is instead the real projective line $RP^1$ whose fundamental group is $\pi_1(RP^1) = \mathbb{Z}/2$ (half-integers). . . . . . . . . . . . . . . . . . . . . . . . . 3

2 The quantum Hall triumvirate (reproduced from Ref. [57]) in electronic media. The years refer to the corresponding time of discovery. Unlike the quantum Hall effect that requires an external magnetic field to supports charge currents on the edge, both quantum spin and anomalous Hall effects rely on spin-orbit coupling. In addition, the quantum spin Hall effect being time-reversal invariant supports spin currents on the edge, while the anomalous Hall effect breaks time reversal symmetry due to ferromagnetic ordering. . . . . . . . . . . . . . . . . . . . . . . . . 6

3 Graphene kirigami structures (reproduced from Ref. [150]) patterned by lithography compared against their macroscopic counterparts in paper. 10

4 Some examples of active matter displaying the diversity in scale and of constituent active units. Images of the active colloids and vibrated grains have been reproduced from Ref. [224] and Ref. [225] respectively. The active metamaterial example is a topological lattice with individually motorized gyroscopes, taken from Ref. [226]. . . . . . . . 12

5 Kirigami and frames. (a) A periodic kirigami pattern composed of square frames. (b) The response of the pattern in (a) to a large deformation when stretched along the $x$ direction, enabled by the escape of the frame elements into the third dimension. (c) An individual square frame of size $L$, frame width $w$ and hole dimension $H = L-2w$, forming the building block of the pattern in (a). (d-f) Different locally stable configurations of a square frame subjected to an external force along its diagonal (in the horizontal direction), distinguished by the relative orientations of the four inner corners: (d) The left and right inner corners are curved up and down, respectively (denoted by $+$ and $-$, respectively), whereas the top and bottom inner corners point to the left (as shown by the red needles normal to the surface and denoted by L. This configuration is thus denoted by $+:\mathrm{L/L}:-$). (e) The left and right corners both point up here, while the top and bottom corners point in opposite directions, hence denoted by $+:\mathrm{L/R}:+$. (f) Here both the left and right corners once again point up, but the top and bottom corners point in the same direction, hence $+:\mathrm{L/L}:+$. The remaining configuration $+:\mathrm{L/R}:-$ is not stable at this hole size. . . 22

6 The analytic solution (in red) for an annulus subjected to pure external shear ($\sigma_0$) on its external boundary. The undeformed annulus is shown in a dashed black line. . . . . . . . . . . . . . . . . . . . . . . . . . . 26

7 The geometric function $\Phi_{1,2}(w/L)$ that captures the aspect ratio dependence of the induced quadrupolar charge under plane-stress conditions (a), or plane-strain conditions (b). . . . . . . . . . . . . . . . . . . . . . 32

8 The deformation of a square frame (as calculated by Eq. 2.15) constrained to be planar and subjected to a fixed force $F/(YL) = 0.1$ along the diagonal (from the lower left to the upper right). The frame size is fixed at $L = 1$ and hole size varied with (a) $H = 0.5$, (b) $H = 0.6$ and (c) $H = 0.8$. The configurations are colored by the energy density on a linear scale from blue (low) to white (high). Although the force is fixed, for an appropriate choice of the effective thickness, and if allowed to escape into the third dimension, configuration (a) remains planar, (b) is planar but at the buckling threshold, and (c) is beyond the critical force threshold for buckling. Note that the interior angles of the frames deviate from $\pi/2$ with the application of the force, signalling the formation of localized partial disclinations that concomitantly focus stresses as well. . . . . . . . . . . . . . . . . . . . . . . . . . . . . 34

9 Three dimensional energy minimizing configurations after buckling, obtained by a finite element computation. (a) Triangular and (b) circular frames subjected to uniaxial forces applied at opposing ends. The colour refers to the local energy density ranging from blue (low) to white (high). The screening charges responsible for this energy distribution are still of a quadrupolar nature, though they are evenly smeared out in the annular geometry. The triangular hole being incommensurate with the symmetry of the quadrupole, frustrates it and as a result, part of the charge is spread on one side of the triangle, while the rest concentrates at the three corners. This leads to the observed curvature localization. . . . . . . . . . . . . . . . . . . . . . . . . . . . . . . 36

10 The effective spring constant $k_{\mathrm{eff}}$ for a planar frame as a function of the aspect ratio $w/L$. Parameter values used are $L = 1$ and $t = 5 \times 10^{-4}$. The blue dots are from the numerical simulations. The solid line is the analytical prediction in Eq. 2.22 with no fitting parameters. . . . . . 39

11 Experimental measurements of square frames subjected to tensile load along the diagonal. (a) Force-displacement curves for frames with $w/L = 0.25$ and thicknesses varying between 0.01 and 0.02 cm. (b) When normalized by thickness, curves collapse at small displacement, confirming that the frames are planar at this regime. (c) When normalized by thickness cubed, curves collapse in the post-buckling regime, confirming that energy increase is predominately bending. (d) Effective spring constant in the post-buckled regime as function of frame aspect ratio $w/L$ in the intermediate and large hole regimes for a frame of thickness $t = 0.0198$ cm, confirming the multiscale behavior in (Table 1). The curve in the large hole regime ($w/L < 1/8$) is linear as given in Eq. 2.26, while the curve in the intermediate hole regime ($1/8 < w/L < 1/4$) corresponds to Eq. 2.24, with the prefactor $c$ and regularizing cutoff $a$ taken as fitting parameters. (e) Critical displacement as function of thickness for a frame of $w/L = 0.25$, growing as $t^{1.9}$ (solid line), in good agreement with Eq. 2.27. (f) Critical displacement as function of the frame's aspect ratio for a frame of thickness $t = 0.00794$ cm in the intermediate hole size regime, in agreement with Eq. 2.27 (solid line). 42

12 Comparison between the predicted and observed deformations in a pulled frame right after buckling (a) An undeformed frame with a laser printed Cartesian mesh (gray) and a set of parametric lines (red) fitted to the printed mesh. (b) A deformed frame. Here, the red lines are computed from theory using the original parametric lines as a starting point and the fictitious elastic charges as fitting parameters. . . . . . 45

13 A regular conical annulus with an angle deficit. When flattened under a piece of acrylic with a small gap, the thin sheet forms wrinkles. Including azimuthal slits (middle row) does not affect the pattern of wrinkles, while a radial array of slits (bottom row) results in azimuthally aligned quadrupoles that minimize the interaction energy with the background stress. Hence when flattened, the radial kirigami pattern locally relaxes stresses allowing the material to accommodate the curvature of the cone without wrinkling. . . . . . . . . . . . . . . . . . . . . . . . . . 46

14 A conical annulus with an angle surplus (e-cone). In the three images on the left, the e-cone (with and without the kirigami slit pattern) achieves its equilibrium shape in 3D. On the right, the same annulus is flattened under an acrylic plate. Both the intact non-perforated e-cone as well as the one with azimuthal slits develop wrinkles when flattened, while the radial kirigami pattern of slits relaxes stresses in the flattened e-cone (as in the case of the regular cone shown in Fig. 13), leaving it devoid of wrinkles. . . . . . . . . . . . . . . . . . . . . . . . . . 47

15 (a) Phase diagram in the noise ($\eta$) and density ($\rho_0$) plane, obtained from a numerical investigation of a particle model for 2D active nematics, reproduced from Ref. [348]. Disclinations in two experimental model systems - (b) Reconstituted active nematics assembled from microtubule bundles and kinesin motor complexes depleted to an oil-water interface [349], (c) cellular nematics organized by proliferating a monolayer of spindle shaped fibroblasts [258]. The spontaneous propulsion of $+1/2$ defects in active nematics shown as temporal snapshots (from top to bottom) in two distinct systems - (d) Microtubule-kinesin active nematic film [273] and (e) vibrated granular nematic [225]. In both (d) and (e), the $+1/2$ defect (red) is self-propelled, while the $-1/2$ defect (green) remains largely static. . . . . . . . . . . . . . . . . . . . . . . . . 50

16 Potential $V(r)$ for a neutral defect pair for the configuration in which the direction of motility of the $+1/2$ disclination points away from the $-1/2$ and is held fixed. This naïve picture suggests that incipient active defect pairs have an exponentially small, but finite, rate $\propto e^{-V(r_c)/T}$ ($T$ is the temperature) to overcome the barrier at low temperature, and hence always unbind. . . . . . . . . . . . . . . . . . . . . . . . . . . . . 53

17 The active backflow due to the nematic distortion of a ±1/2 disclination. The white lines indicate the nematic director orientation $\hat{\mathbf{n}}$ and the black arrows, the flow velocity $\mathbf{u}$ (with the colour map being $|\mathbf{u}|$). The red arrow is $\mathbf{e} = a\boldsymbol{\nabla} \cdot \mathbf{Q}(\mathbf{r}^{+})$, the geometric polarity for the $+1/2$ disclination. The flow field for the $+1/2$ disclination has a characteristic double vortex structure, while the $-1/2$ disclination presents a six-fold symmetric flow field. The flow at the core of the $+1/2$ defect is non-vanishing and is directed towards the comet head here (opposite to $\mathbf{e}$), as is the case for an extensile active nematic ($\alpha < 0$) plotted here. For a contractile active nematic ($\alpha > 0$), the arrows of flow reverse direction. 56

18 Configurations of defect pairs whose orientations, for an imposed fixed separation, are stable to transverse fluctuations of the $+1/2$ polarization(s). The active backflow is shown in blue and the director configuration in black. The polarization and force on each $+1/2$ defect is shown in red and in purple respectively. The top row shows a neutral $\pm 1/2$ defect pair orientationally stable for (a) extensile ($v < 0$) and (b) contractile ($v > 0$) systems. Similarly, in the bottom row we have a pair of $+1/2$ defects that are orientationally stable. The far field nematic texture for these two-defect configurations has an aster-like structure when (c) extensile ($v < 0$) and a vortex-like structure when (d) contractile ($v > 0$). . . . . . . . . . . . . . . . . . . . . . . . . . . . 60

19 Phase boundary in the $|v| - T$ plane (Eq. 3.26) for different values of $\mu\gamma$. The region enclosed by the curve $|v_c(T)|$ for a given $\mu\gamma$ corresponds to the ordered nematic. . . . . . . . . . . . . . . . . . . . . . . . . . . . 68

20 Steady-state statistics for a ±1/2 defect pair in a periodic box of size $L = 50a$ ($T/T_c^{\rm eq} = 0.51$, all other parameters are unity). (a) The pair separation distribution $\rho_{ss}(\mathbf{r})$ for low ($|v| = 0.5, 1.2$, bound phase) and high ($|v| = 1.5$, unbound phase) activity, suggesting that Eq. 3.26 which gives $|v_c| \simeq 2.06$, overestimates the unbinding threshold. (b) The distribution of the relative angle ($\Delta = \theta - \psi$) between the polarization $\mathbf{e}$ and the force $\mathbf{F}$ on the $+1/2$ defect for extensile (□) and contractile (◯) systems. . . . . . . . . . . . . . . . . . . . . . . . . . . . 69

21 (a) The normalized density profile of a polar flock on a sphere given in Eq. 4.12, for $\eta = 0.5$ (blue), 1 (orange) and 2 (green). (b) The density and polarization profiles for $\eta = 2$, now shown on the sphere. The color describes the density from the maximum (red) at the center of the polar band to $\rho_c$ (blue) at the poles of the sphere. The polarization also vanishes at the poles. . . . . . . . . . . . . . . . . . . . . . . . . 94

22 The peak (maximum) density at the equator on a sphere, as we vary the mean density $\rho_0$. For $\rho_0 < \rho_c$, we are in the disordered phase with $\rho_{ss}(\pi/2) = \rho_0$. For $\rho_0 > \rho_c$, we have a polar band with the density profile given in Fig. 21. The density reaches its maximum at the center of the band and grows with $\rho_0$, with a slope $A_\eta > 1$. When the convective parameter $\lambda \to 0$, $\eta \to 0$, resulting in $A_\eta \to 1$ and we go back to the homogeneous profile as in the flat plane. . . . . . . . . . . 97

23 The relevant (slow) sound modes. (a) $m = 0$ and the gap between the two bands is closed. (b) and (c) are the dispersion bands for $m = 0.2$ (Eq. 4.26) and we directly see that a gap has opened in the real part of the spectrum, while the imaginary part of the frequency has a single crossing line at $q_y = 0$. The variables are chosen to be $\theta_0 \simeq 78°$, $\alpha \simeq 2.03$, $c_{||} \simeq 1.03$ and $\beta = c_\perp = 1$. . . . . . . . . . . . . . . . . . . . . . 100

24 The Berry curvature $\mathcal{F}_\pm(\mathbf{q})$ plotted as a function of wavevector $\mathbf{q}$ as a heat map on top of the two bands $\omega_\pm(\mathbf{q})$. The colour ranges from blue (positive) to red (negative). Parameters used are $m = 1$, $v_s = 1.5$, $c_{||} = 1$.104

25 The bulk and edge mode spectrum in the frame comoving with the longitudinal sound with speed $c_{||}$, for the case when $v_s > c_{||}$ and $v_s < c_{||}$ (shown here for the simple case when $\eta = 1$) and $m(y)$ varying from $-1$ to $+1$. This is the situation when $K_G > 0$ (as on the sphere), where the density mode is equatorially localized and topologically protected. 107

26 (a) The normalized density profile of a polar flock on a catenoid given in Eq. 4.41, for $\eta = 0.5$ (blue), 1 (orange) and 2 (green). Note that, in contrast to the sphere, the density grows near the edge of the catenoid. (b) The density and polarization (for $\eta = 2$) now shown on the catenoid. As before, blue corresponds to low density regions (at the neck) and red to high density. . . . . . . . . . . . . . . . . . . . . . . . . . . . . 110

27 A representative snapshot of the equatorial density mode on a sphere (Eq. 4.37) and the localized Goldstone mode on the catenoid (Eq. 4.43). For clear visualization we have chosen the perturbation $\mathsf{a}_6, \mathsf{b}_6 = 0.5$ and all other $\mathsf{a}_n, \mathsf{b}_n = 0$ $(n \neq 6)$. We have also taken $\eta = 2$ in both cases. . 111

# Chapter 1

# Introduction

## 1.1 Topology, order and phase transitions in condensed matter

The central goal of condensed matter physics is to classify and categorize the various possible phases of matter, along with their properties and the nature of phase transitions between them. Landau [1] gave structure to this endeavour by introducing the paradigmatic notion of an order parameter whose non-vanishing value characterizes a phase of matter. He consequently developed a phenomenological theory to describe continuous phase transitions, with superconductivity being an early application [2]. This foundational work firmly set the basic idea of phase transitions resulting from the spontaneous breaking of symmetry [3]. The modern theory of critical phenomena was eventually refined, culminating in Wilson's sophisticated theory of the renormalization group [4, 5] that could account for all of the singular scaling features observed in a vast number of equilibrium continuous phase transitions.

Although incredibly successful both conceptually and quantitatively, it became clear rather early on itself that this paradigm had its limitations. In the late 1960's, independent results [6–9] had rigorously shown the absence of spontaneous continuous symmetry breaking at finite temperature in low (one and two) dimensional systems. This is now the celebrated Mermin-Wagner-Hohenberg-Coleman theorem in equilibrium statistical mechanics. Now, for a two dimensional (2D) superfluid or superconductor, the relevant order parameter is a complex scalar field with a continuous $\mathsf{U}(1)$ symmetry. So one might immediately conclude that a two dimensional superconducting or superfluidity transition never occurs at finite temperature and the corresponding ordered phase does not exist in the thermodynamic limit. The same naïve conclusion is reached for the planar XY ferromagnet ($\mathsf{O}(2)$ classical spins on a 2D lattice), a two dimensional crystal or a nematic liquid crystal film. Soon after, in the early 1970's, Berezinskii [10, 11] and later Kosterlitz and Thouless [12, 13] showed that a finite temperature continuous phase transition (with a diverging correlation length) was nevertheless possible in these systems, *without* breaking symmetry and violating the theorem. This important discovery is remarkable from the point of view of the Landau-Ginzburg-Wilson paradigm which associates critical phenomena with spontaneous symmetry breaking. The resulting Berezinskii-Kosterlitz-Thouless (BKT) phase transition is ubiquitous in two dimensional systems and it surprisingly requires non-perturbative effects (topological defects) to be realized.

### 1.1.1 Topological defects in ordered media

Topological defects are distinctive singular distortions of the order parameter field that cannot be removed by any local deformation. The order parameter itself vanishes at the core of a defect. Defects in ordered media have been studied for over a century, initially constructed as elastic singularities in continuum solids by Volterra [14] and later as dislocations and line disclinations in both crystals [15, 16] and liquid crystals [17, 18]. Such defects are often characterized by a nontrivial winding or twisting of

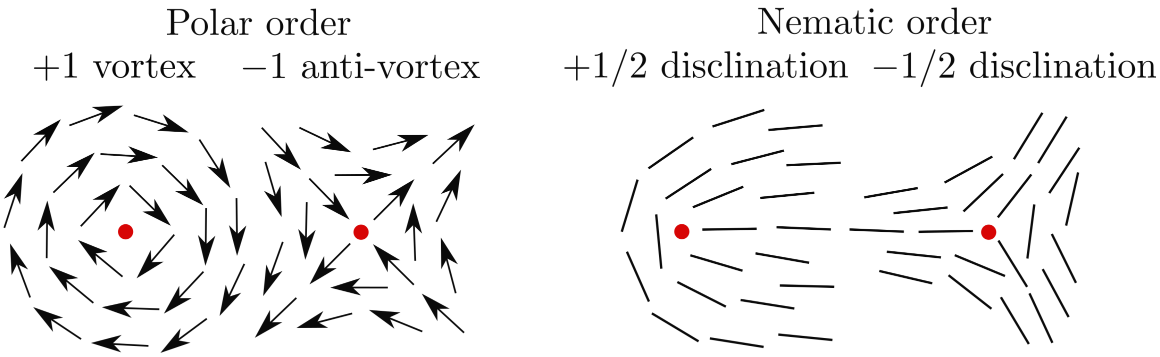

Figure 1 : Lowest strength topological defects in two-dimensional orientationally ordered media. The red dots indicate the defect cores. In the case of polar order in the plane, the order parameter manifold is the circle $S^1$ and defects are classified by the fundamental group $\pi_1(S^1) = \mathbb{Z}$ (the integers). For planar nematic order, the order parameter manifold is instead the real projective line $RP^1$ whose fundamental group is $\pi_1(RP^1) = \mathbb{Z}/2$ (half-integers).

the order parameter around the defect core. More technically, topological defects are classified using homotopy theory [19] by broadly considering equivalence classes of maps from physical space into the order parameter manifold [20, 21]. Translationally ordered materials such as crystals, smectics and cholesterics can support defects with more complex geometric and topological structure as well [22–25]. For orientational order in two dimensions, disclinations are point defects labelled by the winding angle of the broken symmetry variable relative to the angle traversed by a loop around the defect core. Hence spin models with vectorial order support integer strength defects (vortices), while nematic liquid crystals, being apolar (head-tail symmetric), can have disclinations of half-integer strength (see Fig. 1). Although topological defects are often energetically expensive, they constitute elementary yet nontrivial excitations of the homogeneous ordered state. When viewed as effective quasiparticles, the statistical mechanics and dynamics of defects offers a dual picture to that of the conventional order parameter.

Kosterlitz and Thouless' crucial insight was that neutral pairs of topological defects can entropically unbind at a finite temperature leading to the possibility of a continuous transition without breaking symmetry. The BKT scenario sets aside a characteristic universality class of defect-driven phase transitions that now encompasses a wide range of disparate equilibrium phenomena, including, superfluid $\text{He}^4$ films [26], disordered superconducting thin films [27] and coupled arrays of superconducting junctions [28]. Furthermore, the classical 2D XY model (which canonically exhibits the BKT transition) can be mapped onto a two dimensional Coulomb gas [13] and the sine-Gordon model [29, 30]. Hence conductor-insulator transitions in a dilute ionic film [31] and two dimensional surface roughening transitions [32] also fall in the BKT class. In a series of papers [33–35], Nelson and Halperin expanded on the ideas of defect mediated phase transitions to the problem of melting in two dimensions. In doing so, they discovered the hexatic liquid crystal along with a two-step melting transition that has since been observed in colloidal experiments [36, 37] and simulations [38]. A recent review summarizes many of these connections along with the relevant experimental verification of BKT phenomenology [39]. The basic idea of topological defects controlling a phase transition has had far reaching consequences in various contexts outside condensed matter as well. Shortly after the BKT papers, Polyakov extended their scenario to gauge theories with the hope of describing confinement in quantum chromodynamics. Although unsuccessful in the nonabelian case, he showed that topological excitations can proliferate in $2+1$D quantum electrodynamics, generating a photon mass without breaking gauge invariance [40, 41]. A similar topological effect also allows fermions in the $\mathsf{SU}(N)$ Thirring model to condense and develop a mass gap without breaking chiral symmetry [42]. More recently, topological defects that acquire additional quantum numbers have been found to be instrumental in "deconfined" quantum phase transitions in planar antiferromagnets [43, 44]. Such novel quantum criticality mirrors the original BKT scenario by allowing a direct continuous transition between two unrelated ordered phases, once again outside the conventional Landau-Ginzburg-Wilson paradigm.

### 1.1.2 Topological insulators and beyond

Although both the phases on either side of the BKT transition have a vanishing local order parameter (in the thermodynamic limit), they are still distiguished by the nature of correlations in local observables. The next topological revolution in physics occured when even this constraint was finally given up. In 1980, von Klitzing [45] discovered that the Hall conductivity in a silicon MOSFET was fully quantized in the presence of a strong magnetic field, which Laughlin [46] ingeniously argued a year later on the basis of gauge invariance. Nonetheless, it wasn't until the landmark paper by Thouless *et al.* [47] that the integer quantization of the Hall conductivity was identified with a topological invariant, a Chern number [19]. The quantum Hall state breaks no symmetry, yet each integral plateau of the Hall conductivity corresponds to a *different* phase of matter. Hence these phases cannot be distinguished by *any* local order parameter within the Landau-Ginzburg-Wilson framework, but they instead correspond to ground states with differing wavefunction topologies [48–51]. A remarkable departure from conventional wisdom, topology then provided a dramatically new way to organize exotic states of matter. A few years later, Haldane [52] proposed a model of noninteracting fermions without time-reversal symmetry that exhibited a quantum Hall effect in the *absence* of an external magnetic field. The Haldane model is a prototypical Chern insulator [53], i.e., a bulk insulating state of matter adiabatically disconnected from a trivial insulator (including conventional Mott and Anderson insulators [54]) with metallic surface or edge states [55] protected by a bulk Chern invariant. The topological nature of the edge states endows them with a particular robustness against disorder and backscattering from impurities [55], an attractive feature for technological applications [56] .

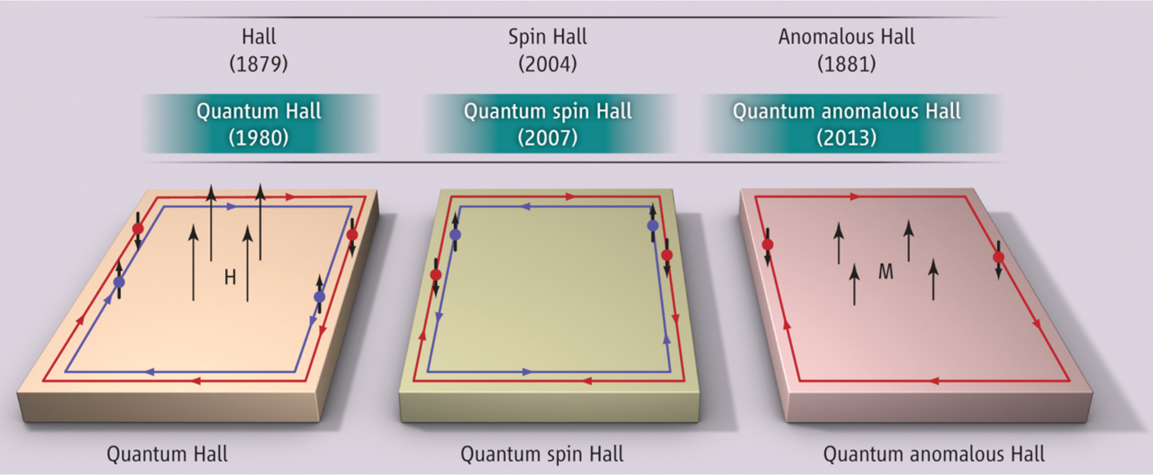
Hall
(1879)
Spin Hall
(2004)
Anomalous Hall
(1881)
Quantum Hall
(1980)
Quantum spin Hall
(2007)
Quantum anomalous Hall
(2013)
H
M
Quantum Hall
Quantum spin Hall
Quantum anomalous Hall

Figure 2 : The quantum Hall triumvirate (reproduced from Ref. [57]) in electronic media. The years refer to the corresponding time of discovery. Unlike the quantum Hall effect that requires an external magnetic field to supports charge currents on the edge, both quantum spin and anomalous Hall effects rely on spin-orbit coupling. In addition, the quantum spin Hall effect being time-reversal invariant supports spin currents on the edge, while the anomalous Hall effect breaks time reversal symmetry due to ferromagnetic ordering.

In the last decade or so, there has been an incredible surge in uncovering topological materials (Fig. 2) initiated partly by Kane and Mele's [58, 59] discovery of a time-reversal *invariant* topological insulator with a quantum spin Hall effect [60], and also three dimensional topological insulators with conducting surface states [61, 62], and topological Weyl semimetals [63]. A general symmetry and dimensionality based classification scheme [64, 65] has been proposed to categorize various topological insulators and superconductors [66]. More recently, it has been recognized that such topological phenomena[1] are not specific to just quantum electronic systems but apply to classical photonic [71–73], acoustic [74, 75], and mechanical [76–79] systems equally well. This has lead to intense efforts in realizing exotic topological metamaterials to provide robust waveguides and designer mechanical properties [79, 80].

It is clear from the previous subsection and above that topological ideas have fundamentally changed the way we think of materials in general. Thouless, Kosterlitz and Haldane received the Nobel prize in 2016 [81] in due recognition of their pioneering work on topological matter and phase transitions. This field of research continues to hold exciting promise and is growing rapidly, with both fundamental and applied interests. Having focused on the topological aspects of condensed matter, I will now switch to discuss an older, but intimately related cousin - geometry and its prominent role in describing structure and order, crucially in two-dimensions.

---

[1] Here we only refer to symmetry-protected topological phases [67] which lack long-ranged quantum entanglement [68], so called "topological order" that is present in more exotic phases of matter such as the fractional quantum Hall effect [69, 70].

## 1.2 Geometry, mechanics and frustration in two-dimensional matter

While topology only concerns properties related to the shape of an object that remain immutable under continuous deformation, geometry on the other hand deals with *both shape and size*. In 1966, M. Kac [82] famously asked if one can "hear the shape of a drum?", popularizing the concept that background geometry often strongly imprints on physical phenomena. When considering more complex ordered structures, the notion of *geometric frustration* or *incompatibility* starts becoming relevant. Perhaps one of the earliest geometric descriptions of a physical model involving frustration was that of an Ising spin glass [83, 84] and of a simple liquid as a random sphere packing problem [85–88]. An important characteristic of geometric frustration is curvature, a property most easily visualized in two-dimensional surfaces. Much like the curvature of the earth makes planar map projections in cartography impossible without distortion, spatial curvature in general frustrates order and often necessitates the presence of topological defects even in the ground state. Furthermore, there is deep relation between the topological ideas discussed earlier in Sec. 1.1 and the presence of (a possibly abstract) geometric curvature. A canonical example of such a relation is the

Gauss-Bonnet theorem [89] for a closed surface, that relates the integrated Gaussian curvature to a topological invariant, the Euler characteristic.

The frustration associated with the interplay of curvature and order [90–92] has many remarkable consequences for crystals [93–97], colloidal assemblies [98], tethered [99, 100] and liquid crystalline [101, 102] membranes, and jammed or glassy systems [103, 104]. In particular, geometric effects take on a central role in the mechanics (statistical or otherwise) of extended objects, such as polymers [105] and membranes [106]. Focusing on two-dimensional membranes below, I will highlight the impact of geometric nonlinearity on the rich physics of thin elastic sheets.

### 1.2.1 From membranes to metamaterials

Random surfaces have long been known to show very rich phenomenology, ranging from their use in string theory [107] and quantum gravity [108, 109] to thermally fluctuating physical membranes [106, 110]. In particular, elastic or polymerized two-dimensional membranes rather famously exist in a flat phase at non-zero temperature, achieving long-ranged order of their normals (which breaks continuous rotational symmetry) [99]. This of course flies in the face of the Mermin-Wagner-Hohenberg-Coleman theorem mentioned earlier in Sec. 1.1. The presence of elasticity (more precisely a non-vanishing shear modulus) mediates a long-ranged interaction between the Gaussian curvature at distant points on the membrane, allowing it to evade the theorem[2]. In turn, the bending rigidity renormalizes strongly in the thermodynamic limit, diverging as a power law on large scales [99]. Hence, elastic (phantom) membranes have a stable flat phase and a finite temperature crumpling transition, beyond which they entropically crumple. The flat phase also exhibits *auxetic* behaviour with a universal negative Poisson ratio of $-1/3$ [106], which is extremely rare in natural materials. There have been numerous theoretical studies of this phenomenon including $\varepsilon$-expansions [113, 114], large-$d$ expansions [115–117], and the self-consistent screening approximation [118] along with the inclusion of a possible buckling transition for a sheet with constrained boundaries [119, 120]. In the crumpled phase, self-avoidance becomes relevant for real membranes and this happens to completely eliminate the crumpled phase, stabilizing the flat phase for all finite temperature [121–123]. It is worth emphasizing the salient role of geometry here. Thin elastic sheets favourably trade energetically expensive in-plane stretching for easy bending deformations [124], but at the same time, any nontrivial out-of-plane deformation necessarily generates local Gaussian curvature that in turn induces elastic stresses in the material. This inevitable consequence of geometry coupling to mechanics lies at the heart of many of the dramatic properties of thin elastic bodies [125].

---

[2] This argument involves integrating out the soft in-plane displacements of phonon modes in favour of the out-of-plane height fluctuations [99]. While physically reasonable and correct, it obscures the underlying technical mechanism by which thin sheets evade the Mermin-Wagner-Hohenberg-Coleman theorem. This was first pointed out in a different context by Polyakov [111], where he noted that at low temperatures, the unit normal to the 2D surface embedded in 3D has the real Grassmanian $\mathsf{Gr}(2,3) = \mathsf{O}(3)/(\mathsf{O}(2) \times \mathsf{O}(1))$ as an order parameter manifold. Unlike standard non-linear sigma models used to treat spin systems, the inextensibility of the sheet due to the large cost to stretch leads to a nontrivial isometry constraint that is differential in nature. In terms of the normals, this then translates to a nonlocal Frobenius integrability condition [112] that forces the unit vectors to be a genuine normal to the surface. It is hence this deep geometric feature of surfaces that permits fluctuating elastic membranes to have a flat phase.

Apart from the impressive finite temperature properties, the geometric nonlinearity of thin sheets also has many ramifications for its zero temperature mechanics. Under external load, a thin sheet relieves stresses by either buckling [124] or wrinkling [126–128], possibly followed by secondary instabilities [129–131]. All of these mechanical instabilities are accompanied by complex morphological characteristics [131–134], providing an attractive combination of form and mechanical functionality. Harnessing such behaviour to design three-dimensional shapes and structures in elastic materials with novel mechanical properties is the realm of mechanical metamaterials [135–137]. This is often achieved via local prescriptions of material geometry, and has been

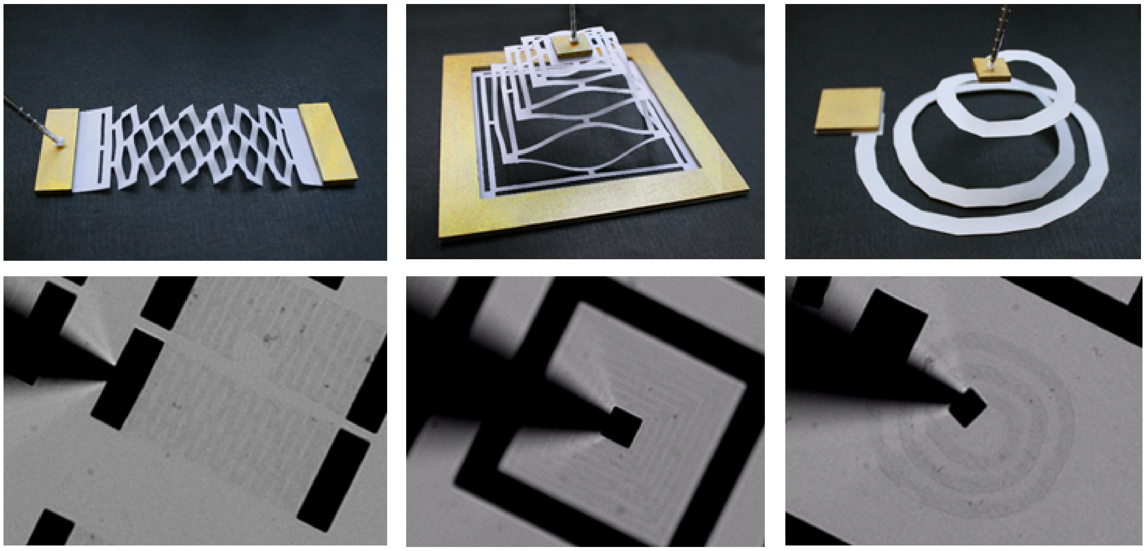

Figure 3 : Graphene kirigami structures (reproduced from Ref. [150]) patterned by lithography compared against their macroscopic counterparts in paper.

explored in a variety of systems, like nematic elastomers [138–141], hydrogels [142–145], shape memory polymers [146, 147] and 4D printed composites [148, 149]. The creation of three-dimensional shapes from planar sheets is particularly interesting as out-of-plane deformations provide highly responsive routes to locally relax stresses. Shape change is then naturally viewed as a mechanism by which an elastic material accommodates geometric incompatibility. Tuning and controlling the intrinsic geometry then automatically furnishes both adaptive and programmable responses.

In this regard, the ancient paper-based art forms of *origami* (‘ori’, fold; ‘kami’, paper) and *kirigami* (‘kiru’, cut) offer intriguing solutions to the deployment of complex 3D geometries with distinctive mechanics [151, 152]. Since both origami and kirigami are scale invariant (Fig. 3), they can be combined with rapid miniaturization to design metamaterial response and structures at the smallest scales [153, 154]. The design of origami [155–172] and kirigami [173–193] metamaterials has hence emerged as a powerful geometry based tool to dramatically modify, reconfigure and program material properties. Such approaches were recently demonstrated in monolayer graphene

[150, 194] and now provide unprecendented opportunities for designing devices with novel electronic and mechanical properties. With the advent of such technologies, it has become increasingly important to characterize and understand the various ways material deformations accomodate and relax stress through instabilities in thin 2D elastic sheets. In addition, as described in Sec. 1.1.2, topological mechanics [78, 79, 195] is a rapidly developing field that has brought the notion of topological robustness to control and direct material response [196, 197, 197–206], failure [207–210] and buckling [184, 211]. As a result, classical elasticity has been reinvigorated within the context of such designer materials [135].

It is amply evident from all of the previous discussions that both topology and geometry have been vastly influential in an extraordinarily diverse range of fields. While most progress has been made in the context of passive or inert materials, the inclusion of nonequilibrium driving permits many new possibilities that were otherwise forbidden by requirements of thermal equilibrium. The significance of geometric and topological ideas in such systems has only slowly begun to be appreciated. In the next section, I will introduce active matter and discuss the possibility of topology and geometry playing an important role in our understanding of nonequilibrium physics.

## 1.3 Active matter

Living organisms distinguish themselves from passive inanimate matter through their ability to adapt, reproduce and evolve, and also autonomously move, perform work and process information. Although the vast complexity of biological systems has posed enormous challenges to any general theoretical description, progress can be made by restricting our attention to a relatively common feature of living matter, its capacity to self-propel. By doing so, we shall delineate a distinct category of

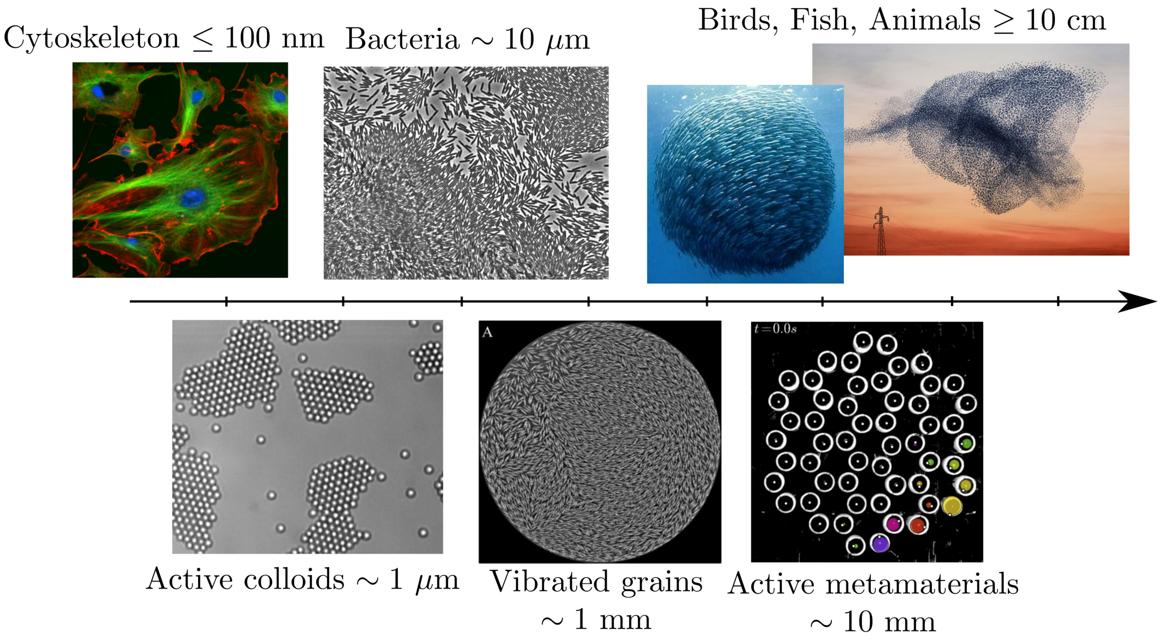
Cytoskeleton $\leq$ 100 nm
Bacteria $\sim$ 10 $\mu$m
Birds, Fish, Animals $\geq$ 10 cm
A
$t=0.0s$
Active colloids $\sim$ 1 $\mu$m
Vibrated grains $\sim$ 1 mm
Active metamaterials $\sim$ 10 mm

Figure 4 : Some examples of active matter displaying the diversity in scale and of constituent active units. Images of the active colloids and vibrated grains have been reproduced from Ref. [224] and Ref. [225] respectively. The active metamaterial example is a topological lattice with individually motorized gyroscopes, taken from Ref. [226].

nonequilibrium systems characterized by the sustained uptake and dissipation of free-energy by individual particles, which in turn execute sustained motion [212]. Collections of such *active* agents [213, 214] constitute an active material [215–220] whose large scale collective and emergent [221] properties are of great interest and wide applicability (see Fig. 4). As a novel class of internally driven nonequilibrium systems, active matter provides a framework to fruitfully view living systems as a material [222, 223], amenable to the methods of condensed matter physics.

It is important to note the defining feature of active matter is that the drive is *local* and it consequently breaks detailed balance [227] at the microscopic scale. In other words, the endeavour of active matter may be regarded as elucidating the material consequences of locally broken detailed balance. This is fundamentally different from external bulk forcing as encountered in problems of sedimentation [228] or periodic

Floquet systems [229]. It is also distinct from the case of boundary driving, as in sheared turbulent fluids [230] or systems in contact with differing heat baths or particle reservoirs (for instance, dissipative patterns in Rayleigh-Bénard convection [231]). In all of these situations, the drive acts externally and breaks time-reversal (and perhaps spatial) symmetry globally. A third manner of being out of equilibrium is through relaxation phenomena [232] that focuses on the transient dynamics to (eventual) equilibrium. If the relaxation time-scale is very large, then one is in the realm of glassy physics associated with kinetic traps [233] or meta-stable states that can lead to broken ergodicity [234]. Once again, this differs from the basic premise of active matter[3] and we shall not address it any further.

In the past few years, there have been a growing number of experimental realizations of active matter with both living and synthetic analogues [238]. Examples span a wide range of scales from natural bird flocks [239, 240], fish schools [241, 242], insect swarms [243–246] and human crowds [247–250] to bacterial suspensions [251–254], cellular monolayers [255–263] and sub-cellular structures as well [264, 265]. There has been equal amount of progress in developing synthetic model active systems, including vibrated grains [225, 266, 267], self-propelled colloids [224, 268], artificial robots [269–271] and reconstituted biofilament liquid crystals [272–277], allowing for quantitative tests of various active matter theories. As active units such as cells or bacteria are often elongated in shape, they can organize in active liquid crystalline states with orientational order. Although liquid crystal textures had been identified in the biological setting very early on [278], their active and energy transducing nature had been overlooked, thereby missing all of their dramatic nonequilibrium consequences [218].

---

[3] Of course, a given active system may also exhibit glassy dynamics and arrest into jammed states [235–237].

## 1.4 Outline

In this thesis, I will focus on two classes of problems. The first will deal with the mechanics of kirigami metamaterials and the second will address active liquid crystals with both polar (ferromagnetic) and apolar (nematic) order, primarily restricted to two dimensions. In a metamaterial, accounting for the detailed microstructure in a general fashion and answering the notoriously difficult *inverse* design question are the main challenges. Traditional methods of classical elasticity and mechanics [124] are often ill-suited to address these problems. Nonequilibrium active driving further complicates the issue as the tools of equilibrium statistical mechanics [279] remain inapplicable to active systems, unlike their well understood passive counterparts. An important lesson learnt from Sec. 1.1 is that geometric and topological tools that transcend notions of equilibrium, can have manifest physical ramifications and often provide a natural description of a system. This is the central tenet of this thesis. My goal is to substantiate this by illustrating how novel topological and geometric phenomena can arise in metamaterials and active systems, which in turn succinctly capture the relevant physics of the problem. By emphasizing the geometric and topological aspects of the problem, difficult to intuit phenomena may acquire a simple explanation and one may uncover many surprising and unexpected effects as well.

In Chapter 2, I will begin with kirigami metamaterials and present the problem of kirigami mechanics. It is evident even from simple table-top experiments that a given kirigami hole pattern has a dramatic effect on the effective elastic properties of a thin sheet. While much of the novel mechanics of kirigami relies on local bending modes, treating the same within conventional elasticity is mired by nontrivial boundary conditions and the extreme nonlinearity of far from threshold buckling. Hence I adopt a different approach that instead highlights the geometric incompatibility of a hole as the appropriate mechanical degree of freedom in a perforated thin elastic sheet. The method of strain-dependent image elastic charges recognizes the buckling response of a hole under external load as a geometrically tuned mechanism of stress relief. Using a diagonally pulled square paper frame as a model system, I find a strong softening of the force response accompanied by curvature localization at the inner corners of the buckled frame, in addition to nontrivial multiscaling behaviour and defect driven buckling phenomena. A single frame can now be viewed as a modular element to build more complex kirigami structures. Upon extending the framework to many holes, I demonstrate that interacting elastic image charges can also provide a useful kirigami design principle to selectively relax stresses in elastic materials, a first step towards addressing the inverse problem.

Moving on from metamaterials to active matter, in Chapter 3, I will introduce the active nematic [280, 281]. An important consequence of the nonequilibrium drive is that the $+1/2$ disclination in an active nematic is spontaneously motile or self-propelled [282]. Given that defects play a key role in two dimensional passive matter, it is natural to ask how defect motility changes the equilibrium story. A paradox immediately arises regarding the survival of nematic order in the face of ballistic defects. To address this puzzle, I develop a systematic description of defects as effective particles, expanding on a vastly successful venture in equilibrium [283–292]. The stochastic dynamics of defects thus derived faithfully captures the important physics of an active nematic and allows us to comprehensively address defect unbinding and proliferation. The resulting “motile”-BKT phase transition leads to spatio-temporal defect chaos and active turbulence. The extension of a canonical defect mediated phase transition to the active realm allows us to then finally resolve the original paradox, providing insight into mechanisms that maintain order in active systems.

In the Chapter 4, I will switch to describe an active polar fluid and the phenomenon of flocking [293]. While rotating vortices and asters are present in active polar films [294–297], they remain strongly confined with diffusive translational dynamics[4] and the order-disorder transition is not mediated by topological defects. Instead, the onset of collective motion is now best understood as a liquid-gas like transition with an intermediary coexistence phase of travelling smectic bands [301–306]. Upon ordering into a collectively moving state, the active polar fluid breaks time-reversal symmetry macroscopically. When considered on a curved surface, one necessarily finds topological defects due to the geometric frustration imposed by the curvature [91, 92], but another more intriguing topological defect also arises, one in Fourier space. I will demonstrate that polar fluids on curved surfaces are analogous to quantum Hall states in the precise sense that the flock supports localized sound waves that are topologically protected. Ordered lattices [226, 307] and amorphous networks [308] with active units such as spinning gyroscopes or annular cells with circulating active fluids have been shown to support localized edge states that are topologically protected. Unlike these structured metamaterials with broken time-reversal symmetry, the polar flock provides a natural and spontaneous realization of topological protection far from equilibrium.

Finally in Chapter 5, I will summarize the various results presented. To conclude, I will end with a discussion of future directions and implications of geometry and topology in both designer and living matter.

---

[4] An ordered polar flock in two dimensions has *long-ranged order* [293, 298, 299] unlike an equilibrium planar magnet, violating the Mermin-Wagner-Hohenberg-Coleman theorem by virtue of being active. As a consequence, vortex-antivortex pairs are expected to experience a strongly confining attractive potential $\sim r^{0.8}$, where $r$ is the pair separation (there is some indication for this in Ref. [300]).

# Chapter 2

# Mechanics of kirigami metamaterials: stress relief by elastic charges

*This chapter is based on work primarily presented in the articles "Kirigami mechanics as stress relief by elastic charges" [192] and "Nonlinear mechanics of thin frames" [193] co-authored by Michael Moshe, Edward Esposito, Suraj Shankar, Baris Bircan, Itai Cohen, David R. Nelson and Mark J. Bowick, and published in the journals Physical Review Letters and Physical Review E respectively, in the year 2019. Both Michael Moshe and I performed the theoretical analysis and wrote the primary draft of both papers together, barring the experimental sections. All our co-authors provided valuable suggestions and edits to improve the presentation and the content of both papers.*

## 2.1 Geometry in elasticity

Classical elasticity is a scale-free continuum theory [124] and yet scale-dependent features are routinely observed in elastic materials [125]. The elastic theory of thin plates and shells [309] is a good example: the plate/shell thickness, compared to the overall size, is a purely geometric dimensionless parameter controlling both the structural bendability and the degree of nonlinearity. As a result, one often finds complex mechanical behavior and rich pattern formation in these structures. Thin sheets, for example, display compressional buckling [124], wrinkling [126–128, 310], folding [130, 311, 312] and crumpling [129, 131], all as a result of the interplay between the external load and the sheet thickness. In addition to these instabilities with a characteristic length scale, geometric nonlinearities can also lead to unusual scale-free instabilities, a well known example of which is the surface instability of compressed soft solids leading to cusped sulci [313, 314].

Another class of elastic solids characterized by multiple length scales are *non-euclidean* thin sheets [315]. Here the (preferred) curvature of the sheets provides an additional length scale. Structures with a non-euclidean geometry are widely prevalent in nature and play an important role in determining the morphology of flowers [316, 317], leaves [132, 318], growing tissues [319] and seed pods [320, 321]. This has also inspired the design of mechanically-responsive materials [322, 323] and actuators [145].

A common feature in all these examples is the presence of multiple widely-separated length scales that affect both mechanics and structure. Such multiscale behavior can also show up in the scaling of the total energy with system size [324]. From this point of view, *kirigami* - the Japanese art of cutting and folding paper, is a powerful means of manipulating the geometry and intrinsic length scales of an elastic sheet. The presence of holes then provides a new handle for controlling both the onset of instabilities and the effective mechanical response. One finds that the conventional linear response of the planar state transitions to a mechanically softer nonlinear response as the applied force increases due to force-induced buckling. The effective elastic properties that arise here may be tuned by varying the geometry of the holes. Eventually, for large loads the displacement eventually reaches the order of the hole size itself and we find a cross-over to a stiffer, but still nonlinear, response. This pattern of mechanical responses, passing from a linear regime through an instability-induced softening to eventual nonlinear stiffening, is seen in other systems as well, such as the force-induced denaturation of double-stranded DNA [325], metal alloys, solid polymeric foams [326, 327], and nematic elastomers [328].

The properties noted above have recently been exploited to generate mechanically actuated 3D configurations [178, 179, 187, 188] and highly stretchable devices [177, 180, 182]. Blees et al. [150] succesfully demonstrated that kirigami can be performed at the extreme nanoscale to modify the effective mechanical properties of atomically-thin graphene in the presence of strong thermal fluctuations. For small feature sizes, the geometry and deformation of a nanoscale graphene kirigami structure might modify its electronic transport properties as well [329]. Lattice kirigami structures have also been used, although without direct reference to their mechanics, to create complex 3D macro-structures [181, 186], much in the spirit of origami-based designs. Unlike previous studies of mechanical metamaterials involving in-plane instabilities of periodically perforated thick sheets [173, 175, 330–332], here we shall focus primarily on thin elastic sheets that easily buckle into the third dimension, as is most relevant for kirigami.

The mechanics of thin elastic sheets is controlled by the dimensionless Föppl-von Kármán (FvK) number $\gamma = YR^2/\kappa$ [124] that indicates the relative ease of in-plane stretching versus out-of-plane bending. Here $R$ is a characteristic linear dimension of the sheet, $Y$ the 2D Young's modulus and $\kappa$ the bending rigidity. By introducing holes or cuts, kirigami now provides a distinct route to locally relieve stresses through these geometric features, though a general characterization of its effective mechanical response is not known. The much harder *inverse problem* of predicting the correct kirigami pattern to relax a given pre-stress in a material also remains an open problem, complicated by the notorious nonlinearity inherent to thin sheet elasticity.

### 2.1.1 Geometric mechanics of kirigami

Here we develop a geometric framework to address some of the general mechanical consequences of kirigami and later compare with experimental measurements of force-extension curves of pulled paper frames. Starting with a single square frame, we use the technique of strain-dependent image elastic charges to show that a hole under external load acts as a geometrically tunable source of local stress, which is relaxed by local buckling. This method crucially recognizes the fact that holes provide a source of *geometric incompatibility*. The lowest order image elastic charge induced in a hole is a quadrupolar singularity in Gaussian curvature [25, 333]. When permitted by the shape of the hole, this singularity can fractionalize into partial disclinations, naturally explaining the curvature localization at interior corners seen experimentally for square frames. Thus, the buckling response of the sheet can be viewed as the sheet screening the image charges by adopting a curved 3D configuration thereby leading to a softer force response. By exploiting the quasiparticle nature of these geometric charges, this method naturally explains the geometry tuned buckling threshold and the multiscale behaviour of the force response in the most economical fashion possible.

Similar buckling induced softened mechanical response has been previously investigated in periodic arrays of slits under uniaxial tension [180, 185, 188]. Motivated by Ref. [187], we go beyond slits and use square holes as a nontrivial yet simple illustration of our framework. This rationalizes previous results, extends to arbitrary hole shapes[1], and provides a systematic approach to handle many holes. In addition, collective effects arising from interactions between holes are neglected in previous works that just analyze the unit cell of a periodic lattice, but are easily captured using the elastic charge framework. Using a flattened cone as an example, we will later demonstrate how interactions between image charges can guide the design of appropriate kirigami patterns to relax the pre-existing stress in the system. It is worth emphasizing that the formalism of interacting image elastic charges offers general principles to organize the mechanics of kirigami structures, and the mechanics of a single frame [Fig. 5(c)] provides a modular building block for more complex arrays [Fig. 5(a)].

## 2.2 Table-top observations: Multistability and curvature localization

As mentioned above, we will focus on the mechanics of isolated square frames, whose edge length ($L$), hole size ($H$), and frame width ($w = (L-H)/2$) are shown in Fig. 5(c). Pulling on such a square frame along diagonally opposite ends, we first note that the frame readily buckles out of the plane but can adopt multiple configurations in doing so. In Figs. 5(d-f) three locally stable configurations of a diagonally pulled square frame are shown, distinguished just by the relative orientations of the buckled inner corners: corners with angles less than $\pi/2$ in the stretched configuration (before buckling) are *positive* partial disclinations, and can either buckle up or down ($\pm$).

---

[1] Our focus is mainly on square holes, because the concentration of elastic charges at sharp corners simplifies the analysis; elastic charges are delocalized around the rim when one considers, say, circular holes instead (see Fig. 9).

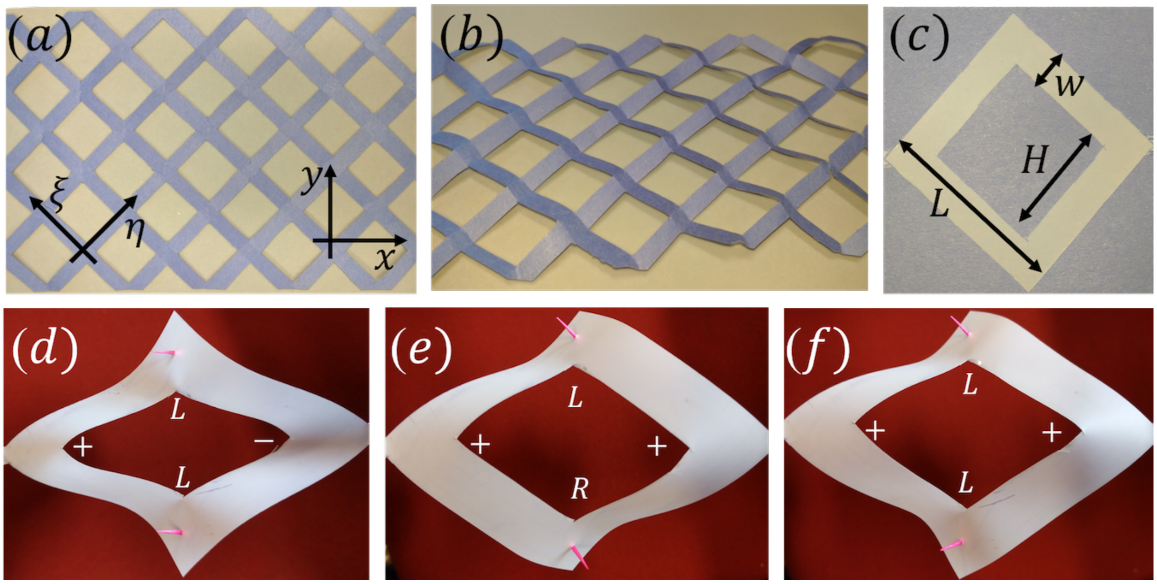

Figure 5 : Kirigami and frames. (a) A periodic kirigami pattern composed of square frames. (b) The response of the pattern in (a) to a large deformation when stretched along the $x$ direction, enabled by the escape of the frame elements into the third dimension. (c) An individual square frame of size $L$, frame width $w$ and hole dimension $H = L - 2w$, forming the building block of the pattern in (a). (d-f) Different locally stable configurations of a square frame subjected to an external force along its diagonal (in the horizontal direction), distinguished by the relative orientations of the four inner corners: (d) The left and right inner corners are curved up and down, respectively (denoted by $+$ and $-$, respectively), whereas the top and bottom inner corners point to the left (as shown by the red needles normal to the surface and denoted by L. This configuration is thus denoted by $+ : \mathrm{L/L} : -$). (e) The left and right corners both point up here, while the top and bottom corners point in opposite directions, hence denoted by $+ : \mathrm{L/R} : +$. (f) Here both the left and right corners once again point up, but the top and bottom corners point in the same direction, hence $+ : \mathrm{L/L} : +$. The remaining configuration $+ : \mathrm{L/R} : -$ is not stable at this hole size.

Corners with angles greater than $\pi/2$ in the stretched configuration before buckling are *negative* partial disclinations, and the associated square plaquettes can tilt either to the left or right (L or R). The configurations in Figs. 5(d-f) can thus be compactly denoted as $+ : \mathrm{L/L} : -$ (d), $+ : \mathrm{L/R} : +$ (e), and $+ : \mathrm{L/L} : +$ (f).

Here we focus primarily on the global energy-minimizing configuration for a given strain, and the associated energy landscape of the planar and buckled configurations for varying hole sizes and loading conditions. We neglect the effects of strong thermal fluctuations uncovered in Ref. [150]. In principle, for the square frame, there could be $2^4 = 16$ different buckled configurations in all, with many related by global rotations and reflections. The relative parity of opposing corners ($+$ versus $-$ and L versus R) completely classifies the 4 distinct buckled configurations, up to symmetry-related degeneracies. However, the configuration $+ : \mathrm{L/R} : -$ (and its symmetry related cousins) is unstable in the parameter range we study. The other three locally stable ones are shown in Figs. 5(d-f). Such multistability induced by geometric frustration can yield programmability [163, 175, 334] when coupled in large complex kirigami arrays. As an aside, we do note that the presence of such multiple local energy minimizers (metastable states) and their associated degeneracies would also play an important role when thermal fluctuations are present, and might have nontrivial consequences for, say, the free-energy of thermalized kirigami microstructures under stress (see for instance Ref. [335]).

There are three main observations that drive our work. First, as demonstrated in Fig. 5(b),(d) ,the presence of a hole, or an array of holes, significantly softens the response of a frame to external forces. Quantifying this softening as a function of frame width, or equivalently hole size, is an important prerequisite for a thorough understanding of kirigami mechanics. Second, we find that the frame localizes curvature in the vicinity of the inner corners of a hole, much like that of a conical surface. Similar singularities and softened force-response have been observed previously in the buckling of other shapes such as slits [185, 188]. Third, for small hole sizes the frame does not buckle, implying that there is a threshold hole size for buckling (at a fixed displacement). Alternately, the buckling transition may be triggered by varying the external diagonal displacement ($\delta x$), for a given hole geometry. We shall denote the critical displacement for the buckling transition in a fixed geometry by $\delta x_c$. Guided by these observations, we now proceed to develop a theoretical framework which naturally captures and emphasizes these features of frames and kirigami.

## 2.3 Image charges in thin plate elasticity

The mechanics of an elastic frame is governed by an elastic energy functional composed of a stretching term depending on the 2D Young's modulus $Y$ and a bending term proportional to the bending modulus $\kappa$. For a Hookean material, both the stretching and bending terms are quadratic in the stress ($\boldsymbol{\sigma}$) and extrinsic curvature ($\mathbf{b}$) tensors, respectively. Upon minimizing the total energy, we obtain the covariant Föppl-von Kármán (FvK) equations [309, 336],

$$\frac{1}{Y}\Delta\Delta\chi = K_{\mathrm{Im}} - K_G \ , \tag{2.1a}$$

$$\kappa\Delta\mathrm{tr}(\mathbf{b}) = \sigma^{\mu\nu}b_{\mu\nu} \ . \tag{2.1b}$$

Here $\Delta \equiv \nabla^2$ is the Laplacian and we have used the 2D Airy stress function $\chi$ ($\sigma^{\alpha\beta} = \epsilon^{\alpha\mu}\epsilon^{\beta\nu}\nabla_\mu\nabla_\nu\chi$, $\epsilon^{\alpha\beta}$ is the 2D Levi-Civita tensor) to simplify the force balance equation. The extrinsic curvature tensor is defined by $b_{\alpha\beta} = \hat{\mathbf{n}} \cdot \nabla_\alpha \mathbf{t}_\beta$, where $\hat{\mathbf{n}}$ and $\mathbf{t}_\beta$ are the local normal and tangent vectors to the surface, and whose determinant gives the Gaussian curvature $K_G$ of the surface. Note that these equilibrium equations reduce to the standard Föppl-von Kármán (FvK) system [124] upon geometrically linearizing the 3D configuration in a Monge patch.

The two elastic moduli together define a characteristic length scale, commonly interpreted as the effective thickness of the sheet. Working in terms of a 3D Young's modulus $\bar{Y}$, we have $Y = \bar{Y}t$ and $\kappa = \bar{Y}t^3/[12(1-\nu^2)]$, where $t$ is the effective sheet thickness (from now on referred to only as thickness) and $\nu$ is the Poisson ratio [125]. Unlike the conventional FvK equations for thin plates, we have additionally included a source of Gaussian curvature $K_{\mathrm{Im}}$ that plays the same role that defects play in crystals [92], though in our case this function describes a distribution of *image* elastic charges that are induced within the hole and depend on the external load, serving to enforce the appropriate boundary conditions required by the hole. Here the analogy with electrostatics helps, in that the hole under external stress functions like a conductive shell in an external electric field.

To understand the precise meaning of $K_{\mathrm{Im}}$, we shall now look at the plane-stress problem for an annulus and set $\mathbf{b} = \mathbf{0}$ ($K_G = 0$). The annulus being circularly symmetric, the planar problem is exactly solvable in terms of the Michell solution [337]. Below, we will reinterpret this classic solution in terms of image charges instead, and give a concrete calculation for $K_{\mathrm{Im}}$ in the annular geometry and then generalize it for other hole shapes.

### 2.3.1 Planar frames: Sheared annulus

The primary complication in solving the plane-stress problem is the presence of a nontrivial hole geometry and the corresponding boundary conditions that come with it. As the circular hole is most amenable to a simple solution by virtue of its high symmetry, we will use that to compute expressions for the induced image charges and later argue an analogous expression for the square hole as well. The inner and outer radii of the annulus are denoted by $R_1$ and $R_2$ ($R_2 > R_1$), respectively as shown

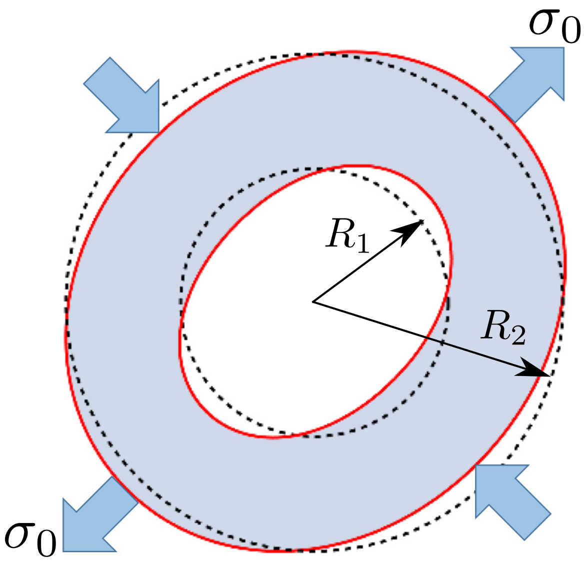

Figure 6 : The analytic solution (in red) for an annulus subjected to pure external shear ($\sigma_0$) on its external boundary. The undeformed annulus is shown in a dashed black line.

in Fig. 6. Working in polar coordinates $\{r, \theta\}$, the plane-stress problem reduces to solving the biharmonic equation $\Delta\Delta\chi = 0$ (Eq. 2.1a with $K_G = 0 = K_{\mathrm{Im}}$) on the annulus, with boundary conditions

$$\sigma^{rr}\big|_{R_2} = -\,\sigma^{\theta\theta}\big|_{R_2} = \sigma_0 \sin 2\theta \;, \quad \sigma^{r\theta}\big|_{R_2} = \sigma_0 \cos 2\theta \;, \tag{2.2}$$

$$\sigma^{rr}\big|_{R_1} = \sigma^{r\theta}\big|_{R_1} = 0 \;. \tag{2.3}$$

Here we only treat the case of an imposed diagonal pure shear stress controlled by $\sigma_0$ for simplicity, with simple shear and isotropic tension or compression being trivial to include. The well known solution for the stress function is [337]

$$\chi(r, \theta) = \left[ar^4 + br^2 + c + \frac{d}{r^2}\right] \sin 2\theta \;, \tag{2.4}$$

where the coefficients are

$$a = \frac{2R_2^2 - 3R_1^2}{12\left(R_2^2 - R_1^2\right)^2}\sigma_0 \ , \quad b = \frac{2R_1^2 - R_2^2}{4\left(R_2^2 - R_1^2\right)^2}R_1^2\sigma_0 \ , \tag{2.5}$$

$$c = -\frac{R_1^6}{4\left(R_2^2 - R_1^2\right)^2}\sigma_0 \ , \quad d = \frac{R_1^6 R_2^2}{12\left(R_2^2 - R_1^2\right)^2}\sigma_0 \ . \tag{2.6}$$

The corresponding equilibrium configuration is plotted with a red outline in Fig. 6 . At this stage we note that the same problem can be solved formally using the method of image charges, often used for solving the Laplace equation in the context of classical electromagnetism [338]. In electrostatics, the electric charge density provides a source for the Coulomb potential (via Gauss's law) which makes them dual to each other as generalized conjugate variables. Eq. 2.1a tells us that the Airy stress function $\chi$ and the Gaussian curvature are related to each other in a similar fashion [339]. This identification allows a straightforward generalization of the electrostatic image charge procedure to elastic problems. Hence for the problem at hand, instead of solving Eq. 2.1a on an annulus with stress free boundary conditions on the boundary of the hole, the same solution can be obtained by solving

$$\frac{1}{Y}\Delta\Delta\chi = K_{\mathrm{Im}} \ , \tag{2.7}$$

in the *whole disk* of radius $R_2$, where $K_{\mathrm{Im}}$ is now non-zero and compactly supported in the region that was previously the hole (circular disk of radius $R_1$). By doing this, we have traded the annulus for a simply connected disc by introducing a source term $K_{\mathrm{Im}}$ in the force balance equation, which precisely corresponds to the image elastic charges required to enforce the requisite boundary conditions on the hole. It is useful to compare against the electrostatic analogue, where the equipotential boundary condition of a conducting surface in a background electric field can be equivalently replaced by an appropriate image charge distribution that serves to enforce the same boundary condition.

The first two terms ($a$ and $b$) in Eq. 2.4 can be viewed as resulting from image charges at infinity. For now, we shall let these be as they are. The remaining two terms ($c$ and $d$) can be viewed as being induced by a singular source term at the origin of the form

$$K_{\mathrm{Im}}(\mathbf{x}) = 2Q\partial_x\partial_y\delta\left(\mathbf{x}\right) + 2D\partial_x\partial_y\Delta\delta\left(\mathbf{x}\right) \ , \tag{2.8}$$

where $\mathbf{x}$ is the position vector in the plane and $\Delta \equiv \partial_x^2 + \partial_y^2$ is the planar Laplacian. There are two induced image charges, with magnitudes given by

$$Q = -\frac{\sigma_0}{Y}\left[\frac{\pi R_1^6}{\left(R_2^2 - R_1^2\right)^2}\right] \ , \quad D = -\frac{\sigma_0}{Y}\left[\frac{\pi R_1^6 R_2^2}{6\left(R_2^2 - R_1^2\right)^2}\right] \ . \tag{2.9}$$

The two singularities in Eq. 2.8, when viewed as part of a multipole expansion, correspond to a fictitious quadrupolar charge ($Q$) and a fictitious hexadecapolar charge ($D$). In general, for more complicated hole shapes and external loading conditions, one can perform a multipole expansion of $K_{\mathrm{Im}}$ [333] and an infinite number of terms are present. Topological constraints, though, require that the monopole and dipole terms in $K_{\mathrm{Im}}$, corresponding to a global disclination and dislocation, respectively, must vanish [25]. The lowest order allowed multipole in $K_{\mathrm{Im}}$ is therefore generically the quadrupole [333].

For the case of a circular hole under pure shear, only two image charges (Eq. 2.9) are required to exactly solve the full plane-stress problem, and the image charge procedure being entirely equivalent to the classical solution, offers no apparent advantage. The benefit of using image charges becomes evident once we begin looking at less symmetric hole shapes, such as the square hole. For a square frame pulled along its diagonal, one has to include higher order multipoles to exactly solve the problem, though the quadrupole is most often still the dominant contribution[2]. The crucial point here is that the mechanics of a frame can be accurately captured by a finite (and hopefully small) number of image charges. The magnitude and number of these charges will of course depend on the shape and size of the hole along with the external loading conditions. In this way the geometric formulation of elastic charges characterizes perforations in an elastic sheet under stress as sources of geometric incompatibility and provides a useful solution technique even for situations where traditional elasticity methods are inapplicable.

### 2.3.2 Arbitrary planar frames: General strategy

The basic idea, a kind of variational ansatz for the frame configuration, is then to guess a distribution of image charges, interpreted as sources of Gaussian curvature. This distribution determines the stress function such that it satisfies the appropriate boundary conditions on the hole. Since Eq. 2.7 is linear in $\chi$ for planar frames, we can superpose the different multipolar image charges to obtain a $K_{\mathrm{Im}}$ that satisfies the appropriate boundary conditions. The displacement field $\mathbf{u}_i$ and the stress tensor $\boldsymbol{\sigma}_i$ generated by the $i$th elastic charge $\lambda_i$, is then

$$u^{\mu}(\mathbf{x}) = \sum_i \lambda_i u_i^{\mu}(\mathbf{x}) \ , \tag{2.10a}$$

$$\sigma^{\mu\nu}(\mathbf{x}) = \sum_i \lambda_i \sigma_i^{\mu\nu}(\mathbf{x}) \ . \tag{2.10b}$$

---

[2] For very thin frames (large holes) higher order multipole terms can be as important as the leading quadrupolar image charge. A different approach is needed in this ribbon or ring-polymer like limit (see Sec. 2.4.2).

Note that $\mathbf{u}_i$ and $\boldsymbol{\sigma}_i$ are explicit functions for each individual image charge[3], and different hole geometries only correspond to including a different number of terms with different charge magnitudes in the above sums. The functions $\mathbf{u}_i$ and $\boldsymbol{\sigma}_i$ can be found separately for each multipole as shown in Ref. [339]. Here these charges can be thought of as physically motivated variational parameters, one for each force or displacement imposed on a frame.

The elastic energy in a domain $\Omega$, including forces at the boundaries, is then

$$E = \frac{1}{2}\int_{\Omega} \mathcal{A}_{\mu\nu\rho\sigma}\sigma^{\mu\nu}\sigma^{\rho\sigma}\mathrm{d}S - \oint_{\partial\Omega} T_{\mu}u^{\mu}\mathrm{d}\ell \tag{2.11}$$

Here $\mathcal{A}$ is the elastic tensor [315], $\Omega$ is the domain of the entire frame, and $T$ is the boundary force. For an intrinsically flat, isotropic and homogeneous material with a 2D Young's modulus $Y$ and Poisson ratio $\nu$,

$$\mathcal{A}_{\mu\nu\alpha\beta} = \frac{1}{Y}\left[\frac{(1+\nu)}{2}\left(\delta_{\mu\alpha}\delta_{\nu\beta} + \delta_{\mu\beta}\delta_{\nu\alpha}\right) - \nu\delta_{\mu\nu}\delta_{\alpha\beta}\right] . \tag{2.12}$$

Writing the stress and displacement fields in terms of the elastic charges yields

$$E = \sum_{i,j} M_{ij}\lambda_i\lambda_j - \sum_i m_i\lambda_i \tag{2.13}$$

with

$$M_{ij} = \frac{1}{2}\int_{\Omega} \mathcal{A}_{\mu\nu\rho\sigma}\sigma_i^{\mu\nu}\sigma_j^{\rho\sigma}\mathrm{d}S \tag{2.14a}$$

---

[3] The stress tensor $\boldsymbol{\sigma}_i$, and the corresponding strain tensor, generated by each individual charge is linear in the charge $\lambda_i$ itself for a Hookean material. On the other hand, the displacement field $\mathbf{u}_i$ in general depends nonlinearly on the charge $\lambda_i$ due to geometric nonlinearities in the metric tensor. For fixed load applied at the boundary, the linear charge approximation is only valid for small charges. For fixed external displacement, the most relevant case here, the variational problem is exactly linear in the membrane limit.

$$m_i = \oint_{\partial\Omega} T_\mu u_i^\mu \mathrm{d}\ell \tag{2.14b}$$

Since all the $\boldsymbol{\sigma}_i$ and $\mathbf{u}_i$ are known explicitly, given a specific frame geometry, we can integrate over the domain $\Omega$ and obtain an expression for the matrix $M$ and the vector $m$. After minimizing the energy with respect to the image charges $\lambda_i$, simple linear algebra leads to an explicit formula for the magnitude of the $i$th charges, namely

$$\lambda_i = \frac{1}{2}\sum_j M_{ij}^{-1} m_j \tag{2.15}$$

This is the general expression to compute the image charges for a given hole geometry and external loading conditions. In practice, the sum is truncated to a finite number of terms approximating the exact solution. For single frames, often times, the quadrupole alone is the most dominant contribution and all other terms can be neglected. In the case of the sheared annulus, as we have direct access to the exact solution (Eq. 2.4), we can compare it to the pure quadrupole approximation, i.e., setting $D = 0$ in Eq. 2.8. We find that the error in the total energy is less then 5% for moderately large frame widths $(R_2 - R_1)/R_2 > 0.3$, which provides a guide for the pure quadrupole approximation when applied to other hole shapes as well. A similar analysis can be done for the plane-*strain* problem as well, and one finds that a pure quadrupole approximation works well (to $\sim 5\%$ accuracy) for $(R_2 - R_1)/R_2 \gtrsim 0.125$. The difference arises because a vanishingly narrow frame has a diverging deformation under fixed tension (plane-stress), but not so under fixed external displacement (plane-strain).

We can repeat the above procedure to compute the induced quadrupole charge in a square frame. First we consider the more complex setup of a square frame with two localized tensile forces $F$ acting along a diagonal, that is the analogue of the plane-stress problem. The induced fictitious quadrupolar charge as a function of the

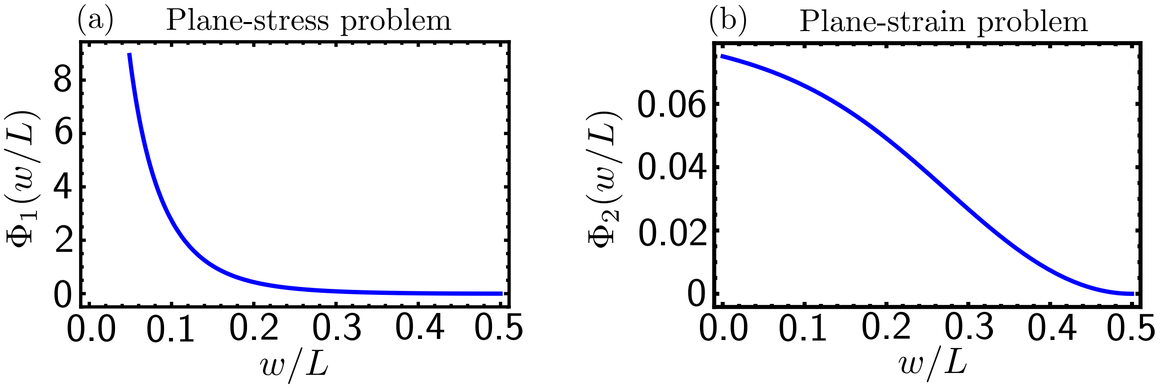

Figure 7 : The geometric function $\Phi_{1,2}(w/L)$ that captures the aspect ratio dependence of the induced quadrupolar charge under plane-stress conditions (a), or plane-strain conditions (b).

external force is

$$Q(F) = \frac{FL}{Y}\Phi_1\left(w/L\right) \ , \tag{2.16}$$

where $\Phi_1(w/L)$ is a dimensionless rational function of the frames aspect ratio $w/L$, plotted in Fig. 7(a). As can be seen $\Phi_1(w/L)$ vanishes in the absence of a hole ($w/L \to 1/2$) and diverges for a vanishingly narrow frame ($w/L \to 0$). As noted above, the divergence of the induced charge as the frame width $w \to 0$ is due to the unbounded deformation of a vanishing amount of material in the narrow frame, under fixed tension. For the quite different setup of fixing the displacement ($\delta x$) of the two diagonal ends of the frame (akin to the plane-strain problem), the quadrupolar charge induced instead becomes

$$Q(\delta x) = L^2\Phi_2\left(w/L\right)\frac{\delta x}{L} \ . \tag{2.17}$$

In this case the dimensionless geometric function $\Phi_2(w/L)$ [plotted in Fig. 7(b)] remains finite for a narrow frame ($w/L \to 0$), and vanishes as before in the absence of a hole ($w/L \to 1/2$), as expected. An explicit expression can be obtained for both $\Phi_{1,2}(w/L)$, but the functional form itself is not very illuminating apart from the above discussed limits. Similar expressions hold for higher order charges as well. The important point is that all the details of the shape and geometry of the hole and the loading condition are concisely subsumed by this single geometric function $\Phi_{1,2}(w/L)$.

Solutions parametrized with just a few image charges become more accurate for weak charges; the regime of validity of the approximation depends on the specific protocol of the prescribed deformation. For a given narrow frame ($w/L \ll 1/2$), the corresponding charge induced by a prescribed force will be much larger than that induced by a prescribed displacement. A small prescribed displacement, for example, results in charges that decrease as the frame narrows. Hence using the estimates obtained for the annulus, we expect that for a fixed prescribed force, the pure quadrupole approximation is valid for $0.3 \lesssim w/L < 0.5$ (within $\sim 5\%$ accuracy), while for prescribed displacements, $0.125 \lesssim w/L < 0.5$ is perhaps more appropriate as the validity range.

Before we move on to treating buckled frames within this framework, we note that the analogy with electrostatics provides simple interpretations of various features of these image elastic charge as well. The hole plays the role of a conductor in electrostatics. Just as induced electric charges concentrate at regions of high curvature on conductors in an external electric field, the elastic charges induced within a hole in response to an external load tend to localize at the sharp corners of the hole. In the planar case, this is evident in energy density plots of Fig. 8 resulting in stress localization at the corners. In the 3D case, as we shall see below, this elastic charge localization in turn leads to curvature localization upon buckling, explaining the observations from the table-top demonstrations.

### 2.3.3 Buckled frames: Screening of charges

A 2D elastic sheet embedded in 3D space may also escape into the third dimension to relieve any local stresses. Under load, it will first stretch and then buckle beyond

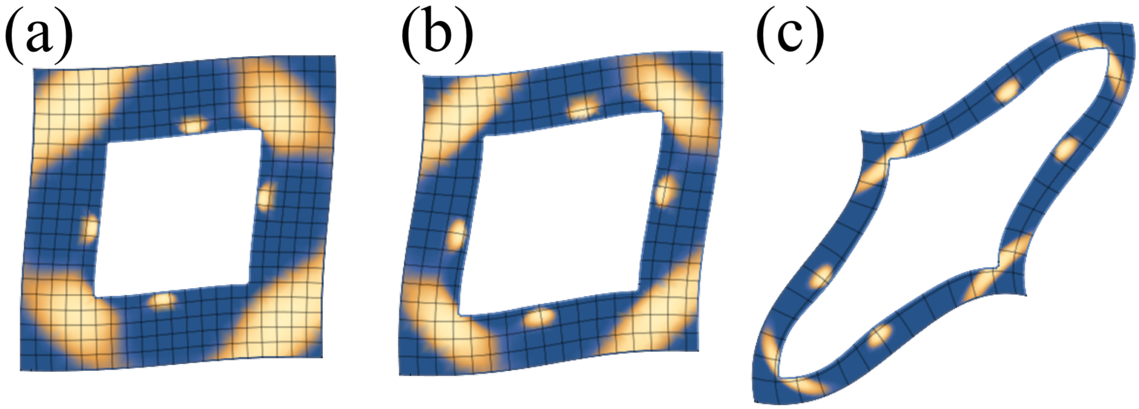

Figure 8 : The deformation of a square frame (as calculated by Eq. 2.15) constrained to be planar and subjected to a fixed force $F/(YL) = 0.1$ along the diagonal (from the lower left to the upper right). The frame size is fixed at $L = 1$ and hole size varied with (a) $H = 0.5$, (b) $H = 0.6$ and (c) $H = 0.8$. The configurations are colored by the energy density on a linear scale from blue (low) to white (high). Although the force is fixed, for an appropriate choice of the effective thickness, and if allowed to escape into the third dimension, configuration (a) remains planar, (b) is planar but at the buckling threshold, and (c) is beyond the critical force threshold for buckling. Note that the interior angles of the frames deviate from $\pi/2$ with the application of the force, signalling the formation of localized partial disclinations that concomitantly focus stresses as well.

the instability threshold. As mentioned earlier in Sec. 2.1, the relevant dimensionless parameter that quantifies the ease with which an elastic sheet can bend rather than stretch is the Föppl-von Kármán (FvK) number ($\gamma$). For a frame, as will be explained below, the appropriate definition of $\gamma$ involves the frame width $w$ as the macroscopic length scale, which gives $\gamma = Yw^2/\kappa$. When $\gamma \ll 1$, the frame preferentially stretches in-plane, while for $\gamma \gg 1$, it more easily trades stretching energy for bending energy and buckles out of plane instead. Let's take the case when bending is energetically much easier than stretching for a given area sheet ($\gamma \gg 1$). In this post-buckling or far from threshold regime the 3D configuration will be approximately stretchless. As a consequence, the frame adopts curved shape with spatially inhomogeneous Gaussian curvature, particularly on the boundaries and near the corners. This allows $K_G \neq 0$ in Eq. 2.1a. The presence of the hole can still be captured by the same image charges in $K_{\mathrm{Im}}$ as computed in the planar problem (Sec. 2.3.1 and Sec. 2.3.2). Hence we immediately see that

$$K_G = K_{\mathrm{Im}} \implies \chi = 0 \ , \tag{2.18}$$

and the zero stress state becomes accessible to the buckled sheet. In other words, the frame trades energetically expensive stretching for bending by adopting a 3D shape with Gaussian curvature ($K_G$) that *screens* out the induced image charges in the hole ($K_{\mathrm{Im}}$). By buckling, the frame thereby accommodates the geometric incompatibility of the hole generated by the external load. This screening effect strongly resembles the one found for the buckling of topological defects in crystalline membranes [100]. Importantly, the image charge approach affords an immediate simplification wherein the complex mechanical properties of the buckled configuration can be directly inferred by virtue of screening the induced charges, which are themselves computed in the much simpler planar setting. By relating the post-buckling solution to the pre-buckled one through screening, we circumvent the primary hurdle of thin plate elasticity, its geometric nonlinearity. The screening argument naturally also explains the localization of curvature at corners upon buckling.

In Fig. 9(a), one sees a clear manifestation of this phenomenon even in a triangular hole, whose shape is incommensurate with the symmetry of a quadrupole. For the annulus with no sharp corners, the charge instead distributes smoothly with curvature following suite [Fig. 9(b)]. Having fixed the Gaussian curvature of the 3D shape, the configuration of the buckled frame is now determined upto isometries (that preserve $K_G$). The energy minimizing configuration is then picked out by requiring it satisfy the second FvK equation (Eq. 2.1b). As $\chi = 0$, so is $\boldsymbol{\sigma} = \mathbf{0}$, and the equation simplifies to

$$\Delta H = 0 \ , \tag{2.19}$$

i.e., the mean curvature $H = \mathrm{tr}(\mathbf{b})$ is harmonic (under the constraint of $K_G = K_{\mathrm{Im}}$).

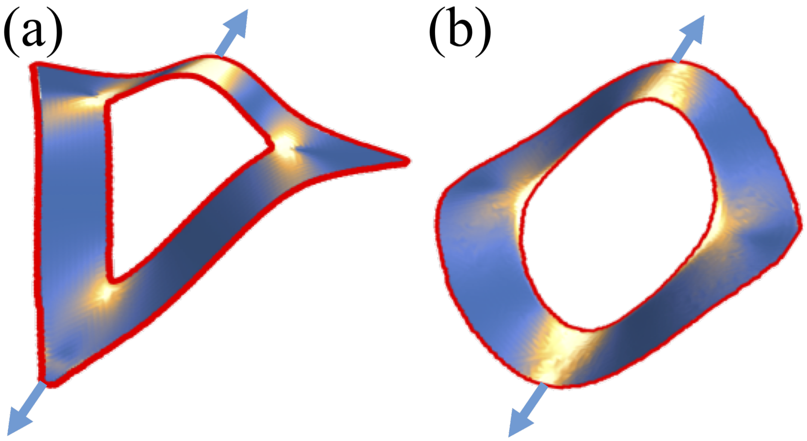

Figure 9 : Three dimensional energy minimizing configurations after buckling, obtained by a finite element computation. (a) Triangular and (b) circular frames subjected to uniaxial forces applied at opposing ends. The colour refers to the local energy density ranging from blue (low) to white (high). The screening charges responsible for this energy distribution are still of a quadrupolar nature, though they are evenly smeared out in the annular geometry. The triangular hole being incommensurate with the symmetry of the quadrupole, frustrates it and as a result, part of the charge is spread on one side of the triangle, while the rest concentrates at the three corners. This leads to the observed curvature localization.

This completes the solution procedure to analyze both the planar and buckled states of frames with arbitrarily shaped holes. In the next section, we will use this procedure to study in detail the mechanics of an isolated square frame that is pulled along its diagonal.

## 2.4 Nonlinear mechanics of a square frame

In this section, we shall characterize the mechanics of pulled square frames and compare it against experimental measurements of force-extension curves (Fig. 11) in paper frames. We will focus exclusively on the setup involving a prescribed displacement ($\delta x$) of diagonal corners of the square frame. Extensive comparisons to numerical finite element computations are given in Ref. [193], while details of the experimental setup and protocol are provided in Ref. [192]. As noted earlier in Sec. 2.3.2 and 2.3.3, in the presence of sharp corners in the hole geometry, the induced image elastic charge can fractionalize into *partial* disclinations that localize at the corners, just as in the electrostatic analogue. These partial disclinations generate stress fields similar to their topological counterparts [100], but unlike them, these induced partial disclinations have a charge that continuously depends on the external strain or stress imposed. The choice of a square frame as a model system to study kirigami mechanics then becomes clear in light of the image charge framework, as its shape is commensurate with the symmetry of a quadrupole allowing for complete unfrustrated fractionalization, unlike in triangular or circular frames (Fig. 9).

The fractionalized quadrupole naturally delineates different geometric regimes. As the deformation induced by each partial disclination is mainly confined to a plaquette region of size $\sim w$ (the frame width), we obtain three different regimes depending on the aspect ratio $w/L$. For $w/L < 1/4$, the partial disclinations remain well separated and are essentially non-interacting, allowing one to approximately superpose their planar or buckled solutions. In contrast for $w/L > 1/4$, the hole size is small and the interaction between overlapping partial disclinations becomes important. We shall not treat this case of small hole sizes, where other effects involving fracture and crack propagation also become relevant allowing the material to fail before it buckles. The relevant regime for kirigami is $w/L < 1/4$, which can be further split into two sub-regimes -

- Narrow size frames ($w/L < 1/8$): The single quadrupole approximation breaks down and higher order charges become equally important as the quadrupole (see Sec. 2.3.2).
- Intermediate size frames ($1/8 < w/L < 1/4$): Here the single quadrupole approximation is accurate and can be treated entirely in terms of its fractionalized degrees of freedom, i.e., non-interacting partial disclinations localized at the

corners.

Both these size regimes are discussed in Sec. 2.4.2 in the context of post-buckling mechanics. The charge of the partial disclination is given by

$$s = \frac{Q(\delta x)}{H^2} = \Phi(w/L)\frac{\delta x}{L} \ , \tag{2.20}$$

where $\Phi(w/L) = (L/H)^2 \Phi_2(w/L)$ [see Eq. 2.17 and Fig. 7(b)] now encodes the hole geometry in terms of the aspect ratio. As $w \to L/2$ ($H \to 0$; no hole), $\Phi(w/L) \propto (1-2w/L)^2$ vanishes as expected and remains finite in the opposite narrow frame limit ($w \to 0$, $H \to L$). We shall use this setup to understand both the buckling instability and the force response curve as measured in the experiment (Fig. 11).

### 2.4.1 Pre-buckling planar mechanics

For very small diagonal displacements ($\delta x < \delta x_c$, with $\delta x_c$ the buckling threshold), it is clear that the frame responds linearly by stretching [Fig. 11(b)]. Though the frame is still planar, the effective spring constant is modified by the hole geometry. Setting $\mathbf{b} = \mathbf{0}$ ($K_G = 0$) in Eq. 2.1a, we only have $K_{\text{Im}}$, the image elastic charge, present within the hole. Having noted the localization and complete fractionalization of the induced quadrupole at the corners, we can easily estimate the total energy as of four unbuckled partial disclinations,

$$E \approx 4\frac{Yw^2}{32\pi}s^2 \ , \tag{2.21}$$

where $s = (\delta x/L)\Phi(w/L)$ is the partial disclination charge (Eq. 2.20). Using this we can compute the force $F = \mathrm{d}E/\mathrm{d}\delta x$ and the effective linear spring constant

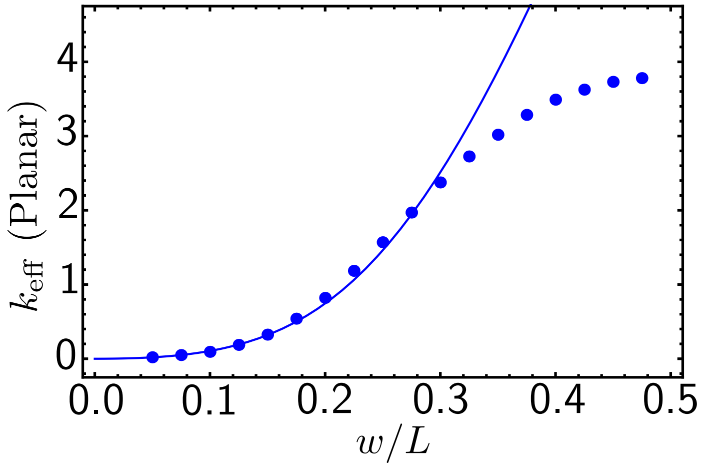

Figure 10 : The effective spring constant $k_{\text{eff}}$ for a planar frame as a function of the aspect ratio $w/L$. Parameter values used are $L = 1$ and $t = 5 \times 10^{-4}$. The blue dots are from the numerical simulations. The solid line is the analytical prediction in Eq. 2.22 with no fitting parameters.

$$k_{\text{eff}} = \left.\frac{\mathrm{d}^2 E}{\mathrm{d}\delta x^2}\right|_0 \propto Y \left(\frac{w}{L}\right)^2 [\Phi(w/L)]^2 \ , \tag{2.22}$$

where we have neglected all geometry independent order unity numerical prefactors. As the pre-buckling regime in the paper experiments is very narrow, an accurate estimation of the effective spring constant is not possible. Instead we compare the above expression in Eq. 2.22 to the effective spring constant from numerical finite element simulations (as used for example in [321, 340]) of a planar frame (Fig. 10) and we find perfect agreement (except for very small holes), without any fitting parameters. For small holes ($w/L > 1/4$), we can improve the agreement if we consider the full quadrupole without any fractionalization into partial disclinations (not shown).

### 2.4.2 Post-buckling mechanics: Multiscaling

The energy of the buckled 3D configuration of the frame is estimated by following arguments similar to those used in the planar case. Unlike the planar case, however, the buckled quadrupoles controlling force-extension curves have multiple locally stable configurations corresponding to various combinations of up-down buckling of each partial disclination (see Sec. 2.2 and Fig. 5). Although, each of these states have a different energy due to interactions between the buckled partial disclinations, in the intermediate hole size regime ($1/8 < w/L < 1/4$), these differences can be neglected. Moreover, the different modes of buckling that lead to multistability all scale the same way with both thickness ($t$) and the hole geometry ($w/L$), only differing from each other in numerical prefactors. By virtue of the localized partial disclinations, the buckled frame adopts a locally conical shape near the inner corners. Therefore, just as in the planar case, we estimate the total energy as the sum of now conical buckled partial disclinations at each corner [100, 341, 342]

$$E = 4\kappa \ln\left(\frac{w}{a}\right)\left[c_1 s + c_2 s^2 + \cdots\right] \ , \tag{2.23}$$

where $a \sim t$ is a microscopic core cutoff regularizing the conical singularity, and $c_1,\ c_2$ are order unity numerical coefficients that depend on the precise mode by which each partial disclination buckles. The partial disclination charge $s$ remains the same as before (Eq. 2.20). We have additionally neglected additive $\delta x$ independent constants to the energy that are irrelevant to mechanics. Note the logarithmic dependence of the energy on the frame width $w$, which is typical for conical surfaces, and is a direct consequence of the curvature localization. We emphasize that the above energy estimate is valid only in the post-buckled regime ($\delta x \gg \delta x_c$).

Once again, since $F = \mathrm{d}E/\mathrm{d}\delta x$, we obtain the linearized force-displacement relation $F = k_{\text{eff}}\delta x$, that defines the effective linear spring constant $k_{\text{eff}}$ in the post-buckled regime to be

$$k_{\text{eff}} \propto \frac{\kappa}{L^2}\left[\Phi\left(w/L\right)\right]^2 \ln\left(w/a\right) \ . \tag{2.24}$$

Comparing Eq. 2.24 to the planar case (Eq. 2.22), we recognize that the dramatic softening of the mechanical response in the post-buckled plateau can be seen as

| Configuration | | Aspect ratio | $k_{\text{eff}}$ |
|---|---|---|---|
| Planar | | – | $\propto Y \left[\Phi\left(w/L\right)\right]^2 \left(\frac{w}{L}\right)^2$ |
| Buckled | $\{$ | $\frac{1}{8} < \frac{w}{L} < \frac{1}{4}$ | $\propto \frac{\kappa}{L^2} \left[\Phi\left(w/L\right)\right]^2 \ln\left(\frac{w}{a}\right)$ |
| | | $\frac{w}{L} < \frac{1}{8}$ | $\propto \frac{\kappa}{L^2} \left(\frac{w}{L}\right)$ |

Table 1 : A summary of the effective spring constants $k_{\text{eff}}$ for different frame aspect ratios $w/L$, for planar and buckled configurations.

replacing $Y \to \kappa/w^2$ (upto a logarithmic correction). As $Yw^2/\kappa = \gamma \gg 1$, this essentially corresponds to the buckled linear response being a factor $\gamma$ smaller than the planar response. Note that this response is appropriate for intermediate hole sizes $(1/8 < w/L < 1/4)$ whose buckling is controlled by the buckling of localized partial disclinations.

To calculate the buckled force response of narrow frames $(w/L < 1/8)$ we use an alternate approach. Here, an infinite series of multipolar charges higher than the quadrupole become important, suggesting that the relevant weakly interacting degrees of freedom are not elastic charges. Instead, we treat the frame edges as quasi-1D ribbons joined in a ring. Neglecting the high energy splay modes, the bending and twisting elastic energy of a ribbon is approximated by

$$E \approx 4\kappa\, wL \left(\frac{\delta\theta}{L}\right)^2 , \tag{2.25}$$

where $\delta\theta \propto \delta x/L$ is the net rotation of the ribbon across its length [125]. Once again computing the effective linearized spring constant for buckled narrow frames, we obtain

$$k_{\text{eff}} \propto \frac{\kappa w}{L^3} . \tag{2.26}$$

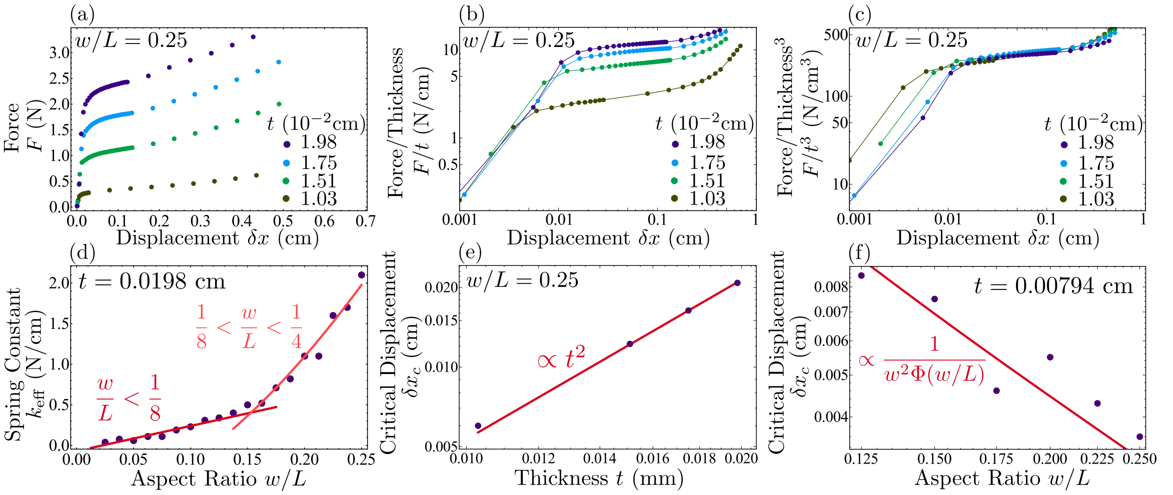

Figure 11 : Experimental measurements of square frames subjected to tensile load along the diagonal. (a) Force-displacement curves for frames with $w/L = 0.25$ and thicknesses varying between 0.01 and 0.02 cm. (b) When normalized by thickness, curves collapse at small displacement, confirming that the frames are planar at this regime. (c) When normalized by thickness cubed, curves collapse in the post-buckling regime, confirming that energy increase is predominately bending. (d) Effective spring constant in the post-buckled regime as function of frame aspect ratio $w/L$ in the intermediate and large hole regimes for a frame of thickness $t = 0.0198$ cm, confirming the multiscale behavior in (Table 1). The curve in the large hole regime ($w/L < 1/8$) is linear as given in Eq. 2.26, while the curve in the intermediate hole regime ($1/8 < w/L < 1/4$) corresponds to Eq. 2.24, with the prefactor $c$ and regularizing cutoff $a$ taken as fitting parameters. (e) Critical displacement as function of thickness for a frame of $w/L = 0.25$, growing as $t^{1.9}$ (solid line), in good agreement with Eq. 2.27. (f) Critical displacement as function of the frame's aspect ratio for a frame of thickness $t = 0.00794$ cm in the intermediate hole size regime, in agreement with Eq. 2.27 (solid line).

Upon contrasting Eq. 2.24 and Eq. 2.26, we find a clear signature of multiscale behaviour in the disparate geometric dependence of $k_{\text{eff}}$ on the aspect ratio, for different hole size regimes. We fit the experimentally measured spring constants of the buckled frames to the theoretical expressions for $k_{\text{eff}}$ as shown in Fig. 11(d), with good agreement. The geometric dependence of the various linearized spring constants is also summarized for both buckled and planar frames in Table 1.

### 2.4.3 Buckling transition

Since $F = \mathrm{d}E/\mathrm{d}\delta x$, we rescale the measured force-extension curve by $t$ and $t^3$ for a given aspect ratio ($w/L = 0.25$) in Fig. 11(b),(c). We find excellent collapse in the pre-buckling and post-buckling regimes, which are controlled by $Y$ and $\kappa$ respectively. The $t^3$ scaling in the post-buckling plateau [Fig. 11(c)] indicates that the force response is governed by $\kappa$ and the hole geometry alone, as explained above in Sec. 2.4.2.

For intermediate frame widths $1/8 < w/L < 1/4$, given that the frame mechanics is dictated by the partial disclinations, we can estimate the geometry dependence of the frame's buckling threshold $\delta x_c$ by adapting previous results on the buckling of topological disclinations [100]. In Ref. [100] it was shown that a single disclination of charge $s$ in a finite crystalline membrane (of linear size $\sim R$) buckles only when the defect charge exceeds a critical threshold $|s_c| = \gamma_c/\gamma$ with $\gamma_c \approx 120$. Note that $\gamma = YR^2/\kappa \to \infty$ as $R \to \infty$ which means the threshold vanishes and *all* topological disclinations buckle in the thermodynamic limit. In our case, the partial disclination charge $s = \Phi(w/L)\delta x/L$ clearly depends on both the prescribed displacement and the frame's geometry, the latter feature having no analogue in the topological case. As the region of influence of the partial disclination is a corner plaquette of area $\sim w^2$, using the relevant FvK number $\gamma = Yw^2/\kappa$, we obtain a threshold charge $|s_c| \simeq \gamma_c/\gamma$ in order to buckle ($\gamma_c$ is a numerical geometry independent constant). Upon using the expression for the charge, we find the critical strain,

$$\frac{\delta x_c}{L} \approx \frac{\gamma_c}{\Phi(w/L)} \left(\frac{t}{w}\right)^2 , \tag{2.27}$$

where we have used the fact that $\kappa/Y \propto t^2$. The quadratic scaling of $\delta x_c$ with $t$ is consistent with the observed data [Fig. 11(e)], with $\delta x_c$ determined by the intersection of linear fits to the data just before and after the transition. From numerical simulations of buckled frames, we estimate $\gamma_c \simeq 75 - 80$ which is smaller than the value expected for topological disclinations ($\gamma_c \simeq 100 - 120$) [100]. The precise value of $\gamma_c$ is of course hard to determine and is likely to be different for different frame shapes.

The dependence of $\delta x_c$ on the frame width $w$ crucially captures the geometric tunability of the local propensity to relax stresses via buckling. Though we expect ultra-narrow frames ($w \to 0$) to have a vanishing threshold for buckling[4] due to sheer loss of material, within the intermediate range of hole sizes Eq. 2.27 in fact suggests a counterintuitive trend, with wider frames buckling prior to narrow ones. This feature is observed for a thin enough sheet in Fig. 11(f).

### 2.4.4 Local deformation field

Apart from the above global characterizations of frame mechanics in terms of effective spring constants, we also probe local measures such as the nonuniform displacement field over the entire frame, thereby allowing for a stronger test of the theory. Using grid lines etched into the paper, painted black to improve the contrast in imaging, we measure the displacement field of the frame by comparing its projected mesh just past buckling to a reference undeformed mesh. As the uniaxial tensile load prescribes the orientation of the induced quadrupoles, with just the scalar charge magnitudes as fitting parameters[5], we find the entire spatial deformation field is well captured within our image charge framework (red lines in Fig. 12).

---

[4] The buckling of narrow frames modeled as a series of coupled ribbons cannot be estimated by a simple crossover argument. In this case, both bending and stretching energy are quadratic in $\delta x$ and the transition is not determined by balancing the two energy estimates. Instead, nonlinearity and local buckling become important in setting the buckling threshold.

[5] As we are close to the buckling threshold, there is significant amount of in-plane stretching and hence the image charges are only partially screened, and the extent of screening is *aprioi* unknown. As a consequence, we cannot fit for the charge magnitudes independently using force-extension measurements and then use the same parameter values to obtain the mesh distortion. Note the deformation is nonetheless still described by a quadrupole.

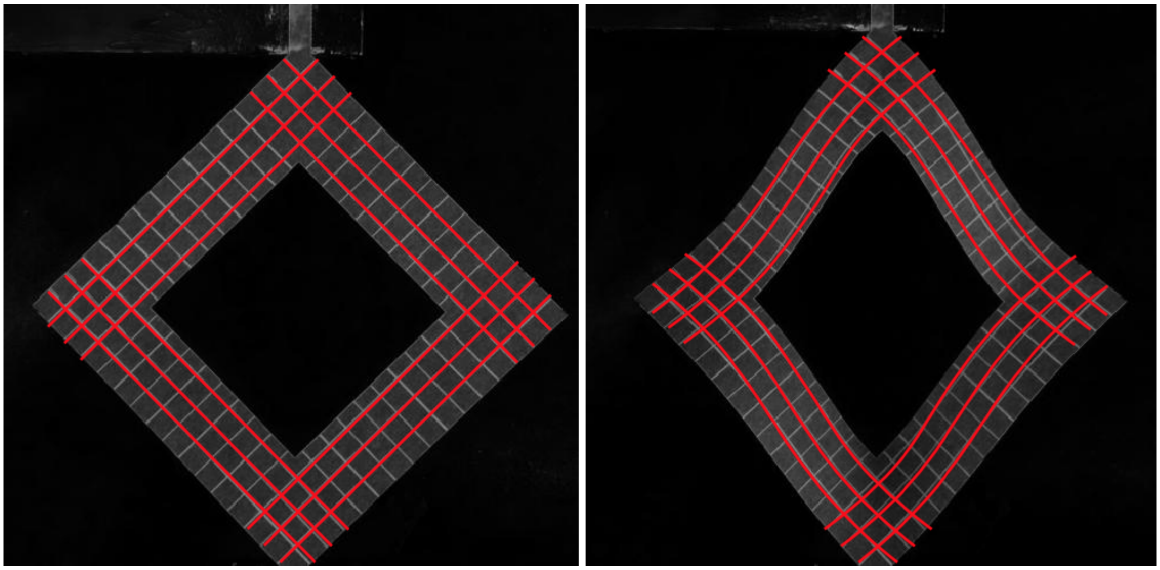

Figure 12 : Comparison between the predicted and observed deformations in a pulled frame right after buckling (a) An undeformed frame with a laser printed Cartesian mesh (gray) and a set of parametric lines (red) fitted to the printed mesh. (b) A deformed frame. Here, the red lines are computed from theory using the original parametric lines as a starting point and the fictitious elastic charges as fitting parameters.

## 2.5 Kirigami as interacting charges: Relaxing pre-stress

The quantitative success of our theory in describing the mechanics of isolated frames encourages us to take a step further and exploit the method of charges to analyze kirigami patterns, which now involves interactions between the charges in different holes. In 2D, the quadrupole is written as $Q_{ij} = Q(\hat{d}_i \hat{d}_j - \delta_{ij}/2)$ with $\hat{\mathbf{d}} = (\cos\psi, \sin\psi)$, $\psi$ being its orientation and $Q$ its magnitude. The elastic interaction energy of two planar quadrupoles $\mathbf{Q}_1, \mathbf{Q}_2$ a distance $\mathbf{r}_{12}$ apart is given by [331, 339]

$$E_{\text{int}} = \frac{Y Q_1 Q_2}{\pi r_{12}^2} \cos(2\psi_1 + 2\psi_2) \ , \tag{2.28}$$

where the quadrupole orientations $\psi_1, \psi_2$ are with respect to the pair separation $\mathbf{r}_{12}$. To demonstrate that interacting elastic charges can fruitfully guide design of kirigami metamaterials, we shall focus on the simple problem of a flattened cone as an example

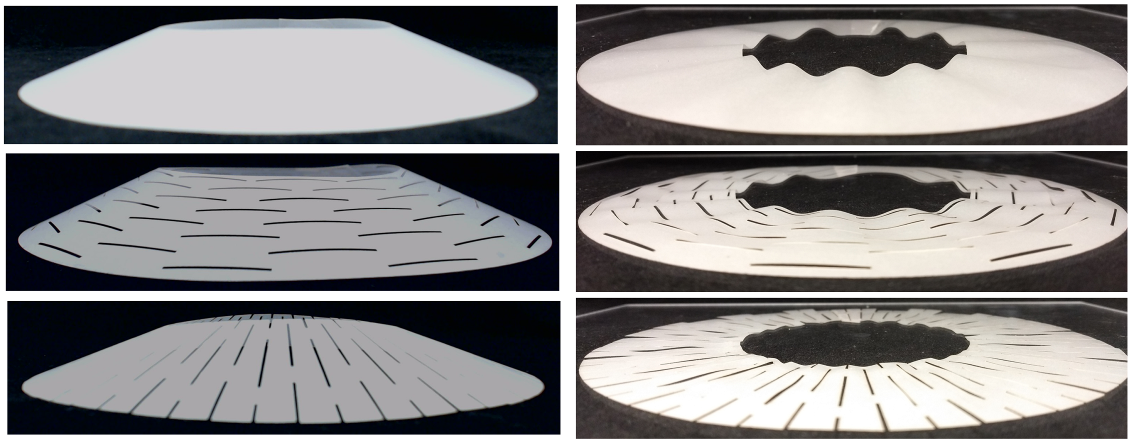

Figure 13 : A regular conical annulus with an angle deficit. When flattened under a piece of acrylic with a small gap, the thin sheet forms wrinkles. Including azimuthal slits (middle row) does not affect the pattern of wrinkles, while a radial array of slits (bottom row) results in azimuthally aligned quadrupoles that minimize the interaction energy with the background stress. Hence when flattened, the radial kirigami pattern locally relaxes stresses allowing the material to accommodate the curvature of the cone without wrinkling.

of the inverse problem in kirigami mechanics. A conical frustum (either with an angle deficit or excess) when confined with a small gap in the plane is stressed due to its intrinsic geometry, a state that can be relaxed for a sufficiently thin sheet by wrinkling (Fig. 13 and Fig. 14, top row). Patterning an appropriate kirigami design affords the sheet a new mechanism of locally relaxing in-plane stress *without* wrinkling.

In the case of both an angle deficit (regular cone) or an excess (e-cone) [341], the planar state of the cone is stressed and the Airy stress function is $\chi = (Y\Delta\varphi/8\pi)r^2\ln(r/R)$ [100], where $\Delta\varphi$ is the angle excess or deficit from $2\pi$ and $R$ is the size of the sample. Both radial $\sigma_{rr}$ and hoop $\sigma_{\varphi\varphi}$ stresses are non-vanishing, while $\sigma_{r\varphi} = 0$. For not too big samples with a sufficiently large core excised out, these stresses are relaxed in the absence of kirigami patterns by the formation of radial wrinkles when the sample is flattened in the plane, as seen for the regular cone in Fig. 13 and for e-cones in Fig. 14.

Considering a periodic kirigami pattern of slits, as the quadrupole-quadrupole interaction decays quadratically with their separation [331, 339], we restrict our

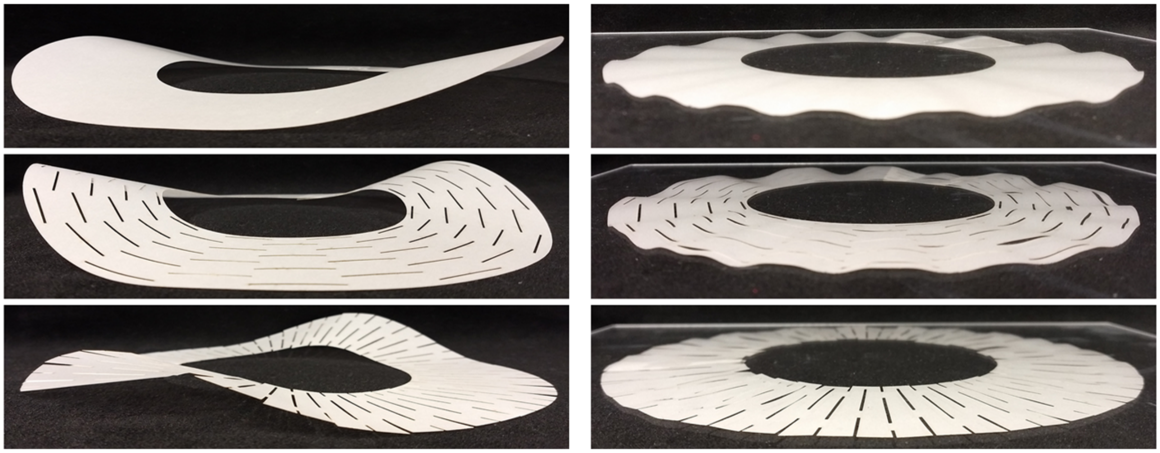

Figure 14 : A conical annulus with an angle surplus (e-cone). In the three images on the left, the e-cone (with and without the kirigami slit pattern) achieves its equilibrium shape in 3D. On the right, the same annulus is flattened under an acrylic plate. Both the intact non-perforated e-cone as well as the one with azimuthal slits develop wrinkles when flattened, while the radial kirigami pattern of slits relaxes stresses in the flattened e-cone (as in the case of the regular cone shown in Fig. 13), leaving it devoid of wrinkles.

analysis to nearest neighbour quadrupole interactions, which is the dominant term. By flattening the cone, as we are interested in the possibility of local buckling as permitted by the kirigami pattern, the relevant interaction to consider is the one between *buckled* quadrupoles. Upon buckling, the curvature of the buckled configuration screens out the induced quadrupolar charge and the interaction between two buckled quadrupoles is no longer long-ranged $\sim 1/r^2$, but instead becomes effectively short-ranged due to screening. This justifies our use of only nearest neighbour interactions in our calculation. In addition, even in the plane, Matsumoto and Kamien [331] have shown that the effective interaction between quadrupoles can be screened by other quadrupoles as well, which leads to a short ranged interaction after angular averaging. This justifies our consideration of only nearest neighbour interactions. Hence we have a pair of quadrupoles $\mathbf{Q}_1$ and $\mathbf{Q}_2$ at a separation of $\mathbf{r}_{12}$ in the presence of a background stress. Aligning the local coordinate frame so that the $x$-axis conincides with the azimuthal direction, we have the total elastic energy given by

$$E = \frac{Y}{\pi r_{12}^2} Q_1 Q_2 \cos(2\psi_1 + 2\psi_2 - 4\theta_{12}) - \frac{Q_1}{4}\sigma_0 \cos 2\psi_1 - \frac{Q_2}{4}\sigma_0 \cos 2\psi_2 \ , \qquad (2.29)$$

where $\sigma_0 = \sigma_{rr} - \sigma_{\varphi\varphi} = \Delta\varphi Y/(4\pi)$, $\theta_{12}$ is the angle made by $\mathbf{r}_{12}$ with the $x$-axis and $\psi_1, \psi_2$ are the angles of the quadrupoles measured from the $x$-axis. As the two holes are otherwise identical, the magnitudes of the two induced charges are the same ($Q_1 = Q_2 = Q$). This energy is minimized when the quardupoles align with the external field ($\psi_1 = \psi_2 = 0$) and the angle of their pair separation is $\theta_{12} = \pi/4$. So a staggered array of quadrupoles aligned in the azimuthal direction relaxes the stressed state of a flattened cone (both regular and excess). The geometry of a slit is such that when pulled, negative partial disclinations form at its ends and the positive partial disclinations are spread around its length leading to the induced quadrupole direction being essentially orthogonal to the long axis of the slit. Unlike square holes that lock the quadrupole orientation to either diagonal, slits only permit quadrupolar charges perpendicular to their long axis. Hence, while azimuthal slits leave the wrinkles unaltered (Fig. 13 and Fig. 14, middle row), radial slits in a staggered array around the cone locally relax stress when flattened (Fig. 13 and Fig. 14, bottom row).

# Chapter 3

# Melting the active nematic: defect unbinding and the motile BKT class

*This chapter is based on work primarily presented in the article "Defect Unbinding in Active Nematics" [343] co-authored by Suraj Shankar, Sriram Ramaswamy, M. Cristina Marchetti, and Mark J. Bowick and published in the journal Physical Review Letters in the year 2018. I was responsible for doing most of the work and the paper itself was equally written by all co-authors.*

## 3.1 Active nematics

Liquid crystals exhibit remarkable orientationally ordered phases, the simplest being the nematic phase in which particles macroscopically align along a single preferred orientation, without a head-tail distinction. The name nematic itself comes from $\nu\eta\mu\alpha$, meaning thread, for the line-like topological defects (disclinations) that are inevitably produced in quenches from the high-temperature disordered phase to the nematic phase

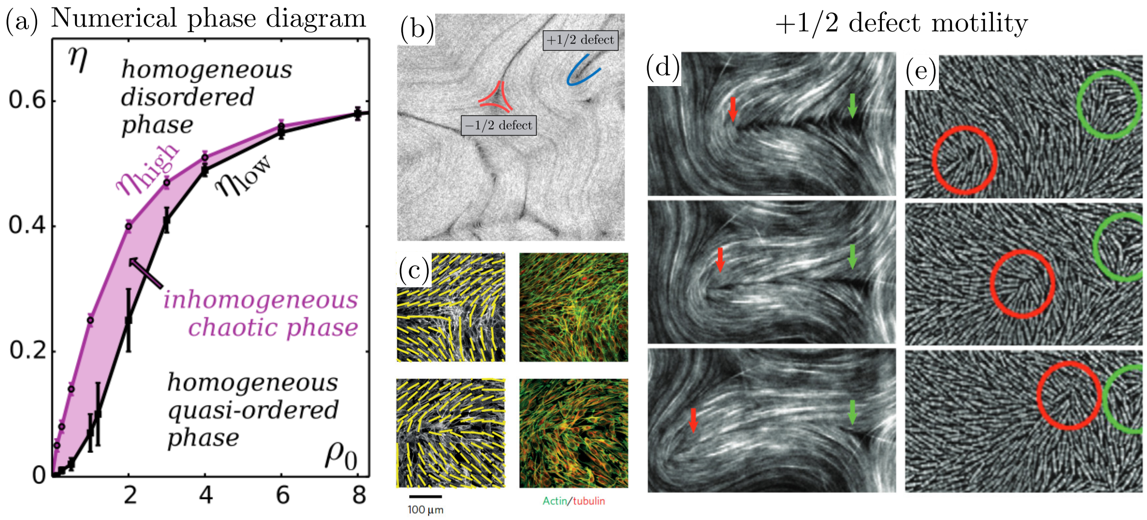

Figure 15 : (a) Phase diagram in the noise ($\eta$) and density ($\rho_0$) plane, obtained from a numerical investigation of a particle model for 2D active nematics, reproduced from Ref. [348]. Disclinations in two experimental model systems - (b) Reconstituted active nematics assembled from microtubule bundles and kinesin motor complexes depleted to an oil-water interface [349], (c) cellular nematics organized by proliferating a monolayer of spindle shaped fibroblasts [258]. The spontaneous propulsion of $+1/2$ defects in active nematics shown as temporal snapshots (from top to bottom) in two distinct systems - (d) Microtubule-kinesin active nematic film [273] and (e) vibrated granular nematic [225]. In both (d) and (e), the $+1/2$ defect (red) is self-propelled, while the $-1/2$ defect (green) remains largely static.

[344–347]. In two dimensions though, as already noted in the Sec. 1.1.1, disclinations are point-like defects, and so may be thought of as localized particles. The nematic pattern around a disclination is a distinctive fingerprint of the spontaneous symmetry-breaking that characterizes nematic order and distinguishes the elementary defects from, say, integer strength vortices in two-dimensional spin systems (see Fig. 1). The nematic director rotates through a half-integer multiple of $2\pi$ as one circumnavigates a defect. Thus, the lowest-energy defects are referred to as carrying strength $\pm 1/2$. As summarized in Sec. 1.1.1, the entropic unbinding of such point disclinations drives the nematic to isotropic (NI) transition in two dimensional equilibrium nematics [10, 12, 13, 350].

In recent years there has been much focus on nematics composed of elongated units that are self-driven - hence *active* nematics [280, 351]. An active nematic is by far the simplest realization of an active system that can display orientational order. Unlike its polar counterpart, where the appearance of macroscopic polar order results in collective directed motion or flocking [215, 293], the active nematic involves driven *apolar* constituents, which means on average the system goes nowhere [280] making its properties far more subtle. Examples include collections of living cells [253–256, 259, 260, 352], synthetic systems built of cellular extracts [273, 274, 276], and vibrated granular rods [225]. Active nematics exhibit enormous density fluctuations and complex spatio-temporal dynamics, accompanied by spontaneous defect proliferation, features that have all come to be viewed as characteristic of this phase of matter [281].

The theoretical study of active nematics began with coarse-grained approaches [280, 353], followed by numerical agent-based [348, 354] or lattice gas simulations [355] of minimal microscopic models. In two dimensions, numerical work by Ngo et al. [348] revealed an order-disorder transition that involved three phases - (i) a homogeneous disordered gas at high noise and low density, (ii) an intermediate locally banded, chaotic, macroscopically isotropic but segregated phase, and (iii) a homogeneous but fluctuating (quasi)-ordered nematic phase at low noise and high density. The numerically obtained phase diagram is given in Fig. 15(a). The segregated phase [purple region in Fig. 15(a)] is presumably a result of the instability of the homogeneous nematic phase to band formation close to the mean-field transition [356–359]. The lines delimiting the chaotic band phase determine the binodal lines. The linear instability of the ordered phase then corresponds to the spinodal (not shown) which falls well within the band forming region. The inhomogeneous bands are themselves unstable to transverse fluctuations (in a large enough system), leading to the intermediate chaotic and phase-separated but isotropic phase between the binodals. This should be contrasted with the polar case, where a spatially periodic phase of coherently moving stable bands is seen just past the flocking transition [306]. An analytical understanding of the transition from the chaotic biphasic state to the ordered nematic phase is unavailable, and strong density fluctuations obscure its character even in numerical studies [348]. The defect unbinding transition presented here provides a candidate scenario, although the impact of density inhomogeneities remains unclear. In "metric-free" models, in which the interaction neighbourhood is the first Voronoi shell, numerical studies [348] find only two phases, both homogeneous: a quasi-long-range ordered nematic and an isotropic phase, separated by a transition of BKT type. There has also been a lot of previous work at the continuum level (in the absence of noise) on "wet" active nematic systems, i.e., including flow and hydrodynamic interactions [282, 360–365].

Although much progress has been made in understanding the properties of the ordered phase [280, 348, 358, 359, 366, 367], a complete theory of order, fluctuations, defects and phase transitions of active nematics still eludes us. The nematic itself has no net polarity, but the director pattern around a strength +1/2 defect has a local comet-like geometric polarity (Fig. 16). In an active system this renders +1/2 defects motile [225, 282] with a self-propelling speed proportional to activity [282] [see Fig. 15(d),(e)]. Both experiments [253, 273–276, 349, 368] and simulations [282, 361–363, 365, 369–371] have shown that motile defects play a key role in driving self-sustained active flows.

## 3.2 The paradox: do ordered active nematics exist?

The spontaneous motility of +1/2 disclinations immediately raises a puzzle with regard to the existence of a low-activity quasi-long-range ordered active nematic in 2D [366, 367]. A naïve yet physical argument (detailed below) suggests that defect

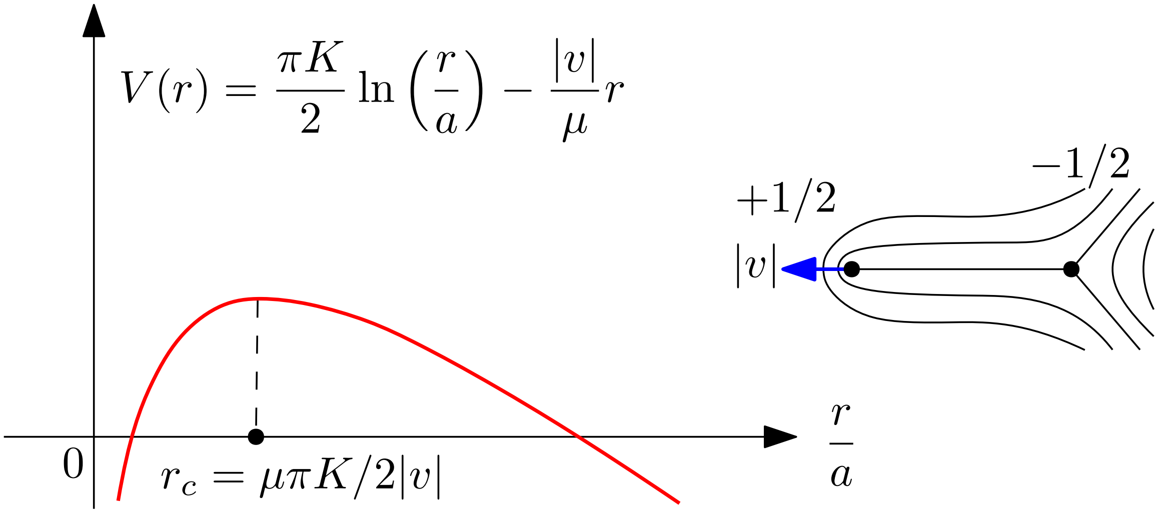

Figure 16 : Potential $V(r)$ for a neutral defect pair for the configuration in which the direction of motility of the $+1/2$ disclination points away from the $-1/2$ and is held fixed. This naïve picture suggests that incipient active defect pairs have an exponentially small, but finite, rate $\propto e^{-V(r_c)/T}$ ($T$ is the temperature) to overcome the barrier at low temperature, and hence always unbind.

motility *always* causes incipient defects to unbind destroying *any* nematic order in an active system. In an equilibrium nematic, two $\pm 1/2$ defects at a distance $r$ experience an attractive interaction $V_0(r) = (\pi K/2)\ln(r/a)$, with $K$ a Frank elastic constant and $a$ the size of the defect core. Hence, neglecting inertia, they are drawn towards each other according to $\dot{r} = -\mu \partial_r V_0$, with $\mu$ a defect mobility. One could then argue that the dynamics of a suitably oriented $\pm 1/2$ defect pair in an *active* nematic is governed by relaxation in an effective potential [282]

$$\dot{r} = -\mu \partial_r V \ , \quad V(r) = \frac{\pi K}{2} \ln\left(\frac{r}{a}\right) - \frac{|v|}{\mu} r \ , \tag{3.1}$$

where $|v| > 0$ is the self-propelling speed with which the $+1/2$ disclination is moving away from the $-1/2$ disclination (see Fig. 16). The resulting barrier $V(r_c) = (\pi K/2)\left[\ln\left(\pi \mu K/(2|v|a)\right) - 1\right]$ at distance $r_c = \pi \mu K/(2|v|)$ is finite, which means that the defect pair is always unbound, and active nematic order thus destroyed, at any nonzero temperature (Fig. 16). As activity is increased, more and more defect pairs will be liberated [273, 282, 362] suggesting that nematic order would be completely destroyed by the swarming disordered cores, much like driven vortices in superconducting films can destroy superconductivity. In this simple argument, motility acts analogous to an external electric field in a superfluid or superconducting thin film, that would dissociate vortex pairs at a finite rate $\propto e^{-V(r_c)/T}$, given by a thermally assisted Kramer's escape process [372]. Yet, defect free active nematic order has been reported in both simulations [348] and experiments [254], indicating that the simplistic one-dimensional picture of defect unbinding in Fig. 16 is incomplete.

Evidently the resolution of this paradox relies on ingredients not included in the heuristic argument. In particular, in Sec. 3.4, we show that the above argument fails because rotational noise, by disrupting the directed motion of the $+1/2$ defects, counterintuitively restores the ordered nematic phase. We do this by precisely mapping the dynamics of active defects onto that of a mixture of motile $(+1/2)$ and passive $(-1/2)$ particles with interaction forces and aligning torques, putting on firm ground previous phenomenological models [274, 282, 373]. A key new result is the derivation of the angular dynamics of the $+1/2$ defects. Below, we shall explicitly derive these effective equations for defect dynamics that can also provide a simple model capable of quantifying the dynamics of interacting active defects in confined geometries.

## 3.3 Defects as quasiparticles

### 3.3.1 Hydrodynamic model

We begin with the hydrodynamic equations of a two-dimensional nematic liquid crystal written in terms of the tensor order parameter $Q_{\mu\nu} = S(2\hat{n}_\mu\hat{n}_\nu - \delta_{\mu\nu})$ and the flow velocity $\mathbf{u}$, where $S$ is the scalar order parameter and $\hat{\mathbf{n}}$ is the director field. We ignore density fluctuations, although we expect this restriction could be dropped without qualitatively changing the results. The $\mathbf{Q}$ equation is as for passive nematics [374],

$$\gamma \mathcal{D}_t \mathbf{Q} = \left[a_2 - a_4 \operatorname{tr}(\mathbf{Q}^2)\right] \mathbf{Q} + K\nabla^2 \mathbf{Q} \ , \tag{3.2}$$

where $\mathcal{D}_t = \partial_t + \mathbf{u} \cdot \boldsymbol{\nabla} - [\cdot, \boldsymbol{\Omega}]$ is the comoving and corotational derivative with the vorticity tensor $\Omega_{\mu\nu} = (\nabla_\mu u_\nu - \nabla_\nu u_\mu)/2$. Only the relaxational part of the dynamics is retained in Eq. 3.2, with $\gamma$ a rotational viscosity, $K$ a Frank elastic constant and $a_2, a_4$ the parameters that set the mean-field NI transition at $a_2 = 0$. A treatment including various flow alignment terms is given in Appendix 3.A. At equilibrium, the homogeneous ordered state for $a_2 > 0$ has $S_0 = \sqrt{a_2/(2a_4)}$ and an elastic coherence length $\xi = \sqrt{K/a_2}$. For an isolated static ±1/2 defect in equilibrium, the director $\hat{\mathbf{n}}(\varphi) = (\cos(\varphi/2), \pm\sin(\varphi/2))$ rotates by $\pm\pi$ with the azimuthal angle $\varphi$, and $S$ vanishes at the core of the defect, assuming its bulk value on length scales larger than the defect core size $a \sim \xi$. Activity enters in the force balance equation, which, ignoring inertia and in-plane viscous dissipation, is given by $-\Gamma \mathbf{u} + \boldsymbol{\nabla} \cdot \boldsymbol{\sigma}^a = \mathbf{0}$, where $\Gamma$ is the friction with the substrate and $\boldsymbol{\sigma}^a = \alpha \mathbf{Q}$ is the active stress tensor that captures the internal forces generated by active units [216, 218]. We neglect elastic and Ericksen stresses as they are higher order in gradients. The system is extensile for $\alpha < 0$ and contractile for $\alpha > 0$. For a +1/2 disclination, the active backflow at its core gives rise to a self-propulsion speed $\sim |\alpha|/(\Gamma a)$ [282, 373].

The +1/2 disclination has a local geometric polarization $\mathbf{e}_i = a\boldsymbol{\nabla} \cdot \mathbf{Q}(\mathbf{r}_i^+)$ (evaluated at the core of the defect), defined here to be dimensionless. Note that $\mathbf{e}_i$ is *not* a unit vector. Our treatment does not require the mode expansion used in Ref. [375] to treat multi-defect configurations. An isolated +1/2 defect has a non-vanishing flow velocity at its core ($\mathbf{u}(\mathbf{r}_i^+) = v\mathbf{e}_i$, $v = \alpha S_0/\Gamma a$), while the −1/2 defect does not, due to its

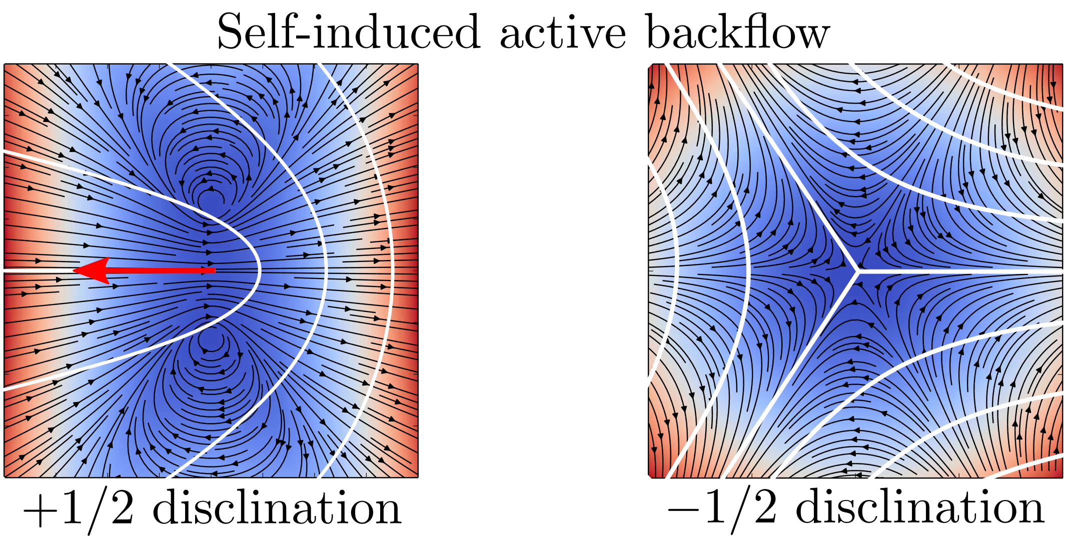

Figure 17 : The active backflow due to the nematic distortion of a ±1/2 disclination. The white lines indicate the nematic director orientation $\hat{\mathbf{n}}$ and the black arrows, the flow velocity $\mathbf{u}$ (with the colour map being $|\mathbf{u}|$). The red arrow is $\mathbf{e} = a\boldsymbol{\nabla}\cdot\mathbf{Q}(\mathbf{r}^+)$, the geometric polarity for the +1/2 disclination. The flow field for the +1/2 disclination has a characteristic double vortex structure, while the −1/2 disclination presents a six-fold symmetric flow field. The flow at the core of the +1/2 defect is non-vanishing and is directed towards the comet head here (opposite to $\mathbf{e}$), as is the case for an extensile active nematic ($\alpha < 0$) plotted here. For a contractile active nematic ($\alpha > 0$), the arrows of flow reverse direction.

three-fold symmetry ($\mathbf{u}(\mathbf{r}_i^-) = \mathbf{0}$)[1]. The self-induced active backflow generated by an isolated defect is shown in Fig. 17.

### 3.3.2 Defect positional dynamics

Combining the defect motility with the passive interaction[2], the resulting equations for the positional dynamics of defects is given by

$$\dot{\mathbf{r}}_i^+ = v\mathbf{e}_i - \mu\boldsymbol{\nabla}_i\mathcal{U} + \sqrt{2\mu T}\boldsymbol{\xi}_i(t) \ , \tag{3.3a}$$

---

[1] Including a “second” active force $\sim \alpha'\mathbf{Q}\cdot(\boldsymbol{\nabla}\cdot\mathbf{Q})$ does not affect the ballistic motion of the +1/2 defect [376].

[2] Apart from the motility of the +1/2 defect, both charge disclinations are also entrained by active flows generated by other defects. This leads to $\dot{\mathbf{r}}_i^\pm \sim \alpha\boldsymbol{\sigma}_3\cdot\boldsymbol{\nabla}_i\sum_{j\neq i} q_j \ln|(\mathbf{r}_i - \mathbf{r}_j)/a|$, where $\boldsymbol{\sigma}_3$ is a Pauli matrix, and provides an anisotropic active correction to bend and splay elasticity. Including fluctuations, this term is $\sim \mathcal{O}(r_{ij}^{-1-\eta})$ [367] where $r_{ij}$ is the distance between two defects and $\eta = T/(2\pi K)$, so it is subdominant to the passive interaction $\boldsymbol{\nabla}_i\mathcal{U}$.

$$\dot{\mathbf{r}}_i^- = -\mu \boldsymbol{\nabla}_i \mathcal{U} + \sqrt{2\mu T}\boldsymbol{\xi}_i(t) \ , \tag{3.3b}$$

where $\mu \propto 1/\gamma$ is a defect mobility, $\boldsymbol{\xi}_i(t)$ Gaussian white noise and

$$\mathcal{U} = -2\pi K \sum_{i \neq j} q_i q_j \ln \left| \frac{\mathbf{r}_i - \mathbf{r}_j}{a} \right| \ , \tag{3.4}$$

is the usual Coulomb interaction between defects, with $q_i = \pm 1/2$ the strength of the $i$th defect. The elastic constant $K$ includes corrections from hydrodynamic flows linear in activity which can destabilize the nematic state even in the absence of topological defects [376, 377]. Here we take $K > 0$ (permitted in a domain of parameter space [376, 377]) to guarantee an elastically stable nematic. Note that $v \propto \alpha$ can be of either sign. The translational noise strength $T$ arises from thermal or active noise in the $\mathbf{Q}$ equation (Eq. 3.2).

The defect mobility $\mu$ can be computed explicitly in a more sophisticated calculation given in Appendix 3.A, by adapting similar computations performed for defect motion in equilibrium and dissipative systems [289, 292, 378–383]. Such a calculation proceeds via a perturbative solution of Eq. 3.2 for a slowly moving isolated defect whose far-field distortion is matched onto that of other distant defects. When computed correctly, no divergences are encountered and the defect velocity is obtained as an explicit combination of motility from active flow (only for the +1/2 defect) and motion due to an imposed phase gradient (corresponding to the passive interaction). This calculation gives exactly Eqs. 3.3a, 3.3b with the defect mobility weakly (logarithmically) dependent on the defect speed. To simplify things, we neglect the weak logarithmic correction and take $\mu$ to be a constant, valid for slowly moving defects or when screening is present.

### 3.3.3 Defect orientational dynamics

The important feature of activity is that it elevates the geometric structural polarity of the +1/2 disclination to a *dynamical* degree of freedom, one that drives motion. In turn, $\mathbf{e}_i$ also has its own dynamics, which is, in principle, contained in the $\mathbf{Q}$ equation. Neglecting noise for now and using the quasistatic approximation in a frame comoving with the +1/2 defect, i.e., $[\partial_t \mathbf{Q}]_{\mathbf{r}_i^+(t)} = \mathbf{0}$, we have $\dot{\mathbf{e}}_i(t) = a[\mathbf{v}_i(t) \cdot \boldsymbol{\nabla}] \boldsymbol{\nabla} \cdot \mathbf{Q}(\mathbf{r}_i^+(t))$, where $\mathbf{v}_i = v\mathbf{e}_i - \mu \boldsymbol{\nabla}_i \mathcal{U}$ is the deterministic part of $\dot{\mathbf{r}}_i^+$ (Eq. 3.3a). Our approximation neglects elastic torques on $\mathbf{e}_i$ due to smooth director distortions, shown to be unimportant for the dynamics of neutral pairs [384, 385] [this is justified in greater detail when considering noise in the non-quasistatic solution (see Appendix 3.C)]. Assuming a dilute gas of slowly moving defects, we perturbatively expand Eq. 3.2 about the equilibrium defect configuration and solve for $\mathbf{Q}$. Using this solution, we evaluate $\boldsymbol{\nabla}\boldsymbol{\nabla} \cdot \mathbf{Q}$ at the core of the defect to obtain (the details are given in Appendix 3.B)

$$\dot{\mathbf{e}}_i = -\frac{5\gamma}{8K} \left[\mathbf{v}_i \cdot (\mathbf{v}_i - v\mathbf{e}_i)\right] \mathbf{e}_i - \frac{v\gamma}{8K} (\mathbf{v}_i \times \mathbf{e}_i) \, \boldsymbol{\epsilon} \cdot \mathbf{e}_i \ , \tag{3.5}$$

where $\mathbf{v}_i = v\mathbf{e}_i - \mu \boldsymbol{\nabla}_i \mathcal{U}$ is the deterministic part of the +1/2 defect velocity and $\boldsymbol{\epsilon}$ is the two-dimensional Levi-Civita tensor. Since $\mathbf{e}_i$ is not a unit vector, its deterministic dynamics has a term along $\mathbf{e}_i$ fixing its preferred magnitude and one transverse to it aligning the polarization to the force. Note that Eq. 3.5 remains unchanged even when flow alignment terms are included in the hydrodynamic description (Appendix 3.B), in particular both longitudinal and transverse active terms in Eq. 3.5 arise exclusively from the convective term $(\mathbf{u} \cdot \boldsymbol{\nabla}\mathbf{Q})$ in the dynamics of $\mathbf{Q}$ (Eq. 3.2), i.e., the fact that active flows are genuine velocities that cause motion. This is an exceedingly general and fundamental feature of active driving and hence we expect analogous orientational dynamics of active defects in other situations as well, such as upon including viscous flows, density variations or incompressibility.

To elucidate the nature of the torques on the polarization, we write $\mathbf{e}_i = |\mathbf{e}_i|(\cos\theta_i, \sin\theta_i)$ and decompose the elastic force acting on the $i$th defect ($\mathbf{F}_i = -\boldsymbol{\nabla}_i\mathcal{U}$) as $\mathbf{F}_i = |\mathbf{F}_i|(\cos\psi_i, \sin\psi_i)$. For the defect orientation $\theta_i$, Eq. 3.5 then reduces to

$$\partial_t\theta_i = v\frac{\mu\gamma}{8K}|\mathbf{F}_i||\mathbf{e}_i|\sin(\theta_i - \psi_i)\ . \tag{3.6}$$

Active backflows tend to align the defect polarization with the force acting on the defect. A similar alignment kernel has been used previously to phenomenologically model flocking and jamming in cellular systems [235, 257], but here it arises naturally from the active dynamics of a two-dimensional nematic. Importantly, here the torque is controlled by activity ($v \propto \alpha$). An extensile system ($v \propto \alpha < 0$) favors *alignment* of the polarization with the force, while a contractile system ($v \propto \alpha > 0$) favors *anti-alignment* of polarization and force (Fig. 18). The equations obtained here also predict patterns for four $+1/2$ defects on a sphere as obtained in Ref. [274].

For configurations in which the $+1/2$ is running *away* from the $-1/2$ in an isolated neutral defect pair, the active aligning torque (Eq. 3.6) stabilizes the $+1/2$ defect polarization against transverse fluctuations [see Fig. 18(a),(b)], irrespective of the sign of activity. Hence activity not only renders the $+1/2$ defect motile, but enhances the persistence of defect motion through the torques, favoring the unbinding of defect pairs. This feature breaks the symmetry between pair creation and annihilation events for both extensile and contractile systems and justifies the one-dimensional cartoon in Fig. 16. As we will see below, however, the stochastic part of the defect dynamics (neglected so far) can disrupt these configurations, preventing unbinding. We finally remark that one can also obtain configurations for pairs of $+1/2$ disclinations [Fig. 18(c),(d)] that are stable against transverse deflections of either polarization.

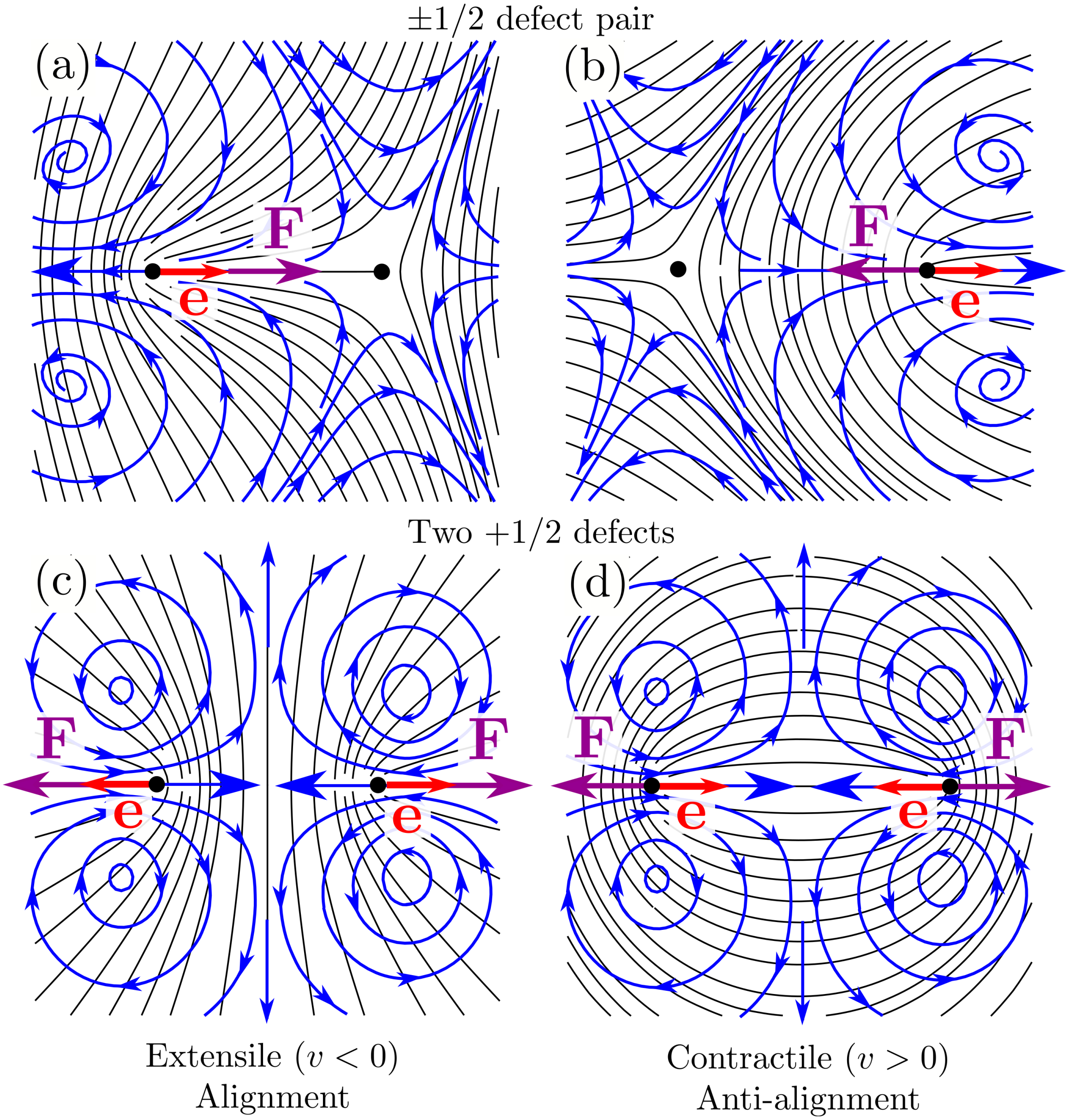
±1/2 defect pair
(a)
F
e
(b)
F
e
Two +1/2 defects
(c)
F
e
(d)
F
e
Extensile ($v < 0$)
Alignment
Contractile ($v > 0$)
Anti-alignment

Figure 18 : Configurations of defect pairs whose orientations, for an imposed fixed separation, are stable to transverse fluctuations of the +1/2 polarization(s). The active backflow is shown in blue and the director configuration in black. The polarization and force on each +1/2 defect is shown in red and in purple respectively. The top row shows a neutral ±1/2 defect pair orientationally stable for (a) extensile ($v < 0$) and (b) contractile ($v > 0$) systems. Similarly, in the bottom row we have a pair of +1/2 defects that are orientationally stable. The far field nematic texture for these two-defect configurations has an aster-like structure when (c) extensile ($v < 0$) and a vortex-like structure when (d) contractile ($v > 0$).

As shown, in the far-field of these two-defect configurations, aster-like structures are favored in an extensile system while vortex-like structures are favored in a contractile one, as seen in confined fibroblasts [258].

### 3.3.4 Including noise

The stochastic part of the dynamics of $\mathbf{e}_i$ also derives from noise in the dynamics of $\mathbf{Q}$, but a full calculation is challenging and beyond the scope of the present work. As $\mathbf{e}_i$ is a two-dimensional vector, its dynamics has two kinds of noise, longitudinal and transverse. Including both noise terms, we write the full stochastic equation for the polarization dynamics as,

$$\dot{\mathbf{e}}_i = \frac{5\mu\gamma}{8K}\left[\boldsymbol{\nabla}_i\mathcal{U}\cdot(v\mathbf{e}_i-\mu\boldsymbol{\nabla}_i\mathcal{U})\right]\mathbf{e}_i + \frac{v\mu\gamma}{8K}(\boldsymbol{\nabla}_i\mathcal{U}\times\mathbf{e}_i)\,\boldsymbol{\epsilon}\cdot\mathbf{e}_i - \sqrt{2D_R}\,\boldsymbol{\epsilon}\cdot\mathbf{e}_i\;\eta_i(t)+\boldsymbol{\nu}_i(t)\;, \tag{3.7}$$

where we have written $\mathbf{v}_i$ in terms of the force $-\boldsymbol{\nabla}_i\mathcal{U}$. Smooth director phase fluctuations can be shown (see Appendix 3.C) to generate rotational noise $\sim D_R$ that changes the direction of $\mathbf{e}_i$, while keeping $|\mathbf{e}_i|$ fixed (this is hence the transverse component of the noise). Here $\eta_i(t)$ is unit white noise and $D_R = \mu T/\ell_R^2$ is the rotational diffusivity of the $+1/2$ defect, with $\ell_R \sim a$. At low activity, rotational noise is primarily thermal in origin with $D_R \propto T$, but it can receive nonequilibrium and nonthermal corrections at higher activity.

Unlike rotational noise that is more systematically derivable from smooth "spin-wave" like director fluctuations, the longitudinal component of the noise $\boldsymbol{\nu}_i(t)$ is much harder to derive explicitly from noise in the $\mathbf{Q}$ equation of motion. This noise generates fluctuations in the magnitude of the polarization $|\mathbf{e}_i|$ and derives predominantly from noise in the scalar order parameter $S$ instead of the director phase. Within the low activity expansion, the properties of the longitudinal component $\boldsymbol{\nu}_i(t)$ of the noise are inferred from its equilibrium limit, determined by requiring that the probability distribution of the defect gas relaxes to the corresponding equilibrium form where (for one Frank constant) defect position and polarization are decoupled in the absence of activity (i.e., for $v = 0$). To do this, we first look at the derived deterministic dynamics for $\mathbf{e}_i$ (Eq. 3.5), which in equilibrium, setting $v = 0$, reduces to

$$\dot{\mathbf{e}}_i = -\frac{5\mu^2\gamma}{8K}|\boldsymbol{\nabla}_i\mathcal{U}|^2 \; \mathbf{e}_i \; . \tag{3.8}$$

As the dynamics is overdamped and relaxational, both positional and orientational (polarization) dynamics must derive from a *single* energy functional.

In the one-Frank constant approximation at equilibrium, spatial rotations and order parameter rotations get decoupled and become independent symmetries of the system. By virtue of this enhanced symmetry, the joint probability distribution of defect positions and polarizations must then decouple, with the positions governed by a Boltzmann weight with respect to the pair potential $\mathcal{U}$. This is also consistent with the derived deterministic dynamics, where the positional dynamics (Eqs. 3.3a, 3.3b) is independent of $\mathbf{e}_i$ when $v = 0$. Hence the $|\boldsymbol{\nabla}_i\mathcal{U}|^2$ term in Eq. 3.8 is naturally viewed as being part of a kinetic coefficient governing the relaxation of the polarization.

In order to really determine what constitutes the thermodynamic force in Eq. 3.8, we need to write down the energy involving $\mathbf{e}_i$. As $\mathbf{e}_i = a\boldsymbol{\nabla}\cdot\mathbf{Q}(\mathbf{r}_i^+)$, to lowest order, the energetic contribution involving the polarization is $\sim |\mathbf{e}_i|^2$. This term penalizes gradients of the alignment tensor as is expected of the elasticity of a nematic liquid crystal. Note that, a more complicated symmetry breaking Mexican hat like potential for $\mathbf{e}_i$ is unnatural as it favours the spontaneous creation of gradients and modulation of nematic order. Including higher order even polynomials is possible but it complicates the noise statistics by making it multiplicative. The simplest choice that retains just additive noise is the quadratic energy, which is what we choose. The polarization $\mathbf{e}_i$ itself being dimensionless, we use $K$ for units of energy (the only thermodynamic parameter available). With this in place, the energetic contribution from $\mathbf{e}_i$ is written as $K|\mathbf{e}_i|^2/2$, where the factor of two (fixing an overall scale for $\mathbf{e}_i$) is chosen for convenience. In this form, $\mathbf{e}_i$ being an internal degree of freedom that depends on the defect core structure, the term $K|\mathbf{e}_i|^2/2$ then represents the simplest contribution to the defect core energy [279].

Putting it all together, we obtain the joint probability distribution of defect positions $\mathbf{r}_i$ and polarizations $\mathbf{e}_i$ at equilibrium to be

$$P_{\text{eq}}^{2N} = \frac{1}{Z_{2N}} e^{-\mathcal{U}/T} \prod_{i=1}^{N} \left( \frac{K}{2\pi T} e^{-K|\mathbf{e}_i|^2/2T} \right) \ , \tag{3.9}$$

where $Z_{2N}$ is the Coulomb gas partition function for $N$ neutral defect pairs. Using this probability distribution and the fluctuation-dissipation relation [386] fixes the kinetic coefficient in Eq. 3.8 to be $(5\mu^2\gamma/8K^2)|\boldsymbol{\nabla}_i\mathcal{U}|^2$ which upon multiplying with $2T$ gives the two point correlation of the longitudinal noise $\boldsymbol{\nu}_i(t)$ to be

$$\langle \boldsymbol{\nu}_i(t)\boldsymbol{\nu}_j(t')\rangle = \mathbf{1}\delta_{ij} T \frac{5\mu^2\gamma}{4} \frac{|\boldsymbol{\nabla}_i\mathcal{U}|^2}{K^2} \delta(t-t') \ . \tag{3.10}$$

No summation on repeated indices is implied. As written, the noise has no stochastic ambiguity and is independent of any thermodynamic parameters, involving only the defect mobility $\mu$ and rotational viscosity $\gamma$, as it should. This completes the derivation of effective equations for the dynamics of defects as particles, with the crucial inclusion of both defect polarization dynamics and noise.

## 3.4 Defect unbinding and re-entrant melting

To study defect unbinding, we now examine the dynamics of an isolated ±1/2 defect pair governed by coupled Langevin equations for the pair separation $\mathbf{r} = \mathbf{r}^+ - \mathbf{r}^-$ (obtained from Eqs. 3.3a, 3.3b) and the +1/2 polarization $\mathbf{e}$ (Eq. 3.7). These are given by

$$\dot{\mathbf{r}} = v\mathbf{e} - 2\mu\boldsymbol{\nabla}\mathcal{U} + \sqrt{4\mu T}\boldsymbol{\xi}(t) \ , \tag{3.11}$$

$$\dot{\mathbf{e}} = -\frac{\mu\gamma}{K}\boldsymbol{\zeta}\cdot\left[\mu\mathbf{e}|\boldsymbol{\nabla}\mathcal{U}|^2 - v|\mathbf{e}|^2\boldsymbol{\nabla}\mathcal{U}\right] - \sqrt{2D_R}\ \boldsymbol{\epsilon}\cdot\mathbf{e}\ \eta(t) + \boldsymbol{\nu}(t) \ , \tag{3.12}$$

where $\boldsymbol{\zeta} = (\mathbf{1} + 4\hat{\mathbf{e}}\hat{\mathbf{e}})/8$ has been used to simplify notation and $\mathcal{U}(\mathbf{r}) = (\pi K/2)\ln(r/a)$ is the pair potential. Both $\boldsymbol{\xi}(t)$ and $\eta(t)$ are unit Gaussian white noise and $\boldsymbol{\nu}(t)$ has correlations given in Eq. 3.10. The corresponding Fokker-Planck equation for the joint probability distribution $P(\mathbf{r}, \mathbf{e}; t)$ is given by

$$\begin{aligned}\partial_t P + v\mathbf{e}\cdot\boldsymbol{\nabla}P + \frac{v\mu\gamma}{2K}\boldsymbol{\nabla}_{\mathbf{e}}\cdot\left[(\mathbf{e}\cdot\boldsymbol{\nabla}\mathcal{U})\mathbf{e}P + \frac{1}{4}|\mathbf{e}|^2\boldsymbol{\nabla}\mathcal{U}P\right] \\ = D_R(\mathbf{e}\times\boldsymbol{\nabla}_{\mathbf{e}})^2P + 2\mu\boldsymbol{\nabla}\cdot\left[P\boldsymbol{\nabla}\mathcal{U} + T\boldsymbol{\nabla}P\right] + \frac{5\mu^2\gamma|\boldsymbol{\nabla}\mathcal{U}|^2}{8K^2}\boldsymbol{\nabla}_{\mathbf{e}}\cdot\left[K\mathbf{e}P + T\boldsymbol{\nabla}_{\mathbf{e}}P\right] \ .\end{aligned} \tag{3.13}$$

Taking moments of the polarization and suppressing the temporal argument, $\rho(\mathbf{r}) = \int \mathrm{d}^2e\ P(\mathbf{r}, \mathbf{e})$, $\mathbf{w}(\mathbf{r}) = \int \mathrm{d}^2e\ \mathbf{e}P(\mathbf{r}, \mathbf{e})$ and $\mathbf{M}(\mathbf{r}) = \int \mathrm{d}^2e\ \mathbf{e}\mathbf{e}P(\mathbf{r}, \mathbf{e})$, we have

$$\partial_t\rho + v\boldsymbol{\nabla}\cdot\mathbf{w} = 2\mu\boldsymbol{\nabla}\cdot\left[\rho\boldsymbol{\nabla}\mathcal{U} + T\boldsymbol{\nabla}\rho\right] \ , \tag{3.14}$$

$$\begin{aligned}\partial_t\mathbf{w} + v\boldsymbol{\nabla}\cdot\mathbf{M} - \frac{v\mu\gamma}{2K}\left[\mathbf{M}\cdot\boldsymbol{\nabla}\mathcal{U} + \frac{\mathrm{tr}(\mathbf{M})}{4}\boldsymbol{\nabla}\mathcal{U}\right] = -\left(D_R + \frac{5\mu^2\gamma|\boldsymbol{\nabla}\mathcal{U}|^2}{8K}\right)\mathbf{w} \\ + 2\mu\boldsymbol{\nabla}\cdot\left[\boldsymbol{\nabla}\mathcal{U}\mathbf{w} + T\boldsymbol{\nabla}\mathbf{w}\right] \ ,\end{aligned} \tag{3.15}$$

$$\partial_t\mathbf{M} = -4D_R\left(\mathbf{M} + \mathrm{tr}(\mathbf{M})\frac{\mathbf{1}}{2}\right) + 2\mu\boldsymbol{\nabla}\cdot(\boldsymbol{\nabla}\mathcal{U}\mathbf{M} + T\boldsymbol{\nabla}\mathbf{M}) - \frac{5\mu^2\gamma|\boldsymbol{\nabla}\mathcal{U}|^2}{4K^2}(K\mathbf{M} - T\rho\mathbf{1}) \ , \tag{3.16}$$

where in the final Eq. 3.16, we have neglected the third and all higher moments of the polarization $\mathbf{e}$ by setting $\langle\mathbf{eee}\rangle \simeq \mathbf{0}$ as a closure ansatz for the moment hierarchy. As we shall see below, this closure is well-controlled in a small activity expansion. Upon integrating out the polarization, by rotational symmetry, we have $\rho = \rho(r)$, $\mathbf{w} = w(r)\hat{\mathbf{r}}$ and $\mathbf{M} = A(r)\mathbf{1} + B(r)\hat{\mathbf{r}}\hat{\mathbf{r}}$, where $r = |\mathbf{r}|$ and $\hat{\mathbf{r}} = \mathbf{r}/r$.

At equilibrium ($v = 0$), $w = 0$, $B = 0$ and all higher order odd moments vanish as well. Hence for small activity, we can estimate that to leading order the third moment decays at least as quickly as $\langle\mathbf{eee}\rangle \sim v\rho/r$, as any anisotropy must derive from $\boldsymbol{\nabla}\mathcal{U} \sim 1/r$. Similarly, the anisotropic part of $\mathbf{M}$, i.e., $B$ must also decay at least as fast as $\sim v^2\rho/r^2$ at leading order in $v$ (it is even in $v$ as $\mathbf{M}$ is even in $\mathbf{e}$). We shall use these estimates below to argue their neglect.

We now wish to eliminate the fast dynamics of $\mathbf{w}$ and $\mathbf{M}$ to obtain a steady state solution for the density $\rho$. We let $\mathrm{tr}(\mathbf{M}) = 2A + B \equiv m$ and obtain an equation for $m$ as

$$\partial_t m = 2\mu\boldsymbol{\nabla}\cdot(\boldsymbol{\nabla}\mathcal{U}m + T\boldsymbol{\nabla}m) - \frac{5\mu^2\gamma|\boldsymbol{\nabla}\mathcal{U}|^2}{4K^2}(Km - 2T\rho) \ . \tag{3.17}$$

Balancing the order of various terms in this equation, we obtain that $m \sim \rho$ in terms of scaling. Comparing this against the estimate for the anisotropic part $B \sim v^2\rho/r^2$, we find that $B$ is negligible at large distances and small activity and hence it can be safely discarded. In addition, all the third order moments enter Eq. 3.17 with an additional factor of $\sim v/r$ (from either active advection or the active torques), which in total combines to give a correction of order $\sim v^2\rho/r^2$. Just like $B$, this contribution is also negligible compared to the terms retained and justifies our closure scheme to leading order in activity and at large distances.

On large scales, the fast mode $\mathbf{w}$ relaxes on time scales $\sim D_R^{-1}$ and can be slaved to $m$ by neglecting $\partial_t \mathbf{w}$, with the result, to leading order in gradients,

$$\mathbf{w} = -\frac{v}{2D_R}\left[\boldsymbol{\nabla} m - \frac{3\mu\gamma}{4K} m \boldsymbol{\nabla}\mathcal{U}\right] + \mathcal{O}\left(v\frac{m}{r^3}\right) \ . \tag{3.18}$$

This equation can then be used to also eliminate $\mathbf{w}$ from the equation for $\rho$, which gives

$$\partial_t \rho = 2\mu \boldsymbol{\nabla}\cdot\left[\left(\rho - \frac{3\gamma v^2}{16KD_R} m\right)\boldsymbol{\nabla}\mathcal{U} + T\boldsymbol{\nabla}\rho + \frac{v^2}{4\mu D_R}\boldsymbol{\nabla} m\right] \ . \tag{3.19}$$

We now seek a steady state solution of the coupled Eqs. 3.17 and 3.19 by letting $\partial_t m = \partial_t \rho = 0$. Since we are interested in the behavior of the defect pair for large pair separation, we seek to solve the equations to leading order in gradients. Naïvely one may be tempted to write a solution of Eq. (3.17) as $m_{ss} = (2T/K)\rho_{ss}$, but the fact that the last term on the right hand side of Eq. (3.17) is proportional to $|\boldsymbol{\nabla}\mathcal{U}|^2$ invalidates this simple approximation. We then have the following two coupled equations for $\rho_{ss}$ and $m_{ss}$

$$\rho_{ss} = \frac{K}{2T}\left\{m_{ss} - \frac{8K}{5\mu\gamma}\frac{\boldsymbol{\nabla}\cdot[\boldsymbol{\nabla}\mathcal{U} m_{ss} + T\boldsymbol{\nabla} m_{ss}]}{|\boldsymbol{\nabla}\mathcal{U}|^2}\right\} \ . \tag{3.20}$$

$$\left[\rho_{ss} - \frac{3\gamma v^2}{16KD_R} m_{ss}\right]\boldsymbol{\nabla}\mathcal{U} + T\boldsymbol{\nabla}\rho_{ss} + \frac{v^2}{4\mu D_R}\boldsymbol{\nabla} m_{ss} = c \ , \tag{3.21}$$

where $c$ is an arbitrary constant. In the absence of currents at steady state, $c = 0$. Substituting Eq. 3.20 into Eq. 3.21 and using $\mathcal{U}(\mathbf{r}) = (\pi K/2)\ln(r/a)$, we obtain a homogeneous differential equation of Cauchy-Euler form,

$$(8D_R K^2 - 3Tv^2\gamma) m_{ss}(r) = 8r\left[-\frac{v^2 T}{\pi\mu} + \frac{2D_R}{5\pi^3\mu\gamma}\left(8(K\pi + 2T)^2 - 5K\pi^2 T\mu\gamma\right)\right] m'_{ss}(r)$$

$$+\frac{512D_RT}{5\pi^3\mu\gamma}(K\pi+3T)\ r^2m''_{ss}(r)+\frac{512D_RT^2}{5\pi^3\mu\gamma}\ r^3m'''_{ss}(r)\ , \tag{3.22}$$

where we have set $c = 0$ and the prime denotes a derivative with respect to $r$. This equation is solved by a power law solution, $m_{ss}(r) = m_0(r/a)^{-J}$, where the undetermined exponent $J$ satisfies the following cubic equation,

$$512D_RTJ^2(K\pi-TJ)+8\pi^2J[5v^2T\gamma+2D_RK(5T\mu\gamma-8K)]+5\pi^3\mu\gamma(3v^2T\gamma-8D_RK^2)=0\ . \tag{3.23}$$

Of the three roots to this equation, only the branch that connects to the equilibrium exponent $J = K\pi/2T$ when $v = 0$ is physical. Perturbatively expanding the exponent $J$ around $v = 0$, we obtain

$$J=\frac{K\pi}{2T}-\frac{\pi v^2}{4\mu D_RT}\left(1+\mu\gamma\frac{3T}{4K}\right)+\mathcal{O}(v^4)\ . \tag{3.24}$$

The next order correction to $J$ at $\mathcal{O}(v^4)$ will also involve the neglected terms $B$ and the third moment $\langle\mathbf{eee}\rangle$. Using the power law form of $m_{ss}(r)$ in Eq. 3.20 we also have $\rho_{ss}(r) \propto (r/a)^{-J}$ with the prefactor fixed by normalization ($\int \mathrm{d}\mathbf{r}\rho_{ss}(\mathbf{r}) = 1$). Assuming a Boltzmann like form, we identify an effective pair potential that governs the defect pair separation, defined as $\mathcal{U}_{\text{eff}}(\mathbf{r}) = -T\ln[\rho_{ss}(\mathbf{r})]$. Hence, writing $J = \pi K_{\text{eff}}/2T$, we obtain $\mathcal{U}_{\text{eff}}(\mathbf{r}) = (\pi K_{\text{eff}}/2)\ln(r/a)$ with

$$K_{\text{eff}}(v)=K-\frac{v^2}{2\mu D_R}\left[1+\mu\gamma\frac{3T}{4K}\right]+\mathcal{O}(v^4)\ , \tag{3.25}$$

to leading order in activity. Hence, for large pair separation, the defect interaction is weakened by activity. A small activity reduces the entropic BKT transition temperature $T_c^{\text{eq}} = \pi K/8$ to $T_c(v) = \pi K_{\text{eff}}(v)/8$. Inverting this equation for small $|v|$, we obtain

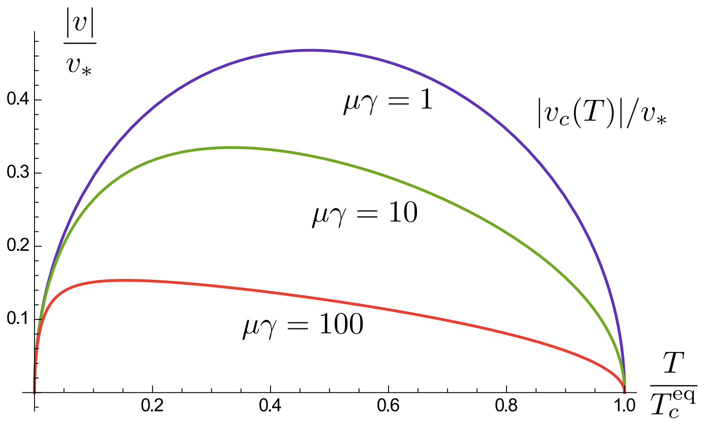

Figure 19 : Phase boundary in the $|v| - T$ plane (Eq. 3.26) for different values of $\mu\gamma$. The region enclosed by the curve $|v_c(T)|$ for a given $\mu\gamma$ corresponds to the ordered nematic.

the phase boundary below which the ordered nematic is stable,

$$\frac{|v_c(T)|}{v_*} = \sqrt{\frac{16\ \tilde{T}(1-\tilde{T})}{\pi\left[1+(3\pi/32)\mu\gamma\tilde{T}\right]}}\ , \tag{3.26}$$

with $\tilde{T} = T/T_c^{\rm eq}$ and $v_* = \mu T_c^{\rm eq}/\ell_R$. This identifies a temperature-activity locus of a BKT-like active-nematic/isotropic transition, with a nematic dome below which homogeneous order exists. As shown in Fig. 19, this implies re-entrant behavior[3] as a function of $T$. Rotational diffusion ($D_R$) of the $+1/2$ defect is suppressed at low noise, where self-propulsion directly drives defect unbinding with a threshold that vanishes as $D_R$ goes to zero. This yields a disordered phase at low enough temperatures for any nonzero activity, as also predicted by the simplified model in Fig. 16[4]. If the rotational diffusivity $D_R$ has a nonthermal part $D_R^a$, then there is a nonzero activity threshold $\sim \sqrt{D_R^a}$ for unbinding as $T \to 0$ and no re-entrance at low activity. If $D_R^a$

---

[3] Ananyo Maitra and Mike Cates, personal communication.

[4] Many-body screening enhances the stability of the ordered phase at low temperatures, but does not change the qualitative structure of the phase diagram (Shankar *et al.*, in preparation). In particular, re-entrance persists as $D_R \propto T \to 0$. A similar situation is encountered in 2D equilibrium spin models with random Dzyaloshinskii-Moriya couplings [387] or crystals with random impurities [388].

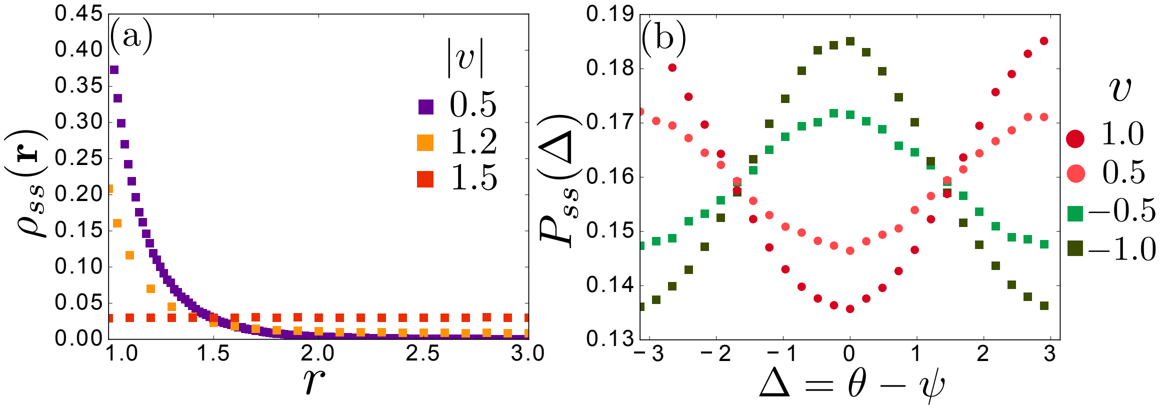

Figure 20 : Steady-state statistics for a $\pm 1/2$ defect pair in a periodic box of size $L = 50a$ ($T/T_c^{\mathrm{eq}} = 0.51$, all other parameters are unity). (a) The pair separation distribution $\rho_{ss}(\mathbf{r})$ for low ($|v| = 0.5, 1.2$, bound phase) and high ($|v| = 1.5$, unbound phase) activity, suggesting that Eq. 3.26 which gives $|v_c| \simeq 2.06$, overestimates the unbinding threshold. (b) The distribution of the relative angle ($\Delta = \theta - \psi$) between the polarization $\mathbf{e}$ and the force $\mathbf{F}$ on the $+1/2$ defect for extensile (□) and contractile (◯) systems.

is large enough then re-entrance is abolished altogether.

For $|v| > |v_c(T)|$, the effective pair potential $\mathcal{U}_{\mathrm{eff}}$ develops a maximum as in Fig. 16, thereby implying that incipient defect pairs unbind for arbitrarily small temperature. The physical picture is then quite clear. At low activity, rotational diffusion randomizes the orientation of the $+1/2$ disclination and makes its motion less persistent, allowing the defect pair to remain bound. It is in this way that noise counterintuitively stabilizes the ordered nematic phase, resolving the paradox. At higher activity, the active torques compete with rotational diffusion, but ultimately enhance the persistent nature of defect motion. In this case, rotational noise becomes irrelevant and we recover the scenario sketched in Fig. 16. The simple one-dimensional model predicts defect unbinding self-consistently if the persistence length of the $+1/2$ disclination ($|v|/D_R$) is greater than the position of the barrier in the potential ($r_c = K/(|v|\gamma)$). Equating the two lengths, we obtain the same threshold scaling as in Eq. 3.26 at low $T$. We have verified this scenario by numerically integrating Eqs. 3.3 and 3.7 for either sign of $v$, as shown in Fig. 20. Of course, at large enough activity, active forces always exceed thermal ones and defects always remain unbound leading to a disordered state of defect chaos[5].

## Appendix 3.A Derivation of equations of motion for ±1/2 disclinations

Consider the following general continuum equations for the hydrodynamics of a nematic liquid crystal written in terms of the tensor order parameter $\mathbf{Q} = S(2\hat{\mathbf{n}}\hat{\mathbf{n}} - \mathbf{1})$ and the flow velocity $\mathbf{u}$.

$$\partial_t \mathbf{Q} + \mathbf{u}\cdot\boldsymbol{\nabla}\mathbf{Q} - [\mathbf{Q},\boldsymbol{\Omega}] = \mathbf{L}(\mathbf{Q},\mathbf{u}) + \frac{1}{\gamma}\left[a_2 - a_4\ \mathrm{tr}(\mathbf{Q}^2)\right]\mathbf{Q} + \frac{K}{\gamma}\nabla^2\mathbf{Q}\ , \tag{3.27}$$

$$\mathbf{L}(\mathbf{Q},\mathbf{u}) = \lambda_1\mathbf{D} + \lambda_2\mathbf{Q}\boldsymbol{\nabla}\cdot\mathbf{u} - \lambda_3\mathbf{Q}\mathrm{tr}(\mathbf{Q}\cdot\boldsymbol{\nabla}\mathbf{u})\ ,$$

where $[A,B] = AB - BA$ is the matrix commutator, $2\Omega_{\mu\nu} = \nabla_\mu u_\nu - \nabla_\nu u_\mu$ is the vorticity tensor and $2D_{\mu\nu} = \nabla_\mu u_\nu + \nabla_\nu u_\mu - \delta_{\mu\nu}\boldsymbol{\nabla}\cdot\mathbf{u}$ is the symmetrized and traceless strain rate tensor. We work in the one Frank elastic constant ($K$) approximation, but have included various flow alignment terms ($\lambda_{1,2,3}$) in $\mathbf{L}(\mathbf{Q},\mathbf{u})$. Since the system is in contact with a substrate, we neglect inertia and determine the flow velocity through the Stokes equation that balances friction and active stresses as

$$\Gamma\mathbf{u} = \nabla\cdot\boldsymbol{\sigma}^a\ , \tag{3.28}$$

---

[5] It has been suggested that there are two dynamical routes to spatio-temporal chaos in active nematics [389], one of which is related to the well known linear bend-splay instability of active nematics [376, 377]. The second route presumably relates to our motility driven defect unbinding scenario presented here.

where $\Gamma$ is the friction with the substrate and $\boldsymbol{\sigma}^a = \alpha \mathbf{Q}$ is the active stress. We neglect the passive elastic and viscous stresses as they are all higher order in gradients. We assume the nematic density to be constant even though, in distinction from previous work [370, 373], we do not consider the flow to be incompressible ($\nabla \cdot \mathbf{u} \neq 0$). We will explore elsewhere the effect of incompressibility or a density field with conserving dynamics, but do not expect these to introduce drastic differences with respect to the behavior described here. We assume we are deep in the nematic state where $a_2 > 0$.

We rescale $\mathbf{r} \to \mathbf{r}/\xi$, $t \to t/\tau$ and $\mathbf{Q} \to \mathbf{Q}/S_{\mathrm{max}}$, where

$$\xi = \sqrt{\frac{K}{a_2}} \,, \quad \tau = \frac{\gamma}{a_2} \quad \text{and} \quad S_{\mathrm{max}} = \sqrt{\frac{a_2}{2a_4}} \,. \tag{3.29}$$

The active stress is also non-dimensionalized as $\bar{\alpha} = \alpha \tau S_{\mathrm{max}}/(\Gamma \xi^2)$. The order parameter $\mathbf{Q}$ is a rank-2 symmetric and traceless tensor. Hence it can be rewritten in terms of a single complex variable $\chi = Q_{xx} + iQ_{xy} = Se^{2i\theta}$, where $\theta$ is the angle of the director $\hat{\mathbf{n}} = (\cos\theta, \sin\theta)$. In terms of $\chi$, Eq. 3.27 now becomes (in dimensionless form)

$$\partial_t \chi + \mathbf{u} \cdot \boldsymbol{\nabla} \chi - i(\boldsymbol{\nabla} \times \mathbf{u})\chi = (\bar{\lambda}_1 - \bar{\lambda}_3 |\chi|^2) D - \bar{\lambda}_3 \chi^2 D^* + \lambda_2 \chi (\boldsymbol{\nabla} \cdot \mathbf{u}) + (1 - |\chi|^2)\chi + \nabla^2 \chi \,, \tag{3.30}$$

where $D = D_{xx} + iD_{xy} = [\partial_x u_x - \partial_y u_y + i(\partial_x u_y + \partial_y u_x)]/2$ is the strain rate tensor $\mathbf{D}$ in complex notation. Additionally, we have rescaled the flow alignment parameters as $\bar{\lambda}_{1,3} = \lambda_{1,3}/2S_{\mathrm{max}}$.

Finally, we boost to a frame which is comoving and corotating with an isolated slowly moving ±1/2 disclination. To do this, we perform the following coordinate and field transformations,

$$\mathbf{r} = \mathbf{R}(t)\cdot\mathbf{r}'(t)+\mathbf{b}(t)\ , \quad \mathbf{u}(\mathbf{r},t) = \mathbf{R}(t)\cdot\mathbf{u}'(\mathbf{r}'(t),t)\ , \quad \mathbf{Q}(\mathbf{r},t) = \mathbf{R}(t)\cdot\mathbf{Q}'(\mathbf{r}'(t),t)\cdot\mathbf{R}(t)^T\ , \tag{3.31}$$

where $\mathbf{R}(t) = \mathbf{1}\cos\omega t + \boldsymbol{\epsilon}\sin\omega t$ with $\boldsymbol{\epsilon}$ as the Levi-Civita tensor is the rotation matrix rotating the frame counter-clockwise at a constant rate of $\omega$ ($\dot{\mathbf{R}}(t) = \omega\boldsymbol{\epsilon}\cdot\mathbf{R}(t)$ and $\mathbf{R}^T\cdot\mathbf{R} = \mathbf{1}$), which is taken to be the angular rotation rate of the defect. The translational shift is determined to be $\mathbf{b}(t) = -\mathbf{R}(t)\cdot\boldsymbol{\epsilon}\cdot\mathbf{v}/\omega$ by requiring $\dot{\mathbf{r}}'(t) = -\omega\boldsymbol{\epsilon}\cdot\mathbf{r}'(t) - \mathbf{v}$, where $\mathbf{v}$ is the constant translational velocity of the defect. The same transformation in terms of the complex field $\chi$ is given as

$$\chi(\mathbf{r},t) = \chi'(\mathbf{r}'(t),t)e^{-2i\omega t}\ . \tag{3.32}$$

Using this, we obtain $\partial_t\chi = e^{-2i\omega t}[\partial_t\chi' - \mathbf{v}\cdot\boldsymbol{\nabla}'\chi' + \omega\mathbf{r}'\times\boldsymbol{\nabla}'\chi' - 2i\omega\chi']$ and $\boldsymbol{\nabla}\chi = e^{-2i\omega t}\mathbf{R}\cdot\boldsymbol{\nabla}'\chi'$ and similar expressions involving $\mathbf{u}$. Assuming the dynamics is quasistatic in this moving frame of reference ($\partial_t\chi' = 0$), we neglect any explicit time dependence and drop the primes on all the variables to get

$$\begin{aligned}(\mathbf{u}-\mathbf{v})\cdot\boldsymbol{\nabla}\chi + \omega\mathbf{r}\times\boldsymbol{\nabla}\chi - i(2\omega + \nabla\times\mathbf{u})\chi = (\bar{\lambda}_1 - \bar{\lambda}_3|\chi|^2)D - \bar{\lambda}_3\chi^2 D^* + \lambda_2\chi(\boldsymbol{\nabla}\cdot\mathbf{u}) \\ + (1-|\chi|^2)\chi + \nabla^2\chi\ ,\end{aligned} \tag{3.33}$$

where $\mathbf{v}$ and $\omega$ are the velocity and angular rotation rate of the ±1/2 disclination. Assuming the defect is moving and rotating slowly, and the activity is also small, we take $\mathbf{v}, \omega, \bar{\alpha} = \mathcal{O}(\eta)$, where $\eta \ll 1$ will be used as a book-keeping parameter to do perturbation theory in. This allows us to treat all the backflow terms perturbatively.

Expanding $\chi = \chi_0 + \eta\chi_1 + \mathcal{O}(\eta^2)$ and $\mathbf{u} = \mathbf{u}_0 + \eta\mathbf{u}_1 + \mathcal{O}(\eta^2)$, we have at $\mathcal{O}(\eta^0)$,

$$\mathbf{u}_0 = \mathbf{0} \ , \quad \text{and} \quad \nabla^2\chi_0 + (1 - |\chi_0|^2)\chi_0 = 0 \ . \tag{3.34}$$

This is the static equilibrium equation which is easily solved to obtain the configuration of a single stationary disclination. For a ±1/2 disclination, we have $\chi_0(\mathbf{r}) = S_0(r)e^{\pm i\varphi + 2i\theta_0}$, where $r, \varphi$ are standard polar coordinates in the plane with the defect centered at the origin and $\theta_0$ is a constant related to the orientation of the ±1/2 disclination. $S_0(r)$ satisfies the following differential equation

$$S_0'' + \frac{S_0'}{r} + \left(1 - \frac{1}{r^2} - S_0^2\right) S_0 = 0 \ . \tag{3.35}$$

whose solution can be written in terms of a Padé approximant (with upto 3% error) with the correct asymptotic behavior ($S_0 \simeq 1 - 1/2r^2$ as $r \to \infty$ and $S_0 \simeq 0.5831r$ as $r \to 0$), given by [382]

$$S_0(r) = r\sqrt{\frac{0.34 + 0.07r^2}{1 + 0.41r^2 + 0.07r^4}} \ . \tag{3.36}$$

We shall use this approximate form of $S_0(r)$ later on to compute the defect mobility.

The equations for the first order corrections $\chi_1(\mathbf{r})$ and $\mathbf{u}_1(\mathbf{r})$ are obtained by retaining terms of $\mathcal{O}(\eta)$ in Eqs. (3.33) and (3.28),

$$\nabla^2\chi_1 + (1 - 2|\chi_0|^2)\chi_1 - \chi_0^2\chi_1^* = \mathcal{I}(\mathbf{r}) \tag{3.37}$$

$$\begin{aligned}\mathcal{I}(\mathbf{r}) = (\mathbf{u}_1 - \mathbf{v}) \cdot \boldsymbol{\nabla}\chi_0 - i(2\omega + \boldsymbol{\nabla} \times \mathbf{u}_1)\chi_0 + \omega\mathbf{r} \times \boldsymbol{\nabla}\chi_0 - (\bar{\lambda}_1 - \bar{\lambda}_3|\chi_0|^2)D_1 \\ + \bar{\lambda}_3\chi_0^2 D_1^* - \lambda_2\chi_0(\boldsymbol{\nabla} \cdot \mathbf{u}_1)\end{aligned} \tag{3.38}$$

$$\mathbf{u}_1 = \bar{\alpha}\boldsymbol{\nabla}\cdot\mathbf{Q}_0 \ , \tag{3.39}$$

where $\mathbf{Q}_0$ is the tensor form of $\chi_0$ corresponding to the static defect solution and $D_1$ is the corresponding complex deviatoric strain rate computed using $\mathbf{u}_1$. The first order velocity correction is easily determined to be

$$\mathbf{u}_1 = \bar{\alpha}\left(S_0'(r) + \frac{S_0(r)}{r}\right)(\cos 2\theta_0, \sin 2\theta_0) \ . \tag{3.40}$$

The corresponding first order corrections to the vorticity ($\boldsymbol{\nabla} \times \mathbf{u}$), divergence ($\boldsymbol{\nabla} \cdot \mathbf{u}$) and deviatoric shear in complex form ($D$) are also easily obtained to be

$$\boldsymbol{\nabla} \times \mathbf{u}_1 = \bar{\alpha}\sin(\varphi - 2\theta_0)S_0(r)\left[1 - S_0(r)^2\right] \ , \tag{3.41}$$

$$\boldsymbol{\nabla} \cdot \mathbf{u}_1 = -\bar{\alpha}\cos(\varphi - 2\theta_0)S_0(r)\left[1 - S_0(r)^2\right] \ , \tag{3.42}$$

$$D = -\bar{\alpha}S_0(r)\left[1 - S_0(r)^2\right] \ e^{i(\varphi + 2\theta_0)} \ . \tag{3.43}$$

These terms contribute to the inhomogeneity $\mathcal{I}(\mathbf{r})$ as shown in Eq. 3.37,3.38. The linear complex differential operator on the left-hand side of Eq. 3.37 given by

$$\mathcal{L}(f, f^*) = \nabla^2 f + (1 - 2|\chi_0|^2)f - \chi_0^2 f^* \ , \tag{3.44}$$

has three zero modes, denoted by $\Psi$: two corresponding to translations ($\Psi = \nabla\chi_0$) and one for rotation ($\Psi = i\chi_0$) of the defect. Multiplying Eq. 3.37 by a complex conjugated zero mode $\Psi^*$ and integrating by parts, we get the following solvability condition for $\chi_1$ (Fredholm alternative)

$$\mathrm{Re}\left[\int_\Sigma \mathrm{d}^2 r \ \mathcal{I}(\mathbf{r})\Psi^*(\mathbf{r})\right] = \mathrm{Re}\left[\oint_{\partial\Sigma} (\Psi^*\partial_\perp\chi_1 - \chi_1\partial_\perp\Psi^*)\right] \ , \tag{3.45}$$

where $\Sigma$ is any region of space and $\partial_\perp$ is the normal derivative along the boundary $\partial\Sigma$. We shall apply this solvability condition on a circular region of radius $r_0 = \mathcal{O}(\eta^{-1/2})$.

This choice of $r_0$ is motivated by the fact that the perturbative expansion of $\chi$ breaks down in the very far-field ($r \sim \eta^{-1}$), while a pure phase analysis performed later is valid on scales all the way from infinity down to $r \sim \eta^{-1/2}$. So for $r_0 = \mathcal{O}(\eta^{-1/2})$, both inner and outer expansion can be asymptotically matched.

Projecting onto the rotational zero mode ($\Psi = i\chi_0$), we find that all the terms involving the flow (independent of $\omega$) in the $\mathcal{I}$ integral have a vanishing real part as required in the left hand side of Eq. 3.45 and so $\omega = 0$ at this order. Using the translational eigenmodes ($\Psi = \nabla\chi_0$), as $\mathbf{u} \sim 1/r$ for $r \to \infty$, all the integrals involving the flow velocity are convergent for large $r$ (so we extend the integral to infinity), while only the term involving the defect velocity $\mathbf{v}$ is log-divergent. So we have for the $+1/2$ disclination

$$\mathrm{Re}\left[\int_0^{r_0} \mathrm{d}^2 r \mathcal{I}(\mathbf{r}) \boldsymbol{\nabla}\chi_0^*\right] = \bar{\alpha}\ \hat{\mathbf{e}}_0(5.735 + 0.6284\lambda_2) - \pi\mathbf{v}\ln\left(\frac{r_0}{1.126}\right) \ , \tag{3.46}$$

where $\hat{\mathbf{e}}_0 = (\cos 2\theta_0, \sin 2\theta_0)$ is the unit polarization of the $+1/2$ disclination. Note that, as expected by symmetry, the active backflow terms don't contribute for the $-1/2$ disclination (the $\bar{\alpha}$ term is absent). Interestingly, we find that both $\bar{\lambda}_1$ and $\bar{\lambda}_3$ don't contribute to the mobility calculation at this order, though they do enter the linear stability analysis of fluctuations about the homogeneous ordered state [377].

For the line integral on the RHS of Eq. 3.45, we have to evaluate $\chi_1$ at $r_0 = \mathcal{O}(\eta^{-1/2})$. For arbitrary $\mathbf{v}$ and $\bar{\alpha}$ ($\mathcal{O}(\eta^0)$), we now have for large $r_0$, $S = 1 - \mathcal{O}(\eta)$ and $\boldsymbol{\nabla}\mathbf{u}_1 = \mathcal{O}(\eta)$ on the scale of $r_0$. So in the very far-field, we set $S = 1$ and have only the phase $\theta$ at leading order,

$$\mathbf{v} \cdot \boldsymbol{\nabla}\theta + \nabla^2\theta = 0 \ . \tag{3.47}$$

This equation, when solved with the correct winding condition on $\theta$ ($\oint \mathrm{d}\theta = \pm\pi$ around the origin for the $\pm 1/2$ defect), gives rise to a highly anisotropic phase profile given by [382]

$$\boldsymbol{\nabla}\theta = \pm\frac{1}{2}e^{-\mathbf{v}\cdot\mathbf{r}/2}\boldsymbol{\epsilon}\cdot\left[\mathbf{v}K_0\left(\frac{|\mathbf{v}|r}{2}\right) - |\mathbf{v}|\hat{\mathbf{r}}K_1\left(\frac{|\mathbf{v}|r}{2}\right)\right] + \boldsymbol{\epsilon}\cdot\mathbf{v}A\ , \tag{3.48}$$

where $\boldsymbol{\epsilon}$ is the antisymmetric Levi-Civita tensor; $K_0(x)$, $K_1(x)$ are modified Bessel functions of the first kind and $A$ is a constant that we will later relate to a weak external phase gradient. This gives the far-field phase solution for both $+1/2$ and $-1/2$ defects when moving. Expanding this outer solution for small $\mathbf{r}$ to match the inner solution at $r \sim r_0$, we use it in the line integral in Eq. 3.45 to get

$$\mathrm{Re}\left[\int_0^{2\pi} \mathrm{d}\varphi\ r_0\left(\boldsymbol{\nabla}\chi_0^*\partial_r\chi_1 - \chi_1\partial_r\boldsymbol{\nabla}\chi_0^*\right)|_{r=r_0}\right] = -\pi\mathbf{v}\ln\left(\frac{|\mathbf{v}|r_0}{4}e^{\gamma_E-1/2\mp2A}\right)\ , \tag{3.49}$$

where $\gamma_E$ is the Euler-Mascheroni number. Putting all this together into Eq. 3.45 and writing $\mathbf{v}A = -\boldsymbol{\epsilon}\cdot\boldsymbol{\nabla}\theta_{\mathrm{ext}}$ (a weak external phase gradient orthogonal to the defect motion), the $r_0$ dependence cancels out leaving us with the following defect mobility relation for both $+1/2$ and $-1/2$ disclinations (denoted using ± correspondingly),

$$\mathbf{v}_\pm\ln\left(\frac{3.29}{|\mathbf{v}_\pm|}\right) = \pm2\boldsymbol{\epsilon}\cdot\boldsymbol{\nabla}\theta_{\mathrm{ext}} + \delta_{q_i,1/2}\ \bar{\alpha}\ \hat{\mathbf{e}}_0(5.735 + 0.6284\lambda_2)\ . \tag{3.50}$$

The $-1/2$ disclination unlike the $+1/2$ disclination, moves only under the influence of passive phase gradients through a Magnus like force. The active self-induced flow vanishes for the $-1/2$ disclination. Also note that, the numerical prefactors present in Eq. 3.50 are not universal (though the structure of the equation is) and they can change by using a different model for the profile of the defect core. One can restore dimensions appropriately using the length and times scales used previously (see Eq. 3.29). In the presence of other distant defects, $\boldsymbol{\nabla}\theta_{\mathrm{ext}}$ is given by the cumulative phase gradient at the core of the considered defect due to the presence of other defects, which in the pure phase approximation can be obtained by linear superposition as

$$\boldsymbol{\nabla}\theta_{\rm ext}(\mathbf{r}_i) = -\boldsymbol{\epsilon}\cdot\boldsymbol{\nabla}_{\mathbf{r}_i}\sum_{j\neq i} q_j \ln\left|\frac{\mathbf{r}_i-\mathbf{r}_j}{a}\right| \ , \tag{3.51}$$

where $q_j = \pm 1/2$ is the charge of the $j$th defect and $a \sim \xi$ is the defect core size that functions as a microscopic cutoff. The motion of the defect transverse to the phase gradient at its core is a manifestation of the equilibrium Magnus like force, which when eventually written in terms of the defect positions using Eq. 3.51, exactly corresponds to a force arising from the equilibrium Coulombic interaction between defects. In general, we find that the mobility relation is nonlinear with a logarithmic correction depending on the speed of the defect. As this correction is rather weak, to simplify matters, we use a constant mobility in the main text which should be valid for slowly moving defects or when the defect density is large enough that the interactions are screened.

Note that the above calculation still misses some features of active defect motion. As can be seen from Eq. 3.40, though the velocity field is frictionally screened, it decays slowly as $\mathbf{u}_1 \sim 1/r$. Hence, along with the self-induced active backflow of the $+1/2$ defect that leads to its spontaneous motility, one must also include in $\mathbf{u}_1$ the instantaneous active flow generated by all other distant $\pm 1/2$ defects, as this flow is of the same order as the phase gradient that generates the equilibrium passive defect interaction (Eq. 3.51). One can write $\mathbf{u}_1 = \bar{\alpha}\boldsymbol{\nabla}\cdot\mathbf{Q}_0 + \tilde{\mathbf{u}}_1$, where $\mathbf{Q}_0$ is the defect configuration for the $i$th defect and $\tilde{\mathbf{u}}_1$ includes the entrainment of the $i$th defect by the flow of other defects. A full calculation of $\tilde{\mathbf{u}}_1$ including many defects is not analytically tractable as of now, but for weak phase gradients if we approximately linearize $\mathbf{Q}$ assuming $S \simeq 1$ to be constant in the far-field, then the phase due to various defects just adds up linearly. In this case, $\tilde{\mathbf{u}}_1 \simeq 2\bar{\alpha}(\partial_y\theta, \partial_x\theta)$ and using Eq. 3.51

for the phase gradient gives

$$\tilde{\mathbf{u}}_1(\mathbf{r}) = 2\bar{\alpha}\boldsymbol{\sigma}_3 \cdot \boldsymbol{\nabla} \sum_{j \neq i} q_j \ln \left| \frac{\mathbf{r} - \mathbf{r}_j}{a} \right| , \tag{3.52}$$

where $\boldsymbol{\sigma}_3$ is the third Pauli matrix (so $\boldsymbol{\sigma}_3 \cdot \boldsymbol{\nabla} = (\partial_x, -\partial_y)$). Including a “second” active coefficient [376], we have an additional force contribution to the right hand side of the flow equation (Eq. 3.28) $\sim \alpha' \mathbf{Q} \cdot (\boldsymbol{\nabla} \cdot \mathbf{Q})$. This term does not affect the self-propulsion of a $+1/2$ defect, but it does contribute a term $\sim \alpha' \boldsymbol{\nabla}\theta$ to the flow entrainment term $\tilde{\mathbf{u}}_1$. As is evident, both active terms are comparable to the passive elastic one and in general generate an anisotropic, linear in activity, correction to the Frank elastic constant. This is akin to effectively having a different bend ($K_3$) and splay ($K_1$) elastic constant. Depending on where one is in parameter space, the linear active corrections to nematic elasticity may be stabilizing or destabilizing in nature, recovering the same effect obtained in a linear stability calculation about the homogeneous ordered state [376, 377]. In all of our work, we shall remain in the regime where both $K_1$ and $K_3$ are always positive even after including the linear activity corrections, allowing for a stable base nematic. Additionally, upon including fluctuations in a homogeneous active nematic, following the arguments in Ref. [367], the $\bar{\alpha}$ contribution to $\tilde{\mathbf{u}}_1$ in Eq. 3.52 being anisotropic, is irrelevant on large scales, hence we neglect it in our calculations and discussion in the main text.

## Appendix 3.B Derivation of polarization dynamics of the $+1/2$ disclination

Here we obtain the dynamics of the polarization vector $\mathbf{e}_i(t) = a\boldsymbol{\nabla} \cdot \mathbf{Q}(\mathbf{r}_i^+(t))$ for the $i$th $+1/2$ defect. Let $\mathbf{E}(\mathbf{r}, t) = a\boldsymbol{\nabla} \cdot \mathbf{Q}$. Then $\mathbf{e}_i(t) = \mathbf{E}(\mathbf{r}_i^+(t), t)$. Taking a time derivative we get

$$\frac{\mathrm{d}\mathbf{e}_i(t)}{\mathrm{d}t} = \partial_t \mathbf{E}(\mathbf{r}_i^+, t) + \frac{\mathrm{d}\mathbf{r}_i^+}{\mathrm{d}t} \cdot \boldsymbol{\nabla}_{\mathbf{r}_i^+} \mathbf{E}(\mathbf{r}_i^+, t) \ . \tag{3.53}$$

From Appendix 3.A, we found the self-induced rotation of the +1/2 defect to be zero ($\omega = 0$) at the order we are working, so we do not include it here and don't consider it further. This simplifies things greatly as it allows us to set the time-dependent rotation matrix to the constant unit tensor ($\mathbf{R} = \mathbf{1}$). As $\partial_t \mathbf{E} = \mathbf{0}$ in the quasistatic approximation, we only have the second term. We shall address the implications of relaxing this upon including smooth director distortions in Appendix 3.C. Writing $\mathbf{v}_i(t) = \dot{\mathbf{r}}_i^+(t)$ (the +1/2 defect velocity) and using the definition of $\mathbf{E}$, we have

$$\frac{\mathrm{d}\mathbf{e}_i(t)}{\mathrm{d}t} = a\mathbf{v}_i(t) \cdot \left( \lim_{\mathbf{r}\to\mathbf{r}_i(t)} \boldsymbol{\nabla\nabla} \cdot \mathbf{Q}(\mathbf{r}, t) \right) \ . \tag{3.54}$$

Computing $\boldsymbol{\nabla\nabla} \cdot \mathbf{Q}$ perturbatively about the stationary equilibrium defect, we expand Eq. 3.33 as before to $\mathcal{O}(\eta)$ (where $\mathbf{v}, \bar{\alpha} \sim \eta$). As we eventually have to take the $\mathbf{r} \to \mathbf{r}_i(t)$ limit (at the center of the defect core), we find it easier to expand in $S$ and $\theta$ instead of the complex variable $\chi$. Using the same notation as before and setting $\omega = 0$, Eq. 3.33 in terms of $S$ and $\theta$ is given as

$$\begin{aligned}(\mathbf{u} - \mathbf{v}) \cdot \boldsymbol{\nabla} S = (\bar{\lambda}_1 - \bar{\lambda}_3 S^2)\mathrm{Re}\left\{e^{-2i\theta} D\right\} - \bar{\lambda}_3 S^2 \mathrm{Re}\left\{e^{2i\theta} D^*\right\} + \lambda_2 S \boldsymbol{\nabla} \cdot \mathbf{u} \\ + (1 - S^2)S + \nabla^2 S - 4S|\boldsymbol{\nabla}\theta|^2 \ , \end{aligned} \tag{3.55}$$

$$\begin{aligned}2(\mathbf{u} - \mathbf{v}) \cdot \boldsymbol{\nabla}\theta - \boldsymbol{\nabla} \times \mathbf{u} = \left(\frac{\bar{\lambda}_1}{S} - \bar{\lambda}_3 S\right) \mathrm{Im}\left\{e^{-2i\theta} D\right\} - \bar{\lambda}_3 S \ \mathrm{Im}\left\{e^{2i\theta} D^*\right\} \\ + 2\nabla^2\theta + \frac{2}{S}\boldsymbol{\nabla} S \cdot \boldsymbol{\nabla}\theta \ . \end{aligned} \tag{3.56}$$

We have dropped the subscript $i$ to keep the notation uncluttered. Writing $S = S_0(r) + \eta S_1 + \mathcal{O}(\eta^2)$ and $2\theta = \varphi + 2\theta_0 + \eta 2\theta_1 + \mathcal{O}(\eta^2)$ ($\theta_0$ is a constant setting the orientation of the +1/2 defect polarization), we use Eqs. 3.41, 3.42 and 3.43 to get the following linearized equations

$$\begin{aligned}-\bar{\alpha}\left(S_0'+\frac{S_0}{r}\right)\frac{\sin(\varphi-2\theta_0)}{r}+\frac{|\mathbf{v}|\sin\varphi}{r}+\bar{\alpha}\sin(\varphi-2\theta_0)\left(S_0''+\frac{S_0'}{r}-\frac{S_0}{r^2}\right)&\\ =2\nabla^2\theta_1+\frac{2}{S_0}S_0'\partial_r\theta_1+\frac{1}{S_0}\frac{\partial_\varphi S_1}{r^2}\ ,&\end{aligned} \tag{3.57}$$

$$\begin{aligned}\left(1-3S_0^2-\frac{1}{r^2}\right)S_1+\nabla^2 S_1-\frac{2S_0}{r^2}\partial_\varphi\theta_1=\bar{\alpha}\left(S_0'+\frac{S_0}{r}\right)S_0'\cos(\varphi-2\theta_0)-|\mathbf{v}|S_0'\cos\varphi&\\ -\bar{\alpha}\left[\bar{\lambda}_1-2\bar{\lambda}_3S_0^2+\lambda_2S_0\cos(\varphi-2\theta_0)\right]\left(S_0''+\frac{S_0'}{r}-\frac{S_0}{r^2}\right)\ .&\end{aligned} \tag{3.58}$$

Here the defect is centered at the origin and $\mathbf{v}$ has been taken along the $x$-axis without loss of generality. Note that for $\theta_0\neq 0,\pi$, the defect polarization $\mathbf{e}$ is not aligned with its velocity $\mathbf{v}$. We note, by inspection that the following ansatz solves the above equations,

$$S_1=\psi_0(r)+\psi_1(r)\cos\varphi+\psi_2(r)\cos(\varphi-2\theta_0)\ , \tag{3.59}$$

$$\theta_1=\Theta_1(r)\sin\varphi+\Theta_2(r)\sin(\varphi-2\theta_0)\ . \tag{3.60}$$

The first order corrections ($\psi_{0,1,2}(r)$ and $\Theta_{1,2}(r)$) satisfy the following equations.

$$2\left(\Theta_1''+\frac{\Theta_1'}{r}-\frac{\Theta_1}{r^2}\right)+\frac{2S_0'}{S_0}\Theta_1'-\frac{\psi_1}{S_0r^2}-\frac{|\mathbf{v}|}{r}=0\ , \tag{3.61}$$

$$\bar{\alpha}\left[S_0(1-S_0^2)+\frac{1}{r}\left(S_0'+\frac{S_0}{r}\right)\right]+2\left(\Theta_2''+\frac{\Theta_2'}{r}-\frac{\Theta_2}{r^2}\right)+\frac{2S_0'}{S_0}\Theta_2'-\frac{\psi_2}{S_0r^2}=0\ , \tag{3.62}$$

$$\left(1-3S_0^2-\frac{1}{r^2}\right)\psi_0+\psi_0''+\frac{\psi_0'}{r}=\bar{\alpha}S_0(\bar{\lambda}_1-2\bar{\lambda}_3S_0^2)(1-S_0^2)\ , \tag{3.63}$$

$$\left(1-3S_0^2-\frac{2}{r^2}\right)\psi_1+\psi_1''+\frac{\psi_1'}{r}-\frac{2S_0}{r^2}\Theta_1+|\mathbf{v}|S_0'=0\ , \tag{3.64}$$

$$\left(1 - 3S_0^2 - \frac{2}{r^2}\right)\psi_2 + \psi_2'' + \frac{\psi_2'}{r} - \frac{2S_0}{r^2}\Theta_2 = \bar{\alpha}\left[S_0'\left(S_0' + \frac{S_0}{r}\right) + \lambda_2 S_0^2(1 - S_0^2)\right] \ . \tag{3.65}$$

Using the first order solution, we expand $\mathrm{d}\mathbf{e}/\mathrm{d}t$ to $\mathcal{O}(\eta)$ (not counting the explicit factor of $\mathbf{v}$ multiplying $\nabla\nabla\cdot\mathbf{Q}$ in Eq. 3.54). Projecting $\mathrm{d}\mathbf{e}/\mathrm{d}t$ along and transverse to $\mathbf{e}$, we have

$$\frac{1}{|\mathbf{e}|^2}\mathbf{e}\cdot\frac{\mathrm{d}\mathbf{e}}{\mathrm{d}t} = \eta|\mathbf{v}|\left[\frac{2S_0'(0)\Theta_1'(0) + 3\psi_1''(0)}{4S_0'(0)} + \cos 2\theta_0\left(\frac{2S_0'(0)\Theta_2'(0) + 3\psi_2''(0)}{4S_0'(0)}\right) + \mathcal{O}(\eta)\right] \ , \tag{3.66}$$

$$\frac{1}{|\mathbf{e}|^2}\mathbf{e}\times\frac{\mathrm{d}\mathbf{e}}{\mathrm{d}t} = -\eta|\mathbf{v}|\left(\sin 2\theta_0\frac{6S_0'(0)\Theta_2'(0) + \psi_2''(0)}{4S_0'(0)} + \mathcal{O}(\eta)\right) \ . \tag{3.67}$$

As $r \to 0$ (at the core of the defect), the scalar order parameter must vanish ($S \to 0$). Taking the $r \to 0$ limit of the first order equations (Eqs. 3.61-3.65), we can deduce the leading behaviour of all the first order corrections for small $r$. Requiring that the physical solution not blow up at the core and $\chi$ be single valued, we obtain

$$\psi_0(0) = \psi_1(0) = \psi_2(0) = 0 \ , \quad \Theta_1(0) = \Theta_2(0) = 0 \ , \tag{3.68}$$

$$\psi_0'(0) = \bar{\lambda}_1\bar{\alpha}S_0'(0) \ , \quad \psi_1'(0) = \psi_2'(0) = 0 \ , \tag{3.69}$$

$$\psi_1''(0) = -|\mathbf{v}|S_0'(0) \ , \quad \psi_2''(0) = 2\bar{\alpha}S_0'(0)^2 \ , \quad \psi_0''(0) = 0 \ , \tag{3.70}$$

$$\Theta_1'(0) = \frac{|\mathbf{v}|}{4} \ , \quad \Theta_2'(0) = -\frac{\bar{\alpha}}{2}S_0'(0) \ . \tag{3.71}$$

Using this, along with the fact that $|\mathbf{e}| = 2S_0'(0) + \mathcal{O}(\eta)$ ($a \sim \xi$) and writing $|\mathbf{v}|\cos 2\theta_0$, $|\mathbf{v}|\sin 2\theta_0$ in terms of scalar and cross products of $\mathbf{v}$ and $\mathbf{e}$, we obtain for the $i$th $+1/2$ disclination (now setting the book-keeping parameter $\eta = 1$)

$$\frac{\mathrm{d}\mathbf{e}_i}{\mathrm{d}t} = -\frac{5}{8}\mathbf{v}_i\cdot(\mathbf{v}_i - \bar{\alpha}\mathbf{e}_i)\,\mathbf{e}_i - \frac{\bar{\alpha}}{8}(\mathbf{v}_i\times\mathbf{e}_i)\boldsymbol{\epsilon}\cdot\mathbf{e}_i \ , \tag{3.72}$$

with $\mathbf{v}_i = \dot{\mathbf{r}}_i^+(t)$ as the +1/2 defect velocity. Restoring appropriate dimensional units, we obtain the equation quoted in Sec. 3.3.3.

## Appendix 3.C Non-quasistatic solution for +1/2 disclination: Rotational diffusion

In the previous section, the systematic part of the polarization dynamics was derived from the deterministic equations for the evolution of $\mathbf{Q}$. In particular the equation was derived under the assumption of having a single isolated +1/2 defect in whose comoving and corotating frame, the dynamics is stationary. There are two effects that invalidate this assumption - the presence of noise which induces random fluctuations in the local frame and the contribution of the motion of other distant defects (over and above their effect included in $\mathbf{v}_i$ through the passive Coulomb interaction). We shall include both here. As we are interested in the term $\partial_t\mathbf{E}$ (Eq. 3.53) in the local defect frame, the main contribution comes from the slow relaxation of director distortions and not from the fast relaxation of the scalar order parameter. Working then in the pure-phase approximation, we have

$$\theta(\mathbf{r}, t) = \sum_i q_i \varphi(\mathbf{r} - \mathbf{r}_i(t)) + \delta\theta(\mathbf{r}, t) + \theta_0 \ , \tag{3.73}$$

where $\theta_0$ is a constant, $\varphi(\mathbf{r}) = \tan^{-1}(y/x)$ is the angle function and $q_i = \pm 1/2$ are the defect strengths. The decomposition of $\theta(\mathbf{r})$ is unambiguous if we demand $\delta\theta$ to be smooth and univalued everywhere so that $\boldsymbol{\nabla} \times \boldsymbol{\nabla}\delta\theta = 0$. This captures all the smooth distortions of the director field present along with the topological defects. Deep in the ordered phase of a fluctuating 2D nematic liquid crystal (even when active), the smooth and single-valued director distortions analogous to “spin-waves” in magnets are a broken symmetry variable and so they are long-lived and easy to excite at low noise. These fluctuations cause random rotations of the $+1/2$ defect polarization. The smooth phase fluctuations in a 2D dry active nematic (number conserving [367] or not [366]) satisfy

$$\partial_t \delta\theta = \frac{K}{\gamma} \nabla^2 \delta\theta + f(\mathbf{r}, t) \ , \tag{3.74}$$

at long wavelengths, where $f(\mathbf{r}, t)$ is non-conserving white noise with zero mean and correlation $\langle f(\mathbf{r}, t) f(\mathbf{r}', t')\rangle = 2\Delta\delta(\mathbf{r} - \mathbf{r}')\delta(t - t')$. Using Eq. 3.73 we obtain for $\partial_t \mathbf{E}(\mathbf{r}, t) = \partial_t \boldsymbol{\nabla} \cdot \mathbf{Q}(\mathbf{r}, t)$ evaluated at the $i$th defect core,

$$\lim_{\mathbf{r} \to \mathbf{r}_i^+(t)} \partial_t \mathbf{E}(\mathbf{r}, t) = -\boldsymbol{\epsilon} \cdot \mathbf{e}_i \left( \omega_i + 2 \sum_{j \neq i} q_j \omega_j + 2\partial_t \delta\theta(\mathbf{r}_i^+) \right) \ , \tag{3.75}$$

where we have $\omega_j = \hat{\mathbf{r}}_j \times \partial_t \hat{\mathbf{r}}_j$ as the rotation speed of the $j$th defect (both $\pm 1/2$). Note that all the terms above being purely transverse, correspond to a torque on the polarization $\mathbf{e}_i$. At leading order in perturbation theory, as shown in Appendix 3.A, we obtain the self-induced rotation $\omega_i = 0$ for all the defects[6]. That leaves us with the torque due to the elastic director distortions encoded in $\partial_t \delta\theta$. Note that specifying the positions and orientations of defects *does not* uniquely define the smooth director distortion to interpolate between the defects. For a given configuration of defects and an *independently* specified smooth director phase $\delta\theta$, one can solve Eq. 3.74 setting the noise $f = 0$, to obtain the torque experienced by the defects due to the particular imposed director configuration. This is precisely the computation performed by Vromans and Giomi [384], albeit numerically. Tang and Selinger [385] recognize the fact that for a given orientation of defects, there exist multiple interpolations of the smooth director field, all with differing energies. In the absence of noise ($f = 0$), one can recover what both Refs. [384, 385] call “elastic torques” by rephrasing Eq. 3.74 as an initial value problem to compute the torque $2\partial_t\delta\theta$ for the given configuration.

---

[6] This is a subtle point. In reality, even when passive ($v = 0$), there is relative rotation of defects about other defects. The real reason it does not contribute to an orientational torque at leading order is that the pure-phase approximation is only valid in the far-field, and this contribution from $\omega_j$ does not survive when the far-field solution is matched onto the near-field solution around the defect core.

In the presence of noise, all the smooth director distortions must be accounted for (even those with a higher energy), just with the appropriate statistical weight. Hence at steady state the relevant “elastic” contribution to the torque in a fluctuating description is actually stochastic and *not* deterministic. Using Eq. 3.74, we have

$$\partial_t\delta\theta(\mathbf{r}_i(t),t) = \int \frac{\mathrm{d}^2q}{(2\pi)^2}\int\frac{\mathrm{d}\omega}{2\pi}(-i\omega)\frac{f_{\mathbf{q},\omega}\ e^{-i\omega t+i\mathbf{q}\cdot\mathbf{r}_i(t)}}{-i\omega+(K/\gamma)q^2}\ . \tag{3.76}$$

One trivially has $\langle\partial_t\delta\theta(\mathbf{r}_i)\rangle = 0$ and evaluating its two-point correlation, we obtain

$$\langle\partial_t\delta\theta(\mathbf{r}_i(t),t)\partial_{t'}\delta\theta(\mathbf{r}_j(t'),t')\rangle = 2\Delta\int\frac{\mathrm{d}^2q}{(2\pi)^2}\int\frac{\mathrm{d}\omega}{2\pi}\frac{\omega^2}{[\omega^2+(K/\gamma)^2q^4]}e^{-i\omega(t-t')+i\mathbf{q}\cdot[\mathbf{r}_i(t)-\mathbf{r}_j(t')]}\ , \tag{3.77}$$

$$= 2\Delta\left\{\delta(t-t')\frac{\delta_{ij}}{4\pi a^2}-\frac{K}{2\gamma}\int\frac{\mathrm{d}^2q}{(2\pi)^2}\ q^2\ e^{-(K/\gamma)q^2|t-t'|+i\mathbf{q}\cdot[\mathbf{r}_i(t)-\mathbf{r}_j(t')]}\right\} \tag{3.78}$$

$$= \frac{\Delta}{2\pi a^2}\left\{\delta(t-t')\delta_{ij}+a^2\frac{\gamma^2\left[r_{ij}^2-4(K/\gamma)|t-t'|\right]}{8K^2|t-t'|^3}e^{-\gamma r_{ij}^2/(4K|t-t'|)}\right\}\ , \tag{3.79}$$

where $r_{ij} = |\mathbf{r}_i(t)-\mathbf{r}_j(t')|$ ($r_{ij}\geq 2a$ for $t=t'$, $i\neq j$) with $a$ as the defect core size. The random torque due to smooth director fluctuations has two parts, one that is delta-correlated and the other which retains memory of the past trajectory of defects and is exponentially small for well separated defects. Deep in the ordered phase, as $a$ is a microscopic length scale, the second term in Eq. 3.79 is negligible in comparison to the white noise part. Neglecting memory effects, we write $2\partial_t\delta\theta(\mathbf{r}_i) = \sqrt{2D_R}\eta_i(t)$

and obtain the required rotational diffusion constant to be $D_R = \Delta/(\pi a^2)$. Neglecting active corrections to the noise, the translational noise in the defect dynamics is then $\mu T \sim \Delta$ and hence $D_R \sim \mu T/a^2$ which gives $\ell_R \sim a$ as stated in Sec. 3.3.4.

# Chapter 4

# Topological sound modes and collective motion on curved geometries

*This chapter is based on work presented in the article "Topological Sound and Flocking on Curved Surfaces" [390] co-authored by Suraj Shankar, Mark J. Bowick and M. Cristina Marchetti, and published in the journal Physical Review X in the year 2017. I was responsible for doing most of the work and preparing the entire first draft of the paper, and my co-authors provided valuable suggestions and corrections to add both to the conceptual understanding and the presentation of the work.*

## 4.1 Flocks, curvature & quantum Hall fluids

Flocking, defined as the self-organized and spontaneous ordered motion of a large collection of self-propelled units [215, 391], is one of the most classic phenomena seen in active matter. Large murmurations of starlings are a familiar example, but such collective motion can also be found on much smaller scales, as for instance in groups of cells advancing en masse during growth and development [392]. In many biological processes, collective cellular motion occurs on curved surfaces, such as during gastrulation and tissue morphogenesis [393–396], or when cells migrate in the folds of the gut [397, 398], or on the surface of a growing cornea [399]. Recent *in vitro* work has also demonstrated a direct effect of substrate curvature on cytoskeletal alignment and cell motility in epithelial cells [400]. Understanding the physical aspects of such active processes in the presence of curved geometries hence remains crucial to developing insight into the organizational principles of living matter.

There has been growing recent interest in understanding this at a fundamental level, with the focus divided between the effect of curved confining walls on so-called *scalar* (non-aligning) active matter [401–405] and on aligning active matter systems, of either *nematic* [273, 274, 406] or *polar* [407, 408] symmetry. Even at the level of non-interacting self-propelled particles, the curvature of confining walls can yield surprising features, such as inhomogeneous density and pressure profiles [401, 404] and the breakdown of an equilbrium interpretation [402, 403]. In the presence of aligning interactions that promote orientational order, curvature has an even more profound effect since it frustrates such order, often requiring topological defects [92] that in active systems can become dynamical and are capable of driving spatio-temporal patterns and complex motion [274]. With flexible walls or membranes present, activity can also lead to ratchet effects and rectification [409, 410].

What does this, if at all, have to do with electronic quantum Hall systems? To answer that, we need to think a bit more carefully about the physics of flocking in the presence of curvature. An ordered flock breaks continuous rotational symmetry, though unlike an equilibrium ferromagnet, this symmetry breaking is *dynamical*. While the microscopic motile units constituting the flock individually break detailed balance (DB), polar order realizes this DB violation on macroscopic scales by allowing directed currents and fluxes, i.e., collective motion, to emerge. As a consequence, a generic property of the ordered state of polar active matter is spontaneous flow and thus, the large scale breaking of time-reversal symmetry [218]. Although the active fluid considered here is overdamped due to a frictional substrate, the ordered flock also supports long-wavelength propagating sound modes [411]. The presence of curvature then introduces an additional length scale in the problem that gaps the sound spectrum at long wavelengths. This is a distinct property of active polar fluids and it arises because the polarization field plays the dual role of the order parameter and flow velocity and is therefore subject to the same lensing effect that forces flow to move along geodesics on curved surfaces [408, 412]. The analogy with the integer quantum Hall effect is completed by recalling that, in the electronic system, the external magnetic field breaks time reversal symmetry (TRS) and the spectral gaps provided by the discrete Landau levels cause the Hall conductance to be quantized [47], and the sample supports chiral conducting edge states while the interior bulk remains insulating [55]. These edge states are protected by a bulk topological invariant, the Chern number [19], and exist in systems that lack TRS (though, even without a magnetic field), as in the Haldane model [52]. In a similar fashion, for the polar flock, the spectral gap opened by curvature coupled with the broken TRS of the moving state leads to topologically protected sound modes that are localized to special geodesic curves on the surface (at which the gap in the sound spectrum closes).

In classical systems, it is known that carefully engineered lattice structures with flows induced either spontaneously by activity [307], or through an external drive [74, 413], can host such exotic unidirectional sound modes that are localized at the edges of the sample and are similarly topologically protected. The presence of topologically protected edge states in phononic [76, 77] and photonic [72] systems has lead to an extensive exploration of topological metamaterials, with properties akin to electronic topological insulators and quantum Hall states [53]. Note that the topological modes we find instead occur in a fluid system and do not require any underlying periodicity or carefully designed metamaterial structured on an artificial lattice. The phenomenon reported here is akin to the one recently found in geophysical flows of oceans or the earth's atmosphere, where equatorially trapped Kelvin and Yanai waves were reinterpreted as topologically protected modes [412]. In that case the background flow is imposed externally by the earth's rotation that breaks TRS. In the active fluid, in contrast, flow occurs with no external drive, resulting in *spontaneous* topologically protected sound modes.

The presence of these topological modes relies on three important ingredients:

- the spontaneous polar order and associated flow that breaks TRS;
- the fact that in polar active fluids the order parameter also plays the role of a flow velocity, resulting in distinctly non-equilibrium self-advection not present in equilibrium polar fluids [218];
- the non-zero Gaussian curvature of the underlying substrate.

We emphasize that the long-wavelength topologically protected modes discussed here are *generic*, in the sense that they occur for active polar flow on any curved surface of non-vanishing Gaussian curvature. Recent work has considered active polar patterns on a cylinder [414]. In this case as the Gaussian curvature vanishes, there are consequently no topologically protected sound modes. In the following we demonstrate the phenomenon explicitly for flocking on the sphere, which has constant positive curvature, and on the catenoid, which has negative, spatially varying curvature.

### 4.1.1 Toner-Tu equations on a curved surface

We consider an active polar fluid on a 2D surface. To make generic predictions independent of specific microscopic realizations, we work in the continuum limit and use the well-tested hydrodynamic description of a fluid of overdamped self-propelled particles provided by the Toner-Tu equations [215, 293, 298], appropriately modified to account for the curvature of the underlying substrate [407]. Mass conservation implies a continuity equation for the density field, $\rho$,

$$\partial_t \rho + \nabla_\mu p^\mu = 0 \ , \tag{4.1}$$

with $\mu = 1, 2$ labelling the two internal coordinates of the surface and $\mathbf{p} = \rho\mathbf{u}$ is the polarization density of the active fluid. Due to the presence of a frictional substrate, momentum is not conserved and the particles' velocity is assumed to be aligned with their direction of self-propulsion, leading to the identification of $\mathbf{u}$ with the flow velocity of the active fluid. Note that on a curved surface parallel transport of vectors requires the use of covariant derivatives [89],

$$\nabla_\mu p^\nu = \partial_\mu p^\nu + \Gamma^\nu_{\alpha\mu} p^\alpha \ , \tag{4.2}$$

where $\Gamma^\nu_{\alpha\mu}$ are the appropriate Christoffel symbols. The equation for the polarization density is given by

$$\partial_t p^\mu + \lambda p^\alpha \nabla_\alpha p^\mu = \left[a(\rho - \rho_c) - b\ g_{\alpha\beta} p^\alpha p^\beta\right] p^\mu + \nu\left(\Delta p^\mu + K_G p^\mu\right) + \nu' \nabla^\mu \nabla_\alpha p^\alpha - \chi \nabla^\mu \rho \ , \tag{4.3}$$

where $g_{\alpha\beta}$ is the metric tensor of the surface and $\Delta = \nabla_\mu \nabla^\mu$ is the scalar Laplace-Beltrami operator. Note that $\mathbf{u}$ here plays the dual role of an order parameter field (polarization) and velocity, as discussed in Ref. [218]. The transport coefficients $\nu$ and $\nu'$ are the shear and bulk viscosities (or anisotropic elastic constants when viewed as a liquid crystal), respectively, $a, b > 0$ are coefficients setting the magnitude of the mean field polarized state for $\rho > \rho_c$ (the critical density for the flocking transition), $\lambda$ is a kinematic convective parameter and $\chi > 0$ is a compressional modulus. The last term on the right hand side of Eq. 4.3 is the leading term in a density expansion of the gradient of the swim pressure [415, 416] that describes the flux of propulsive forces across a unit plane of material. There are other nonlinear terms present in the original Toner-Tu equations, but we only retain the most important ones here. In particular, we keep the convective nonlinearity $\lambda \mathbf{p} \cdot \boldsymbol{\nabla} \mathbf{p}$ that is responsible for long-ranged order in 2D [298, 299] and the leading density dependence in the symmetry breaking ($a\rho\mathbf{p}$) and pressure like terms ($\chi \boldsymbol{\nabla} \rho$) that lead to dynamical self-regulation [417], phase-separation [304, 305, 418] and long-wavelength instabilities of the ordered phase [302, 419]. The absence of Galilean invariance means that $\lambda \neq 1/\rho$. Additional nonlinear "advection-like" terms $\sim \lambda_2 \mathbf{p} \boldsymbol{\nabla} \cdot \mathbf{p}$, $\lambda_3 \boldsymbol{\nabla} |\mathbf{p}|^2$ are also present in general, but do not qualitatively change our results below (see Appendix 4.A for an analysis with $\lambda_2, \lambda_3 \neq 0$).

Geometry enters Eq. 4.3 in two crucial places (apart from the covariant derivatives): (i) the cubic term setting the magnitude of the polarization explicitly involves the metric tensor $\mathfrak{g}$ ($|\mathbf{p}|^2 = g_{\alpha\beta} p^\alpha p^\beta$) and (ii) the Gaussian curvature $K_G$ explicitly appears in the viscous term because the strain rate tensor is a symmetrized derivative of the velocity and the covariant derivatives do not commute. The presence of $K_G \neq 0$ is a direct dynamical consequence of the Poincaré-Hopf theorem [420] from which it follows that topological defects or vortices are required to accommodate vector order on a curved closed surface like the sphere. A covariant hydrodynamic treatment of active fluids on a curved surface has also been developed by Fily et al. [407]. These authors derived the continuum equations by coarse-graining a microscopic model of self-propelled particles, which allowed an explicit computation of the transport coefficients in terms of microscopic parameters. The form of the continuum equations obtained in Ref. [407] is identical to those used here, the only distinction being that $\mathcal{O}(\boldsymbol{\nabla}^2)$ terms are neglected in that work, including the explicit $K_G$ term. In the following, we shall similarly neglect $\boldsymbol{\nabla}^2$ terms.

## 4.2 Polar flock on a sphere

As an example of a curved surface with constant positive curvature, we consider an active polar flock on the surface of a sphere of radius $R$. In local spherical polar coordinates $\{\theta, \varphi\}$, the canonical metric and curvature on $S^2$ are

$$\mathfrak{g} = R^2(\mathrm{d}\theta \otimes \mathrm{d}\theta + \sin^2\theta \mathrm{d}\varphi \otimes \mathrm{d}\varphi) \ , \qquad K_G = \frac{1}{R^2} \ . \tag{4.4}$$

The only non-vanishing Christoffel symbols are

$$\Gamma^{\theta}_{\varphi\varphi} = -\sin\theta\cos\theta \quad \text{and} \quad \Gamma^{\varphi}_{\theta\varphi} = \cot\theta \ . \tag{4.5}$$

### 4.2.1 The steady state of a polar flock on the sphere

At low mean density ($\rho_0 < \rho_c$), the isotropic phase with constant density and $\mathbf{p} = \mathbf{0}$ is stable. For $\rho_0 > \rho_c$, where the mean-field solution in flat space is a state of constant density and finite, but uniform polarization, on the sphere one obtains polar, spatially varying states. Since the particle number is conserved, there can be no sinks or sources of flow. The geometric frustration forces polar order to develop inhomogeneous profiles, but the global topology of the sphere additionally necessitates the presence of vortices as per the Poincaré-Hopf theorem [420]. The simplest configuration allowed by the required conservation of topological defect charge that must sum up to the Euler characteristic $\chi = 2$ of the sphere is then a circulating band wrapping around an equator, with two vortices of charge +1 at opposing poles. This yields a density band with polarization in the azimuthal direction that vanishes at the poles, consistent with the band state reported recently in simulations of polar particles on the sphere [408].

An explicit solution can be found analytically by assuming azimuthal symmetry, with $\rho = \rho_{ss}(\theta)$, $p^\theta = 0$ and $p^\varphi = p^\varphi_{ss}(\theta)$. The continuity equation is then satisfied identically. To simplify the polarization equation, we neglect the viscous terms as they are higher order in gradients (suppressed by $1/R^2$) compared to the other terms arising from self-propulsion. In the microscopic realization of self-propelled polar particles with short range repulsive forces and aligning interactions studied in Ref. [408], this approximation corresponds to the regime where inter-particle repulsion (contributing to the pressure) and active self-propulsion dominate over viscous and elastic stresses. We then neglect the laplacian terms entirely by setting $\nu = 0$ (the bulk viscosity $\nu'$ drops out with our assumption of azimuthal symmetry). This leaves us with

$$\lambda \sin\theta \cos\theta \, (p^\varphi_{ss})^2 = \frac{\chi}{R^2} \partial_\theta \rho_{ss} \; , \tag{4.6}$$

$$p^\varphi_{ss}[a(\rho_{ss} - \rho_c) - bR^2 \sin^2\theta \, (p^\varphi_{ss})^2] = 0 \; . \tag{4.7}$$

Writing $X(\theta) = \rho_{ss}(\theta) - \rho_c$, and seeking a solution with $p^\varphi_{ss} \neq 0$ we can eliminate $p^\varphi_{ss}$ from the two equations to obtain

$$\frac{\mathrm{d}X}{\mathrm{d}\theta} = \left(\frac{a\lambda}{b\chi}\right) \cot\theta X \implies X(\theta) = X(\pi/2)(\sin\theta)^\eta \; , \tag{4.8}$$

where

$$\eta = \frac{\lambda a}{b\chi} \tag{4.9}$$

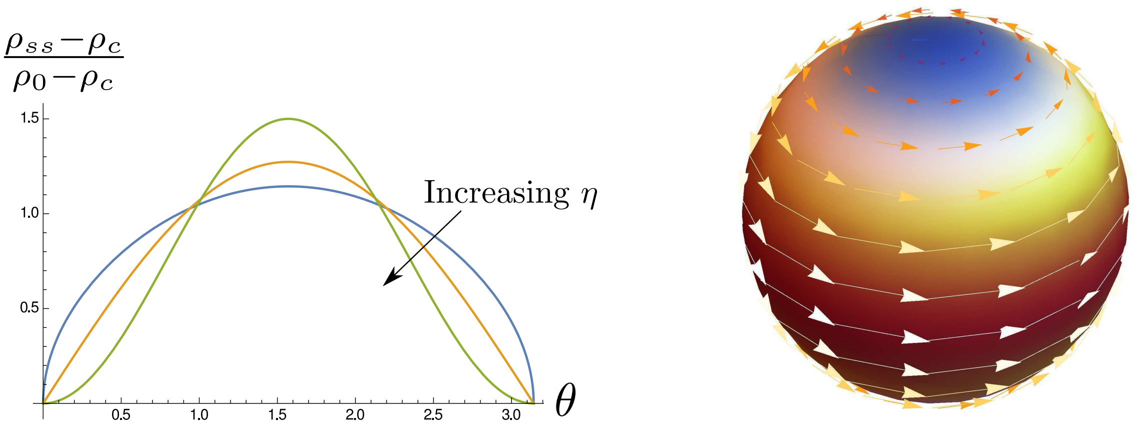

(a)

(b)

Figure 21 : (a) The normalized density profile of a polar flock on a sphere given in Eq. 4.12, for $\eta = 0.5$ (blue), 1 (orange) and 2 (green). (b) The density and polarization profiles for $\eta = 2$, now shown on the sphere. The color describes the density from the maximum (red) at the center of the polar band to $\rho_c$ (blue) at the poles of the sphere. The polarization also vanishes at the poles.

is a dimensionless parameter that controls the shape of the solution, with $\eta > 0$ for the density profile to be a physical solution (as $\sin\theta > 0$ over the entire range $\theta \in [0, \pi]$). By symmetry, the density will be maximum at $\theta = \pi/2$ (the equator). Letting $\rho_{ss}(\pi/2) = \rho_{\max}$ we find

$$\rho_{ss}(\theta) = \rho_c + (\rho_{\max} - \rho_c)\sin^\eta\theta \; . \tag{4.10}$$

We stress that the dependence on $R$ has dropped out from Eq. 4.10, which therefore represents a universal density profile for an ordered flock on any size sphere. Finally, we express $\rho_{\max}$ in terms of the average density $\rho_0 \equiv \langle \rho_{ss} \rangle$ by requiring

$$\rho_0 = \frac{1}{4\pi}\int_0^{2\pi} \mathrm{d}\varphi \int_0^{\pi} \mathrm{d}\theta \sin\theta \rho_{ss}(\theta) \; . \tag{4.11}$$

to obtain the final expression for the density profile as

$$\rho_{ss}(\theta) = \rho_c + (\rho_0 - \rho_c)A_\eta \sin^\eta\theta \; , \tag{4.12}$$

with $A_\eta = 2\Gamma((3+\eta)/2)/[\sqrt{\pi}\Gamma(1+\eta/2)]$. In order for this density profile to exist, we additionally require that $|\mathbf{p}_{ss}|^2 > 0$ and obtain

$$|\mathbf{p}_{ss}|^2 = \frac{a}{b}(\rho_0 - \rho_c) A_\eta \sin^\eta \theta \ . \tag{4.13}$$

As expected, an ordered flock only exists for $\rho_0 > \rho_c$, and the magnitude of the steady state polarization and the density have the same inhomogeneous profile as shown in Fig. 21(a), with the direction of polarization chosen spontaneously. As required by the topology of the sphere, a vortex inhabits each pole, with the polarization vanishing at their core.

This latitudinal band solution is unrelated to the traveling bands found in flat space [302, 304, 305], which occur close to the mean-field transition and are absent deep in the ordered phase. The inhomogeneous solution obtained is simply the ordered flocking state on a sphere. The spatially inhomogeneous profile arises from the interplay of mass fluxes ($\sim \chi \boldsymbol{\nabla} \rho$) and convective fluxes ($\sim \lambda \mathbf{p} \cdot \boldsymbol{\nabla} \mathbf{p}$) that cannot be set to zero on a curved surface, when ordered. Hence the spatial inhomogeneity is made inevitable by curvature. Note that a similar although single vortex solution is obtained when an active polar fluid is circularly confined in the plane [421]. The spatial profile of the confined vortex is qualitatively the same as the one obtained here with curvature, in particular, the density at the core is found to be $\rho_c$ (the critical density for the mean field transition) just as reported in Ref. [421]. In both cases, self-propulsion induced advection balances pressure forces to set this notrivial steady state.

The present solution is expected to break down within a region of angular width $\theta_\mathrm{m} \sim \exp(-a\rho_c R^2/\nu)$ (hence exponentially small on a large sphere) around the poles of the sphere, at the core of the vortices, as the elastic stresses will become important at short scales. Therefore the profile obtained is a robust and universal prediction of the continuum theory, similar to the rotating band seen in particle simulations of Ref. [408]. Note that the depth of the double well symmetry-breaking potential is, amongst other things, controlled by $a/b \propto v_0^2$, where $v_0$ is the self-propulsion of the motile constituents of the flock. Anticipating ourselves, we can use the fact that $c_{||} \sim \lambda v_0$ sets the longitudinal sound speed and $c_\perp \sim \sqrt{\chi}$ sets the transverse sound speed [411], to also get $\eta \sim v_0 c_{||}/c_\perp^2$. As sound speeds have been experimentally measured in 2D flocks of active colloidal rollers [422], one can directly obtain $\eta$ as a material property of the active fluid from flat space measurements alone. This would then provide a concrete prediction for the profile of the active fluid on a sphere, allowing for a nontrivial test of our theory.

For an equilibrium polar or ferroelectric liquid crystal (say, a compressible lyotropic smectic-C film [344]), where the polarization is strictly an order parameter field and does not play the role of a velocity, the important convective nonlinearity in Eq. 4.3 is absent ($\lambda = 0$, though $\lambda_2$ and $\lambda_3$ can be present [423]) and the band solution we have here is absent ($\eta = 0$, see Fig. 22). In this case, even in the ordered phase, the density remains homogeneous and on a large enough sphere, we have nearly uniform polar order everywhere ($|\mathbf{p}_{ss}| \simeq$ const.), except for two isolated defects at the poles, whose core size $\xi \sim \sqrt{\nu/a(\rho_0 - \rho_c)}$ is a microscopic length scale deep into the ordered state. The vortex core size in an equilibrium polar liquid crystal is set by the elastic constant (which is a thermodynamic parameter) and not by a kinematic transport coefficient $\lambda$, implying the steady flocking band solution obtained here is a distinctly nonequilibrium phenomenon.

### 4.2.2 Linearizing about the steady state

Well below the mean-field transition ($\rho_0 < \rho_c$), the isotropic disordered state ($\rho_{ss} = \rho_0$ and $\mathbf{p}_{ss} = \mathbf{0}$) is linearly stable at long wavelengths with fluctuations in the polarization

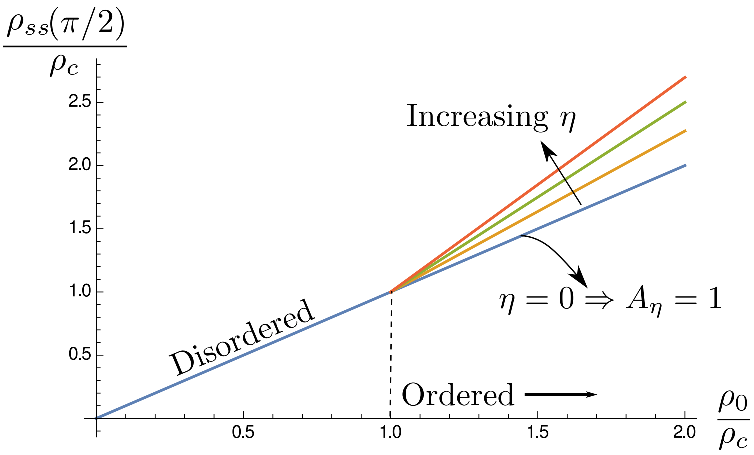

Figure 22 : The peak (maximum) density at the equator on a sphere, as we vary the mean density $\rho_0$. For $\rho_0 < \rho_c$, we are in the disordered phase with $\rho_{ss}(\pi/2) = \rho_0$. For $\rho_0 > \rho_c$, we have a polar band with the density profile given in Fig. 21. The density reaches its maximum at the center of the band and grows with $\rho_0$, with a slope $A_\eta > 1$. When the convective parameter $\lambda \to 0$, $\eta \to 0$, resulting in $A_\eta \to 1$ and we go back to the homogeneous profile as in the flat plane.

relaxing quickly and density perturbations relaxing diffusively at long time, just as in the plane [424]. The curvature does not affect the disordered phase in any important way. It is only in the ordered state that we find novel excitations with nontrivial topological properties.

Here we consider the linearized dynamics of small amplitude perturbations about the steady ordered flock, letting $\rho = \rho_{ss}(\theta) + \delta\rho$ and $\mathbf{p} = \mathbf{p}_{ss}(\theta) + \delta\mathbf{p}$. We focus on the long-wavelength propagating sound modes that are present even in the plane for an ordered flock [411], and continue to neglect all the viscous and elastic couplings. These are higher order in gradients and only give rise to damping of the sound modes. As the base state we are linearizing about is inhomogeneous, we additionally confine ourselves to a tangent plane linearization about a fixed latitude away from the poles (a preferred local coordinate system is picked out spontaneously by the polar order allowing for an unambiguous notion of latitude). Setting $\theta = \theta_0 + y$ for a given latitude $\theta_0$, with $\theta_0 < \pi/2$ corresponding to the northern hemisphere and $\theta_0 > \pi/2$ to the southern hemisphere, relabelling $\varphi$ as $x$, and letting $\delta p^\theta \to \mathsf{v}$ and $\delta p^\varphi \to \mathsf{u}$, we obtain

$$\partial_t \delta\rho + \partial_x \mathsf{u} + \partial_y \mathsf{v} + \mathsf{v} \cot\theta_0 = 0 \ , \tag{4.14}$$

$$\begin{aligned} &\partial_t \mathsf{u} + \lambda p_0 \partial_x \mathsf{u} + \frac{\chi}{R^2 \sin^2\theta_0} \partial_x \delta\rho \\ &\quad = p_0(a\delta\rho - 2bR^2 p_0 \sin^2\theta_0 \ \mathsf{u}) - \mathsf{v}\frac{\lambda p_0(\eta+2)}{2} \cot\theta_0 \ , \end{aligned} \tag{4.15}$$

$$\partial_t \mathsf{v} + \lambda p_0 \partial_x \mathsf{v} + \frac{\chi}{R^2} \partial_y \delta\rho = 2\mathsf{u}\lambda p_0 \sin^2\theta_0 \cot\theta_0 \ , \tag{4.16}$$

with $p_0 = p^\varphi_{ss}(\theta_0)$ the azimuthal polarization at latitude $\theta_0$, which is finite as long as we are away from the poles ($\theta_0 \neq 0, \pi$). Note that stability of the steady state requires $\eta > 0$, hence $\lambda > 0$. The only terms that can be negative are those proportional to $\cot\theta_0$, arising from the Christoffel symbols, which changes sign as one crosses the equator at $\theta_0 = \pi/2$.

Next we perform a Galilean boost to a comoving frame by letting $x \to x - \lambda p_0 t$ (comoving with the logitudinal sound and *not* the flock itself), and suggestively relabel parameters as $c_{||} = \lambda p_0$, $\alpha = a p_0 > 0$, $\beta = 2bp_0^2 R^2 \sin^2\theta_0 > 0$, $c_\perp^2 = \chi/R^2 > 0$ and

$$m = -\cot\theta_0 \ . \tag{4.17}$$

The redefined parameters are summarized in Table 2. Since the flock breaks Galilean invariance, this is not a symmetry operation, and yields

$$\partial_t \delta\rho - c_{||}\partial_x \delta\rho + \partial_x \mathsf{u} + \partial_y \mathsf{v} = m \ \mathsf{v} \ , \tag{4.18}$$

$$\partial_t \mathsf{u} + \frac{c_\perp^2}{\sin^2\theta_0} \partial_x \delta\rho = \alpha\delta\rho - \beta\mathsf{u} + \frac{c_{||}(\eta+2)}{2} m \ \mathsf{v} \ , \tag{4.19}$$

$$\partial_t \mathsf{v} + c_\perp^2 \partial_y \delta\rho = -2c_{||}\sin^2\theta_0 m \ \mathsf{u} \ . \tag{4.20}$$

Here $m$ is a constant of fixed sign at any given non-equatorial latitude and changes sign across the equator, with $m < 0$ in the northern hemisphere and $m > 0$ in the southern half, vanishing only at the equator where $\theta_0 = \pi/2$. We show below that a non-vanishing value of $m$ leads to a band or "mass" gap [Fig. 23(b) and 23(c)] in the sound mode spectrum that acquires the necessary structure for nontrivial band topology. This, along with the vanishing of $m$ at the equator, naturally suggests that the equator behaves as a "boundary" between two different "bulk" media (the northern and southern hemispheres), thereby allowing for localized topologically protected excitations on it.

| $\lambda$ | $a$ | $b$ | $\chi$ |
|---|---|---|---|
| $c_{\|\|} = \lambda p_0$ | $\alpha = a p_0$ | $\beta = 2b p_0^2 R^2 \sin^2\theta_0$ | $c_\perp^2 = \chi/R^2$ |

Table 2 : A summary of the parameters redefinitions in the model.

To simplify the notation we let $|\delta\Psi\rangle \equiv (\delta\rho, \mathsf{u}, \mathsf{v})$ and recast the linearized equations that control the linear stability of the steady state in the form of a Schrödinger like equation (in Fourier space, with $\Psi(\mathbf{q}) = \int \mathrm{d}^2 r \; e^{-i\mathbf{q}\cdot\mathbf{r}}\Psi(\mathbf{r})$), as

$$i\partial_t|\delta\Psi\rangle = \mathcal{H}|\delta\Psi\rangle \; , \tag{4.21}$$

$$\mathcal{H}(\mathbf{q}) = \begin{pmatrix} -c_{||}q_x & q_x & im + q_y \\ i\alpha + \dfrac{c_\perp^2 q_x}{\sin^2\theta_0} & -i\beta & imc_{||}\left(\dfrac{\eta}{2}+1\right) \\ c_\perp^2 q_y & -2imc_{||}\sin^2\theta_0 & 0 \end{pmatrix} . \tag{4.22}$$

The eigenvalues of $\mathcal{H}(\mathbf{q})$ directly give the sound mode frequencies ($|\delta\Psi\rangle \propto e^{-i\omega t}$). An important distinction compared to the Schrödinger equation is that the matrix $\mathcal{H}$ is not Hermitian and therefore the linearized mode spectrum is not purely real, due to dissipative terms describing the overdamped dynamics and the absence of Galilean

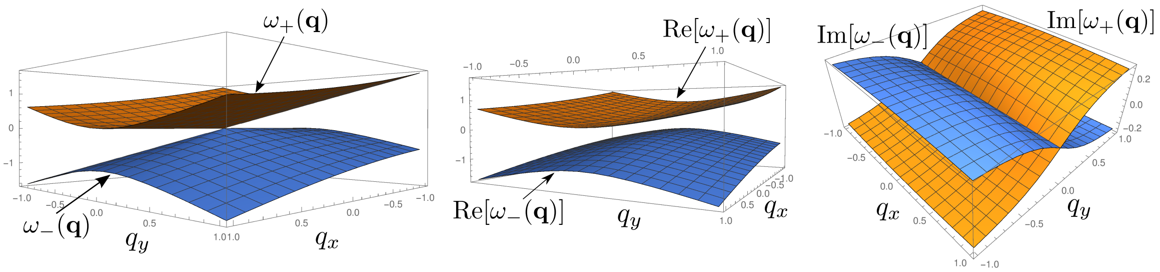

(a) (b) (c)

Figure 23 : The relevant (slow) sound modes. (a) $m = 0$ and the gap between the two bands is closed. (b) and (c) are the dispersion bands for $m = 0.2$ (Eq. 4.26) and we directly see that a gap has opened in the real part of the spectrum, while the imaginary part of the frequency has a single crossing line at $q_y = 0$. The variables are chosen to be $\theta_0 \simeq 78°$, $\alpha \simeq 2.03$, $c_{||} \simeq 1.03$ and $\beta = c_\perp = 1$.

invariance. For $m = 0$ ($\theta_0 = \pi/2$) the equations reduce to those of the planar case. Fluctuations in the polarization magnitude ($\mathsf{u}$) are controlled by a fast mode that decays on microscopic time scales $\sim \beta^{-1}$,

$$i\omega_0(\mathbf{q}) = \beta - i\frac{\alpha}{\beta}q_x + \mathcal{O}(q^2)\ . \tag{4.23}$$

The density ($\delta\rho$) and the transverse Goldstone mode ($\mathsf{v}$) are the only slow modes that remain propagating at long wavelengths (as $\mathbf{q} \to 0$),

$$\omega_\pm(\mathbf{q}) = \frac{1}{2}\left[(v_s - c_{||})q_x \pm \sqrt{(v_s - c_{||})^2 q_x^2 + 4c_\perp^2 q_y^2}\right] + \mathcal{O}(q^2)\ , \tag{4.24}$$

where $v_s = \alpha/\beta$ is proportional to the speed of the flock. For $q_y = 0$, there are two sound modes that propagate in the direction of the flock. Density excitations travel with a linear dispersion $\omega_+(q_x) = (v_s - c_{||})q_x$, which in the lab frame corresponds to a longitudinal sound speed $v_s = \alpha/\beta$ set by the speed of the flock itself. Orientational fluctuations travel with a different linear dispersion $\omega_-(q_x) = c_{||}q_x$ (in the lab frame), where $c_{||} = \lambda p_0$ is the second longitudinal speed of sound. The fact that the two longitudinal sound speeds $v_s$ and $c_{||}$ are in general unequal signals the absence of

Galilean invariance [411]. Orthogonal to the motion of the flock, for $q_x = 0$, both density and orientational perturbations travel with the same transverse sound speed given by $c_\perp = \sqrt{\chi}/R$.

For non-zero but small $m \neq 0$ ($\theta_0 \neq \pi/2$), corresponding to the regions close to the equator in either hemisphere, the dispersion relations can be written as

$$i\omega_0(\mathbf{q}) = \beta - iv_s\left(q_x + \frac{2mc_{||}}{\beta}\sin^2\theta_0 q_y\right) + \mathcal{O}(q^2)\ , \tag{4.25}$$

$$\omega_\pm(\mathbf{q}) = \frac{1}{2}\left[q_x(v_s - c_{||}) \pm \sqrt{q_x^2(v_s - c_{||})^2 + 4(m - iq_y)(2mv_sc_{||}\sin^2\theta_0 + ic_\perp^2 q_y)}\right]\ , \tag{4.26}$$

valid upto $\mathcal{O}(m^2, q^2, mq)$ terms. In the next section we analyze this mode structure.

## 4.3 Symmetry protected topological sound

From Eq. 4.26, we immediately see that the two branches of the propagating modes have a spectral gap at $\mathbf{q} = \mathbf{0}$ of width $\Delta = |\omega_+(0) - \omega_-(0)|$ proportional to $|m|$, with

$$\Delta = 2|m|\sin\theta_0\sqrt{2v_sc_{||}} + \mathcal{O}(|m|^3)\ . \tag{4.27}$$

The gap vanishes in the absence of ordered collective motion ($v_s = 0$) and in the absence of active convection ($\lambda = 0 \implies c_{||} = 0$). Writing it in terms of the original variables, we have

$$\Delta = 2\frac{|m|}{R}\sqrt{\frac{a\lambda}{b}} + \mathcal{O}(|m|^3) \propto \sqrt{K_G}\ , \tag{4.28}$$

where we directly see that Gaussian curvature $K_G$ introduces a new length scale that controls the gap in the sound spectrum. Additionally, we note that the gap is also directly controlled by the depth of the double well potential through $a/b$. The terms explicitly involving $m$ in the dispersion relations, responsible for the opening of the gap, are obtained only in the presence of *both* curvature *and* spontaneous active flow. In the plane, *static* long-wavelength deformations of both the density and the broken symmetry mode leave the system unchanged. On a curved surface, in contrast, spatially uniform deformations of either "slow" field ($\delta\rho$ and $\mathsf{v}$) cannot be static and invariably lead to dynamics in the system. As a result of curvature-induced forces, long-wavelength deformations of would be slow modes are required to have a finite frequency, resulting generically in the $\mathbf{q} = \mathbf{0}$ gap of the sound spectrum, in sharp contrast to the conventional behavior of hydrodynamics in a flat geometry [425].

It is useful to compare the effect at hand with one that occurs in geophysical flows. In a frame comoving with the flock, the finite curvature of the sphere in conjunction with fluid advection plays a role similar to the Coriolis force that would be present for a passive fluid on a rotating sphere. In the case of the earth's atmosphere, this has recently been shown to give a gapped sound spectrum and equatorially confined Kelvin and Yanai waves [426] that are topological in origin [412]. In our active system, no external flow or rotation needs to be imposed and the absence of Galilean invariance allows for independent tuning of the material parameters (such as $\lambda$) in order to probe regimes that are not accessible to passive fluids.

On times scales $t \gg \beta^{-1}$ we can slave the fast mode $\mathsf{u}$ to the slow fields, $\mathsf{u} \simeq \alpha\delta\rho/\beta + \mathcal{O}(\nabla\delta\rho)$[1]. Upon eliminating $\mathsf{u}$ we get a reduced set of dynamical equations involving only $\delta\rho$ and $\mathsf{v}$. The linear matrix controlling the dynamics of $\delta\rho, \mathsf{v}$ fluctuations is compactly given by

$$\mathcal{D}(\mathbf{q}) = \begin{pmatrix} (v_s - c_{||})q_x & q_y + im \\ c_\perp^2(q_y - i\eta m) & 0 \end{pmatrix} , \tag{4.29}$$

---

[1] The term involving $c_{||}(\eta+2)m\mathsf{v}$ is not relevant as its contribution to the dispersion is subdominant, as can be seen from its absence in Eq. 4.26.

where $\eta = \lambda a/(b\chi) > 0$ is the same exponent as before. One can easily check that the eigen-frequencies of $\mathcal{D}(\mathbf{q})$ are exactly given by $\omega_{\pm}(\mathbf{q})$ in Eq. 4.26. As $\mathcal{D}(\mathbf{q})$ is still non-Hermitian, we need to evaluate its right and left (adjoint) eigenvectors

$$\mathcal{D}(\mathbf{q})|\psi_i\rangle = \omega_i(\mathbf{q})|\psi_i\rangle \ , \tag{4.30}$$

$$\mathcal{D}^{\dagger}(\mathbf{q})|\chi_i\rangle = \omega_i^*(\mathbf{q})|\chi_i\rangle \ , \quad (i = \pm) \tag{4.31}$$

with the biorthogonality relation $\langle\chi_i|\psi_j\rangle = \delta_{ij}$. It is important to keep in mind the regime in which $\mathcal{D}(\mathbf{q})$ provides a valid approximation to the complete dynamics. For

$$\frac{1}{\beta} \ll t \ll \frac{\beta}{\eta c_{||}^2 m^2} \ , \quad \frac{c_{||}|m|}{\beta} \ll 1 \ , \tag{4.32}$$

we can neglect the fast $\mathsf{u}$ mode and not worry about higher order terms in both $\mathbf{q}$ and $m$. This can be achieved deep in the ordered phase on a large enough sphere, in which case $\beta$ is large, allowing for a large window of time in which the dynamics is dominated by $\mathcal{D}(\mathbf{q})$. With this set of simplifications, the linear dynamical matrix is always diagonalizable and $\omega_+ \neq \omega_-$ as long as $m \neq 0$ or $\mathbf{q} \neq 0$ allowing one to adiabatically deform our model to have purely real eigenvalues by smoothly taking $\eta \to 1$. In the process, the spectral gap remains open as long as $m \neq 0$.

In order to establish the topological nature of the band structure, we compute the associated $\mathsf{U}(1)$ Berry gauge connection and curvature [427]

$$\mathcal{A}_{\pm} = i\langle\chi_{\pm}|\boldsymbol{\nabla}_{\mathbf{q}}|\psi_{\pm}\rangle \ , \quad \mathcal{F}_{\pm}(\mathbf{q}) = \boldsymbol{\nabla}_{\mathbf{q}} \times \mathcal{A}_{\pm} \ . \tag{4.33}$$

The Berry curvature itself is plotted as a heat map in Fig. 24 and is localized essentially near the center of the band (around $\mathbf{q} = \mathbf{0}$). In addition, the Berry curvature in the two bands is of opposite sign, as expected. Finally computing the Chern numbers [19]

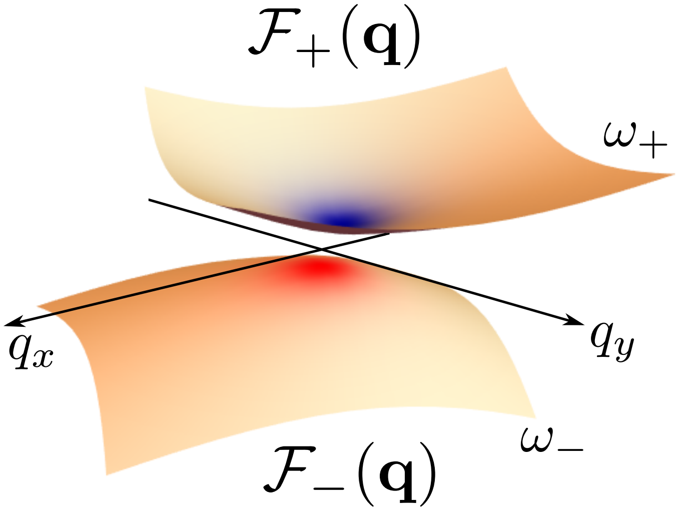

Figure 24 : The Berry curvature $\mathcal{F}_\pm(\mathbf{q})$ plotted as a function of wavevector $\mathbf{q}$ as a heat map on top of the two bands $\omega_\pm(\mathbf{q})$. The colour ranges from blue (positive) to red (negative). Parameters used are $m = 1$, $v_s = 1.5$, $c_{||} = 1$.

for each band, we get

$$C_\pm = \int \frac{\mathrm{d}^2 q}{2\pi} \mathcal{F}_\pm = \pm\frac{1}{2}\,\mathrm{sgn}(v_s - c_{||})\,\mathrm{sgn}(m) \ . \tag{4.34}$$

The Chern number here is only quantized to a half integer as we work directly in the continuum long-wavelength approximation and we only account for the single Dirac cone like structure at $\mathbf{q} = \mathbf{0}$ that arises when the gap closes [347, 428]. This is the contribution to the "parity anomaly" or Hall conductance associated to a single Dirac cone in a Chern insulator [52]. An appropriate regularization for large $\mathbf{q}$ guarantees the Chern number to be an integer [53, 429]. This calculation though still does have worth in predicting the correct number of topologically protected edge modes present when we stitch two regions with different Chern numbers together, via the bulk-boundary correspondence. So each gap closing (change in sign of $m$) leads to a single localized edge mode which, as we shall see, is unidirectional.

We briefly digress to address a subtle but important technical point. As both the hemispheres along with their respective steady state density and polarization profiles are related to each other by a reflection symmetry ($\rho_{ss}$ and $\mathbf{p}_{ss}$ are symmetric about the equator), the Chern numbers of the respective bands must be of opposite sign in each hemisphere[2]. As the microscopically regulated Chern number has to be an integer by the Nielsen-Ninomiya theorem [430], this immediately tells us that the number of equatorial modes must be *even* by virtue of reflection symmetry across the equator. Instead our calculation above only predicts a single equatorial mode. In order to resolve this discrepency, we regulate $\mathcal{D}(\mathbf{q})$ by using a discrete lattice that respects the reflection symmetry for all $\mathbf{q}$, by writing $q_{x,y} \to \sin q_{x,y}$ and $m \to m(3 - \cos q_x - \cos q_y)$. For $\mathbf{q} \to \mathbf{0}$, we recover the continuum $\mathcal{D}(\mathbf{q})$ in Eq. 4.29, but at the edge of the Brillouin zone, there are now three additional gap closings at $(\pm\pi, 0)$, $(0, \pm\pi)$ and $(\pm\pi, \pm\pi)$ as $m \to 0$. These provide the missing contribution to the Chern number to make it an integer. In a real active fluid though, the edge modes that reside at the special high $\mathbf{q}$ points will be rapidly dissipated on short time scales $\sim (\nu q^2)^{-1}$, where $\nu$ is the viscosity of the fluid. Note that in an active *chiral* fluid, the absence of local parity allows an odd or Hall viscous term [431–433] to be present that provides a non-dissipative regularizer at short distances (albeit still in the continuum) [434, 435]. Hence in our achiral polar fluid, the only long-lived topological mode that survives is the single mode at $\mathbf{q} = \mathbf{0}$, which is the only one we shall focus on.

As expected, the Chern number of the acoustic band is different in the northern ($m < 0$) and southern ($m > 0$) hemispheres, vanishing at the equator ($m = 0$). Hence going across the equator, we have one gap closing (at $\mathbf{q} = \mathbf{0}$) with a band inversion, leading to a single topological sound excitation localized at the equator. Note that the Chern number also vanishes when $v_s = c_{||}$, leading to a topologically trivial band structure. The case $v_s = c_{||} = 0$ corresponds to the absence of spontaneous active flow while when $v_s = c_{||} \neq 0$, we have a partial restoration of Galilean invariance (in this limit, both density and Goldstone mode excitations propagate with the same speed in the direction of the flock). So the vanishing of the Chern number and associated band triviality for $v_s = c_{||}$ is *not* due to the closure of a gap, but is instead due to the restoration of a protecting symmetry. As both $v_s = \alpha/\beta$ and $c_{||} = \lambda p_0$ depend on the latitude $\theta_0$ at which we are, setting $v_s = c_{||}$ provides a condition on the polar angle $\theta_0$. There is a critical density

---

[2] We thank Cenke Xu for pointing this out.

$$\rho^* = \rho_c + \frac{1}{2A_\eta \lambda}, \tag{4.35}$$

such that for $\rho_c < \rho_0 < \rho^*$, $v_s \neq c_{||}$ on the entire sphere. Deeper into the ordered state ($\rho_0 > \rho^*$), there are two latitudes at angles $\theta_\pm$ such that $\sin^\eta \theta_\pm = (\rho^* - \rho_c)/(\rho_0 - \rho_c)$, at which $v_s$ and $c_{||}$ coincide. Even though the band topology changes as we cross the latitudes at $\theta_\pm$ (Eq. 4.34), the spectrum remains gapped throughout and hence we *do not* have any gapless excitations localized at $\theta_\pm$. The change in the Chern number across these special latitudes is due to an accidental additional symmetry (Galilean invariance) instead of the gap closing, thereby circumventing the bulk-boundary correspondence. This is a well known point in quantum topological insulators, only realized here in a peculiar fashion as the protecting "symmetry" varies spatially in a single sample.

To summarize, there are three crucial ingredients in this system that lead to and protect the topologically nontrivial band structure-

- Breaking of time-reversal symmetry and Galilean invariance by the active polar flow.
- The presence of the convective nonlinearity $\lambda \neq 0$; an equilibrium passive polar liquid crystal will therefore not exhibit these modes.

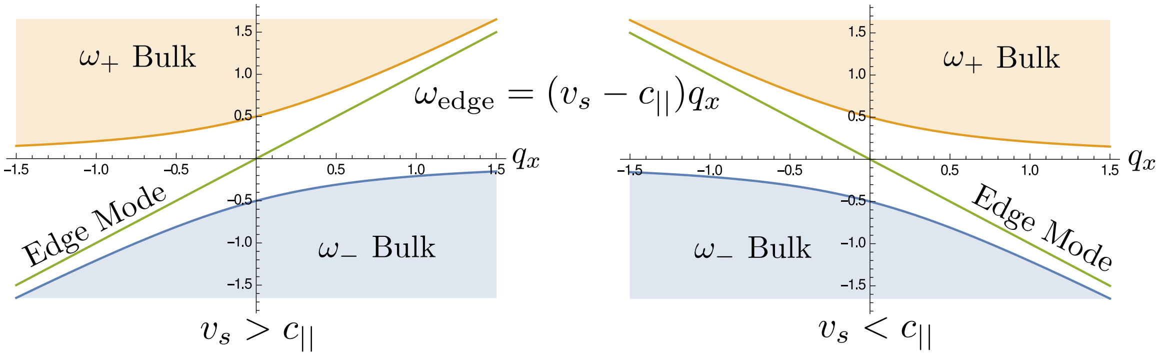

Figure 25 : The bulk and edge mode spectrum in the frame comoving with the longitudinal sound with speed $c_{||}$, for the case when $v_s > c_{||}$ and $v_s < c_{||}$ (shown here for the simple case when $\eta = 1$) and $m(y)$ varying from $-1$ to $+1$. This is the situation when $K_G > 0$ (as on the sphere), where the density mode is equatorially localized and topologically protected.

- The curvature of the base surface which opens up a gap in the sound spectrum. Changing the Gaussian curvature exchanges the regions with positive and negative "mass" $m$.

This is entirely analogous to the Haldane model [52] where the closing of the gap at the Dirac point is protected by time-reversal symmetry, which when broken by the local magnetic field leads to a band structure with a nontrivial topology. Though the active system is not Hermitian with purely real frequencies, the structure of the localized equatorial mode for varying $m(y)$ is adiabatically connected to its Hermitian analogue [436], the Jackiw-Rebbi soliton [437].

$$|\delta\Psi_{\rm edge}\rangle = \psi_0 e^{-\eta\int_0^y m(y')\mathrm{d}y' + iq_x[x-(v_s-c_{||})t]} \begin{pmatrix} 1 \\ 0 \end{pmatrix} , \tag{4.36}$$

where $\psi_0$ is a normalization constant. The edge mode spectrum $\omega_{\rm edge}(q_x) = (v_s - c_{||})q_x$ corresponds, in the comoving frame, to a pure one-way density wave that connects the two bulk bands (see Fig. 25). This edge mode is valid when $m(y) \to \pm m_0$ ($m_0 > 0$) for $y \to \pm\infty$.

On the sphere, reverting back to angular coordinates $\{\theta, \varphi\}$, $m(\theta) = -\cot\theta$, which is positive in the southern hemisphere for $\theta > \pi/2$ ($y > 0$). This gives a chiral equatorial density mode ($\mathsf{v} = 0$) propagating with speed $v_s$, which in the lab frame looks like

$$\delta\rho_{\text{edge}}(\theta, \varphi; t) = \sin^{\eta}\theta \sum_{n \geq 0} \left[\mathsf{a}_n \, e^{in(\varphi - v_s t)} + \text{c.c.}\right], \tag{4.37}$$

where $\mathsf{a}_n$ are complex constants depending on the initial perturbation applied and $v_s = \alpha/\beta$ is evaluated at $\theta = \pi/2$ (the equator), where the edge state is localized. A snapshot of this density mode is shown in Fig. 27 for $n = 6$ (and all other $\mathsf{a}_n$ vanishing). Equation 4.37 defines a localization length $\ell_{\text{loc}} = R/\sqrt{\eta} \sim Rc_{\perp}/\sqrt{v_0 c_{||}}$ set by the curvature and material parameters of the active fluid involving a ratio of the longitudinal and transverse sound speeds, and diverging as self-propulsion $v_0 \to 0$ (no localized mode in the passive system). Note that the result given in Eqs. 4.36 and 4.37 applies for $\lambda_3 = 0$. The general case of $\lambda_2, \lambda_3 \neq 0$ is given in Appendix 4.A and yields a different localization width for the equatorial mode. This topological edge mode propagates unidirectionally in the direction of the flock and is robust to disorder and obstacles because there are no reverse channels into which it can scatter (though it will eventually dissipate due to viscous and elastic damping). Unlike a Galilean invariant fluid for which $\eta = 1$, here $\eta$ and therefore the localization length can be tuned separately by varying the system's parameters, although the shape of the steady state profile remains unchanged.

## 4.4 Polar flock on a negatively curved surface

The presence of such topological excitations is generic in that they will always be present when one has a polar flock on a curved surface, with the topologically protected modes localized to geodesics that coincide with streamlines of the flock[3]. We illustrate this point on a catenoid, a surface with non-constant negative Gaussian curvature.

In local coordinates $\{y, \varphi\}$ ($\varphi$ once again being the periodic azimuthal direction), the metric and Gaussian curvature on a catenoid are

$$\mathfrak{g} = R^2 \cosh^2 y (\mathrm{d}y \otimes \mathrm{d}y + \mathrm{d}\varphi \otimes \mathrm{d}\varphi) \ , \tag{4.38}$$

$$K_G(y) = -\frac{1}{R^2} \mathrm{sech}^4 y \ , \tag{4.39}$$

where $R$ is the radius of curvature at the neck of the catenoid. In contrast to the sphere, the Gaussian curvature here is both negative and spatially varying. The only non-vanishing Christoffel symbols are

$$\Gamma^{\varphi}_{\varphi y} = \Gamma^{y}_{yy} = -\Gamma^{y}_{\varphi\varphi} = \tanh y \ . \tag{4.40}$$

Taking the same approach as for the sphere, neglecting viscous and elastic stresses, we consider an azimuthally symmetric ansatz for the steady state polar flock: $\rho = \rho_{ss}(y)$, $p^y = 0$ and $p^{\varphi} = p^{\varphi}_{ss}(y)$. One can easily verify that for $\rho_0 > \rho_c$ the steady state density profile is then

$$\rho_{ss}(y) = \rho_c + (\rho_0 - \rho_c) B_{\eta} \cosh^{\eta} y \ , \tag{4.41}$$

where $B_{\eta} < 1$ is a constant that depends on $\eta$ and the height of the catenoid (which unlike the sphere is not compact and has to be taken finite). The details of the computation are given in Appendix 4.B. In contrast to the sphere, which had a polar

---

[3] For the case of surfaces of revolution that we study, we have a Killing field on the surface dictating a symmetry direction, which naturally provides a vector field along which a flock can condense at steady state. This structure is sufficient for the existence of such topological modes, but it is unclear if it is necessary as well.

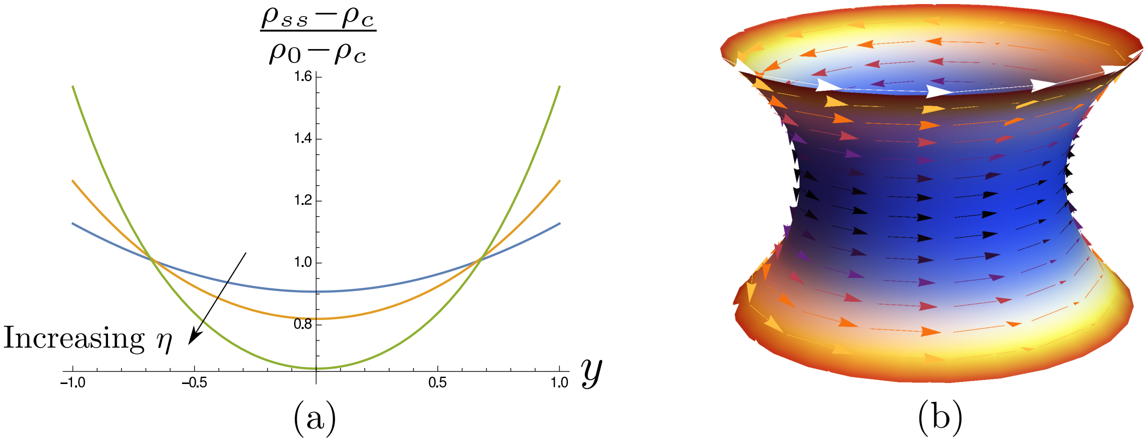

Figure 26 : (a) The normalized density profile of a polar flock on a catenoid given in Eq. 4.41, for $\eta = 0.5$ (blue), 1 (orange) and 2 (green). Note that, in contrast to the sphere, the density grows near the edge of the catenoid. (b) The density and polarization (for $\eta = 2$) now shown on the catenoid. As before, blue corresponds to low density regions (at the neck) and red to high density.

band with maximum density at the equator, the polar flock density is lowest at the neck of the catenoid ($y = 0$), increasing on either side as one moves away from it. The corresponding polarization profile is given by

$$|\mathbf{p}_{ss}|^2 = \frac{a(\rho_0 - \rho_c)}{b} B_\eta \cosh^\eta y \ . \tag{4.42}$$

The density and polarization profiles are plotted in Fig. 26(a),(b). Below the mean-field transition ($\rho_0 < \rho_c$), we recover the isotropic disordered phase ($\rho_{ss} = \rho_0$, $\mathbf{p}_{ss} = \mathbf{0}$).

Linearizing about this steady state, one finds that the equations governing the propagation of sound modes on the catenoid are essentially identical to that on the sphere (Eqs. 4.14, 4.15, and 4.16), but with modified parameters (see Appendix 4.B). As a consequence of the negative curvature, the most important change is that $m = -2\tanh y$ is positive below the neck of the catenoid ($y < 0$) and negative above ($y > 0$), vanishing right at the neck ($y = 0$). This leads to a chiral unidirectional wave of Goldstone mode fluctuations localized at the neck of the catenoid ($\delta\rho = 0$), which

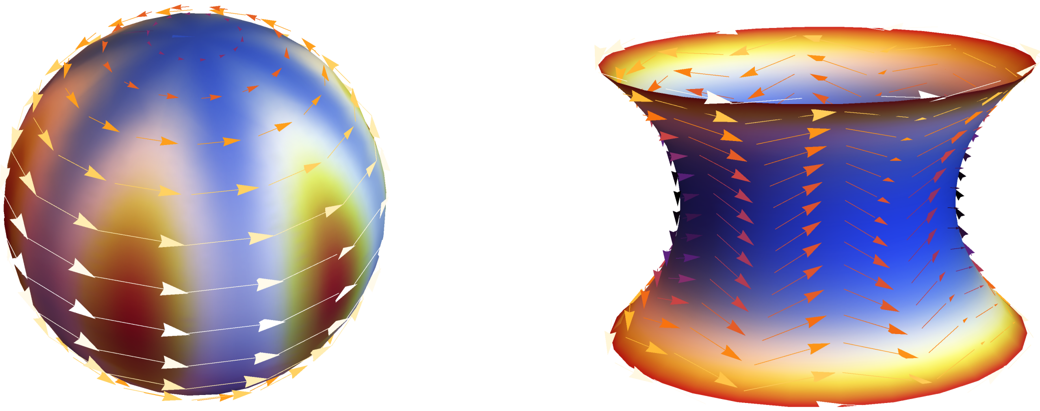

Figure 27 : A representative snapshot of the equatorial density mode on a sphere (Eq. 4.37) and the localized Goldstone mode on the catenoid (Eq. 4.43). For clear visualization we have chosen the perturbation $\mathsf{a}_6, \mathsf{b}_6 = 0.5$ and all other $\mathsf{a}_n, \mathsf{b}_n = 0$ ($n \neq 6$). We have also taken $\eta = 2$ in both cases.

written in the lab frame is given by

$$\mathsf{v}_{\text{edge}}(\varphi, y; t) = \text{sech}^2 y \sum_{n \geq 0} \left[ \mathsf{b}_n \; e^{in(\varphi - c_{||} t)} + \text{c.c.} \right] \; . \tag{4.43}$$

As before, $c_{||} = \lambda p_0$ has to evaluated at the neck of the catenoid ($y = 0$) where the mode is localized, and $\mathsf{b}_n$ are complex coefficients determined by the initial perturbation. A snapshot of this mode is shown as well in Fig. 27. This mode is topologically protected and propagates in the same direction as the flock, but with a different speed ($c_{||}$). The localization length $\ell_{\text{loc}} = R/\sqrt{2}$ is controlled by the scale of the curvature in the system and is seemingly independent of the material parameters of the flock.

## Appendix 4.A Spherical flock: steady state and linearization for $\lambda_2, \lambda_3 \neq 0$

Including the two additional $\lambda_2 \mathbf{p}\boldsymbol{\nabla}\cdot\mathbf{p}$ and $\lambda_3 \boldsymbol{\nabla}|\mathbf{p}|^2$ nonlinearities, the equation for the polarization order parameter is modified to

$$\partial_t p^\mu + \lambda p^\nu \nabla_\nu p^\mu = \left[a(\rho-\rho_c) - b\ g_{\alpha\beta}p^\alpha p^\beta\right] p^\mu + \lambda_2 p^\mu \nabla_\nu p^\nu + \lambda_3 \nabla^\mu (p^\nu p_\nu) - \chi \nabla^\mu \rho \ . \tag{4.44}$$

We don't include the viscous terms $\nu, \nu'$, consistent with our approximations in Sec. 4.2.1. For the azimuthally symmetric ansatz (on the sphere and the catenoid), $\nabla_\mu p^\mu_{ss} = 0$ identically and hence the $\lambda_2$ term does not affect the steady state profile. On the contrary, the $\lambda_3 \boldsymbol{\nabla}|\mathbf{p}|^2$ term acts as an additional polarization dependent contribution to the scalar pressure $P \sim \chi\rho - \lambda_3|\mathbf{p}|^2$, which if large can lead to density and splay instabilities [417]. We shall disregard this instability and only work in the regime where $\lambda_3$ is not large enough to destabilize the entire system. Including it, the steady state equations on the sphere (Eqs. 4.6, 4.7) get modified to

$$\lambda \sin\theta\cos\theta (p^\varphi_{ss})^2 = \frac{\chi}{R^2}\partial_\theta \rho_{ss} - \lambda_3 \partial_\theta(\sin^2\theta (p^\varphi_{ss})^2) \ , \tag{4.45}$$

$$p^\varphi_{ss}\left[a(\rho_{ss}-\rho_c) - 2bR^2\sin^2\theta(p^\varphi_{ss})^2\right] = 0 \ . \tag{4.46}$$

Once again, setting $X(\theta) = \rho_{ss}(\theta) - \rho_c$, we get the same equation as before, only now with a modified coefficient depending on $\lambda_3$.

$$\frac{\mathrm{d}X}{\mathrm{d}\theta} = \frac{\lambda a}{\chi b - a\lambda_3}\cot\theta X \implies X(\theta) = X(\pi/2)\sin^{\eta'}\theta \ , \tag{4.47}$$

with the exponent now changed to $\eta' = \lambda a/(\chi b - a\lambda_3)$. For $\eta' > 0$ (to have a physical density profile), we require $\chi b > a\lambda_3$, which is nothing but a condition to have stable pressure and a positive compressibility. Hence the effect of $\lambda_3 \neq 0$ is to only change the density profile through the $\eta$ exponent, the functional form remaining the same. This is true even for the catenoid where the exponent is the same as on the sphere and given by $\eta' = \lambda a/(\chi b - a\lambda_3)$. Note that this inhomogeneous profile does not exist for an equilbrium polar liquid crystal for which $\lambda = 0$ (but possibly $\lambda_2, \lambda_3 \neq 0$ allowing for spontaneous splay [423]), leading to $\eta' = 0$. Hence the inhomogeneous steady state we obtain is only possible in an active system.

Linearizing about the steady state (on the sphere), now including the $\lambda_2$ and $\lambda_3$ terms, we get

$$\partial_t \delta\rho + \partial_x \mathsf{u} + \partial_y \mathsf{v} = m\ \mathsf{v}\ , \tag{4.48}$$

$$\begin{aligned}\partial_t \mathsf{u} + (c_{||} - \bar{\lambda}_2 - 2\bar{\lambda}_3)\partial_x \mathsf{u} + \frac{\chi}{R^2 \sin^2\theta_0}\partial_x \delta\rho = \\ \alpha\delta\rho - \beta\mathsf{u} + \mathsf{v}\ m\left(c_{||}\frac{\eta' + 2}{2} - \bar{\lambda}_2\right) + \bar{\lambda}_2 \partial_y \mathsf{v}\ ,\end{aligned} \tag{4.49}$$

$$\begin{aligned}\partial_t \mathsf{v} + c_{||}\partial_x \mathsf{u} + \frac{\chi}{R^2}\partial_y \delta\rho = -\left(2c_{||} + (4+\eta')\bar{\lambda}_3\right)\sin^2\theta_0 m\ \mathsf{u} \\ + 2\bar{\lambda}_3 \sin^2\theta_0 \partial_y \mathsf{u}\ .\end{aligned} \tag{4.50}$$

We use the same notation as we used in Sec. 4.2.2 (along with $\bar{\lambda}_{2,3} = \lambda_{2,3} p_0$). At long times ($t \gg \beta^{-1}$), the polarization magnitude $\mathsf{u}$ is still a fast mode and to leading order, it gets slaved to the density fluctuations in the same fashion as before ($\mathsf{u} \simeq \alpha\delta\rho/\beta$). Consistent with the level of approximation stated in Eq. 4.32, the long time and long wavelength dynamics is governed only by the two slow modes $\delta\rho$ and $\mathsf{v}$, with a dynamical matrix $\mathcal{D}(\mathbf{q})$ of the same form as found in the absence of $\lambda_2$ and $\lambda_3$. In a frame comoving with the longitudinal sound speed $c_{||} = \lambda p_0$, we have

$$\mathcal{D}(\mathbf{q}) = \begin{pmatrix} (v_s - c_{||})q_x & q_y + im \\ c_\perp^2 q_y - i\mu m & 0 \end{pmatrix} , \tag{4.51}$$

with $v_s = \alpha/\beta$ as before. The only modification is in the transverse sound speed $c_\perp$ and the coefficient $\mu$, given by

$$c_\perp^2 = \frac{\chi}{R^2} - 2v_s\bar{\lambda}_3 \sin^2\theta_0 = \frac{\chi b - a\lambda_3}{bR^2} , \tag{4.52}$$

$$\mu = v_s(2c_{||} + (4+\eta')\bar{\lambda}_3)\sin^2\theta_0 = [2\lambda + (4+\eta')\lambda_3]\,\frac{a}{2bR^2} . \tag{4.53}$$

It is easy to see now that the profile of the localized equatorial density mode on the sphere, which is $\propto \sin^{\mu/c_\perp^2}\theta$ (for $\lambda_{2,3} = 0$, the exponent coincided with $\eta$ as given in Eq. 4.37) is no longer the same as the steady state density profile of the flock ($\sim \sin^{\eta'}\theta$), when $\lambda_3 \neq 0$.

$$\frac{\mu}{c_\perp^2} = \eta'\left[1 + \left(2 + \frac{\eta'}{2}\right)\frac{\lambda_3}{\lambda}\right] \neq \eta' . \tag{4.54}$$

A similar result also holds true for the catenoid. Hence we find that, even upon including additional nonlinearities of same order as the convective term (but lower order in gradients compared to the viscous terms), all of the qualitative properties of the steady state and the topologically protected modes remains the same, with the only modification being a more detailed dependence of the localization length on some of the material parameters of the system.

## Appendix 4.B Polar flock on the catenoid

For an azimuthally symmetric ordered steady state on the catenoid, just as on the sphere, we neglect the viscous and elastic stresses, and use the ansatz: $\rho = \rho_{ss}(y)$, $p^y = 0$ and $p^\varphi = p^\varphi_{ss}(y)$. Plugging this into the Eqs. 4.1 and 4.3, we find that the continuity equation is satisfied identically and Eq. 4.3 reduces to (for $\nu = 0$)

$$\lambda \tanh y (p^\varphi_{ss})^2 = \frac{\chi}{R^2 \cosh^2 y} \partial_y \rho_{ss} \ , \tag{4.55}$$

$$p^\varphi_{ss} \left[ a(\rho_{ss} - \rho_c) - bR^2 \cosh^2 y (p^\varphi_{ss})^2 \right] = 0 \ . \tag{4.56}$$

Setting $X(y) = \rho_{ss}(y) - \rho_c$, we solve the equations in the same fashion as before to get $\partial_y X = \eta \tanh y X$, where $\eta = \lambda a / b\chi$ (the same exponent as on the sphere). The steady state density profile is then

$$\rho_{ss}(y) = \rho_c + (\rho_{\mathrm{min}} - \rho_c) \cosh^\eta y \ . \tag{4.57}$$

where $\rho_{\mathrm{min}}$ is the minimum density of the flock attained on the neck of the catenoid ($y = 0$). Unlike the sphere, the catenoid is not a compact surface, so in reality one would have a finite sample with boundaries. The mean density $\rho_0$ is given by the spatial average of the steady state profile,

$$\rho_0 = \rho_c + (\rho_{\mathrm{min}} - \rho_c) \langle \cosh^\eta y \rangle \ , \tag{4.58}$$

where $\langle \cdot \rangle$ denotes a spatial average over the entire surface. For a catenoid of height $L$ (Euclidean height in the $z$-direction when embedded in $\mathbb{R}^3$) and radius of curvature $R$

at the minimal neck, we have

$$\langle \cosh^\eta y \rangle \simeq \begin{cases} 1 + \dfrac{\eta}{6}\left(\dfrac{L}{R}\right)^2, & L/R \ll 1 \\ \dfrac{2^{1-\eta}}{2+\eta} e^{\eta L/R}, & L/R \gg 1 \end{cases} . \tag{4.59}$$

Writing $B_\eta = 1/\langle \cosh^\eta y \rangle < 1$, we obtain the density profile quoted in Eq. 4.41.

We expect the viscous and elastic stresses to be less important on a weakly curved surface close to the neck, in particular when the characteristic scale of curvature ($\sim R$) is much greater than the equilibrium correlation length ($\xi \sim \sqrt{\nu/a(\rho_0 - \rho_c)}$). Additionally the density and polarization (along with their gradients) grow larger as we go away from the neck. So close to the boundaries of a large sample, one would have to account for higher order nonlinearities along with the elastic stresses, which would then become important.

### 4.B.1 Linearizing about the steady state

One can perform the same kind of analysis as we did before, for the flock on a sphere. Linearizing about the ordered flock, $\rho = \rho_{ss}(y) + \delta\rho$ and $\mathbf{p} = \mathbf{p}_{ss}(y) + \delta\mathbf{p}$ within the tangent plane at a distance $y_0$ from the $y = 0$ neck, we get (with $x = \varphi$, $\mathsf{u} = \delta p^\varphi$ and $\mathsf{v} = \delta p^y$ just as before)

$$\partial_t \delta\rho + \partial_x \mathsf{u} + \partial_y \mathsf{v} + 2\mathsf{v} \tanh y_0 = 0 \ , \tag{4.60}$$

$$\partial_t \mathsf{u} + \lambda p_0 \partial_x \mathsf{u} + \frac{\chi}{R^2 \cosh^2 y_0} \partial_x \delta\rho$$
$$= p_0 (a\delta\rho - 2bR^2 p_0 \cosh^2 y_0 \ \mathsf{u}) - \mathsf{v} \frac{\lambda p_0 (\eta + 2)}{2} \tanh y_0 \ , \tag{4.61}$$

$$\partial_t \mathsf{v} + \lambda p_0 \partial_x \mathsf{v} + \frac{\chi}{R^2 \cosh^2 y_0} \partial_y \delta\rho = 2\mathsf{u} \lambda p_0 \tanh y_0 \ , \tag{4.62}$$

where $p_0 = p_{ss}^{\varphi}(y_0)$. Galilean boosting to a moving frame $x \to x - \lambda p_0 t$ and relabelling our parameters as before: $c_{||} = \lambda p_0$, $\alpha = a p_0 > 0$, $\beta = 2bR^2 p_0^2 \cosh^2 y_0 > 0$, $c_\perp^2 = \chi/(R^2 \cosh^2 y_0)$ and $m = -2 \tanh y_0$. Having done this, all the arguments used in the case of the sphere apply here as well.

At long time ($t \gg \beta^{-1}$), the fast polarization magnitude $\mathsf{u}$ decays and is slaved to the density field $\mathsf{u} \simeq \alpha \delta\rho/\beta$ (to lowest order) and the slow dynamics at long wavelengths is dominated by

$$\partial_t \delta\rho + \left(v_s - c_{||}\right) \partial_x \delta\rho + \partial_y \mathsf{v} = m \mathsf{v} \ , \tag{4.63}$$

$$\partial_t \mathsf{v} + c_\perp^2 \partial_y \delta\rho = -\frac{1}{2} \eta c_\perp^2 m \ \delta\rho \ . \tag{4.64}$$

Hence at the same level of approximation used earlier for the sphere (neglecting viscous stresses and the parameter regime given in Eq. 4.32), the long time dynamics of sound excitations in a polar flock on a curved surface is generically described by equations of the form given above, or consequently by the linear dynamical matrix $\mathcal{D}(\mathbf{q})$ (Eq. 4.29), possibly upto some irrelevant parameter redefinitions.

As the only modifications are in the definitions of the parameters, many of the predictions made in the case of the sphere apply here too. In particular the sound mode spectrum is still gapped at $\mathbf{q} = \mathbf{0}$ for non-zero $m$ and the bands have a nontrivial topology given by the Chern numbers $C_\pm$ (see Eq. 4.34). As $m = 0$ at the neck of the catenoid ($y = 0$), changing sign on either side, we have one topologically protected mode localized at the neck. A consequence of the negative curvature of the surface is that, in contrast to the sphere, $m < 0$ for $y > 0$. Due to this, the edge mode takes on a different form (in the comoving frame)

$$|\delta\Psi_{\text{edge}}\rangle = \psi_0 e^{\int_0^y m(y')\mathrm{d}y' + iq_x x} \begin{pmatrix} 0 \\ 1 \end{pmatrix} \ . \tag{4.65}$$

Now the edge mode is a localized unidirectional wave of transverse Goldstone mode fluctuations with density fluctuations completely absent. Additionally, the edge mode spectrum is $\omega_{\text{edge}} = 0$ to lowest order in $q_x$ implying that the edge mode is stationary in the comoving (with speed $c_{||}$) frame. This too connects the two bulk bands and is topologically protected. Using $m(y) = -2\tanh y$ for the catenoid, this gives the profile of the localized mode, the lab frame version of which is quoted in Eq. 4.43.

# Chapter 5

# Discussion and conclusion

In this thesis, we have reviewed some recent efforts that extend geometric and topological tools developed for conventional condensed matter to describe metamaterials and active matter. In doing so, we traversed a diverse landscape of phenomena spanning the regimes of classical and quantum physics in both equilibrium and nonequilibrium matter. This ineluctably establishes the power of geometry and topology, let alone their unreasonable effectiveness (paraphrasing Wigner [438]) in distilling the physical nature of a problem.

The first problem we tackled was that of kirigami mechanics. While classical elasticity and continuum mechanics are over two and a half centuries old, they continue to inspire new problems, particularly in the design of mechanical metamaterials. The problem of kirigami mechanics is fairly easy to state *per se*, it is after all just the question of determining the force response of a perforated thin sheet. Yet, in practice, theoretically analyzing this problem is frought with difficulties inherent to thin sheet elasticity and one is forced to resort to a cumbersome case by case numerical treatment. Such an approach though valuable prevents easy access to the general underlying principles of kirigami mechanics that would be essential to developing a conceptual framework that guides kirigami metamaterial design. It is here that a geometric approach provides significant advantage in representing the relevant physics in a tractable and generalizable formulation.

By working within the geometric formulation of elasticity, we propose a useful elastic charge framework to understand kirigami mechanics in thin sheets with perforations. Image elastic charges correspond to fictitious singularities in Gaussian curvature and hence they encapsulate the most important feature of a hole, its geometric incompatibility in the presence of an external load. The image charges are hence geometrically identified to be the relevant physical degrees of freedom in the problem that serve as a convenient variational basis to express the effective mechanics. This basic property underlies the success of the image charge framework. Furthermore, by relating the challenging nonlinear problem of post-buckling mechanics to the simpler pre-buckling computation within the planar problem, we are able to quantitatively test the analytical predictions against experimental measurements through both global and local measures of deformation. Although in all the comparisons presented in Chapter 2 we focused almost exclusively on square frames, the image charge framework is not restricted by the specific simplifications afforded to us by the square hole geometry, and is general enough to handle arbitrary hole shapes as well. In addition, the analogy with electrostatics provides an appealing intuitive picture which now allows us to easily interpret much of the phenomenology of buckled frames and kirigami in general.

One of the interesting characteristics of these stress-induced image charges is that they can fractionalize into partial disclinations within a hole with sharp corners. As this behaviour is intimately linked to the shape of the hole, one promptly realizes that the geometry and topology of the prescribed kirigami design can be used to preferentially pattern, on demand, both the positions and orientations of image charges. This has immediate functionality as a design principle for kirigami structures as image charges characterize the propensity of a hole to generate or screen (upon buckling) local stresses. In recent years, there has been a lot of interest in using geometry to program and control 3D shapes and morphologies in origami [168] and kirigami [181, 189, 439] materials. We envision that the mechanics of more elaborate kirigami structures under stress can profitably be thought of as a problem of interacting elastic charges. This perspective then provides a powerful organizational framework to think about the mechanics of kirigami metamaterials. As a small illustration of this point, we tackle the simple problem of designing an appropriate kirigami pattern to permit the flattening of a cone without wrinkling. The inclusion of interactions between charges furnishes a systematic procedure to predict such a pattern affirming the method's usefulness. It also suggests that our framework can advise possible design strategies to pattern kirigami metamaterials with engineered pathways to locally relax elastic stresses.

A very promising direction for future work in this field is the inclusion of thermal effects on such metamaterials. Strain engineering 2D materials such as graphene [440–443] has emerged as an exciting platform to manipulate electronic states, in addition to providing controlled routes to spontaneously generate complex 3D structures [150, 444]. In order to employ kirigami techniques on such small scales as appropriate for NEMS and MEMS [444] requires an understanding of thermal fluctuations and how they affect both form and functionality of kirigami devices. As is well known, thermal fluctuations have a strong impact on the physics of intact elastic membranes resulting in a dramatic size and geometry dependent scale-up of the flexural rigidity [99, 150, 445–447]. The effect of holes and slits on the renormalization of the bending rigidity and the thermal crumpling transition remains largely unexplored. Recent numerical simulations [448] show that the crumpling transition temperature can be tuned by the geometry of a periodic kirigami pattern, while isolated slits in ribbons can counterintuitively stiffen the system [449]. Such varied and unexpected effects suggest that the interplay of thermal fluctuations, geometry and topology in kirigami structures will provide new avenues for breakthroughs in both fundamental and applied aspects of designer metamaterials.

Until now, we only discussed passive materials. Shifting focus to active matter, we examine how topology may impact nonequilibrium physics. Topology provides us with novel though sometimes unconventional tools to characterize and understand physical phenomena. Although topological defects are the oldest features of a material that have a topological description, they continue to provide fertile new avenues for exploration. Topological disclinations that dominate the physics of a 2D nematic liquid crystal, turn out to be all the more important when active. The nonequilibrium active drive elevates the geometry and structure of the $+1/2$ disclination to a dynamical variable, endowing the topological defect with additional internal degrees of freedom that govern its properties. The spontaneous motility of $+1/2$ disclinations is a remarkable consequence of activity which, in competition with noise, can lead to a nonequilibrium variant of the BKT transition in active nematics. The nature of defect mediated phase transitions in far from equilibrium settings has been a long standing open question. While the equilibrium BKT universality class primarily distinguishes only disclinations (*scalar* Coulomb gases) from dislocations (*vector* Coulomb gases)[1], its broad phenomenology is essentially the same in all equilibrium systems. In contrast, given the great plurality of nonequilibrium driving, defect mediated phase transitions in active and driven matter are expected to have many more diverse possibilities.

---

[1] The difference in the two classes arises because dislocations permit neutral configurations with an odd number of defects when allowed by the underlying lattice, but point defects can only occur in pairs to enforce neutrality [33, 35, 450]. The correlation length diverges in the same essential fashion in both cases $\xi \propto e^{\mathrm{const.}(T-T_c)^{-\nu}}$, with $\nu = 1/2$ for scalar defects [13, 29], while for vector defects, $\nu$ carries an additional nonuniversal dependence on angular terms in the energy [450], ranging between $0.3696\cdots \leq \nu \leq 0.4$.

Our treatment of active defects follows a long tradition of considering defects as particles with effective interactions. We also develop a systematic derivation of the reduced equations for defect dynamics by perturbatively solving for a singular solution of the *continuum* hydrodynamic equations for an active nematic. An important point is that, by construction, our theoretical framework, though based entirely on dynamics, smoothly recovers the known equilibrium static results when activity is turned off. This is a crucial requirement and ensures the derived equations are well founded and not *ad hoc*. Through a Fokker-Planck treatment of an isolated neutral defect pair, we predict the phase boundary beyond which defects unbind in a motile BKT transition, leading to spatio-temporal defect chaos. Although the defect unbound phase is disordered in that the nematic order parameter vanishes, it is in fact *not* a conventional isotropic fluid. Defect motility generates finite currents even at steady state, breaking detailed balance through the swirling motion of unbound defect pairs[2]. This motivates the name for the universality class of this phase transition - motile BKT, as it separates a quiescent yet fluctuating ordered active nematic from an isotropic liquid with chaotic flows and finite entropy production rate. The motile BKT scenario can also be mapped onto a two temperature Coulomb gas model, defining a unique universality class distinct from other nonequilibrium defect mediated transitions that have been recently considered elsewhere. A prominent class to contrast against is that of defect unbinding in the 2D *compact* Kardar-Parisi-Zhang (KPZ) [451, 452] equation that is expected to describe spiral turbulence in pattern forming systems [453, 454], 2D driven dissipative superfluids or exciton-polariton condensates [455–458] and also the melting of driven vortex lattices in disordered superconducting films [459]. Here the KPZ nonlinearity [460] breaks detailed balance and topological defects are found to always proliferate at any temperature. An anisotropic version of the same model

---

[2] Shankar *et al.*, in preparation.

(also related to 2D active smectics [461, 462]) permits a stable ordered phase with a finite temperature vortex unbinding transition [463]. Vortices in these compact KPZ models do not lead to large scale spontaneous flows upon unbinding, vastly distinct from the motile BKT scenario. Different from all the above, recent numerical work [464] on a 2D XY model driven by correlated noise was shown to map onto an effective equilibrium system, with the transition occuring at the equilibrium BKT point in the thermodynamic limit. It is an open question if the newly identified motile BKT class applies to other active systems that perhaps also contain similar excitations such as active dislocations [465, 466] in the melting of active crystals [467].

Increasing activity well beyond the defect unbinding threshold leads to another remarkable transition in the 2D active nematic. The active torques that orient the +1/2 disclinations, when strong enough, can lead to spontaneous condensation of the motile +1/2 defects into a *polar* collectively moving liquid[3]. The appearance of a defect ordered polar flock has only been reported in numerical simulations [377, 468, 469], but our theoretical model naturally explains it through the active torques on defects. Unlike the Abrikosov vortex lattice in Type II superconducting films [470], the alignment of +1/2 defects gives rise to a novel spontaneously flowing defect ordered *liquid* that forces the underlying nematic to develop periodic kink-wall distortions, breaking translational symmetry as well. Having uncovered a wealth of phenomena in active nematics, it is immediately clear that defects play a central role in governing the properties and response of this mesoscopic phase. Furthermore, our particle model for active defect dynamics may be easily extended to achieve both targeted response and directed transport in living matter. Defects have already been used as intrinsic micro-rheological tracers of the active nematic flow field [349] and their chaotic motion can be rectified through confinement [275, 368, 471–475]. In addition, recent works have emphasized the role of active topological defects in the biological context. Disclinations in cellular monolayers viewed as active nematics have been suggested to provide preferential sites for biological functionalization [259] and apoptosis [260], or drive expansion in growing bacterial colonies [476–478]. A quantitative description of these diverse features is incumbent on a comprehensive theory of active defects, as the one we have systematically developed here. Finally, we note that, defects on textured passive colloids can be chemically functionalized [479] opening doors to the design of supra-molecular chemistry [480]. Making such functionalized defects active paves the way to unexplored engineering possibilities, such as the directed self-assembly of active and adaptive metamaterials.

---

[3] Shankar and Marchetti, in preparation.

We now move on to the active polar fluid. Unlike the rather standard case of topological defects in ordered media, here topology enters through reciprocal space via an analogy to quantum Hall systems and topological insulators. The active polar fluid is peculiar as the polarization order parameter is also a velocity that advects the fluid around [218], with this dual role being at the heart of many of the phenomena we have explored in Chapter 4. In particular, unlike a superfluid film on a curved substrate (where the order parameter can be parallel transported trivially) [481], the fact that the order parameter of the flock is a physical velocity implies that it advects itself nontrivially in the presence of curvature. This is nothing but a restatement of the physical fact that self-propelled particles move persistently along geodesics (in the absence of interactions), which get "lensed" by curvature, whereas passive polar particles don't do any such thing. While the frustration associated with the interplay of curvature and order has been previously explored extensively in passive matter [92, 482], the presence of activity adds an entirely new nonequilibrium dimension to the whole story, allowing for completely new physics arising from competing order, curvature and the active drive.

Having generalized the Toner-Tu model for an active polar fluid to an arbitrary curved surface, the continuum model now affords us the privilege of having predictions independent of microscopic details. We find many of the features of the steady ordered state of a polar flock are in fact, quite generic, with positive curvature surfaces having density profiles with a maximum, decreasing on either side of the peak, while negative curvature surfaces have density profiles of the opposite kind, being minimal in the interior and increasing towards the boundary. This is entirely due to the fact that geodesics converge or diverge depending on whether the Gaussian curvature is positive or negative, respectively. Finding such spatially *in*homogeneous exact solutions to the covariant Toner-Tu model provides a crucial starting point to being able to understand how the phenomenology of active matter in flat space translates to its curved variants.

In addition to the steady state with spontaneous flow, flocks in flat space also have dissipative sound modes with a linear (but angle dependent) dispersion [411]. It is here that all three players: curvature, order and activity come together with dramatic consequences. The presence of curvature gaps the sound mode spectrum at long wavelengths leading to a band structure with nontrivial topology protected by the broken time-reversal and Galilean symmetry in the system. We demonstrate this by computing the Chern number for the bands and show that this is a generic feature of flocks on curved surfaces. The most interesting and exotic consequence the nontrivial band topology has, is to localize "edge" modes of density or Goldstone mode fluctuations along special geodesics on the surface, where the gap in the sound spectrum vanishes. The rather novel feature here is that the system is not artificially engineered as a metamaterial with some underlying lattice structure [226, 307], nor does it require any external forcing or fields of any kind [74]. The spontaneous flow is generated by activity, breaking both time-reversal and Galilean invariance simultaneously, while curvature is responsible for the spectral gap in the ordered phase.

Topological excitations of the type described here are “protected” in the sense that they are immune to backscattering by static perturbations and heterogeneities in the medium through which they propagate, providing unidirectional channels for information transport, robust against disorder. While quantifying the limits of such topological protection in active systems will require more detailed numerical and theoretical work that remains to be explored, our work demonstrating that such topologically protected propagating modes are a *generic* consequence of active flows on curved surfaces raises the question of whether nature may use this mechanism to guide and direct the robust transmission of intercellular physical forces in curved environments. It is therefore tempting to offer some speculation to the possible relevance of our findings to biology.

In a number of developmental phenomena, from wound healing to morphogenesis and organ development, living cells migrate collectively, offering an intriguing realization of a polar active fluid. While a full understanding of the mechanisms that regulate collective cell migration is still out of reach, it is now widely recognized that the transmission of physical forces plays an important role, alongside biochemical signalling. For instance, propagating mechanical waves have been shown to mediate cooperative force transmission among epithelial cells in wound healing assays [483]. In many biological processes cellular motion takes place on curved surfaces, as in cell renewal and repair in the highly folded intestine [484] and the shaping of the early limb bud in developing embryos [485]. The effect of curvature on the dynamics of epithelial cells is beginning to be explored *in vitro* by examining collective cell migration on cylindrical capillaries of varying radii [400]. While cylinders have zero Gaussian curvature which would not yield topologically protected states, these experiments clearly demonstrate that curvature affects cell morphology and dynamics by enhancing cell speed and cell extrusion. Recent theoretical work also predicts that certain stochastic reaction networks may support novel topological states that might play a role in the fault-tolerance of some biochemical processes [486], suggesting that topological phenomena in non-equilibrium and biological systems may be more general than previously expected.

A more direct application of the work described here would be to a polar version of the active nematic vesicles reported in Ref. [274]. Here active vesicles were engineered by confining an active suspension of microtubule-kinesin bundles to the surface of a lipid vesicle. The interplay of activity and curvature yields a number of dynamical structures, including spontaneously oscillating defect textures and folding nematic bands, and ultimately activity-driven shape deformations of the vesicle. Our work may also be relevant to the physics of cell membranes that are activated through coupling to the polymerizing acto-myosin cortex, as modeled in recent work by Maitra et al. [409]. Finally, in the spirit of colloidal crystals on curved interfaces [94, 95] and reconstituted active systems [272–274], one might also envision synthetic experimental realizations of the topological sound modes investigated here, by depositing active Janus colloidal particles [224] or active bio-filament motor complexes [273] on the surface of a droplet or a vesicle shell.

# Bibliography

[1] LD Landau. On the theory of phase transitions. *Zh. Eksp. Teor. Fiz.*, 7:19–32, 1937. [Ukr. J. Phys.53,25(2008)].

[2] VL Ginzburg and LD Landau. On the theory of superconductivity. *Zh. Eksp. Teor. Fiz.*, 20:1064–1082, 1950.

[3] LD Landau, EM Lifshitz, and LP Pitaevskii. *Statistical Physics, Part I, Butterworth Heinemann*. Oxford, 1981.

[4] Kenneth G Wilson and John Kogut. The renormalization group and the $\epsilon$ expansion. *Physics Reports*, 12(2):75–199, 1974.

[5] Kenneth G Wilson. The renormalization group: Critical phenomena and the kondo problem. *Reviews of modern physics*, 47(4):773, 1975.

[6] N David Mermin and Herbert Wagner. Absence of ferromagnetism or antiferromagnetism in one-or two-dimensional isotropic heisenberg models. *Physical Review Letters*, 17(22):1133, 1966.

[7] Pierre C Hohenberg. Existence of long-range order in one and two dimensions. *Physical Review*, 158(2):383, 1967.

[8] N David Mermin. Crystalline order in two dimensions. *Physical Review*, 176(1): 250, 1968.

[9] Sidney Coleman. There are no goldstone bosons in two dimensions. *Communications in Mathematical Physics*, 31(4):259–264, 1973.

[10] VL Berezinskii. Destruction of long-range order in one-dimensional and two-dimensional systems having a continuous symmetry group i. classical systems. *Soviet Journal of Experimental and Theoretical Physics*, 32:493, 1971. [ZhETF 59, 907 (1971)].

[11] VL Berezinskii. Destruction of long-range order in one-dimensional and two-dimensional systems possessing a continuous symmetry group ii. quantum systems. *Soviet Journal of Experimental and Theoretical Physics*, 34:610, 1972. [ZhETF 61, 1144 (1972)].

[12] John Michael Kosterlitz and David James Thouless. Ordering, metastability and phase transitions in two-dimensional systems. *Journal of Physics C: Solid State Physics*, 6(7):1181, 1973.

[13] JM Kosterlitz. The critical properties of the two-dimensional xy model. *Journal of Physics C: Solid State Physics*, 7(6):1046, 1974.

[14] Vito Volterra. Sur l'équilibre des corps élastiques multiplement connexes. In *Annales scientifiques de l'École normale supérieure*, volume 24, pages 401–517, 1907.

[15] Geoffrey Ingram Taylor. The mechanism of plastic deformation of crystals. part i.theoretical. *Proc. R. Soc. Lond. A*, 145(855):362–387, 1934.

[16] Frank RN Nabarro. *Theory of crystal dislocations*. Clarendon Pr., 1967.

[17] Georges Friedel. Les états mésomorphes de la matière. In *Annales de physique*, volume 9, pages 273–474, 1922.

[18] Maurice Kléman. Defects in liquid crystals. *Reports on Progress in Physics*, 52 (5):555, 1989.

[19] Mikio Nakahara. *Geometry, topology and physics.* Taylor & Francis, 2003.

[20] N David Mermin. The topological theory of defects in ordered media. *Reviews of Modern Physics*, 51(3):591, 1979.

[21] Gareth P Alexander, Bryan Gin-ge Chen, Elisabetta A Matsumoto, and Randall D Kamien. Colloquium: Disclination loops, point defects, and all that in nematic liquid crystals. *Reviews of Modern Physics*, 84(2):497, 2012.

[22] V Poénaru. Some aspects of the theory of defects of ordered media and gauge fields related to foliations. *Communications in mathematical physics*, 80(1): 127–136, 1981.

[23] H-R Trebin. The topology of non-uniform media in condensed matter physics. *Advances in Physics*, 31(3):195–254, 1982.

[24] Bryan Gin-ge Chen, Gareth P Alexander, and Randall D Kamien. Symmetry breaking in smectics and surface models of their singularities. *Proceedings of the National Academy of Sciences*, 106(37):15577–15582, 2009.

[25] Raz Kupferman, Michael Moshe, and Jake P Solomon. Metric description of singular defects in isotropic materials. *Archive for Rational Mechanics and Analysis*, 216(3):1009–1047, 2015.

[26] DJ Bishop and JD Reppy. Study of the superfluid transition in two-dimensional He 4 films. *Physical Review Letters*, 40(26):1727, 1978.

[27] K Epstein, AM Goldman, and AM Kadin. Vortex-antivortex pair dissociation in two-dimensional superconductors. *Physical Review Letters*, 47(7):534, 1981.

[28] DJ Resnick, JC Garland, JT Boyd, S Shoemaker, and RS Newrock. Kosterlitz-thouless transition in proximity-coupled superconducting arrays. *Physical Review Letters*, 47(21):1542, 1981.

[29] Jorge V José, Leo P Kadanoff, Scott Kirkpatrick, and David R Nelson. Renormalization, vortices, and symmetry-breaking perturbations in the two-dimensional planar model. *Physical Review B*, 16(3):1217, 1977.

[30] Daniel J Amit, Yadin Y Goldschmidt, and S Grinstein. Renormalisation group analysis of the phase transition in the 2d coulomb gas, sine-gordon theory and xy-model. *Journal of Physics A: Mathematical and General*, 13(2):585, 1980.

[31] Yan Levin, Xiao-jun Li, and Michael E Fisher. Coulombic criticality in general dimensions. *Physical review letters*, 73(20):2716, 1994.

[32] ST Chui and JD Weeks. Phase transition in the two-dimensional coulomb gas, and the interfacial roughening transition. *Physical Review B*, 14(11):4978, 1976.

[33] David R Nelson. Study of melting in two dimensions. *Physical Review B*, 18(5):2318, 1978.

[34] BI Halperin and David R Nelson. Theory of two-dimensional melting. *Physical Review Letters*, 41(2):121, 1978.

[35] David R Nelson and BI Halperin. Dislocation-mediated melting in two dimensions. *Physical Review B*, 19(5):2457, 1979.

[36] Klaus Zahn, R Lenke, and Georg Maret. Two-stage melting of paramagnetic colloidal crystals in two dimensions. *Physical review letters*, 82(13):2721, 1999.

[37] Alice L Thorneywork, Joshua L Abbott, Dirk GAL Aarts, and Roel PA Dullens. Two-dimensional melting of colloidal hard spheres. *Physical review letters*, 118 (15):158001, 2017.

[38] Etienne P Bernard and Werner Krauth. Two-step melting in two dimensions: First-order liquid-hexatic transition. *Physical review letters*, 107(15):155704, 2011.

[39] J Michael Kosterlitz. Kosterlitz–thouless physics: a review of key issues. *Reports on Progress in Physics*, 79(2):026001, 2016.

[40] Alexander M Polyakov. Compact gauge fields and the infrared catastrophe. In *Instantons In Gauge Theories*, pages 19–21. World Scientific, 1994.

[41] Alexander M Polyakov. Quark confinement and topology of gauge theories. *Nuclear Physics B*, 120(3):429–458, 1977.

[42] Edward Witten. Chiral symmetry, the 1/n expansion and the su (n) thirring model. *Nuclear Physics B*, 145(1):110–118, 1978.

[43] T Senthil, Ashvin Vishwanath, Leon Balents, Subir Sachdev, and Matthew PA Fisher. Deconfined quantum critical points. *Science*, 303(5663):1490–1494, 2004.

[44] T Senthil, Leon Balents, Subir Sachdev, Ashvin Vishwanath, and Matthew PA Fisher. Quantum criticality beyond the landau-ginzburg-wilson paradigm. *Physical Review B*, 70(14):144407, 2004.

[45] K v Klitzing, Gerhard Dorda, and Michael Pepper. New method for high-accuracy determination of the fine-structure constant based on quantized hall resistance. *Physical Review Letters*, 45(6):494, 1980.

[46] Robert B Laughlin. Quantized hall conductivity in two dimensions. *Physical Review B*, 23(10):5632, 1981.

[47] DJ Thouless, Mahito Kohmoto, MP Nightingale, and M Den Nijs. Quantized hall conductance in a two-dimensional periodic potential. *Physical Review Letters*, 49(6):405, 1982.

[48] Barry Simon. Holonomy, the quantum adiabatic theorem, and berry's phase. *Physical Review Letters*, 51(24):2167, 1983.

[49] JE Avron, R Seiler, and B Simon. Homotopy and quantization in condensed matter physics. *Physical review letters*, 51(1):51, 1983.

[50] Mahito Kohmoto. Topological invariant and the quantization of the hall conductance. *Annals of Physics*, 160(2):343–354, 1985.

[51] Qian Niu, DJ Thouless, and Yong-Shi Wu. Quantized hall conductance as a topological invariant. *Physical Review B*, 31(6):3372, 1985.

[52] F Duncan M Haldane. Model for a quantum hall effect without landau levels: Condensed-matter realization of the "parity anomaly". *Physical Review Letters*, 61(18):2015, 1988.

[53] M Zahid Hasan and Charles L Kane. Colloquium: topological insulators. *Reviews of Modern Physics*, 82(4):3045, 2010.

[54] Walter Kohn. Theory of the insulating state. *Physical Review*, 133(1A):A171, 1964.

[55] Bertrand I Halperin. Quantized hall conductance, current-carrying edge states, and the existence of extended states in a two-dimensional disordered potential. *Physical Review B*, 25(4):2185, 1982.

[56] Joel E Moore. The birth of topological insulators. *Nature*, 464(7286):194, 2010.

[57] Seongshik Oh. The complete quantum hall trio. *Science*, 340(6129):153–154, 2013.

[58] Charles L Kane and Eugene J Mele. Quantum spin hall effect in graphene. *Physical review letters*, 95(22):226801, 2005.

[59] Charles L Kane and Eugene J Mele. Z 2 topological order and the quantum spin hall effect. *Physical review letters*, 95(14):146802, 2005.

[60] B Andrei Bernevig, Taylor L Hughes, and Shou-Cheng Zhang. Quantum spin hall effect and topological phase transition in hgte quantum wells. *Science*, 314 (5806):1757–1761, 2006.

[61] Liang Fu, Charles L Kane, and Eugene J Mele. Topological insulators in three dimensions. *Physical review letters*, 98(10):106803, 2007.

[62] Joel E Moore and Leon Balents. Topological invariants of time-reversal-invariant band structures. *Physical Review B*, 75(12):121306, 2007.

[63] Xiangang Wan, Ari M Turner, Ashvin Vishwanath, and Sergey Y Savrasov. Topological semimetal and fermi-arc surface states in the electronic structure of pyrochlore iridates. *Physical Review B*, 83(20):205101, 2011.

[64] Alexander Altland and Martin R Zirnbauer. Nonstandard symmetry classes in mesoscopic normal-superconducting hybrid structures. *Physical Review B*, 55 (2):1142, 1997.

[65] Alexei Kitaev. Periodic table for topological insulators and superconductors. In *AIP Conference Proceedings*, volume 1134, pages 22–30. AIP, 2009.

[66] Xiao-Liang Qi and Shou-Cheng Zhang. Topological insulators and superconductors. *Reviews of Modern Physics*, 83(4):1057, 2011.

[67] T Senthil. Symmetry-protected topological phases of quantum matter. *Annu. Rev. Condens. Matter Phys.*, 6(1):299–324, 2015.

[68] Xiao-Gang Wen. Topological orders and edge excitations in fractional quantum hall states. *Advances in Physics*, 44(5):405–473, 1995.

[69] Daniel C Tsui, Horst L Stormer, and Arthur C Gossard. Two-dimensional magnetotransport in the extreme quantum limit. *Physical Review Letters*, 48 (22):1559, 1982.

[70] Robert B Laughlin. Anomalous quantum hall effect: an incompressible quantum fluid with fractionally charged excitations. *Physical Review Letters*, 50(18):1395, 1983.

[71] FDM Haldane and S Raghu. Possible realization of directional optical waveguides in photonic crystals with broken time-reversal symmetry. *Physical review letters*, 100(1):013904, 2008.

[72] S Raghu and FDM Haldane. Analogs of quantum-hall-effect edge states in photonic crystals. *Physical Review A*, 78(3):033834, 2008.

[73] Ling Lu, John D Joannopoulos, and Marin Soljačić. Topological photonics. *Nature Photonics*, 8(11):821, 2014.

[74] Zhaoju Yang, Fei Gao, Xihang Shi, Xiao Lin, Zhen Gao, Yidong Chong, and Baile Zhang. Topological acoustics. *Physical review letters*, 114(11):114301, 2015.

[75] Xiujuan Zhang, Meng Xiao, Ying Cheng, Ming-Hui Lu, and Johan Christensen. Topological sound. *Communications Physics*, 1(1):97, 2018.

[76] Emil Prodan and Camelia Prodan. Topological phonon modes and their role in dynamic instability of microtubules. *Physical review letters*, 103(24):248101, 2009.

[77] CL Kane and TC Lubensky. Topological boundary modes in isostatic lattices. *Nature Physics*, 10(1):39–45, 2014.

[78] Sebastian D Huber. Topological mechanics. *Nature Physics*, 12(7):621, 2016.

[79] Xiaoming Mao and Tom C Lubensky. Maxwell lattices and topological mechanics. *Annual Review of Condensed Matter Physics*, 9:413–433, 2018.

[80] Alexander B Khanikaev and Gennady Shvets. Two-dimensional topological photonics. *Nature Photonics*, 11(12):763, 2017.

[81] The nobel prize in physics 2016. nobelprize.org. nobel media ab 2018. mon. 22 oct 2018. URL `https://www.nobelprize.org/prizes/physics/2016/summary/`.

[82] Mark Kac. Can one hear the shape of a drum? *The american mathematical monthly*, 73(4):1–23, 1966.

[83] G Toulouse. Theory of the frustration effect in spin glasses: I. *Spin Glass Theory and Beyond: An Introduction to the Replica Method and Its Applications*, 9:99, 1987.

[84] J Vannimenus and G Toulouse. Theory of the frustration effect. ii. ising spins on a square lattice. *Journal of Physics C: Solid State Physics*, 10(18):L537, 1977.

[85] JD Bernal. Geometry of the structure of monatomic liquids. *Nature*, 185(4706): 68, 1960.

[86] JL Finney. Random packings and the structure of simple liquids. i. the geometry of random close packing. *Proceedings of the Royal Society of London. A. Mathematical and Physical Sciences*, 319(1539):479–493, 1970.

[87] JD Bernal and JL Finney. Random close-packed hard-sphere model. ii. geometry of random packing of hard spheres. *Discussions of the Faraday Society*, 43:62–69, 1967.

[88] JL Finney and JD Bernal. Random close packing and the heats of fusion of simple liquids. *Nature*, 213(5081):1079, 1967.

[89] Manfredo Perdigao do Carmo Valero. *Riemannian geometry*. Prentice-Hall, 1992.

[90] Mark J Bowick and Luca Giomi. Two-dimensional matter: order, curvature and defects. *Advances in Physics*, 58(5):449–563, 2009.

[91] Ari M Turner, Vincenzo Vitelli, and David R Nelson. Vortices on curved surfaces. *Reviews of Modern Physics*, 82(2):1301, 2010.

[92] David R Nelson. *Defects and geometry in condensed matter physics*. Cambridge University Press, 2002.

[93] Mark J Bowick, David R Nelson, and Alex Travesset. Interacting topological defects on frozen topographies. *Physical Review B*, 62(13):8738, 2000.

[94] AR Bausch, MJ Bowick, A Cacciuto, AD Dinsmore, MF Hsu, DR Nelson, MG Nikolaides, A Travesset, and DA Weitz. Grain boundary scars and spherical crystallography. *Science*, 299(5613):1716–1718, 2003.

[95] William TM Irvine, Vincenzo Vitelli, and Paul M Chaikin. Pleats in crystals on curved surfaces. *Nature*, 468(7326):947–951, 2010.

[96] Mark J Bowick and Zhenwei Yao. Crystalline order on catenoidal capillary bridges. *EPL (Europhysics Letters)*, 93(3):36001, 2011.

[97] Enrique Bendito, Mark J Bowick, Agustin Medina, and Zhenwei Yao. Crystalline particle packings on constant mean curvature (delaunay) surfaces. *Physical Review E*, 88(1):012405, 2013.

[98] Vinothan N Manoharan. Colloidal matter: Packing, geometry, and entropy. *Science*, 349(6251):1253751, 2015.

[99] DR Nelson and L Peliti. Fluctuations in membranes with crystalline and hexatic order. *Journal de Physique*, 48(7):1085–1092, 1987.

[100] HS Seung and David R Nelson. Defects in flexible membranes with crystalline order. *Physical Review A*, 38(2):1005, 1988.

[101] Xiangjun Xing, Homin Shin, Mark J Bowick, Zhenwei Yao, Lin Jia, and Min-Hui Li. Morphology of nematic and smectic vesicles. *Proceedings of the National Academy of Sciences*, 109(14):5202–5206, 2012.

[102] N Ramakrishnan, John H Ipsen, and PB Sunil Kumar. Role of disclinations in determining the morphology of deformable fluid interfaces. *Soft Matter*, 8(11): 3058–3061, 2012.

[103] David R Nelson. Liquids and glasses in spaces of incommensurate curvature. *Physical Review Letters*, 50(13):982, 1983.

[104] Carl D Modes and Randall D Kamien. Hard disks on the hyperbolic plane. *Physical review letters*, 99(23):235701, 2007.

[105] Pierre-Gilles De Gennes. *Scaling concepts in polymer physics.* Cornell university press, 1979.

[106] David R Nelson, Tsvi Piran, and Steven Weinberg. *Statistical mechanics of membranes and surfaces.* World Scientific, 2004.

[107] MB Green, JH Schwarz, and E Witten. Superstring theory, vols i and ii, 1987.

[108] David J Gross, Tsvi Piran, and Steven Weinberg. *Two dimensional quantum gravity and random surfaces.* World Scientific, 1991.

[109] François David, Paul Ginsparg, and Jean Zinn-Justin. *Fluctuating geometries in statistical mechanics and field theory.* Elsevier-North-Holland, Amsterdam, 1996.

[110] Mark J Bowick and Alex Travesset. The statistical mechanics of membranes. *Physics Reports*, 344(4):255–308, 2001.

[111] A Polyakov. Fine structure of strings. *Nuclear Physics B*, 268(2):406–412, 1986.

[112] Georg Frobenius. Ueber das pfaffsche problem. *Journal für die reine und angewandte Mathematik*, 82:230–315, 1877.

[113] Joseph A Aronovitz and Tom C Lubensky. Fluctuations of solid membranes. *Physical review letters*, 60(25):2634, 1988.

[114] Maya Paczuski, Mehran Kardar, and David R Nelson. Landau theory of the crumpling transition. *Physical review letters*, 60(25):2638, 1988.

[115] François David and E Guitter. Crumpling transition in elastic membranes: renormalization group treatment. *EPL (Europhysics Letters)*, 5(8):709, 1988.

[116] Maya Paczuski and Mehran Kardar. Renormalization-group analysis of the crumpling transition in large d. *Physical Review A*, 39(11):6086, 1989.

[117] Joseph Aronovitz, Leonardo Golubovic, and TC Lubensky. Fluctuations and lower critical dimensions of crystalline membranes. *Journal de Physique*, 50(6): 609–631, 1989.

[118] Pierre Le Doussal and Leo Radzihovsky. Self-consistent theory of polymerized membranes. *Physical review letters*, 69(8):1209, 1992.

[119] E Guitter, F David, S Leibler, and L Peliti. Thermodynamical behavior of polymerized membranes. *Journal de Physique*, 50(14):1787–1819, 1989.

[120] E Guitter, F David, S Leibler, and L Peliti. Crumpling and buckling transitions in polymerized membranes. *Physical review letters*, 61(26):2949, 1988.

[121] Farid F Abraham and David R Nelson. Fluctuations in the flat and collapsed phases of polymerized membranes. *Journal de Physique*, 51(23):2653–2672, 1990.

[122] Mark J Bowick, Angelo Cacciuto, Gudmar Thorleifsson, and Alex Travesset. Universality classes of self-avoiding fixed-connectivity membranes. *The European Physical Journal E*, 5(2):149–160, 2001.

[123] Mark J Bowick, Simon M Catterall, Marco Falcioni, Gudmar Thorleifsson, and Konstantinos N Anagnostopoulos. The flat phase of crystalline membranes. *Journal de Physique I*, 6(10):1321–1345, 1996.

[124] Lev D Landau and EM Lifshitz. *Theory of Elasticity,*, volume 3. Elsevier, New York, 1986.

[125] Basile Audoly and Yves Pomeau. *Elasticity and geometry: from hair curls to the non-linear response of shells*. Oxford University Press, 2010.

[126] E. Cerda, K. Ravi-Chandar, and L. Mahadevan. Thin films - wrinkling of an elastic sheet under tension. *Nature*, 419:579–580, 2002.

[127] E. Cerda and L. Mahadevan. Geometry and physics of wrinkling. *Phys. Rev. Lett.*, 90:074302, 2003.

[128] Hunter King, Robert D Schroll, Benny Davidovitch, and Narayanan Menon. Elastic sheet on a liquid drop reveals wrinkling and crumpling as distinct symmetry-breaking instabilities. *Proceedings of the National Academy of Sciences*, 109(25):9716–9720, 2012.

[129] M Ben Amar and Y Pomeau. Crumpled paper. *Proceedings of the Royal Society of London. Series A: Mathematical, Physical and Engineering Sciences*, 453 (1959):729–755, 1997.

[130] Luka Pocivavsek, Robert Dellsy, Andrew Kern, Sebastián Johnson, Binhua Lin, Ka Yee C Lee, and Enrique Cerda. Stress and fold localization in thin elastic membranes. *Science*, 320(5878):912–916, 2008.

[131] Thomas A Witten. Stress focusing in elastic sheets. *Reviews of Modern Physics*, 79(2):643, 2007.

[132] Sharon Eran, Michael Marder, and Harry L Swinney. Leaves, flowers and garbage bags: making waves. *American Scientist*, 92(3):254, 2004.

[133] Jan Genzer and Jan Groenewold. Soft matter with hard skin: From skin wrinkles to templating and material characterization. *Soft Matter*, 2(4):310–323, 2006.

[134] Bo Li, Yan-Ping Cao, Xi-Qiao Feng, and Huajian Gao. Mechanics of morphological instabilities and surface wrinkling in soft materials: a review. *Soft Matter*, 8 (21):5728–5745, 2012.

[135] Pedro M Reis, Heinrich M Jaeger, and Martin van Hecke. Designer matter: A perspective. *Extreme Mechanics Letters*, 5:25–29, 2015.

[136] Katia Bertoldi, Vincenzo Vitelli, Johan Christensen, and Martin van Hecke. Flexible mechanical metamaterials. *Nature Reviews Materials*, 2(11):17066, 2017.

[137] Xianglong Yu, Ji Zhou, Haiyi Liang, Zhengyi Jiang, and Lingling Wu. Mechanical metamaterials associated with stiffness, rigidity and compressibility: A brief review. *Progress in Materials Science*, 94:114–173, 2018.

[138] Hillel Aharoni, Eran Sharon, and Raz Kupferman. Geometry of thin nematic elastomer sheets. *Physical review letters*, 113(25):257801, 2014.

[139] Paul Plucinsky, Marius Lemm, and Kaushik Bhattacharya. Programming complex shapes in thin nematic elastomer and glass sheets. *Physical Review E*, 94(1):010701, 2016.

[140] Cyrus Mostajeran, Mark Warner, Taylor H Ware, and Timothy J White. Encoding gaussian curvature in glassy and elastomeric liquid crystal solids. *Proceedings of the Royal Society A: Mathematical, Physical and Engineering Sciences*, 472 (2189):20160112, 2016.

[141] Hillel Aharoni, Yu Xia, Xinyue Zhang, Randall D Kamien, and Shu Yang. Universal inverse design of surfaces with thin nematic elastomer sheets. *Proceedings of the National Academy of Sciences*, 115(28):7206–7211, 2018.

[142] Yael Klein, Efi Efrati, and Eran Sharon. Shaping of elastic sheets by prescription of non-euclidean metrics. *Science*, 315(5815):1116–1120, 2007.

[143] Jungwook Kim, James A Hanna, Myunghwan Byun, Christian D Santangelo, and Ryan C Hayward. Designing responsive buckled surfaces by halftone gel lithography. *Science*, 335(6073):1201–1205, 2012.

[144] Heloïse Therien-Aubin, Zi Liang Wu, Zhihong Nie, and Eugenia Kumacheva. Multiple shape transformations of composite hydrogel sheets. *Journal of the American Chemical Society*, 135(12):4834–4839, 2013.

[145] Leonid Ionov. Hydrogel-based actuators: possibilities and limitations. *Materials Today*, 17(10):494–503, 2014.

[146] Debdatta Ratna and J Karger-Kocsis. Recent advances in shape memory polymers and composites: a review. *Journal of Materials Science*, 43(1):254–269, 2008.

[147] Patrick T Mather, Xiaofan Luo, and Ingrid A Rousseau. Shape memory polymer research. *Annual Review of Materials Research*, 39:445–471, 2009.

[148] A Sydney Gladman, Elisabetta A Matsumoto, Ralph G Nuzzo, L Mahadevan, and Jennifer A Lewis. Biomimetic 4d printing. *Nature materials*, 15(4):413, 2016.

[149] Farhang Momeni, Xun Liu, Jun Ni, et al. A review of 4d printing. *Materials & design*, 122:42–79, 2017.

[150] Melina K Blees, Arthur W Barnard, Peter A Rose, Samantha P Roberts, Kathryn L McGill, Pinshane Y Huang, Alexander R Ruyack, Joshua W Kevek, Bryce Kobrin, David A Muller, et al. Graphene kirigami. *Nature*, 524(7564): 204, 2015.

[151] Christian D Santangelo. Extreme mechanics: self-folding origami. *Annual Review of Condensed Matter Physics*, 8:165–183, 2017.

[152] Sebastien JP Callens and Amir A Zadpoor. From flat sheets to curved geometries: Origami and kirigami approaches. *Materials Today*, 21(3):241–264, 2018.

[153] John A Rogers and Yonggang Huang. A curvy, stretchy future for electronics. *Proceedings of the National Academy of Sciences*, 106(27):10875–10876, 2009.

[154] Shikai Deng and Vikas Berry. Wrinkled, rippled and crumpled graphene: an overview of formation mechanism, electronic properties, and applications. *Materials Today*, 19(4):197–212, 2016.

[155] Kaori Kuribayashi, Koichi Tsuchiya, Zhong You, Dacian Tomus, Minoru Umemoto, Takahiro Ito, and Masahiro Sasaki. Self-deployable origami stent grafts as a biomedical application of ni-rich tini shape memory alloy foil. *Materials Science and Engineering: A*, 419(1-2):131–137, 2006.

[156] C. Py, P. Reverdy, L. Doppler, J. Bico, B. Roman, and C. N. Baroud. Capillary origami: Spontaneous wrapping of a droplet with an elastic sheet. *Phys. Rev. Lett.*, 98:156103, 2007.

[157] Elliot Hawkes, B An, Nadia M Benbernou, H Tanaka, Sangbae Kim, ED Demaine, D Rus, and Robert J Wood. Programmable matter by folding. *Proceedings of the National Academy of Sciences*, 107(28):12441–12445, 2010.

[158] Zhiyan Y Wei, Zengcai V Guo, Levi Dudte, Haiyi Y Liang, and L Mahadevan. Geometric mechanics of periodic pleated origami. *Physical review letters*, 110 (21):215501, 2013.

[159] Mark Schenk and Simon D Guest. Geometry of miura-folded metamaterials. *Proceedings of the National Academy of Sciences*, 110(9):3276–3281, 2013.

[160] Cheng Lv, Deepakshyam Krishnaraju, Goran Konjevod, Hongyu Yu, and Hanqing Jiang. Origami based mechanical metamaterials. *Scientific reports*, 4:5979, 2014.

[161] Zeming Song, Teng Ma, Rui Tang, Qian Cheng, Xu Wang, Deepakshyam Krishnaraju, Rahul Panat, Candace K Chan, Hongyu Yu, and Hanqing Jiang. Origami lithium-ion batteries. *Nature communications*, 5:3140, 2014.

[162] Rui Tang, Hai Huang, Hongen Tu, Hanshuang Liang, Mengbing Liang, Zeming Song, Yong Xu, Hanqing Jiang, and Hongyu Yu. Origami-enabled deformable silicon solar cells. *Applied Physics Letters*, 104(8):083501, 2014.

[163] Jesse L Silverberg, Arthur A Evans, Lauren McLeod, Ryan C Hayward, Thomas Hull, Christian D Santangelo, and Itai Cohen. Using origami design principles to fold reprogrammable mechanical metamaterials. *Science*, 345(6197):647–650, 2014.

[164] Evgueni T Filipov, Tomohiro Tachi, and Glaucio H Paulino. Origami tubes assembled into stiff, yet reconfigurable structures and metamaterials. *Proceedings of the National Academy of Sciences*, 112(40):12321–12326, 2015.

[165] Jun-Hee Na, Arthur A Evans, Jinhye Bae, Maria C Chiappelli, Christian D Santangelo, Robert J Lang, Thomas C Hull, and Ryan C Hayward. Programming reversibly self-folding origami with micropatterned photo-crosslinkable polymer trilayers. *Advanced Materials*, 27(1):79–85, 2015.

[166] Jesse L Silverberg, Jun-Hee Na, Arthur A Evans, Bin Liu, Thomas C Hull, Christian D Santangelo, Robert J Lang, Ryan C Hayward, and Itai Cohen.

Origami structures with a critical transition to bistability arising from hidden degrees of freedom. *Nature materials*, 14(4):389, 2015.

[167] Marcelo A Dias, Levi H Dudte, L Mahadevan, and Christian D Santangelo. Geometric mechanics of curved crease origami. *Physical review letters*, 109(11): 114301, 2012.

[168] Levi H Dudte, Etienne Vouga, Tomohiro Tachi, and L Mahadevan. Programming curvature using origami tessellations. *Nature materials*, 15(5):583, 2016.

[169] Qiuting Zhang, Jonathon Wommer, Connor ORourke, Joseph Teitelman, Yichao Tang, Joshua Robison, Gaojian Lin, and Jie Yin. Origami and kirigami inspired self-folding for programming three-dimensional shape shifting of polymer sheets with light. *Extreme Mechanics Letters*, 11:111–120, 2017.

[170] Matthew B Pinson, Menachem Stern, Alexandra Carruthers Ferrero, Thomas A Witten, Elizabeth Chen, and Arvind Murugan. Self-folding origami at any energy scale. *Nature communications*, 8:15477, 2017.

[171] Menachem Stern, Matthew B Pinson, and Arvind Murugan. The complexity of folding self-folding origami. *Physical Review X*, 7(4):041070, 2017.

[172] Bryan Gin-ge Chen and Christian D Santangelo. Branches of triangulated origami near the unfolded state. *Physical Review X*, 8(1):011034, 2018.

[173] Tom Mullin, S Deschanel, Katia Bertoldi, and Mary C Boyce. Pattern transformation triggered by deformation. *Physical review letters*, 99(8):084301, 2007.

[174] Katia Bertoldi, Pedro M Reis, Stephen Willshaw, and Tom Mullin. Negative poisson's ratio behavior induced by an elastic instability. *Advanced Materials*, 22(3):361–366, 2010.

[175] Bastiaan Florijn, Corentin Coulais, and Martin van Hecke. Programmable mechanical metamaterials. *Physical review letters*, 113(17):175503, 2014.

[176] Toen Castle, Yigil Cho, Xingting Gong, Euiyeon Jung, Daniel M Sussman, Shu Yang, and Randall D Kamien. Making the cut: Lattice kirigami rules. *Physical review letters*, 113(24):245502, 2014.

[177] Zeming Song, Xu Wang, Cheng Lv, Yonghao An, Mengbing Liang, Teng Ma, David He, Ying-Jie Zheng, Shi-Qing Huang, Hongyu Yu, et al. Kirigami-based stretchable lithium-ion batteries. *Scientific reports*, 5:10988, 2015.

[178] Yihui Zhang, Zheng Yan, Kewang Nan, Dongqing Xiao, Yuhao Liu, Haiwen Luan, Haoran Fu, Xizhu Wang, Qinglin Yang, Jiechen Wang, et al. A mechanically driven form of kirigami as a route to 3d mesostructures in micro/nanomembranes. *Proceedings of the National Academy of Sciences*, 112(38):11757–11764, 2015.

[179] Aaron Lamoureux, Kyusang Lee, Matthew Shlian, Stephen R Forrest, and Max Shtein. Dynamic kirigami structures for integrated solar tracking. *Nature communications*, 6, 2015.

[180] Terry C Shyu, Pablo F Damasceno, Paul M Dodd, Aaron Lamoureux, Lizhi Xu, Matthew Shlian, Max Shtein, Sharon C Glotzer, and Nicholas A Kotov. A kirigami approach to engineering elasticity in nanocomposites through patterned defects. *Nature materials*, 14(8):785–789, 2015.

[181] Daniel M Sussman, Yigil Cho, Toen Castle, Xingting Gong, Euiyeon Jung, Shu Yang, and Randall D Kamien. Algorithmic lattice kirigami: A route to pluripotent materials. *Proceedings of the National Academy of Sciences*, 112 (24):7449–7453, 2015.

[182] Changsheng Wu, Xin Wang, Long Lin, Hengyu Guo, and Zhong Lin Wang. Based triboelectric nanogenerators made of stretchable interlocking kirigami patterns. *ACS nano*, 10(4):4652–4659, 2016.

[183] Paul Z Hanakata, Zenan Qi, David K Campbell, and Harold S Park. Highly stretchable MoS 2 kirigami. *Nanoscale*, 8(1):458–463, 2016.

[184] Bryan Gin-ge Chen, Bin Liu, Arthur A Evans, Jayson Paulose, Itai Cohen, Vincenzo Vitelli, and CD Santangelo. Topological mechanics of origami and kirigami. *Physical review letters*, 116(13):135501, 2016.

[185] Midori Isobe and Ko Okumura. Initial rigid response and softening transition of highly stretchable kirigami sheet materials. *Scientific reports*, 6:24758, 2016.

[186] Toen Castle, Daniel M Sussman, Michael Tanis, and Randall D Kamien. Additive lattice kirigami. *Science advances*, 2(9):e1601258, 2016.

[187] Marcelo A Dias, Michael P McCarron, Daniel Rayneau-Kirkhope, Paul Z Hanakata, David K Campbell, Harold S Park, and Douglas P Holmes. Kirigami actuators. *Soft matter*, 13(48):9087–9092, 2017.

[188] Ahmad Rafsanjani and Katia Bertoldi. Buckling-induced kirigami. *Physical Review Letters*, 118(8):084301, 2017.

[189] Gary Choi, Levi H Dudte, and L Mahadevan. Programming shape using kirigami tessellations. *arXiv preprint arXiv:1812.08644*, 2018.

[190] Yi Yang, Marcelo A Dias, and Douglas P Holmes. Multistable kirigami for tunable architected materials. *Physical Review Materials*, 2(11):110601, 2018.

[191] Ahmad Rafsanjani, Yuerou Zhang, Bangyuan Liu, Shmuel M Rubinstein, and Katia Bertoldi. Kirigami skins make a simple soft actuator crawl. *Science Robotics*, 3(15):eaar7555, 2018.

[192] Michael Moshe, Edward Esposito, Suraj Shankar, Baris Bircan, Itai Cohen, David R Nelson, and Mark J Bowick. Kirigami mechanics as stress relief by elastic charges. *Physical Review Letters*, 122(4):048001, 2019.

[193] Michael Moshe, Edward Esposito, Suraj Shankar, Baris Bircan, Itai Cohen, David R Nelson, and Mark J Bowick. Nonlinear mechanics of thin frames. *Physical Review E*, 99(1):013002, 2019.

[194] Marc Z Miskin, Kyle J Dorsey, Baris Bircan, Yimo Han, David A Muller, Paul L McEuen, and Itai Cohen. Graphene-based bimorphs for micron-sized, autonomous origami machines. *Proceedings of the National Academy of Sciences*, 115(3):466–470, 2018.

[195] TC Lubensky, CL Kane, Xiaoming Mao, Anton Souslov, and Kai Sun. Phonons and elasticity in critically coordinated lattices. *Reports on Progress in Physics*, 78(7):073901, 2015.

[196] Bryan Gin-ge Chen, Nitin Upadhyaya, and Vincenzo Vitelli. Nonlinear conduction via solitons in a topological mechanical insulator. *Proceedings of the National Academy of Sciences*, 111(36):13004–13009, 2014.

[197] S Hossein Mousavi, Alexander B Khanikaev, and Zheng Wang. Topologically protected elastic waves in phononic metamaterials. *Nature communications*, 6: 8682, 2015.

[198] Roman Süsstrunk and Sebastian D Huber. Observation of phononic helical edge states in a mechanical topological insulator. *Science*, 349(6243):47–50, 2015.

[199] D Zeb Rocklin, Bryan Gin-ge Chen, Martin Falk, Vincenzo Vitelli, and TC Lubensky. Mechanical weyl modes in topological maxwell lattices. *Physical review letters*, 116(13):135503, 2016.

[200] D Zeb Rocklin, Shangnan Zhou, Kai Sun, and Xiaoming Mao. Transformable topological mechanical metamaterials. *Nature communications*, 8:14201, 2017.

[201] D Zeb Rocklin. Directional mechanical response in the bulk of topological metamaterials. *New Journal of Physics*, 19(6):065004, 2017.

[202] Emil Prodan, Kyle Dobiszewski, Alokik Kanwal, John Palmieri, and Camelia Prodan. Dynamical majorana edge modes in a broad class of topological mechanical systems. *Nature communications*, 8:14587, 2017.

[203] M Miniaci, RK Pal, B Morvan, and M Ruzzene. Experimental observation of topologically protected helical edge modes in patterned elastic plates. *Physical Review X*, 8(3):031074, 2018.

[204] Di Zhou, Leyou Zhang, and Xiaoming Mao. Topological mechanics in quasicrystals. *arXiv preprint arXiv:1809.09188*, 2018.

[205] Marc Serra-Garcia, Valerio Peri, Roman Süsstrunk, Osama R Bilal, Tom Larsen, Luis Guillermo Villanueva, and Sebastian D Huber. Observation of a phononic quadrupole topological insulator. *Nature*, 555(7696):342, 2018.

[206] David J Apigo, Wenting Cheng, Kyle F Dobiszewski, Emil Prodan, and Camelia Prodan. Observation of topological edge modes in a quasiperiodic acoustic waveguide. *Physical Review Letters*, 122(9):095501, 2019.

[207] Jayson Paulose, Bryan Gin-ge Chen, and Vincenzo Vitelli. Topological modes

bound to dislocations in mechanical metamaterials. *Nature Physics*, 11(2):153, 2015.

[208] Anne S Meeussen, Jayson Paulose, and Vincenzo Vitelli. Geared topological metamaterials with tunable mechanical stability. *Physical Review X*, 6(4):041029, 2016.

[209] Guido Baardink, Anton Souslov, Jayson Paulose, and Vincenzo Vitelli. Localizing softness and stress along loops in 3d topological metamaterials. *Proceedings of the National Academy of Sciences*, 115(3):489–494, 2018.

[210] Leyou Zhang and Xiaoming Mao. Fracturing of topological maxwell lattices. *New Journal of Physics*, 20(6):063034, 2018.

[211] Jayson Paulose, Anne S Meeussen, and Vincenzo Vitelli. Selective buckling via states of self-stress in topological metamaterials. *Proceedings of the National Academy of Sciences*, 112(25):7639–7644, 2015.

[212] Frank Schweitzer. *Brownian agents and active particles: collective dynamics in the natural and social sciences*. Springer, 2007.

[213] Pawel Romanczuk, Markus Bär, Werner Ebeling, Benjamin Lindner, and Lutz Schimansky-Geier. Active brownian particles. *The European Physical Journal Special Topics*, 202(1):1–162, 2012.

[214] Clemens Bechinger, Roberto Di Leonardo, Hartmut Löwen, Charles Reichhardt, Giorgio Volpe, and Giovanni Volpe. Active particles in complex and crowded environments. *Reviews of Modern Physics*, 88(4):045006, 2016.

[215] John Toner, Yuhai Tu, and Sriram Ramaswamy. Hydrodynamics and phases of flocks. *Annals of Physics*, 318(1):170–244, 2005.

[216] Sriram Ramaswamy. The mechanics and statistics of active matter. *Annu. Rev. Condens. Matter Phys.*, 1(1):323–345, 2010.

[217] Tamás Vicsek and Anna Zafeiris. Collective motion. *Physics reports*, 517(3-4): 71–140, 2012.

[218] M Cristina Marchetti, JF Joanny, S Ramaswamy, TB Liverpool, J Prost, Madan Rao, and R Aditi Simha. Hydrodynamics of soft active matter. *Reviews of Modern Physics*, 85(3):1143, 2013.

[219] Jacques Prost, Frank Jülicher, and Jean-François Joanny. Active gel physics. *Nature Physics*, 11(2):111, 2015.

[220] Sriram Ramaswamy. Active matter. *Journal of Statistical Mechanics: Theory and Experiment*, 2017(5):054002, 2017.

[221] Philip W Anderson. More is different. *Science*, 177(4047):393–396, 1972.

[222] Karen E Kasza, Amy C Rowat, Jiayu Liu, Thomas E Angelini, Clifford P Brangwynne, Gijsje H Koenderink, and David A Weitz. The cell as a material. *Current opinion in cell biology*, 19(1):101–107, 2007.

[223] Daniel Needleman. The material basis of life. *Trends in cell biology*, 25(12): 713–716, 2015.

[224] Jeremie Palacci, Stefano Sacanna, Asher Preska Steinberg, David J Pine, and Paul M Chaikin. Living crystals of light-activated colloidal surfers. *Science*, 339 (6122):936–940, 2013.

[225] Vijay Narayan, Sriram Ramaswamy, and Narayanan Menon. Long-lived giant number fluctuations in a swarming granular nematic. *Science*, 317(5834):105–108, 2007. Also see Supporting Information, page 4.

[226] Lisa M Nash, Dustin Kleckner, Alismari Read, Vincenzo Vitelli, Ari M Turner, and William TM Irvine. Topological mechanics of gyroscopic metamaterials. *Proceedings of the National Academy of Sciences*, 112(47):14495–14500, 2015.

[227] LD Landau and EM Lifshitz. Physical kinetics. vol. 10. *Course of Theoretical Physics*, 1981.

[228] Sriram Ramaswamy. Issues in the statistical mechanics of steady sedimentation. *Advances in Physics*, 50(3):297–341, 2001.

[229] Peter Jung. Periodically driven stochastic systems. *Physics Reports*, 234(4-5): 175–295, 1993.

[230] Siegfried Grossmann, Detlef Lohse, and Chao Sun. High–reynolds number taylor-couette turbulence. *Annual review of fluid mechanics*, 48:53–80, 2016.

[231] Mark C Cross and Pierre C Hohenberg. Pattern formation outside of equilibrium. *Reviews of modern physics*, 65(3):851, 1993.

[232] Robert Zwanzig. *Nonequilibrium statistical mechanics.* Oxford University Press, 2001.

[233] Juan P Garrahan, Peter Sollich, and Cristina Toninelli. Kinetically constrained models. *Dynamical heterogeneities in glasses, colloids, and granular media*, 150: 111–137, 2011.

[234] Andrea Cavagna. Supercooled liquids for pedestrians. *Physics Reports*, 476(4-6): 51–124, 2009.

[235] Silke Henkes, Yaouen Fily, and M Cristina Marchetti. Active jamming: Self-propelled soft particles at high density. *Physical Review E*, 84(4):040301, 2011.

[236] Ludovic Berthier and Jorge Kurchan. Non-equilibrium glass transitions in driven and active matter. *Nature Physics*, 9(5):310, 2013.

[237] Dapeng Bi, Xingbo Yang, M Cristina Marchetti, and M Lisa Manning. Motility-driven glass and jamming transitions in biological tissues. *Physical Review X*, 6 (2):021011, 2016.

[238] Daniel Needleman and Zvonimir Dogic. Active matter at the interface between materials science and cell biology. *Nature Reviews Materials*, 2(9):17048, 2017.

[239] William Bialek, Andrea Cavagna, Irene Giardina, Thierry Mora, Edmondo Silvestri, Massimiliano Viale, and Aleksandra M Walczak. Statistical mechanics for natural flocks of birds. *Proceedings of the National Academy of Sciences*, 2012.

[240] Andrea Cavagna and Irene Giardina. Bird flocks as condensed matter. *Annu. Rev. Condens. Matter Phys.*, 5(1):183–207, 2014.

[241] Yael Katz, Kolbjørn Tunstrøm, Christos C Ioannou, Cristián Huepe, and Iain D Couzin. Inferring the structure and dynamics of interactions in schooling fish. *Proceedings of the National Academy of Sciences*, 108(46):18720–18725, 2011.

[242] Kolbjørn Tunstrøm, Yael Katz, Christos C Ioannou, Cristián Huepe, Matthew J Lutz, and Iain D Couzin. Collective states, multistability and transitional behavior in schooling fish. *PLoS computational biology*, 9(2):e1002915, 2013.

[243] Jerome Buhl, David JT Sumpter, Iain D Couzin, Joe J Hale, Emma Despland, Edgar R Miller, and Steve J Simpson. From disorder to order in marching locusts. *Science*, 312(5778):1402–1406, 2006.

[244] Douglas H Kelley and Nicholas T Ouellette. Emergent dynamics of laboratory insect swarms. *Scientific reports*, 3:1073, 2013.

[245] Michael Tennenbaum, Zhongyang Liu, David Hu, and Alberto Fernandez-Nieves. Mechanics of fire ant aggregations. *Nature materials*, 15(1):54, 2016.

[246] Michael Sinhuber and Nicholas T Ouellette. Phase coexistence in insect swarms. *Physical review letters*, 119(17):178003, 2017.

[247] Mehdi Moussaid, Elsa G Guillot, Mathieu Moreau, Jérôme Fehrenbach, Olivier Chabiron, Samuel Lemercier, Julien Pettré, Cecile Appert-Rolland, Pierre Degond, and Guy Theraulaz. Traffic instabilities in self-organized pedestrian crowds. *PLoS computational biology*, 8(3):e1002442, 2012.

[248] Jesse L Silverberg, Matthew Bierbaum, James P Sethna, and Itai Cohen. Collective motion of humans in mosh and circle pits at heavy metal concerts. *Physical Review Letters*, 110(22):228701, 2013.

[249] Arianna Bottinelli, David TJ Sumpter, and Jesse L Silverberg. Emergent structural mechanisms for high-density collective motion inspired by human crowds. *Physical review letters*, 117(22):228301, 2016.

[250] Nicolas Bain and Denis Bartolo. Dynamic response and hydrodynamics of polarized crowds. *Science*, 363(6422):46–49, 2019.

[251] Christopher Dombrowski, Luis Cisneros, Sunita Chatkaew, Raymond E Goldstein, and John O Kessler. Self-concentration and large-scale coherence in bacterial dynamics. *Physical review letters*, 93(9):098103, 2004.

[252] Jörn Dunkel, Sebastian Heidenreich, Knut Drescher, Henricus H Wensink,

Markus Bär, and Raymond E Goldstein. Fluid dynamics of bacterial turbulence. *Physical review letters*, 110(22):228102, 2013.

[253] Shuang Zhou, Andrey Sokolov, Oleg D. Lavrentovich, and Igor S. Aranson. Living liquid crystals. *Proceedings of the National Academy of Sciences*, 111(4): 1265–1270, 2014.

[254] Daiki Nishiguchi, Ken H Nagai, Hugues Chaté, and Masaki Sano. Long-range nematic order and anomalous fluctuations in suspensions of swimming filamentous bacteria. *Physical Review E*, 95(2):020601, 2017.

[255] H Gruler, U Dewald, and M Eberhardt. Nematic liquid crystals formed by living amoeboid cells. *The European Physical Journal B-Condensed Matter and Complex Systems*, 11(1):187–192, 1999.

[256] R Kemkemer, D Kling, D Kaufmann, and H Gruler. Elastic properties of nematoid arrangements formed by amoeboid cells. *The European Physical Journal E*, 1(2-3):215–225, 2000.

[257] Balint Szabo, GJ Szöllösi, B Gönci, Zs Jurányi, David Selmeczi, and Tamás Vicsek. Phase transition in the collective migration of tissue cells: experiment and model. *Physical Review E*, 74(6):061908, 2006.

[258] Guillaume Duclos, Christoph Erlenkämper, Jean-François Joanny, and Pascal Silberzan. Topological defects in confined populations of spindle-shaped cells. *Nature Physics*, 13(1):58, 2017.

[259] Kyogo Kawaguchi, Ryoichiro Kageyama, and Masaki Sano. Topological defects control collective dynamics in neural progenitor cell cultures. *Nature*, 545(7654): 327, 2017.

[260] Thuan Beng Saw, Amin Doostmohammadi, Vincent Nier, Leyla Kocgozlu, Sumesh Thampi, Yusuke Toyama, Philippe Marcq, Chwee Teck Lim, Julia M Yeomans, and Benoit Ladoux. Topological defects in epithelia govern cell death and extrusion. *Nature*, 544(7649):212, 2017.

[261] Nicholas Noll, Madhav Mani, Idse Heemskerk, Sebastian J Streichan, and Boris I Shraiman. Active tension network model suggests an exotic mechanical state realized in epithelial tissues. *Nature physics*, 13(12):1221, 2017.

[262] C Blanch-Mercader, V Yashunsky, S Garcia, G Duclos, L Giomi, and P Silberzan. Turbulent dynamics of epithelial cell cultures. *Physical review letters*, 120(20): 208101, 2018.

[263] Ernest Latorre, Sohan Kale, Laura Casares, Manuel Gómez-González, Marina Uroz, Léo Valon, Roshna V Nair, Elena Garreta, Nuria Montserrat, Aránzazu del Campo, et al. Active superelasticity in three-dimensional epithelia of controlled shape. *Nature*, 563(7730):203, 2018.

[264] Jan Brugués and Daniel Needleman. Physical basis of spindle self-organization. *Proceedings of the National Academy of Sciences*, 111(52):18496–18500, 2014.

[265] Abhishek Kumar, Ananyo Maitra, Madhuresh Sumit, Sriram Ramaswamy, and GV Shivashankar. Actomyosin contractility rotates the cell nucleus. *Scientific reports*, 4:3781, 2014.

[266] Julien Deseigne, Olivier Dauchot, and Hugues Chaté. Collective motion of vibrated polar disks. *Physical review letters*, 105(9):098001, 2010.

[267] Nitin Kumar, Harsh Soni, Sriram Ramaswamy, and AK Sood. Flocking at a distance in active granular matter. *Nature communications*, 5:4688, 2014.

[268] Antoine Bricard, Jean-Baptiste Caussin, Nicolas Desreumaux, Olivier Dauchot, and Denis Bartolo. Emergence of macroscopic directed motion in populations of motile colloids. *Nature*, 503(7474):95, 2013.

[269] L Giomi, N Hawley-Weld, and L Mahadevan. Swarming, swirling and stasis in sequestered bristle-bots. *Proceedings of the Royal Society A: Mathematical, Physical and Engineering Sciences*, 469(2151):20120637, 2013.

[270] Mite Mijalkov, Austin McDaniel, Jan Wehr, and Giovanni Volpe. Engineering sensorial delay to control phototaxis and emergent collective behaviors. *Physical Review X*, 6(1):011008, 2016.

[271] Christian Scholz, Michael Engel, and Thorsten Pöschel. Rotating robots move collectively and self-organize. *Nature communications*, 9(1):931, 2018.

[272] Volker Schaller, Christoph Weber, Christine Semmrich, Erwin Frey, and Andreas R Bausch. Polar patterns of driven filaments. *Nature*, 467(7311):73–77, 2010.

[273] Tim Sanchez, Daniel TN Chen, Stephen J DeCamp, Michael Heymann, and Zvonimir Dogic. Spontaneous motion in hierarchically assembled active matter. *Nature*, 491(7424):431–434, 2012.

[274] Felix C Keber, Etienne Loiseau, Tim Sanchez, Stephen J DeCamp, Luca Giomi, Mark J Bowick, M Cristina Marchetti, Zvonimir Dogic, and Andreas R Bausch. Topology and dynamics of active nematic vesicles. *Science*, 345(6201):1135–1139, 2014.

[275] Pau Guillamat, Jordi Ignés-Mullol, and Francesc Sagués. Taming active turbulence with patterned soft interfaces. *Nature communications*, 8(1):564, 2017.

[276] Perry W Ellis, Daniel JG Pearce, Ya-Wen Chang, Guillermo Goldsztein, Luca Giomi, and Alberto Fernandez-Nieves. Curvature-induced defect unbinding and dynamics in active nematic toroids. *Nature Physics*, 14(1):85, 2018.

[277] Nitin Kumar, Rui Zhang, Juan J de Pablo, and Margaret L Gardel. Tunable structure and dynamics of active liquid crystals. *Science Advances*, 4(10): eaat7779, 2018.

[278] Y Bouligand. Liquid crystalline order in biological materials. *Liquid crystalline order in polymers*, pages 261–297, 1978.

[279] Paul M Chaikin and Tom C Lubensky. *Principles of condensed matter physics*. Cambridge university press, 2000.

[280] Sriram Ramaswamy, R Aditi Simha, and John Toner. Active nematics on a substrate: Giant number fluctuations and long-time tails. *EPL (Europhysics Letters)*, 62(2):196, 2003.

[281] Amin Doostmohammadi, Jordi Ignés-Mullol, Julia M Yeomans, and Francesc Sagués. Active nematics. *Nature communications*, 9(1):3246, 2018.

[282] Luca Giomi, Mark J Bowick, Xu Ma, and M Cristina Marchetti. Defect annihilation and proliferation in active nematics. *Physical review letters*, 110(22): 228101, 2013.

[283] Vinay Ambegaokar, BI Halperin, David R Nelson, and Eric D Siggia. Dynamics of superfluid films. *Physical Review B*, 21(5):1806, 1980.

[284] Annette Zippelius, BI Halperin, and David R Nelson. Dynamics of two-dimensional melting. *Physical Review B*, 22(5):2514, 1980.

[285] R Bruinsma, BI Halperin, and Annette Zippelius. Motion of defects and stress relaxation in two-dimensional crystals. *Physical Review B*, 25(2):579, 1982.

[286] TC Lubensky, Sriram Ramaswamy, and John Toner. Dislocation motion in quasicrystals and implications for macroscopic properties. *Physical Review B*, 33(11):7715, 1986.

[287] Harald Pleiner. Dynamics of a disclination point in smectic-c and-c$^*$ liquid-crystal films. *Physical Review A*, 37(10):3986, 1988.

[288] M Cristina Marchetti and David R Nelson. Hydrodynamics of flux liquids. *Physical Review B*, 42(16):9938, 1990.

[289] G Ryskin and M Kremenetsky. Drag force on a line defect moving through an otherwise undisturbed field: Disclination line in a nematic liquid crystal. *Physical review letters*, 67(12):1574, 1991.

[290] LM Pismen and BY Rubinstein. Motion of interacting point defects in nematics. *Physical review letters*, 69(1):96, 1992.

[291] Alan J Bray. Theory of phase-ordering kinetics. *Advances in Physics*, 43(3): 357–459, 1994.

[292] Colin Denniston. Disclination dynamics in nematic liquid crystals. *Physical Review B*, 54(9):6272, 1996.

[293] John Toner and Yuhai Tu. Flocks, herds, and schools: A quantitative theory of flocking. *Physical review E*, 58(4):4828, 1998.

[294] FJ Nédélec, Thomas Surrey, Anthony C Maggs, and Stanislas Leibler. Self-organization of microtubules and motors. *Nature*, 389(6648):305, 1997.

[295] Karsten Kruse, Jean-François Joanny, Frank Jülicher, Jacques Prost, and Ken Sekimoto. Asters, vortices, and rotating spirals in active gels of polar filaments. *Physical review letters*, 92(7):078101, 2004.

[296] J Elgeti, ME Cates, and D Marenduzzo. Defect hydrodynamics in 2d polar active fluids. *Soft Matter*, 7(7):3177–3185, 2011.

[297] Volker Schaller and Andreas R Bausch. Topological defects and density fluctuations in collectively moving systems. *Proceedings of the National Academy of Sciences*, page 201215368, 2013.

[298] John Toner and Yuhai Tu. Long-range order in a two-dimensional dynamical xy model: how birds fly together. *Physical Review Letters*, 75(23):4326, 1995.

[299] John Toner. Reanalysis of the hydrodynamic theory of fluid, polar-ordered flocks. *Physical Review E*, 86(3):031918, 2012.

[300] Kripa Gowrishankar and Madan Rao. Nonequilibrium phase transitions, fluctuations and correlations in an active contractile polar fluid. *Soft matter*, 12(7): 2040–2046, 2016.

[301] Guillaume Grégoire and Hugues Chaté. Onset of collective and cohesive motion. *Physical review letters*, 92(2):025702, 2004.

[302] Shradha Mishra, Aparna Baskaran, and M Cristina Marchetti. Fluctuations and pattern formation in self-propelled particles. *Physical Review E*, 81(6):061916, 2010.

[303] AP Solon and Julien Tailleur. Revisiting the flocking transition using active spins. *Physical review letters*, 111(7):078101, 2013.

[304] Jean-Baptiste Caussin, Alexandre Solon, Anton Peshkov, Hugues Chaté, Thierry Dauxois, Julien Tailleur, Vincenzo Vitelli, and Denis Bartolo. Emergent spatial structures in flocking models: a dynamical system insight. *Physical review letters*, 112(14):148102, 2014.

[305] Alexandre P Solon, Jean-Baptiste Caussin, Denis Bartolo, Hugues Chaté, and Julien Tailleur. Pattern formation in flocking models: A hydrodynamic description. *Physical Review E*, 92(6):062111, 2015.

[306] Alexandre P Solon, Hugues Chaté, and Julien Tailleur. From phase to microphase separation in flocking models: The essential role of nonequilibrium fluctuations. *Physical review letters*, 114(6):068101, 2015.

[307] Anton Souslov, Benjamin C van Zuiden, Denis Bartolo, and Vincenzo Vitelli. Topological sound in active-liquid metamaterials. *Nature Physics*, 13(11):1091, 2017.

[308] Noah P Mitchell, Lisa M Nash, Daniel Hexner, Ari M Turner, and William TM Irvine. Amorphous topological insulators constructed from random point sets. *Nature Physics*, page 1, 2018.

[309] Warner Tjardus Koiter. On the nonlinear theory of thin elastic shells. i- introductory sections. ii- basic shell equations. iii- simplified shell equations(nonlinear theory of thin elastic shells, discussing surface geometry and deformation, equations of equilibrium and boundary conditions and stress functions). *Koninklijke Nederlandse Akademie van Wetenschappen, Proceedings, Series B*, 69(1):1–54, 1966.

[310] Benny Davidovitch, Robert D Schroll, Dominic Vella, Mokhtar Adda-Bedia, and

Enrique A Cerda. Prototypical model for tensional wrinkling in thin sheets. *Proceedings of the National Academy of Sciences*, 108(45):18227–18232, 2011.

[311] Haim Diamant and Thomas A Witten. Compression induced folding of a sheet: An integrable system. *Physical review letters*, 107(16):164302, 2011.

[312] Joseph D Paulsen, Vincent Démery, K Buğra Toga, Zhanlong Qiu, Thomas P Russell, Benny Davidovitch, and Narayanan Menon. Geometry-driven folding of a floating annular sheet. *Physical review letters*, 118(4):048004, 2017.

[313] Evan Hohlfeld and Lakshminarayanan Mahadevan. Unfolding the sulcus. *Physical review letters*, 106(10):105702, 2011.

[314] Tuomas Tallinen, John S Biggins, and L Mahadevan. Surface sulci in squeezed soft solids. *Physical review letters*, 110(2):024302, 2013.

[315] Efi Efrati, Eran Sharon, and Raz Kupferman. Elastic theory of unconstrained non-euclidean plates. *JMPS*, 57(4):762–775, 2009.

[316] Haiyi Liang and L Mahadevan. Growth, geometry, and mechanics of a blooming lily. *Proc. Natl. Acad. Sci. U.S.A.*, 108(14):5516–5521, 2011.

[317] Martine Ben Amar, Martin Michael Müller, and Miguel Trejo. Petal shapes of sympetalous flowers: the interplay between growth, geometry and elasticity. *New J. Phys.*, 14(8):085014, 2012.

[318] Haiyi Liang and Lakshminarayanan Mahadevan. The shape of a long leaf. *Proc. Natl. Acad. Sci. U.S.A.*, 106(52):22049–22054, 2009.

[319] Julien Dervaux and Martine Ben Amar. Morphogenesis of growing soft tissues. *Phys. Rev. Lett.*, 101(6):068101, 2008.

[320] Shahaf Armon, Efi Efrati, Raz Kupferman, and Eran Sharon. Geometry and mechanics in the opening of chiral seed pods. *Science*, 333(6050):1726–1730, 2011.

[321] Shahaf Armon, Hillel Aharoni, Michael Moshe, and Eran Sharon. Shape selection in chiral ribbons: from seed pods to supramolecular assemblies. *Soft Matter*, 10 (16):2733–2740, 2014.

[322] Jungwook Kim, James A Hanna, Ryan C Hayward, and Christian D Santangelo. Thermally responsive rolling of thin gel strips with discrete variations in swelling. *Soft Matter*, 8(8):2375–2381, 2012.

[323] Yael Klein, Efi Efrati, and Eran Sharon. Shaping of elastic sheets by prescription of non-euclidean metrics. *Science*, 315(5815):1116–1120, 2007.

[324] Michael Moshe, Eran Sharon, and Raz Kupferman. Pattern selection and multiscale behaviour in metrically discontinuous non-euclidean plates. *Nonlinearity*, 26(12):3247, 2013.

[325] Steven B. Smith, Yujia Cui, and Carlos Bustamante. Overstretching b-dna: The elastic response of individual double-stranded and single-stranded dna molecules. *Science*, 271(5250):795–799, 1996.

[326] Kieran YG McCullough, Norman A Fleck, and Michael F Ashby. Uniaxial stress–strain behaviour of aluminium alloy foams. *Acta Mater.*, 47(8):2323–2330, 1999.

[327] Lorna J Gibson and Michael F Ashby. The mechanics of three-dimensional cellular materials. *Proc. Roy. Soc. Lond. A*, 382(1782):43–59, 1982.

[328] Mark Warner and Eugene Michael Terentjev. *Liquid crystal elastomers*. OUP Oxford, 2003.

[329] DA Bahamon, Zenan Qi, Harold S Park, Vitor M Pereira, and David K Campbell. Graphene kirigami as a platform for stretchable and tunable quantum dot arrays. *Phys. Rev. B*, 93(23):235408, 2016.

[330] Jongmin Shim, Sicong Shan, Andrej Košmrlj, Sung H Kang, Elizabeth R Chen, James C Weaver, and Katia Bertoldi. Harnessing instabilities for design of soft reconfigurable auxetic/chiral materials. *Soft Matter*, 9(34):8198–8202, 2013.

[331] Elisabetta A Matsumoto and Randall D Kamien. Elastic-instability triggered pattern formation. *Phys. Rev. E*, 80(2):021604, 2009.

[332] Gabriele Librandi, Michael Moshe, Yoav Lahini, and Katia Bertoldi. Porous mechanical metamaterials as interacting elastic charges. *arXiv:1709.00328*, 2017.

[333] Michael Moshe, Ido Levin, Hillel Aharoni, Raz Kupferman, and Eran Sharon. Geometry and mechanics of two-dimensional defects in amorphous materials. *PNAS*, 112(35):10873–10878, 2015.

[334] Sung Hoon Kang, Sicong Shan, Andrej Košmrlj, Wim L Noorduin, Samuel Shian, James C Weaver, David R Clarke, and Katia Bertoldi. Complex ordered patterns in mechanical instability induced geometrically frustrated triangular cellular structures. *Physical Review Letters*, 112(9):098701, 2014.

[335] D Rocklin, Vincenzo Vitelli, and Xiaoming Mao. Folding mechanisms at finite temperature. *arXiv preprint arXiv:1802.02704*, 2018.

[336] Philippe G Ciarlet. *Mathematical Elasticity, Vol III, Theory of Shells*. North-Holland, 2000.

[337] James R Barber. *Elasticity.* Springer, 1992.

[338] John David Jackson. *Classical electrodynamics.* John Wiley & Sons, 2007.

[339] Michael Moshe, Eran Sharon, and Raz Kupferman. Elastic interactions between two-dimensional geometric defects. *Physical Review E*, 92(6):062403, 2015.

[340] Heloise Therien-Aubin, Michael Moshe, Eran Sharon, and Eugenia Kumacheva. Shape transformations of soft matter governed by bi-axial stresses. *Soft Matter*, 11:4600–4605, 2015.

[341] Martin Michael Müller, Martine Ben Amar, and Jemal Guven. Conical defects in growing sheets. *Physical review letters*, 101(15):156104, 2008.

[342] Efi Efrati, Luka Pocivavsek, Ruben Meza, Ka Yee C Lee, and Thomas A Witten. Confined disclinations: Exterior versus material constraints in developable thin elastic sheets. *Phys. Rev. E*, 91(2):022404, 2015.

[343] Suraj Shankar, Sriram Ramaswamy, M. Cristina Marchetti, and Mark J. Bowick. Defect unbinding in active nematics. *Phys. Rev. Lett.*, 121:108002, Sep 2018.

[344] Pierre Gilles De Gennes and Jacques Prost. *The physics of liquid crystals.* Clarendon Press, Oxford, 1993.

[345] Isaac Chuang, Ruth Durrer, Neil Turok, and Bernard Yurke. Cosmology in the laboratory: Defect dynamics in liquid crystals. *Science*, 251(4999):1336–1342, 1991.

[346] Mark J Bowick, L Chandar, Eric A Schiff, and Ajit M Srivastava. The cosmological kibble mechanism in the laboratory: string formation in liquid crystals. *Science*, 263(5149):943–945, 1994.

[347] Grigory E Volovik. *The universe in a helium droplet*, volume 117. Clarendon Press, 2003.

[348] Sandrine Ngo, Anton Peshkov, Igor S Aranson, Eric Bertin, Francesco Ginelli, and Hugues Chaté. Large-scale chaos and fluctuations in active nematics. *Physical review letters*, 113(3):038302, 2014.

[349] Pau Guillamat, Jordi Ignés-Mullol, Suraj Shankar, M Cristina Marchetti, and Francesc Sagués. Probing the shear viscosity of an active nematic film. *Physical Review E*, 94(6):060602, 2016.

[350] DL Stein. Kosterlitz-thouless phase transitions in two-dimensional liquid crystals. *Physical Review B*, 18(5):2397, 1978.

[351] Aphrodite Ahmadi, M Cristina Marchetti, and Tanniemola B Liverpool. Hydrodynamics of isotropic and liquid crystalline active polymer solutions. *Physical Review E*, 74(6):061913, 2006.

[352] Guillaume Duclos, Simon Garcia, HG Yevick, and P Silberzan. Perfect nematic order in confined monolayers of spindle-shaped cells. *Soft matter*, 10(14):2346–2353, 2014.

[353] R Aditi Simha and Sriram Ramaswamy. Hydrodynamic fluctuations and instabilities in ordered suspensions of self-propelled particles. *Physical review letters*, 89(5):058101, 2002.

[354] Hugues Chaté, Francesco Ginelli, and Raúl Montagne. Simple model for active nematics: quasi-long-range order and giant fluctuations. *Physical review letters*, 96(18):180602, 2006.

[355] Shradha Mishra and Sriram Ramaswamy. Active nematics are intrinsically phase separated. *Physical review letters*, 97(9):090602, 2006.

[356] Xia-qing Shi and Yu-qiang Ma. Deterministic endless collective evolvement in active nematics. *arXiv preprint arXiv:1011.5408*, 2010.

[357] Elias Putzig and Aparna Baskaran. Phase separation and emergent structures in an active nematic fluid. *Physical Review E*, 90(4):042304, 2014.

[358] Xia-qing Shi, Hugues Chaté, and Yu-qiang Ma. Instabilities and chaos in a kinetic equation for active nematics. *New Journal of Physics*, 16(3):035003, 2014.

[359] Eric Bertin, Hugues Chaté, Francesco Ginelli, Shradha Mishra, Anton Peshkov, and Sriram Ramaswamy. Mesoscopic theory for fluctuating active nematics. *New journal of physics*, 15(8):085032, 2013.

[360] Ewan J Hemingway, Prashant Mishra, M Cristina Marchetti, and Suzanne M Fielding. Correlation lengths in hydrodynamic models of active nematics. *Soft Matter*, 12(38):7943–7952, 2016.

[361] Sumesh P Thampi, Ramin Golestanian, and Julia M Yeomans. Vorticity, defects and correlations in active turbulence. *Phil. Trans. R. Soc. A*, 372(2029):20130366, 2014.

[362] Sumesh P Thampi, Ramin Golestanian, and Julia M Yeomans. Velocity correlations in an active nematic. *Physical review letters*, 111(11):118101, 2013.

[363] Sumesh P Thampi, Ramin Golestanian, and Julia M Yeomans. Instabilities and topological defects in active nematics. *EPL (Europhysics Letters)*, 105(1):18001, 2014.

[364] Luca Giomi, Lakshminarayanan Mahadevan, Bulbul Chakraborty, and MF Hagan. Excitable patterns in active nematics. *Physical Review Letters*, 106(21): 218101, 2011.

[365] Luca Giomi. Geometry and topology of turbulence in active nematics. *Physical Review X*, 5(3):031003, 2015.

[366] Shradha Mishra, R Aditi Simha, and Sriram Ramaswamy. A dynamic renormalization group study of active nematics. *Journal of Statistical Mechanics: Theory and Experiment*, 2010(02):P02003, 2010.

[367] Suraj Shankar, Sriram Ramaswamy, and M Cristina Marchetti. Low-noise phase of a two-dimensional active nematic system. *Physical Review E*, 97(1):012707, 2018.

[368] Pau Guillamat, Jordi Ignés-Mullol, and Francesc Sagués. Control of active liquid crystals with a magnetic field. *Proceedings of the National Academy of Sciences*, 113(20):5498–5502, 2016.

[369] Xia-qing Shi and Yu-qiang Ma. Topological structure dynamics revealing collective evolution in active nematics. *Nature communications*, 4:3013, 2013.

[370] Luca Giomi, Mark J Bowick, Prashant Mishra, Rastko Sknepnek, and M Cristina Marchetti. Defect dynamics in active nematics. *Phil. Trans. R. Soc. A*, 372 (2029):20130365, 2014.

[371] Tong Gao, Robert Blackwell, Matthew A Glaser, Meredith D Betterton, and Michael J Shelley. Multiscale polar theory of microtubule and motor-protein assemblies. *Physical review letters*, 114(4):048101, 2015.

[372] Subrahmanyan Chandrasekhar. Stochastic problems in physics and astronomy. *Reviews of modern physics*, 15(1):1, 1943.

[373] LM Pismen. Dynamics of defects in an active nematic layer. *Physical Review E*, 88(5):050502, 2013.

[374] Antony N Beris and Brian J Edwards. *Thermodynamics of flowing systems: with internal microstructure*. Number 36. Oxford University Press on Demand, 1994.

[375] Dario Cortese, Jens Eggers, and Tanniemola B Liverpool. Pair creation, motion, and annihilation of topological defects in two-dimensional nematic liquid crystals. *Physical Review E*, 97(2):022704, 2018.

[376] Ananyo Maitra, Pragya Srivastava, M Cristina Marchetti, Juho S Lintuvuori, Sriram Ramaswamy, and Martin Lenz. A nonequilibrium force can stabilize 2d active nematics. *Proceedings of the National Academy of Sciences*, page 201720607, 2018.

[377] Pragya Srivastava, Prashant Mishra, and M Cristina Marchetti. Negative stiffness and modulated states in active nematics. *Soft Matter*, 12(39):8214–8225, 2016.

[378] Eric D Siggia and Annette Zippelius. Dynamics of defects in rayleigh-bénard convection. *Physical Review A*, 24(2):1036, 1981.

[379] Elisabeth Dubois-Violette, Elisabeth Guazzelli, and Jacques Prost. Dislocation motion in layered structures. *Philosophical Magazine A*, 48(5):727–747, 1983.

[380] LM Pismen and JD Rodriguez. Mobility of singularities in the dissipative ginzburg-landau equation. *Physical Review A*, 42(4):2471, 1990.

[381] Lev S Tsimring. Penta-hepta defect motion in hexagonal patterns. *Physical review letters*, 74(21):4201, 1995.

[382] Len M Pismen. *Vortices in nonlinear fields: from liquid crystals to superfluids, from non-equilibrium patterns to cosmic strings*, volume 100. Oxford University Press, 1999.

[383] EI Kats, VV Lebedev, and SV Malinin. Disclination motion in liquid crystalline films. *Journal of Experimental and Theoretical Physics*, 95(4):714–727, 2002.

[384] Arthur J Vromans and Luca Giomi. Orientational properties of nematic disclinations. *Soft matter*, 12(30):6490–6495, 2016.

[385] Xingzhou Tang and Jonathan V Selinger. Orientation of topological defects in 2d nematic liquid crystals. *Soft matter*, 13(32):5481–5490, 2017.

[386] R Kubo. The fluctuation-dissipation theorem. *Reports on progress in physics*, 29(1):255, 1966.

[387] Michael Rubinstein, Boris Shraiman, and David R Nelson. Two-dimensional xy magnets with random dzyaloshinskii-moriya interactions. *Physical Review B*, 27 (3):1800, 1983.

[388] David R Nelson. Reentrant melting in solid films with quenched random impurities. *Physical Review B*, 27(5):2902, 1983.

[389] Li-bing Cai, Hugues Chaté, Yu-qiang Ma, and Xia-qing Shi. Dynamical subclasses of dry active nematics. *Physical Review E*, 99(1):010601, 2019.

[390] Suraj Shankar, Mark J Bowick, and M Cristina Marchetti. Topological sound and flocking on curved surfaces. *Physical Review X*, 7(3):031039, 2017.

[391] Tamás Vicsek, András Czirók, Eshel Ben-Jacob, Inon Cohen, and Ofer Shochet. Novel type of phase transition in a system of self-driven particles. *Physical review letters*, 75(6):1226, 1995.

[392] Vincent Hakim and Pascal Silberzan. Collective cell migration: a physics perspective. *Reports on Progress in Physics*, 80(7):076601, 2017.

[393] Bing He, Konstantin Doubrovinski, Oleg Polyakov, and Eric Wieschaus. Apical constriction drives tissue-scale hydrodynamic flow to mediate cell elongation. *Nature*, 508(7496):392, 2014.

[394] Andrew J Ewald, Audrey Brenot, Myhanh Duong, Bianca S Chan, and Zena Werb. Collective epithelial migration and cell rearrangements drive mammary branching morphogenesis. *Developmental cell*, 14(4):570–581, 2008.

[395] Bakhtier Vasiev, Ariel Balter, Mark Chaplain, James A Glazier, and Cornelis J Weijer. Modeling gastrulation in the chick embryo: formation of the primitive streak. *PLoS One*, 5(5):e10571, 2010.

[396] Sebastian J Streichan, Matthew F Lefebvre, Nicholas Noll, Eric F Wieschaus, and Boris I Shraiman. Global morphogenetic flow is accurately predicted by the spatial distribution of myosin motors. *eLife*, 7:e27454, 2018.

[397] Aliya Fatehullah, Paul L Appleton, and Inke S Näthke. Cell and tissue polarity in the intestinal tract during tumourigenesis: cells still know the right way up, but tissue organization is lost. *Phil. Trans. R. Soc. B*, 368(1629):20130014, 2013.

[398] Laila Ritsma, Saskia IJ Ellenbroek, Anoek Zomer, Hugo J Snippert, Frederic J de Sauvage, Benjamin D Simons, Hans Clevers, and Jacco van Rheenen. Intestinal crypt homeostasis revealed at single-stem-cell level by in vivo live imaging. *Nature*, 507(7492):362–365, 2014.

[399] J. Martin Collinson, Lucy Morris, Alasdair I. Reid, Thaya Ramaesh, Margaret A. Keighren, Jean H. Flockhart, Robert E. Hill, Seong-Seng Tan, Kanna Ramaesh, Baljean Dhillon, and John D. West. Clonal analysis of patterns of growth, stem cell activity, and cell movement during the development and maintenance of the murine corneal epithelium. *Developmental Dynamics*, 224(4):432–440, 2002. ISSN 1097-0177. doi: 10.1002/dvdy.10124.

[400] Hannah G Yevick, Guillaume Duclos, Isabelle Bonnet, and Pascal Silberzan. Architecture and migration of an epithelium on a cylindrical wire. *Proceedings of the National Academy of Sciences*, 112(19):5944–5949, 2015.

[401] Yaouen Fily, Aparna Baskaran, and Michael F Hagan. Dynamics of self-propelled particles under strong confinement. *Soft matter*, 10(30):5609–5617, 2014.

[402] Yaouen Fily, Aparna Baskaran, and Michael F Hagan. Dynamics and density distribution of strongly confined noninteracting nonaligning self-propelled particles in a nonconvex boundary. *Physical Review E*, 91(1):012125, 2015.

[403] Yaouen Fily, Aparna Baskaran, and Michael F Hagan. Equilibrium mappings in polar-isotropic confined active particles. *The European Physical Journal E*, 40 (6):61, 2017.

[404] Nikolai Nikola, Alexandre P Solon, Yariv Kafri, Mehran Kardar, Julien Tailleur, and Raphaël Voituriez. Active particles with soft and curved walls: Equation of state, ratchets, and instabilities. *Physical Review Letters*, 117(9):098001, 2016.

[405] Frank Smallenburg and Hartmut Löwen. Swim pressure on walls with curves and corners. *Physical Review E*, 92(3):032304, 2015.

[406] Richard Green, John Toner, and Vincenzo Vitelli. Geometry of thresholdless active flow in nematic microfluidics. *Physical Review Fluids*, 2(10):104201, 2017.

[407] Yaouen Fily, Aparna Baskaran, and Michael F Hagan. Active particles on curved surfaces. *arXiv preprint arXiv:1601.00324*, 2016.

[408] Rastko Sknepnek and Silke Henkes. Active swarms on a sphere. *Physical Review E*, 91(2):022306, 2015.

[409] Ananyo Maitra, Pragya Srivastava, Madan Rao, and Sriram Ramaswamy. Activating membranes. *Physical review letters*, 112(25):258101, 2014.

[410] SA Mallory, C Valeriani, and A Cacciuto. Curvature-induced activation of a passive tracer in an active bath. *Physical Review E*, 90(3):032309, 2014.

[411] Yuhai Tu, John Toner, and Markus Ulm. Sound waves and the absence of galilean invariance in flocks. *Physical review letters*, 80(21):4819, 1998.

[412] Pierre Delplace, JB Marston, and Antoine Venaille. Topological origin of equatorial waves. *Science*, page eaan8819, 2017.

[413] Alexander B Khanikaev, Romain Fleury, S Hossein Mousavi, and Andrea Alu. Topologically robust sound propagation in an angular-momentum-biased graphene-like resonator lattice. *Nature communications*, 6:8260, 2015.

[414] Pragya Srivastava, Roie Shlomovitz, Nir S Gov, and Madan Rao. Patterning of polar active filaments on a tense cylindrical membrane. *Physical review letters*, 110(16):168104, 2013.

[415] Xingbo Yang, M Lisa Manning, and M Cristina Marchetti. Aggregation and segregation of confined active particles. *Soft matter*, 10(34):6477–6484, 2014.

[416] Sho C Takatori, Wen Yan, and John F Brady. Swim pressure: stress generation in active matter. *Physical review letters*, 113(2):028103, 2014.

[417] Arvind Gopinath, Michael F Hagan, M Cristina Marchetti, and Aparna Baskaran. Dynamical self-regulation in self-propelled particle flows. *Physical Review E*, 85 (6):061903, 2012.

[418] Eric Bertin, Michel Droz, and Guillaume Grégoire. Hydrodynamic equations for self-propelled particles: microscopic derivation and stability analysis. *Journal of Physics A: Mathematical and Theoretical*, 42(44):445001, 2009.

[419] Eric Bertin, Michel Droz, and Guillaume Grégoire. Boltzmann and hydrodynamic description for self-propelled particles. *Physical Review E*, 74(2):022101, 2006.

[420] Murray Eisenberg and Robert Guy. A proof of the hairy ball theorem. *The American Mathematical Monthly*, 86(7):571–574, 1979.

[421] Antoine Bricard, Jean-Baptiste Caussin, Debasish Das, Charles Savoie, Vijayakumar Chikkadi, Kyohei Shitara, Oleksandr Chepizhko, Fernando Peruani, David Saintillan, and Denis Bartolo. Emergent vortices in populations of colloidal rollers. *Nature communications*, 6:7470, 2015.

[422] Delphine Geyer, Alexandre Morin, and Denis Bartolo. Sounds and hydrodynamics of polar active fluids. *Nature materials*, page 1, 2018.

[423] William Kung, M Cristina Marchetti, and Karl Saunders. Hydrodynamics of polar liquid crystals. *Physical Review E*, 73(3):031708, 2006.

[424] Aparna Baskaran and M Cristina Marchetti. Hydrodynamics of self-propelled hard rods. *Physical Review E*, 77(1):011920, 2008.

[425] PC Martin, O Parodi, and Peter S Pershan. Unified hydrodynamic theory for crystals, liquid crystals, and normal fluids. *Physical Review A*, 6(6):2401, 1972.

[426] Adrian E Gill. *Atmosphere - ocean dynamics*. Elsevier, 2016.

[427] Michael V Berry. Quantal phase factors accompanying adiabatic changes. In *Proceedings of the Royal Society of London A: Mathematical, Physical and Engineering Sciences*, volume 392, pages 45–57. The Royal Society, 1984.

[428] GE Volovik. An analog of the quantum hall effect in a superfluid 3 he film. *Soviet Physics-JETP (English Translation)*, 67(9):1804–1811, 1988.

[429] Shinsei Ryu, Andreas P Schnyder, Akira Furusaki, and Andreas WW Ludwig. Topological insulators and superconductors: tenfold way and dimensional hierarchy. *New Journal of Physics*, 12(6):065010, 2010.

[430] Holger Bech Nielsen and Masao Ninomiya. Absence of neutrinos on a lattice:(i). proof by homotopy theory. *Nuclear Physics B*, 185(1):20–40, 1981.

[431] JE Avron. Odd viscosity. *Journal of statistical physics*, 92(3-4):543–557, 1998.

[432] Debarghya Banerjee, Anton Souslov, Alexander G Abanov, and Vincenzo Vitelli. Odd viscosity in chiral active fluids. *Nature Communications*, 8(1):1573, 2017.

[433] Vishal Soni, Ephraim Bililign, Sofia Magkiriadou, Stefano Sacanna, Denis Bartolo, Michael J Shelley, and William Irvine. The free surface of a colloidal chiral fluid: waves and instabilities from odd stress and hall viscosity. *arXiv preprint arXiv:1812.09990*, 2018.

[434] Anton Souslov, Kinjal Dasbiswas, Michel Fruchart, Suriyanarayanan Vaikuntanathan, and Vincenzo Vitelli. Topological waves in fluids with odd viscosity. *Physical Review Letters*, 122(12):128001, 2019.

[435] Clément Tauber, Pierre Delplace, and Antoine Venaille. Odd bulk-interface correspondence in fluids. *arXiv preprint arXiv:1812.05488*, 2018.

[436] Daniel Leykam, Konstantin Y Bliokh, Chunli Huang, YD Chong, and Franco Nori. Edge modes, degeneracies, and topological numbers in non-hermitian systems. *Physical Review Letters*, 118(4):040401, 2017.

[437] Roman Jackiw and Claudio Rebbi. Solitons with fermion number 1/2. *Physical Review D*, 13(12):3398, 1976.

[438] Eugene P Wigner. The unreasonable effectiveness of mathematics in the natural sciences. In *Mathematics and Science*, pages 291–306. World Scientific, 1990.

[439] Yichao Tang, Gaojian Lin, Shu Yang, Yun Kyu Yi, Randall D Kamien, and Jie Yin. Programmable kiri-kirigami metamaterials. *Advanced Materials*, 29(10): 1604262, 2017.

[440] Vitor M Pereira and AH Castro Neto. Strain engineering of graphenes electronic structure. *Physical Review Letters*, 103(4):046801, 2009.

[441] Francisco Guinea, MI Katsnelson, and AK Geim. Energy gaps and a zero-field quantum hall effect in graphene by strain engineering. *Nature Physics*, 6(1):30, 2010.

[442] Vitor M Pereira, AH Castro Neto, HY Liang, and L Mahadevan. Geometry, mechanics, and electronics of singular structures and wrinkles in graphene. *Physical review letters*, 105(15):156603, 2010.

[443] Chen Si, Zhimei Sun, and Feng Liu. Strain engineering of graphene: a review. *Nanoscale*, 8(6):3207–3217, 2016.

[444] John Rogers, Yonggang Huang, Oliver G Schmidt, and David H Gracias. Origami mems and nems. *Mrs Bulletin*, 41(2):123–129, 2016.

[445] Ryan JT Nicholl, Hiram J Conley, Nickolay V Lavrik, Ivan Vlassiouk, Yevgeniy S Puzyrev, Vijayashree Parsi Sreenivas, Sokrates T Pantelides, and Kirill I Bolotin. The effect of intrinsic crumpling on the mechanics of free-standing graphene. *Nature communications*, 6:8789, 2015.

[446] Andrej Košmrlj and David R Nelson. Response of thermalized ribbons to pulling and bending. *Physical Review B*, 93(12):125431, 2016.

[447] Mark J Bowick, Andrej Košmrlj, David R Nelson, and Rastko Sknepnek. Non-hookean statistical mechanics of clamped graphene ribbons. *Physical Review B*, 95(10):104109, 2017.

[448] David Yllanes, Sourav S Bhabesh, David R Nelson, and Mark J Bowick. Thermal crumpling of perforated two-dimensional sheets. *Nature communications*, 8(1):1381, 2017.

[449] Emily R Russell, Rastko Sknepnek, and Mark Bowick. Stiffening thermal membranes by cutting. *Physical Review E*, 96(1):013002, 2017.

[450] AP Young. Melting and the vector coulomb gas in two dimensions. *Physical Review B*, 19(4):1855, 1979.

[451] G Wachtel, LM Sieberer, S Diehl, and E Altman. Electrodynamic duality and vortex unbinding in driven-dissipative condensates. *Physical Review B*, 94(10):104520, 2016.

[452] LM Sieberer, G Wachtel, E Altman, and S Diehl. Lattice duality for the compact kardar-parisi-zhang equation. *Physical Review B*, 94(10):104521, 2016.

[453] Igor S Aranson, Hugues Chaté, and Lei-Han Tang. Spiral motion in a noisy complex ginzburg-landau equation. *Physical review letters*, 80(12):2646, 1998.

[454] Igor S Aranson and Lorenz Kramer. The world of the complex ginzburg-landau equation. *Reviews of Modern Physics*, 74(1):99, 2002.

[455] Georgios Roumpos, Michael Lohse, Wolfgang H Nitsche, Jonathan Keeling, Marzena Hanna Szymańska, Peter B Littlewood, Andreas Löffler, Sven Höfling, Lukas Worschech, Alfred Forchel, et al. Power-law decay of the spatial correlation function in exciton-polariton condensates. *Proceedings of the National Academy of Sciences*, 109(17):6467–6472, 2012.

[456] G Dagvadorj, JM Fellows, S Matyjaśkiewicz, FM Marchetti, I Carusotto, and MH Szymańska. Nonequilibrium phase transition in a two-dimensional driven open quantum system. *Physical Review X*, 5(4):041028, 2015.

[457] Ehud Altman, Lukas M Sieberer, Leiming Chen, Sebastian Diehl, and John Toner. Two-dimensional superfluidity of exciton polaritons requires strong anisotropy. *Physical Review X*, 5(1):011017, 2015.

[458] A Zamora, LM Sieberer, K Dunnett, S Diehl, and MH Szymańska. Tuning across universalities with a driven open condensate. *Physical Review X*, 7(4): 041006, 2017.

[459] Igor S Aranson, Stefan Scheidl, and Valerii M Vinokur. Nonequilibrium dislocation dynamics and instability of driven vortex lattices in two dimensions. *Physical Review B*, 58(21):14541, 1998.

[460] Mehran Kardar, Giorgio Parisi, and Yi-Cheng Zhang. Dynamic scaling of growing interfaces. *Physical Review Letters*, 56(9):889, 1986.

[461] Leiming Chen, John Toner, et al. Universality for moving stripes: A hydrodynamic theory of polar active smectics. *Physical review letters*, 111(8):088701, 2013.

[462] Tapan Chandra Adhyapak, Sriram Ramaswamy, and John Toner. Live soap: stability, order, and fluctuations in apolar active smectics. *Physical review letters*, 110(11):118102, 2013.

[463] L. M. Sieberer and E. Altman. Topological defects in anisotropic driven open systems. *Phys. Rev. Lett.*, 121:085704, Aug 2018.

[464] Matteo Paoluzzi, Umberto Marini Bettolo Marconi, and Claudio Maggi. Effective equilibrium picture in the x y model with exponentially correlated noise. *Physical Review E*, 97(2):022605, 2018.

[465] Ariel Amir and David R Nelson. Dislocation-mediated growth of bacterial cell walls. *Proceedings of the National Academy of Sciences*, 109(25):9833–9838, 2012.

[466] Guillaume Briand, Michael Schindler, and Olivier Dauchot. Spontaneously flowing crystal of self-propelled particles. *Physical review letters*, 120(20):208001, 2018.

[467] Pasquale Digregorio, Demian Levis, Antonio Suma, Leticia F. Cugliandolo, Giuseppe Gonnella, and Ignacio Pagonabarraga. Full phase diagram of active brownian disks: From melting to motility-induced phase separation. *Phys. Rev. Lett.*, 121:098003, Aug 2018.

[468] Stephen J DeCamp, Gabriel S Redner, Aparna Baskaran, Michael F Hagan, and Zvonimir Dogic. Orientational order of motile defects in active nematics. *Nature materials*, 14(11):1110, 2015.

[469] Elias Putzig, Gabriel S Redner, Arvind Baskaran, and Aparna Baskaran. Instabilities, defects, and defect ordering in an overdamped active nematic. *Soft Matter*, 12(17):3854–3859, 2016.

[470] Alexei A Abrikosov. On the magnetic properties of superconductors of the second group. *Sov. Phys. JETP*, 5:1174–1182, 1957.

[471] Miha Ravnik and Julia M Yeomans. Confined active nematic flow in cylindrical capillaries. *Physical review letters*, 110(2):026001, 2013.

[472] Tyler N Shendruk, Amin Doostmohammadi, Kristian Thijssen, and Julia M Yeomans. Dancing disclinations in confined active nematics. *Soft Matter*, 13 (21):3853–3862, 2017.

[473] Michael M Norton, Arvind Baskaran, Achini Opathalage, Blake Langeslay, Seth Fraden, Aparna Baskaran, and Michael F Hagan. Insensitivity of active nematic liquid crystal dynamics to topological constraints. *Physical Review E*, 97(1): 012702, 2018.

[474] Achini Opathalage, Michael M Norton, Michael PN Juniper, Blake Langeslay, S Ali Aghvami, Seth Fraden, and Zvonimir Dogic. Self-organized dynamics and the transition to turbulence of confined active nematics. *Proceedings of the National Academy of Sciences*, 116(11):4788–4797, 2019.

[475] Jérôme Hardoüin, Rian Hughes, Amin Doostmohammadi, Justine Laurent, Teresa Lopez-Leon, Julia M Yeomans, Jordi Ignés-Mullol, and Francesc Sagués. Reconfigurable flows and defect landscape of confined active nematics. *arXiv preprint arXiv:1903.01787*, 2019.

[476] Amin Doostmohammadi, Sumesh P Thampi, and Julia M Yeomans. Defect-mediated morphologies in growing cell colonies. *Physical review letters*, 117(4): 048102, 2016.

[477] Zhihong You, Daniel JG Pearce, Anupam Sengupta, and Luca Giomi. Geometry

and mechanics of microdomains in growing bacterial colonies. *Physical Review X*, 8(3):031065, 2018.

[478] D DellArciprete, ML Blow, AT Brown, FDC Farrell, JS Lintuvuori, AF McVey, D Marenduzzo, and WCK Poon. A growing bacterial colony in two dimensions as an active nematic. *Nature communications*, 9(1):4190, 2018.

[479] Gretchen A DeVries, Markus Brunnbauer, Ying Hu, Alicia M Jackson, Brenda Long, Brian T Neltner, Oktay Uzun, Benjamin H Wunsch, and Francesco Stellacci. Divalent metal nanoparticles. *Science*, 315(5810):358–361, 2007.

[480] David R Nelson. Toward a tetravalent chemistry of colloids. *Nano Letters*, 2 (10):1125–1129, 2002.

[481] Vincenzo Vitelli and Ari M Turner. Anomalous coupling between topological defects and curvature. *Physical review letters*, 93(21):215301, 2004.

[482] Sadoc Jean-François. *Geometry in condensed matter physics*, volume 9. World Scientific, 1990.

[483] Xavier Serra-Picamal, Vito Conte, Romaric Vincent, Ester Anon, Dhananjay T Tambe, Elsa Bazellieres, James P Butler, Jeffrey J Fredberg, and Xavier Trepat. Mechanical waves during tissue expansion. *Nature Physics*, 8(8):628–634, 2012.

[484] Fredrik EO Holmberg, Jakob B Seidelin, Xiaolei Yin, Benjamin E Mead, Zhixiang Tong, Yuan Li, Jeffrey M Karp, and Ole H Nielsen. Culturing human intestinal stem cells for regenerative applications in the treatment of inflammatory bowel disease. *EMBO Molecular Medicine*, 2017. ISSN 1757-4676. doi: 10.15252/emmm.201607260.

[485] Sevan Hopyan, James Sharpe, and Yingzi Yang. Budding behaviors: Growth of the limb as a model of morphogenesis. *Developmental Dynamics*, 240(5): 1054–1062, 2011.

[486] Arvind Murugan and Suriyanarayanan Vaikuntanathan. Topologically protected modes in non-equilibrium stochastic systems. *Nature communications*, 8:13881, 2017.

# Curriculum Vitae

**AUTHOR**: Suraj Shankar

**NATONALITY**: Indian

**DATE OF BIRTH**: 05 October, 1992

**DEGREES AWARDED**:

B. Tech (Honours) in Chemical Engineering, Indian Institute of Technology, Madras, India (2010 - 2014)

**PROFESSIONAL EMPLOYMENT**:

Research Assistant, Department of Physics, Syracuse University (2014 - 2019)

**PUBLICATIONS**:

- M. Moshe, E. Esposito, **S. Shankar**, B. Bircan, I. Cohen, D. R. Nelson, M. J. Bowick; "Kirigami mechanics as stress relief by elastic charges", Phys. Rev. Lett. **122**, 048001 (2019) [arXiv:1808.00925]

- M. Moshe, E. Esposito, **S. Shankar**, B. Bircan, I. Cohen, D. R. Nelson, M. J. Bowick; "Nonlinear mechanics of thin frames", Phys. Rev. E **99**, 013002 (2019) [arXiv:1801.08263]

- **S. Shankar**, S. Ramaswamy, M. C. Marchetti, M. J. Bowick; "Defect unbinding in active nematics", Phys. Rev. Lett. **121**, 108002 (2018) [arXiv:1804.06350]

- **S. Shankar**, M. C. Marchetti; "Hidden entropy production and work fluctuations in an ideal active gas", Phys. Rev. E **98**, 020604(R) (2018) [arXiv:1804.03099]
- **S. Shankar**, S. Ramaswamy, M. C. Marchetti; "Low-noise phase of a two-dimensional active nematic system", Phys. Rev. E **97**, 012707 (2018) [arXiv:1710.05400] (Editor's suggestion)
- **S. Shankar**, M. J. Bowick, M. C. Marchetti; "Topological sound and flocking on curved surfaces", Phys. Rev. X **7**, 031039 (2017) [arXiv:1704.05424] (Featured in Physics Synopsis)
- P. Guillamat, J. Ignés-Mullol, **S. Shankar**, M. C. Marchetti, F. Sagués; "Probing the shear viscosity of an active nematic film", Phys. Rev. E, **94**, 060602(R) (2016) [arXiv:1606.05764]

**AWARDS**:

- Harvard Junior Fellowship (2019)
- Kavli Institute for Theoretical Physics (KITP) Graduate Fellow (Fall 2017)
- Syracuse University IGERT Associate (2017)
- Levinstein Fellowship for Outstanding Junior Graduate Student (2015)
- Syracuse University Graduate Fellowship (2014)
- Prof. M Ramanujam Memorial Award in Chemical Engineering at IIT Madras (2012)

**PRESENTATIONS**:

*Invited Talks*

- “Topological aspects of active & living matter”, Condensed Matter Physics Seminar: Harvard University, Massachusetts, USA, Nov 2018
- “Flocks on a sphere sound topological”, Seminar: Center for Physics of Biological Function, Princeton University, New Jersey, USA, Oct 2018
- “Statistics and Mechanics of Kirigami”, Workshop on **Geometry of Soft Matter** at IIP, Natal, Brazil, May 2018
- “Flocks on a sphere sound topological”, Workshop on **Topological protection in messy matter: disorder, quasicrystals, fluids and emergent states**, Georgia Institute of Technology, Atlanta, USA, May 2018
- “Topological Sound & Flocking on Curved Surfaces”, Berkeley Fluids Seminar: UC Berkeley, Berkeley, USA, Sept 2017
- “Probing Defect Dynamics in a 2D Active Nematic”, Soft/Bio Seminar: MRL, UCSB, Santa Barbara, USA, April 2017
- “Controlling Defect Dynamics in a 2D Active Nematic”, Seminar: TIFR - TCIS Hyderabad, India, Aug 2016

*Contributed Talks & Posters*

- “Defect unbinding and a motile Kosterlitz-Thouless transition in active nematics”, APS March meeting, Boston, USA, March 2019
- **Materials Research Outreach Program Symposium** 2019, UC Santa Barbara, California, USA, Jan 2019 (*Poster Presentation*: When topology gets active!)
- “Flocking on Curved Surfaces and Topological Sound”, APS March Meeting, Los Angeles, USA, March 2018

- Aspen Winter Conference on **Fundamental Problems in Active Matter** at Aspen Center for Physics, Colorado, USA, Jan 2018 (*Best Poster Award*: Irreversibility in an active gas)

- **Gordon Research Seminar & Conference** on Soft Condensed Matter Physics at Colby-Sawyer College, New Hampshire, USA, Aug 2017 (*Poster Presentation*: Topological Sound and Flocking on Curved Surfaces)

- 7th **Northeast Complex Fluids & Soft Matter Workshop** at Princeton University, New Jersey, USA, May 2017 (*Best Poster Award*: Topological Sound and Flocking on Curved Surfaces)

- "Geometry and Mechanics of Kirigami", APS March Meeting, New Orleans, USA, March 2017

- "Controlling Defects and Flow in Active Nematic Suspensions", APS March Meeting, Baltimore, USA, March 2016

- Workshop on **Small Clusters, Polymer Vesicles and Unusual Minima** at ICERM, Providence, USA, March 2015 (*Poster Presentation*: Confined Nematic Defects as Active Particles)

**SCHOOLS**:

- 8th School on Mathematical Physics: **Random Geometries**, at Universidad de los Andes, Bogota, Colombia, May 2016 (*Teaching Assistant*)

- Boulder School for Condensed Matter and Materials Physics: **Soft Matter In and Out of Equilibrium**, at UC Boulder, Boulder, Colorado, USA, July 2015 (*Poster Presentation*: Confined Nematic Defects as Active Particles)

- "Numerical Methods in Fluid Flow Computations", 11th **Indo-German Winter Academy** (Modeling & Algorithms For Fluid Dynamics & Heat Transfer) at CSIR-CMERI, Durgapur, India, Dec 2012

**PROFESSIONAL SERVICES**:

Referee for Nature, Physical Review Letters, Physical Review E, Proceedings of the National Academy of Sciences, Journal of Fluid Mechanics, New Journal of Physics and Soft Matter.